

UNBOUND STATES IN THE LIGHTEST ISLAND OF INVERSION: NEUTRON DECAY
MEASUREMENTS OF ^{11}Li , ^{10}Li , AND ^{12}Be

By

Jenna Kathleen Smith

A DISSERTATION

Submitted to
Michigan State University
in partial fulfillment of the requirements
for the degree of

Physics - Doctor of Philosophy

2014

ABSTRACT

UNBOUND STATES IN THE LIGHTEST ISLAND OF INVERSION: NEUTRON DECAY MEASUREMENTS OF ^{11}Li , ^{10}Li , AND ^{12}Be

By

Jenna Kathleen Smith

The light nuclei in the $N \sim 8$ region provide easily accessible systems for studying the structure of exotic nuclei. The nuclide ^{11}Li is a two-neutron halo system, a Borromean nucleus, and located in the $N \sim 8$ island of inversion. The next lightest lithium isotope, ^{10}Li is neutron unbound, located on the western edge of the island of inversion, and important for the understanding of the ^{11}Li system. ^{12}Be is the heaviest $N = 8$ isotone in the island of inversion. Neutron unbound states from all three systems have been measured and analyzed in this work.

The experiment was conducted at the National Superconducting Cyclotron Laboratory. Beams of exotic boron isotopes (^{12}B and ^{13}B) were provided by the Coupled Cyclotron Facility and delivered to the MoNA-LISA-Sweeper setup, each at 71 MeV/u. The neutron-unbound isotopes were created in a secondary beryllium target where they immediately decayed into a charged daughter fragment and one or two neutrons. The charged daughter fragment was measured by a suite of charged particle detectors and the neutrons were detected by MoNA-LISA.

Measurement of the ^{11}Li unbound system showed a state at 1210 ± 80 keV excitation energy with a width greater than 1200 keV, consistent with previous measurements. Correlations between the three decay products were examined with use of Jacobi spectra and Dalitz plots, which revealed a correlation between the two neutrons stronger than that expected from the decay of two neutrons uncorrelated in the nucleus. This is the first correlation measurement attributable to a specific unbound state in ^{11}Li . Unbound states in ^{10}Li were populated with a two-proton knockout from a ^{12}B beam, a reaction expected to populate primarily positive-parity states. The decay energy spectra of ^{10}Li was fit with three peaks at 110 ± 40 keV, 500 ± 100 keV, and 1100 ± 100 keV. The lowest two of these peaks are expected to be a $1^+/2^+$ doublet. Calculation of the $0p_{1/2}$ single particle energy in the ^{10}Li system and comparison with Faddeev calculations suggests that both states of the $2^-/1^-$ doublet are below 50 keV, consistent with previous measurements of one $\ell = 0$ state at 50 keV or below. In the ^{12}Be system, a measured decay energy of 1243 ± 20 keV corresponds to an excitation energy between 4400 and 4800 keV, depending on the combination of final states populated in ^{11}Be . A lack of decays to ^{10}Be placed an upper limit of 5% on the branching ratio to the ground state of ^{10}Be via $2n$ emission. This low branching ratio, as well as spin and parity selectivity from the $1p$ -knockout production mechanism, suggests that the spin and parity of this state is 1^- or 2^- .

In honor of all those who blazed the trail and made my path possible

ACKNOWLEDGMENTS

Nuclear physics is a team sport and this thesis was no exception. There are scores of people whose collaboration, experience, and friendship have influenced my time in graduate school. My advisor Michael Thoennessen provided guidance and expertise during my five years at Michigan State University and was quite adept at dispensing both words of encouragement and skepticism. The other members of my committee, Filomena Nunes, Artemis Spyrou, Stuart Tessmer, and Kirsten Tollefson I thank for their time, attention, and interesting discussion during our meetings, especially Artemis who served as a secondary advisor and mentor during my time here.

I have enjoyed working with the MoNA Collaboration from day one, both the local group and the larger collaboration. Thomas Baumann is an extraordinary device physicist without whom I'm not sure MoNA-LISA would have worked. These five years were made easier and more enjoyable thanks to the support, collaboration, and comraderie of the other graduate students and post-docs in our group: Michael Strongman, Greg Christian, Shea Mosby, Michelle Mosby, Jesse Snyder, Zach Kohley, Michael Jones, and Krystin Stiefel. Thanks are due to the external collaborators: for building both MoNA and LISA as well as serving as a sounding board and mentors for the past five years. Without all your experience and contributions, my experiment would not have been as successful as it was. I am especially grateful for the opportunity to work closely with Nathan Frank on the development of the CsI(Na) array. Paul DeYoung and Braden Marks made specific contributions to this analysis by correcting the walk in the target scintillator timing and cleaning up the beryllium isotope identification. Though not a member of the MoNA Collaboration, Alexander Volya's work was the basis for the two-neutron decay lineshapes used in this work and I'm also grateful for the clarifying emails he exchanged with me.

The experiment that this work is based on began with a pure and intense secondary beam that was produced by the Coupled Cyclotron Facility and the A1900 Fragment Separator. The high-quality beam they provided gave us a stable running status for which I am eternally grateful. Without Daniel Bazin and Scott Williams and their assistance with the charged-particle detectors, we would only have been able to make a half measurement.

Beyond this specific work, the lab community and graduate student community have made the past five years truly enjoyable. To those graduate students that I have been honored to call friends, thanks for the venting sessions, the laughs, the thoughtful suggestions, the chocolate, and the Happy Hours. Sharing life's highs with you has made them more enjoyable and sharing the lows made them more bearable. I had fantastic office-mates, who served as sounding boards and helped me deal with stress (or celebrate) via Nerf Gun fights. Thanks for listening to my musings and encouraging me to be a better physicist. I'm thankful to the NSCL Cycling and DALMAC crews, with whom I shared many hours in the saddle and possibly just as many rehydrating and refueling. I wouldn't be such an avid cyclist without your company. The Grand Canonical Ensemble welcomed me to the group during my first weeks in East Lansing and served as a needed outlet for my more dramatic tendencies over the next few years. I'm honored they allowed me to direct them for the last two years.

Of course, one does not simply arrive at graduate school without help. I am indebted to the many teachers I have had over the years who have nurtured my curiosity in scientific observation, from worms in elementary school to magnetorheological fluid in college. Thanks in particular to Mark Blachly for showing me that a PhD in physics was a possibility, challenging me every single day in class, and making me earn every single Twix bar.

I would not be here without the full-throated encouragement and never-failing confidence sup-

plied by my family, both immediate and extended. You facilitated and encouraged my interest in science both before and after school. Thanks for teaching me long division over breakfast, nagging me to work on my science projects, and always pushing me to follow my passions, even when they were somewhat unconventional.

Finally, I thank Ragnar for being my rock. You have been a vocal cheerleader, a shoulder to cry on, a neutral sounding board, and my most difficult jury. I am a better person and better physicist because of you. I look forward to our next adventure.

TABLE OF CONTENTS

LIST OF TABLES	ix
LIST OF FIGURES	xix
Chapter 1 Introduction	1
1.1 Chart of nuclides	1
1.2 Shell model	1
1.3 Islands of inversion	4
1.4 Halo nuclei	5
1.5 Three-body correlations and decays	6
1.6 Previous experiments	10
1.6.1 Lithium isotopes: $A = 11, 10, 9$	10
1.6.2 Beryllium isotopes: $A = 12, 11, 10$	15
Chapter 2 Theoretical background	17
2.1 Single neutron decay	17
2.1.1 R-matrix derivation	17
2.1.2 Saturation of resonance lineshape	20
2.2 Two neutron decay	20
2.2.1 Phase space decay	21
2.2.2 Sequential decay	22
2.2.3 Dineutron decay	23
Chapter 3 Experimental techniques	25
3.1 Beam production	25
3.2 Beam detector and target	25
3.3 Sweeper magnet	27
3.4 Charged particle detectors	27
3.4.1 Blocker	27
3.4.2 Cathode Readout Drift Counters	28
3.4.3 Ion chamber	29
3.4.4 Timing scintillator	30
3.4.5 CsI(Na) array	30
3.5 MoNA-LISA	32
3.6 Electronics and Data Acquisition	33
3.7 Invariant mass spectroscopy	34
3.8 Particle correlation techniques	35
3.8.1 Jacobi coordinates	36
3.8.2 Dalitz plots	37
Chapter 4 Data Analysis	41
4.1 Calibrations and corrections	41
4.1.1 Charged particle calibrations and corrections	41
4.1.1.1 CRDCs	41
4.1.1.2 Ion chamber	45

4.1.1.3	Thin scintillator	48
4.1.1.4	Other timing scintillators	53
4.1.1.5	CsI(Na) array	55
4.1.2	MoNA-LISA calibrations and corrections	55
4.1.2.1	Charge calibration	55
4.1.2.2	Position calibration	56
4.1.2.3	Time calibrations	57
4.2	Event selection	60
4.2.1	Beam identification	60
4.2.2	Event quality gates	60
4.2.3	Isotope identification	63
4.2.4	Neutron interaction selection	68
4.3	Inverse tracking	74
4.4	Modeling and simulation	75
4.4.1	Incoming beam parameters	76
4.4.2	Beam energy	78
4.4.3	Reaction parameters	82
4.4.4	Other parameters	84
4.4.5	Additional cuts	84
4.4.6	Decay models	85
4.4.6.1	Single neutron decay	85
4.4.6.2	Two neutron decay	86
4.5	Fitting and error analysis	87
Chapter 5 Results and Discussion		89
5.1	^{11}Li	89
5.2	^{10}Li	102
5.3	^{12}Be	111
Chapter 6 Summary and Conclusions		119
REFERENCES		121

LIST OF TABLES

Table 1.1	Previous measurements of unbound states in ^{11}Li below 5 MeV. The energy shown here is the excitation energy. When papers reported a decay energy, the two-neutron separation energy $S_{2n} = 369.15$ keV [51] was added to produce the excitation energy.	10
Table 1.2	Previous measurements of low-lying unbound states in ^{10}Li under 2 MeV. The energy shown here is the decay energy.	13
Table 4.1	CRDC1 mask calibration slopes and offsets from all CRDC1 mask runs. Because there were so few holes in the y -direction (typically only 3), errors were unreasonably small. Slopes and offsets have been truncated at the same significance as their CRDC2 counterparts (Table 4.2).	46
Table 4.2	CRDC2 mask calibration slopes and offsets from all CRDC2 mask runs.	46
Table 4.3	Ion chamber position and time correction coefficient values.	47
Table 4.4	Thin scintillator locations and gain-matching slopes and offsets.	50
Table 4.5	Thin scintillator position and time correction coefficient values.	51
Table 4.6	Calibration parameters for the timing signals from the A1900 and target scintillators.	53
Table 4.7	Final time offsets for each table of MoNA-LISA, before and after the electronics change.	59
Table 4.8	List of correction factors used to produce the lithium isotope separation parameter. The numbers in the right column were multiplied by the parameter on the left, summed, and added to the time-of-flight from the A1900 to the thin to produce a corrected time-of-flight parameter for the lithium isotopes from the ^{13}B beam. Both position parameters, x and y , were calculated 12.59 cm downstream of CRDC1.	64
Table 4.9	List of correction factors used to produce the beryllium isotope separation parameter. The numbers in the right column were multiplied by the parameter on the left, summed, and added to the time-of-flight from the A1900 to the thin to produce a corrected time-of-flight parameter for the lithium isotopes from the ^{13}B beam. Both position parameters, x and y , were calculated 12.59 cm downstream of CRDC1.	65

Table 4.10	List of simulation parameters used to recreate the incoming ^{13}B beam profile. Part 1 recreated the horizontal peak around 30 mm in the y -position of CRDC2, Part 2 recreated the square background, and Part 3 recreated the slanted peak around -20 mm in the y -position.	78
Table 4.11	List of simulation parameters used to recreate the incoming ^{12}B beam profile. Part 1 recreated the horizontal peak around 30 mm in the y -position of CRDC2, Part 2 recreated the square background, and Part 3 recreated the slanted peak around -20 mm in the y -position.	80
Table 4.12	Widths of the parallel and perpendicular kicks used to reproduce the kicks of the knockout reaction.	83
Table 5.1	Energies and widths for best fits of each two-neutron decay model. Error bars are only statistical.	96
Table 5.2	Energies and widths used for the best dineutron fit shown in Figures 5.9 and 5.10. Decay through a ~ 200 keV $\ell = 1$ state, shown in Figure 5.5, was minimized at zero contribution to the total spectrum.	97
Table 5.3	Sources of systematic error in the ^{11}Li “dineutron” decay. Sources of error in the data are in the top section and sources of error in the simulation are in the second section. Here, MoNA-LISA is abbreviated with ML.	97
Table 5.4	Best fit parameters as used in Figure 5.18. Quantities with error bars were measured. Other parameters, such as relative contribution and the width, are reported without error bars, simply for reference.	102
Table 5.5	Sources of systematic error in the ^{10}Li decay. Sources of error in the data are in the top section. The sources of error from the simulation tabulated in Table 5.3 (ML position resolution, ML time resolution, and ML PMT threshold) were all dominated by the error from the fitting. Here, MoNA-LISA is abbreviated as ML.	105
Table 5.6	Sources of systematic error in the ^{12}Be decay. Sources of error in the data are in the top section and sources of error in the simulation are in the second section.	113
Table 5.7	Parameters for potential decays from positive and negative parity states in ^{12}Be , using $S_n=3169\pm 16$ keV [117].	113

LIST OF FIGURES

Figure 1.1	Chart of the nuclides, showing the principal decay mode of the nuclide. Data from [1].	2
Figure 1.2	Wood-Saxon orbitals (left) and Wood-Saxon plus spin-orbit orbitals. Numbers indicate the number of particles required to fill the levels up to those large shell gaps, commonly called “magic numbers”	3
Figure 1.3	Difference between $0p_{1/2}$ and $1s_{1/2}$ neutron single-particle energies for the $N = 7$ isotones. Data from Ref. [6] and references therein.	4
Figure 1.4	Chart of the nuclides and the five predicted islands of inversion (red circles) [7].	5
Figure 1.5	Drawings of two halo nuclei: ^{11}Be (left) and ^{11}Li (right).	5
Figure 1.6	Deduced neutron (blue), proton (red), and matter (black) radii of lithium and beryllium isotopes. Data from [19].	6
Figure 1.7	Chart of the nuclides, showing the known neutron and proton halo nuclei and the suspected neutron halo nuclei as reported by Tanihata, Savajols, and Kanungo [19]. Red squares indicate confirmed proton halo nuclei, dark blue squares indicate confirmed neutron halo nuclei, and light blue squares indicate potential neutron halo nuclei. Black squares indicate stable nuclei and the gray squares indicate bound nuclei.	7
Figure 1.8	Level diagram for two-neutron decay labeling E_k^1 and Γ_I	8
Figure 1.9	Level diagram of states in $^{11,10,9}\text{Li}$, relative to the ground state of ^{11}Li . Neutron separation energies are from Refs. [51–56]. Excited state energies and parities for $^{10,11}\text{Li}$ are general summaries of measurements presented in Tables 1.2 and 1.1. Ground state spin of ^{11}Li from Ref. [57]. Excited state spins in ^{10}Li are expected spins and parities based on $1s_{1/2}$ and $0p_{3/2}$ neutrons coupling with a $0p_{3/2}$ proton. Energy, spin, and parity of first excited state in ^9Li from Refs. [58–60]	9
Figure 1.10	Previous measurements of ^{11}Li with excitation energies less than 3.5 MeV. .	11
Figure 1.11	Previous measurements of unbound, positive-parity states in ^{10}Li . Measurements reported without error have arrows for error bars. Two different measurements in Chernyshev’s 2013 paper produced two different measurements of 0.7 ± 0.05 and 0.78 ± 0.15 MeV, here the weighted average is used [72]. “Both Gornov’s 1998 paper [97] and Santi’s 2003 paper [101] found two possible fits for the data. Details are in Table 1.2 and footnotes within. . .	14

Figure 1.12	Level diagram of states in $^{12,11,10}\text{Be}$, relative to the ground state of ^{12}Be . Neutron separation energies are from [117, 118]. Bound and resonant state energies are from [107, 108, 111, 113–116].	16
Figure 2.1	Energy-dependent Breit-Wigner lineshapes with varying Γ_0 . For all lineshapes, $\ell = 1$ and $E_0 = 1.0$ MeV. All lineshapes have been normalized to the same peak height.	21
Figure 2.2	A diagram of the sequential decay described.	22
Figure 3.1	Schematic of the Coupled Cyclotron Facility and A1900 Fragment Separator with the production setting for this experiment.	26
Figure 3.2	Schematic of the experimental area.	27
Figure 3.3	Schematic of CRDC operation modified from [139] where the z -direction has been expanded for detail. The field shaping wires mentioned in the text are not included for visibility and simplicity.	28
Figure 3.4	Schematic of ion chamber.	29
Figure 3.5	A schematic of the thin scintillator, as seen from upstream of the detector.	30
Figure 3.6	A mechanical design drawing of the CsI(Na) array.	31
Figure 3.7	A schematic of a MoNA LISA bar.	32
Figure 3.8	Schematic of the MoNA-LISA-Sweeper electronics set-up.	33
Figure 3.9	Three possible coordinate definitions for a three-body system.	36
Figure 3.10	T and Y systems and associated Jacobi coordinates for fragment+ $n + n$ system.	36
Figure 3.11	Example Jacobi plots for a phase space decay (black), a dineutron decay (red), and a sequential decay (blue). The left column shows Jacobi coordinates from the T-system and the right column shows Jacobi coordinates from the Y-system. The energy ratios are shown on the top row and the angular distributions are shown in the bottom row. All distributions are without any acceptances or resolutions applied. In the $\cos\theta$ -T system plot, the dineutron and phase space lines overlap.	38

Figure 3.12	Example Dalitz plots for a phase space decay (upper left), a dineutron decay (upper right), and two sequential decays (bottom row). The sequential decay in the bottom left panel shows a decay through an intermediate state approximately halfway between the initial and final states, while the sequential decay shown in the bottom right has a more asymmetric energy distribution. All distributions are without any acceptances or resolutions applied.	39
Figure 4.1	Examples of total charge spectra for two pads in CRDC2. Pad 64 (left) is an example of a good total charge spectrum and pad 24 (right) is an example of a bad total charge spectrum.	42
Figure 4.2	Example charge distribution on CRDC pads as a function of time. A full charge integration measurement would integrate the shaded area on the left. The sampling method adds the values of a discrete number of points, as shown on the right.	42
Figure 4.3	CRDC y -position versus number of samples collected for each pad (left: CRDC1, right: CRDC2). Both plots are shown with the z -axis on a log scale. Each CRDC collects fewer samples at certain regularly spaced intervals along the y -direction, visible in these plots as enhancements at lower numbers of samples and vacancies at the spectra for four samples.	43
Figure 4.4	An example of a charge distribution fit for CRDC2. The centroid of the Gaussian fit, shown here by the vertical line, would be used as the position of the particle in this detector.	44
Figure 4.5	Left: mechanical design drawing of the CRDC mask. Right: Example of CRDC mask data from run 157.	44
Figure 4.6	A schematic of the CRDC masks and their relation to the lab coordinate frame, the beam, and the pads in each detector.	45
Figure 4.7	An example of fitting used in gain-matching the ion chamber. Left: points show raw charge signal from pad 4, thick solid line is Gaussian fit to data, and thin vertical line indicates centroid of “ideal” pad 8. Right: points show gain-matched charge signal from pad 4 and thin vertical line indicates centroid of “ideal” pad 8.	47
Figure 4.8	Position dependence of the ion chamber. The left panel shows the summed signal from the ion chamber as a function of CRDC2 x -position when using a cocktail beam. The right panel shows the position-corrected summed signal from the ion chamber.	48

Figure 4.9	Time dependence of the summed ion chamber signal. The top panel shows the summed, position-corrected ion chamber signal as a function of run number. The red line is the fitted function 4.3 using parameters from Table 4.3. The bottom panel shows the summed, position-corrected, and time-corrected ion chamber signal as a function of run number.	49
Figure 4.10	Position dependence of the charge signal from the thin scintillator. The left panel shows the total signal from the thin scintillator as a function of CRDC2 x -position when using a cocktail beam. The right panel shows the position-corrected summed signal from the thin scintillator. The correction was chosen so that the isotopes of interest (lithium and beryllium) had no position dependence. The remaining position dependence was primarily for the heavier isotopes, nitrogen and carbon.	51
Figure 4.11	Time dependence of the total thin scintillator charge signal. The top panel shows the summed, position-corrected thin scintillator charge signal as a function of run number. The red line is the fitted function 4.3 using parameters from Table 4.5. The bottom panel shows the summed, position-corrected, and time-corrected charge signal as a function of run number. . .	52
Figure 4.12	Timing signal from the target scintillator before (left) and after (right) the walk correction.	54
Figure 4.13	Target scintillator timing spectra from run 41 (black), taken while the target exhibited double peaking, and from run 90 (blue), taken after the double peaking was fixed.	55
Figure 4.14	An example of MoNA-LISA's charge calibration procedure. The raw charge from each QDC channel is plotted (left). The cosmic peak around channel 1200 is fit with a red Gaussian line. The inset shows channels 500 to 2000 with a linear scale on the y-axis. Those values are used to construct a linear fit whose slope and offset are applied to produce a calibrated charge signal in MeVee (right).	56
Figure 4.15	An example of the raw time spectrum during MoNA-LISA's TDC calibration procedure. A pulser pulses the system every 40 ns, creating a spectrum with peaks at intervals that correspond to 40 ns.	57
Figure 4.16	TDC slope values for MoNA and LISA.	58
Figure 4.17	X-position calibration example. The final x -position spectrum (right) for one bar was calculated based on the time difference between the two PMTs (left).	58
Figure 4.18	Schematics showing the differences used to calibrate the time measurement in MoNA-LISA. The view on the left is from the front of the array and the schematic on the right shows the side view of the array, looking head-on at the PMTs.	59

Figure 4.19	Calibrated timing spectra for each table. Impinging the beam on a thick target produced many γ -rays and neutrons. Vertical lines indicating the expected arrival of γ -rays and neutrons at the front of that table. The left panel shows the time-of-flight to the MoNA table, the center panel shows the time-of-flight to the first LISA table, and the right panel shows the time-of-flight to the second LISA table.	60
Figure 4.20	Beam component identification using energy loss through the ion chamber (y -axis), and time-of-flight from the A1900 scintillator to the target scintillator (x -axis).	61
Figure 4.21	Time difference between the A1900 and thin scintillators, showing “echos” from events in which the A1900 scintillator recorded the time of a different particle than the thin scintillator. The vertical lines indicate the limits of the gate used to eliminate these events.	62
Figure 4.22	Event quality gates applied to the CRDC1 parameters TAC (left) and pad sum (right). Red vertical lines with arrows indicate the requirements for an event to pass through the gate.	62
Figure 4.23	Event quality gates applied to the CRDC2 parameters TAC (left), pad sum (center), and χ^2 (right). Thick red vertical lines indicate the requirements for an event to pass through the gate.	63
Figure 4.24	Element identification.	64
Figure 4.25	Three-dimensional plot showing lithium isotope identification by plotting x -position, x -angle, and time-of-flight.	65
Figure 4.26	Lithium (top) and beryllium (bottom) particle identification from the ^{13}B beam and in coincidence with an interaction in MoNA-LISA.	66
Figure 4.27	Lithium (top) and beryllium (bottom) particle identification from the ^{12}B beam and in coincidence with an interaction in MoNA-LISA.	67
Figure 4.28	Top: Raw neutron time-of-flight spectrum. Bottom: Charge deposited vs. time-of-flight for the first interaction in MoNA-LISA.	69
Figure 4.29	A breakdown of the time-of-flight spectrum of Figure 4.28 by sections (tables) of the detector.	70

Figure 4.30	Top: Time-of-flight breakdown of events with two (and only two) interactions in the section of LISA at 0 degrees. The blue line shows the first interaction spectrum, while the green line shows the spectrum of the second interaction. The black line is the sum of those two components. Bottom: Comparison of the time-of-flight spectrum for events with one interaction (red line) and the summed spectrum from above (black line). The red line has been normalized to the flat background before the gamma peak of the black line.	71
Figure 4.31	The γ -ray peak in MoNA-LISA during the ^{13}B production runs.	72
Figure 4.32	The arrival time of the large γ -ray peak, as observed by MoNA (left), the LISA table at 0 degrees (center), and the LISA table at 30 degrees (right). Vertical lines indicate expected arrival time of γ -rays from the target area. .	72
Figure 4.33	Difference of time differences between two of the three detectors. The left panel shows the comparison between LISA at 0° and LISA at 30° , and the right panel shows the comparison between MoNA and LISA at 30° . Black lines indicate the possible locations of a point gamma source to produce the measured time difference between the two detectors.	73
Figure 4.34	The two zero-lines from Figure 4.33 overlaid on the vault layout. The intersection of these lines indicates the likely location of a point gamma source. Within the error of the calculation, and given the layout of the experimental vault, a gamma source was identified inside the Sweeper box.	73
Figure 4.35	Final time-of-flight spectrum for MoNA-LISA. This spectrum requires that each interaction not only have a valid charge but also a valid time.	74
Figure 4.36	A flow chart of the simulation process and the various data that are used as input.	76
Figure 4.37	Incoming beam distributions in CRDC1 (top row) and CRDC2 (bottom row). The left column shows the two-dimensional positional profile, the middle column shows the x-projection, and the right column shows the y-projection.	77
Figure 4.38	Simulated (blue) and data (black) position and angular spectra for the incoming ^{13}B beam profile. Top row: CRDC1 x -position, CRDC2 x -position, and x -angle. Bottom row: CRDC1 y -position, CRDC2 y -position, y -angle. .	79
Figure 4.39	CRDC2 position spectra from data (left) and simulation (right) for the incoming ^{13}B beam.	80
Figure 4.40	Simulated (blue) and data (black) position and angular spectra for the incoming ^{12}B beam profile. Top row: CRDC1 x -position, CRDC2 x -position, and x -angle. Bottom row: CRDC1 y -position, CRDC2 y -position, y -angle. .	81

Figure 4.41	CRDC2 position spectra from data (left) and simulation (right) for the incoming ^{12}B beam.	82
Figure 4.42	Simulated (blue) and data (black) position and angular spectra for the ^9Li fragments from the ^{13}B beam. Top row: CRDC1 x -position, CRDC2 x -position, and x -angle. Bottom row: CRDC1 y -position, CRDC2 y -position, y -angle. See Section 4.4.5 for information about the cut on CRDC2 y -position.	83
Figure 4.43	Total momentum of the ^9Li fragments in the data (black line) and simulation (blue line).	84
Figure 4.44	CRDC1 x -angle versus CRDC1 x -position for a beam sweep run with no target (left) and for production (right). The red polygon indicates the “sweep” gate.	85
Figure 4.45	Full x -position spectrum for ^{11}Be , data (black line) and simulation (blue line).	86
Figure 5.1	Decay energy for the $^9\text{Li}+n+n$ system. No causality cuts are applied.	90
Figure 5.2	Number of real two neutron events (green, top line), and fake two neutron events (red, bottom line) that pass the causality cut as a function of the magnitude of the distance cut, based on a simulation of a phase space decay from ^{11}Li	90
Figure 5.3	Decay energy for the $^9\text{Li}+n+n$ system. Causality cuts are applied.	91
Figure 5.4	Jacobi plots for the $^9\text{Li}+n+n$ system. Causality cuts are applied, as well as a requirement that the total three-body decay energy be less than 1.6 MeV.	92
Figure 5.5	Possible decay paths from an ≈ 1 MeV state in ^{11}Li populated using a 2p knockout from the ^{13}B beam. The red, blue, green, and magenta decay paths go through intermediate states in ^{10}Li , while the orange and cyan decay paths explicitly bypass those states in favor of correlated (dineutron) or uncorrelated (phase space) two-neutron emission.	93
Figure 5.6	Possible decay paths from states in ^{10}Li populated using a 2p1n knockout from the ^{13}B beam. The gray path indicates population of and decay from a much higher-lying state.	93
Figure 5.7	Decay energy plots used when fitting simulation to data. The upper left panel shows the two-body decay energy in coincidence with ^9Li and one neutron. The upper right panel shows the same two-body decay energy spectrum, but this time requiring only one interaction in MoNA-LISA. The lower left panel shows the three-body decay energy spectrum, as shown in Figure 5.1. The lower right panel shows the same three-body decay energy spectrum but with causality cuts, as shown in Figure 5.3.	94

Figure 5.8	χ^2 minimization plots for the ^{11}Li energy (left) and width (right), for many different decay paths.	95
Figure 5.9	The best fits to the decay energy spectra from Figure 5.7 with all four decay models. The upper left panel shows the two-body decay energy in coincidence with ^9Li and one neutron. The upper right panel shows the same two-body decay energy spectrum, but this time requiring only one interaction in MoNA-LISA. The lower left panel shows the three-body decay energy spectrum. The lower right panel shows the same three-body decay energy spectrum but with causality cuts.	96
Figure 5.10	The Jacobi coordinate spectra (as shown in Figure 5.4) compared to the same spectra from the best fits of the four decay models.	98
Figure 5.11	The best fit to the decay energy spectra of Figure 5.7 with the dineutron model. Different colored curves show the different components as labeled in Figures 5.5 and 5.6. The black line shows the summed total. The upper left panel shows the two-body decay energy in coincidence with ^9Li and one neutron. The upper right panel shows the same two-body decay energy spectrum, but this time requiring only one interaction in MoNA-LISA. The lower left panel shows the three-body decay energy spectrum. The lower right panel shows the same three-body decay energy spectrum but with causality cuts.	99
Figure 5.12	Previous measurements of ^{11}Li with excitation energies less than 3.5 MeV. The result from this work is shown by the box.	100
Figure 5.13	The Jacobi coordinate spectra (as shown in Figure 5.4) compared to the same spectra from the best fit from the dineutron model. Different colored curves show the different components as labeled in Figures 5.5 and 5.6. The black line shows the summed total.	101
Figure 5.14	Dalitz plots for ^{11}Li . The top set is the data and the bottom set is the best fit simulation using the dineutron model. The data only uses events with a three-body decay energy less than 1.6 MeV that also passed the causality cuts.	103
Figure 5.15	Two different dineutron models in comparison to the experimental data. The solid line simulation used a scattering length of -18.7 fm while the dashed line simulation used a scattering length of -100 fm, implying stronger correlation.	104
Figure 5.16	Decay energy in coincidence with ^9Li and one neutron, populated by two-proton knockout from a ^{12}B beam.	105
Figure 5.17	A fit of a single $\ell = 1$ decay energy lineshape to the data from Figure 5.16 (top) and the residual (bottom).	106
Figure 5.18	A fit of three $\ell = 1$ decay energy lineshapes to the data from Figure 5.16.	107

Figure 5.19	χ^2 plots that show the minimization of the central energies of the blue, green, and magenta lineshapes in Figure 5.18. Dashed lines indicate statistical error and solid lines indicate the total error margin.	107
Figure 5.20	Previous measurements of unbound, $\ell = 1$ states in ^{10}Li (same as Figure 1.11) with the limits of the new measurements overlaid in blue, green, and magenta lines. Measurements reported without error have arrows for error bars. Two different measurements in Chernyshev’s 2013 paper produced two different measurements of 0.7 ± 0.05 and 0.78 ± 0.15 MeV, here the weighted average is used [72]. ^a Both Gornov’s 1998 paper [97] and Santi’s 2003 paper [101] found two possible fits for the data. Details are in Table 1.2 and footnotes within.	108
Figure 5.21	Calculations of $0p_{1/2}$ (red) and $1s_{1/2}$ single-particle levels of ^{10}Li , ^{11}Be , ^{12}B , and ^{13}C . Energies of single-particle levels and relevant energy eigenstates are given relative to the calculated $0p_{1/2}$ single particle energy level. Dashed line shows the extrapolation of the linear fit to the $1s_{1/2}$ single-particle levels. ⁹ He levels are from Ref. [155], ^{10}Li levels are from this work, ^{11}Be and ^{12}B levels are from Ref. [156], and ^{13}C levels are from Ref. [157].	109
Figure 5.22	Calculations by Thompson and Zhukov show the relationship between the ^{11}Li binding energy and the ^{10}Li $0p_{1/2}$ single-particle energy as a function of the $1s_{1/2}$ scattering length [80]. The line at -0.369 MeV shows the limits imposed by the measurements of Smith <i>et al.</i> [51] and this thesis.	110
Figure 5.23	Decay energy of the $^{11}\text{Be}+n$ system after population of ^{12}Be via a two-proton knockout from a ^{13}B beam.	112
Figure 5.24	Different simulated lineshapes fitted or compared to the $^{11}\text{Be}+n$ decay energy lineshape shown in Figure 5.23. Left panel: data is fit with a single $\ell = 1$ resonant lineshape and a background. Right panel: data is compared to two lineshapes assuming total decay from a previously measured state at 4580 keV in ^{12}Be to the excited $1/2^-$ state in ^{11}Be (left lineshape) and to the $1/2^+$ ground state (right lineshape).	112
Figure 5.25	χ^2 plots for the energy (left) and width (right) of the single $\ell = 1$ decay fit to the data in the upper left panel of Figure 5.24. Dashed vertical lines show the statistical 1σ limits and the solid vertical lines indicate the additional systematic error.	113
Figure 5.26	Fits of the ^{12}Be decay energy spectrum with an $\ell = 0$ (left) or $\ell = 2$ (right) lineshape. The fits are shown on the top row and the bin-by-bin contributions to the χ^2 value are shown in the bottom row.	114

Figure 5.27	<p>Various decay energy spectra in coincidence with ^{10}Be fragments. Upper left panel: two-body decay energy. Upper right panel: two-body decay energy spectrum, requiring only one interaction per event in MoNA-LISA. Lower left panel: three-body decay energy spectrum. Lower right panel: three-body decay energy spectrum with causality cuts applied.</p>	115
Figure 5.28	<p>The data from Figure 5.27, fitted with simulated spectra. The green, red, and purple lineshape show single-neutron decays from ^{11}Be as used by Peters <i>et al.</i> [115]. The blue line shows a two-neutron decay. The energies and widths of each decay were fixed, leaving only the relative amplitudes to vary in the fitting. All spectra except the lower right were included in the fitting.</p>	116
Figure 5.29	<p>Level diagram of measured states in ^{12}Be from Figure 1.12 compared to a continuum shell model calculation of states in ^{12}Be [132]. The state presented here is represented by the grey box. The width of the box represents the error of the energy measurements.</p>	117

Chapter 1

Introduction

1.1 Chart of nuclides

The atomic nucleus is a many-body system of protons and neutrons. A nuclide is a species of atomic nucleus defined by the number of protons (Z) and neutrons (N) it has. Nuclear scientists use a chart of nuclides to organize information (Figure 1.1). Like the periodic table, this chart organizes the systems under study and presents an easy way to view patterns.

The chart of nuclides is organized by neutron number (along the x -axis) and proton number (along the y -axis). Straight down a diagonal of the chart, denoted in Figure 1.1 by the black squares, is the valley of stability. These are the common, stable nuclei, many of which are naturally occurring. Nuclides on either side of the valley of stability tend to decay toward that valley. The way a nuclide decays is called its decay mode and the time constant that defines how long it will live is called its half-life. Figure 1.1 shows the most common mode of decay for each nuclide from its ground state. On the proton-rich side of the valley of stability, most nuclides decay by emitting a positron and turning a proton into a neutron (β^+ decay, shown by the pink squares). On the neutron-rich side, the primary mode of decay is β^- decay (blue squares): turning a neutron into a proton by emitting an electron.

Far out from the valley of stability are the proton and neutron driplines. These are the limits beyond which the nuclides are unbound with respect to neutron or proton emission and decay by emission of a proton (purple squares in Figure 1.1) or a neutron (orange squares). These limits are called driplines because beyond these lines, the protons and neutrons just “drip” off the nucleus. Beyond the neutron dripline, the nuclides have a half-life on the order of 10^{-21} s. Two other primary modes of decay employed by nuclei are alpha decay (the emission of a ^4He nucleus) and fission (the splitting of the nucleus into two or more fragments).

1.2 Shell model

The nuclear landscape is not a smooth, continuously changing landscape with the valley of stability as the lowest point. Already visible in Figure 1.1 are signs of more intricate structure: nuclides with even Z or even N seem to be more stable than their odd Z or N neighbors and there are some “ridges” where the nuclei are more stable than their neighbors ($Z = 50$ for example). In 1933, Elsasser noted that nuclides with particular numbers of protons or neutrons appeared to be more stable [2]. Fifteen years later, Maria Goeppert Mayer summarized the increased experimental evidence for the stability of certain nuclei with neutron numbers of 50, 82, or 126 and proton numbers of 20, 50, or 82 [3]. One year later, Mayer and the collaboration of Haxel, Jensen, and Suess independently published shell models with strong spin-orbit splitting that resulted in increased stability via large shell gaps at these numbers [4,5].

The nuclear shell model shares some properties with the electronic shell model. Both begin by placing particles in a single-particle potential. This potential has eigenstates which can be

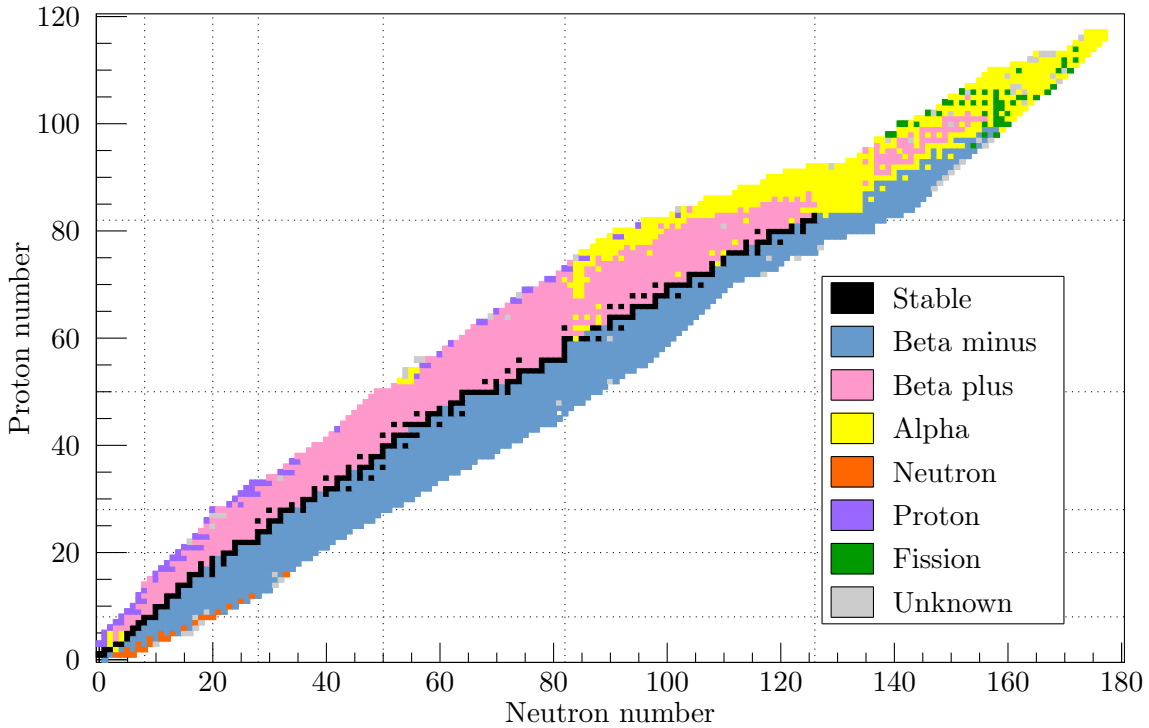


Figure 1.1: Chart of the nuclides, showing the principal decay mode of the nuclide. Data from [1].

characterized by their quantum numbers (n and ℓ) and energies. A spin-orbit term is then added to the original potential. This spin-orbit term lifts the degeneracies of some eigenstates and defines single-particle orbitals, which are identified by their total angular momentum (j) value. These eigenstates are filled consecutively by energy, beginning with the lowest energy, and following the Pauli principle: no identical particles may be placed in eigenstates with the same quantum numbers. Each model has gaps of varying size between the orbitals. Gaps that are large correspond to “magic numbers”. Systems filled to these numbers are observed to be more stable than others (i.e. noble gases, “magic” nuclei).

There are some differences between electronic and nuclear shell models. In the nuclear shell model, the potential felt by each particle is generated by the other particles considered in the system (other nucleons), rather than by a central body (for electrons, this would be the atomic nucleus). The length scales are different, 10^{-15} m for the nuclear shell model and 10^{-12} m for the atomic shell model. The spin-orbit term, while a small correction to energy levels in the electronic shell model, plays a larger role in the nuclear shell model and is observed to have a different sign. Also, while there is a clear physical reason for including the spin-orbit term in the electronic shell model, the physical reason for including the nuclear spin-orbit term is less clear.

Two common bases for the initial potential are the harmonic oscillator and a Wood-Saxon potential. The harmonic oscillator is chosen because its basis states are simple and analytic, while the shape of the Wood-Saxon potential is closer to the empirically observed shape of the nuclear densities. The low-lying Wood-Saxon and Wood-Saxon plus spin-orbit orbitals are shown in Figure 1.2, along with the “magic numbers”.

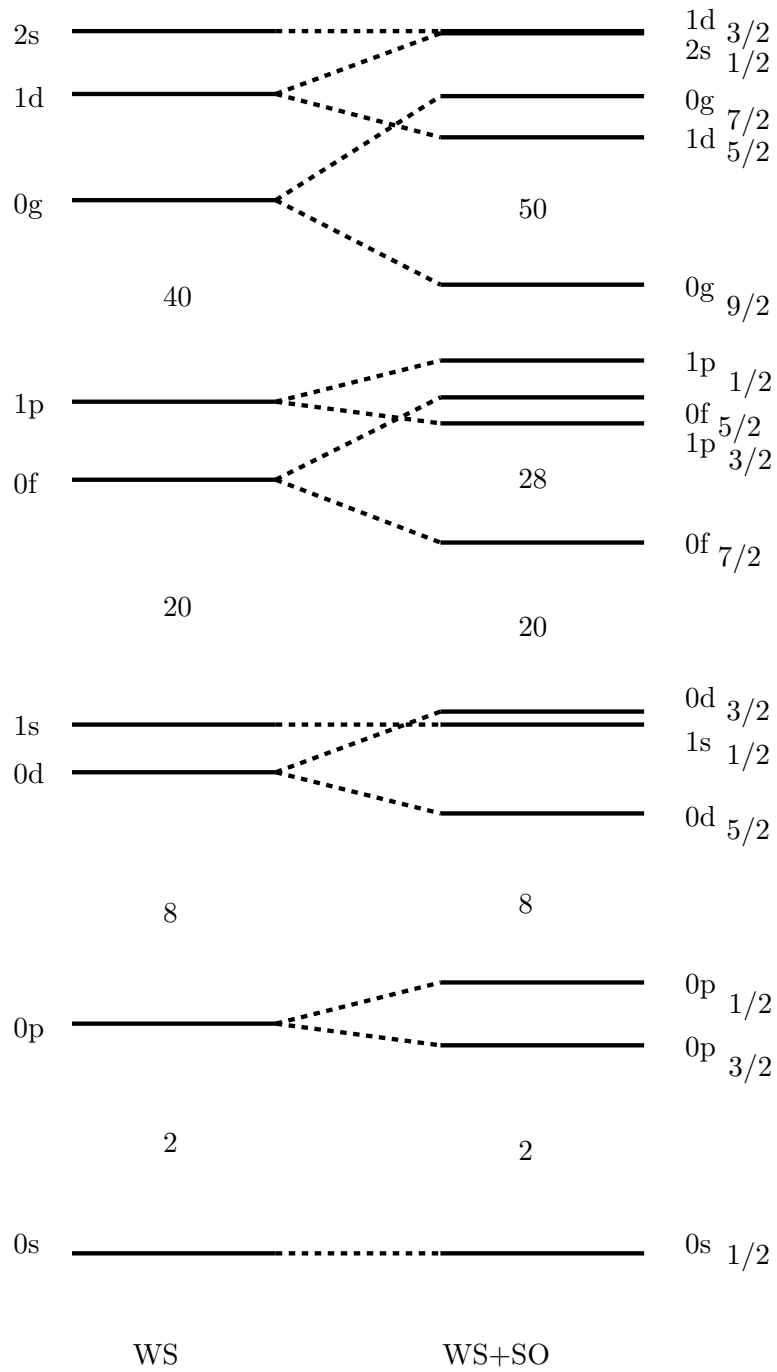


Figure 1.2: Wood-Saxon orbitals (left) and Wood-Saxon plus spin-orbit orbitals. Numbers indicate the number of particles required to fill the levels up to those large shell gaps, commonly called “magic numbers”.

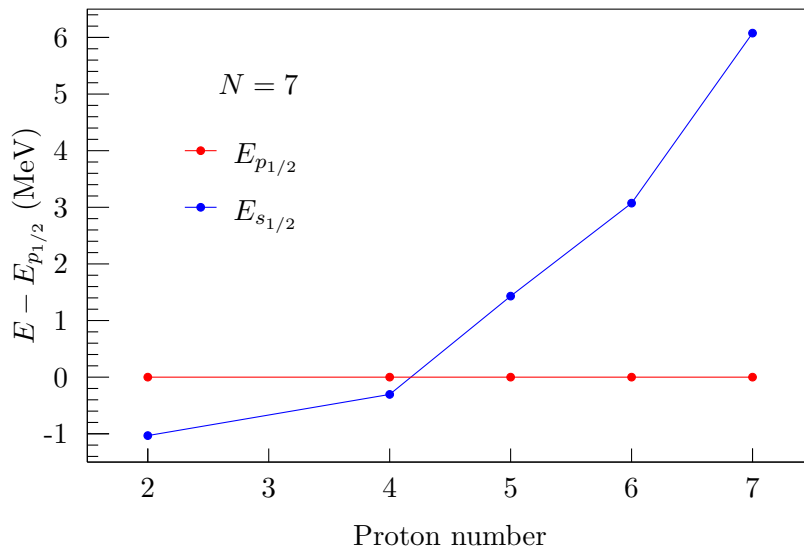


Figure 1.3: Difference between $0p_{1/2}$ and $1s_{1/2}$ neutron single-particle energies for the $N = 7$ isotones. Data from Ref. [6] and references therein.

1.3 Islands of inversion

As the exploration of the nuclear chart has expanded beyond the stable isotopes, some of the large shell gaps observed in the stable nuclei have disappeared and other gaps have appeared. The energies associated with each single-particle orbital are not universal. Nuclides that have either protons or neutrons filled up to a large shell gap display increased stability because excitations of protons or neutrons to the next orbital takes a significant amount of energy. As single-particle orbitals on either side of a large gap approach each other, those excitations take less energy and the “magic number” associated with that shell gaps becomes less “magic”. In some cases, known as “islands of inversion”, states from either side of magic numbers cross each other. One example of this is shown in Figure 1.3 that shows the energy difference between the $0p_{1/2}$ and $1s_{1/2}$ neutron single-particle energies for the $N = 7$ isotones. As protons are removed from ^{14}N ($Z = 7$), the difference between those levels decreases until at ^{11}Be ($Z = 4$), when the levels invert.

These “islands of inversion” are located throughout the chart of the nuclides. Figure 1.4 shows the islands identified by B.A. Brown in 2010 [7] around the major shell closures of $N = 8$ and 20, as well as the sub-shell closures of $N = 14, 20$ and 40. There is experimental evidence for shell breaking in all of these islands centered around ^{12}Be , ^{20}C , ^{32}Mg , ^{42}Si , and ^{64}Cr [8–14].

In the island of inversion centered around ^{12}Be , used as an example previously, the $1s_{1/2}$ level from the sd shell (the group of $0d_{3/2}$, $1s_{1/2}$, and $0d_{5/2}$ states shown in Figure 1.2) drops down into the p shell (comprised of the $0p_{3/2}$ and $0p_{1/2}$ levels), breaking the $N = 8$ shell closure. The breaking of the $N = 8$ closure was first predicted by Talmi and Unna in 1960 [15] based on indications of a parity inversion in β -decay measurements by Wilkinson and Alburger [16]. The first experimental confirmation of this inversion was a measurement of the ground state parity of ^{11}Be performed by Alburger *et al.* four years later [8]. In normal shell model ordering, the ground state of ^{11}Be should be $1/2^-$, with a $0s_{1/2}^2 0p_{3/2}^2$ structure in the protons and a $0s_{1/2}^2 0p_{3/2}^4 0p_{1/2}^1$ structure in the neutrons. Alburger *et al.*, however, found that the parity of the ^{11}Be ground state was positive. The inversion is also evident in the ground state structure of ^{11}Li and ^{12}Be in which the two valence neutrons are

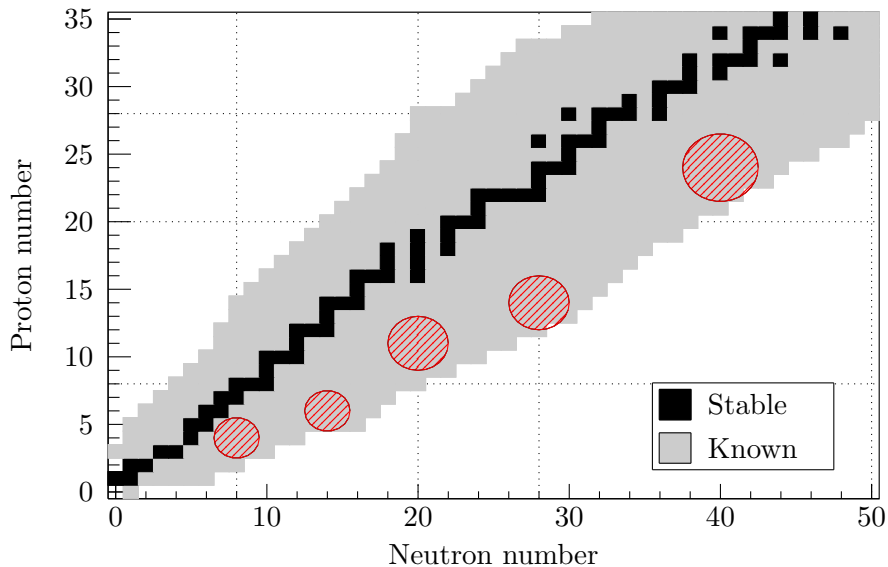


Figure 1.4: Chart of the nuclides and the five predicted islands of inversion (red circles) [7].

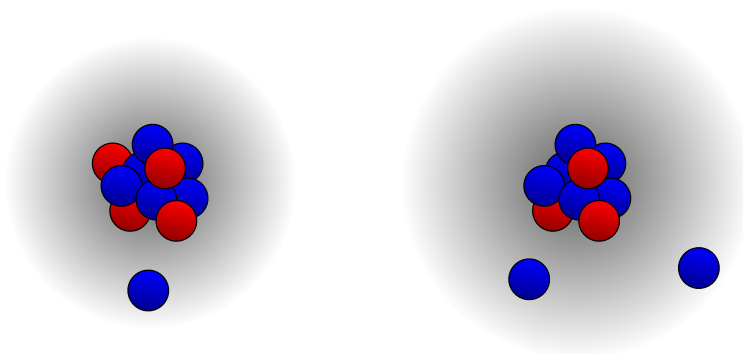


Figure 1.5: Drawings of two halo nuclei: ^{11}Be (left) and ^{11}Li (right).

shared between the $0p_{1/2}^2$ and $1s_{1/2}^2$ configurations [17, 18].

1.4 Halo nuclei

Far from stability and near the driplines, the binding energy of the last nucleon or two becomes increasingly small. As the binding of that last nucleon decreases, the nucleon can exist at greater distances from the core. It can exist at such a distance that instead of modeling a nucleus with mass A as an A -body system, it can be considered a two-body system, with an $A - 1$ core and one additional nucleon. These systems are commonly called one neutron (or proton) halo nuclei. There are also two- and four- nucleon halo systems. Figure 1.5 shows the known and suspected halo nuclei.

Halo nuclei are commonly associated with increased neutron or proton radii. Plots showing the neutron, proton, and matter radii of lithium and beryllium isotopes are presented in Figure 1.6. The halo nuclei ^{11}Be , ^{14}Be and ^{11}Li are clearly indicated by the sudden increase in neutron and matter radii but (relatively) constant proton radii. Experimentally, halo nuclei are identified by

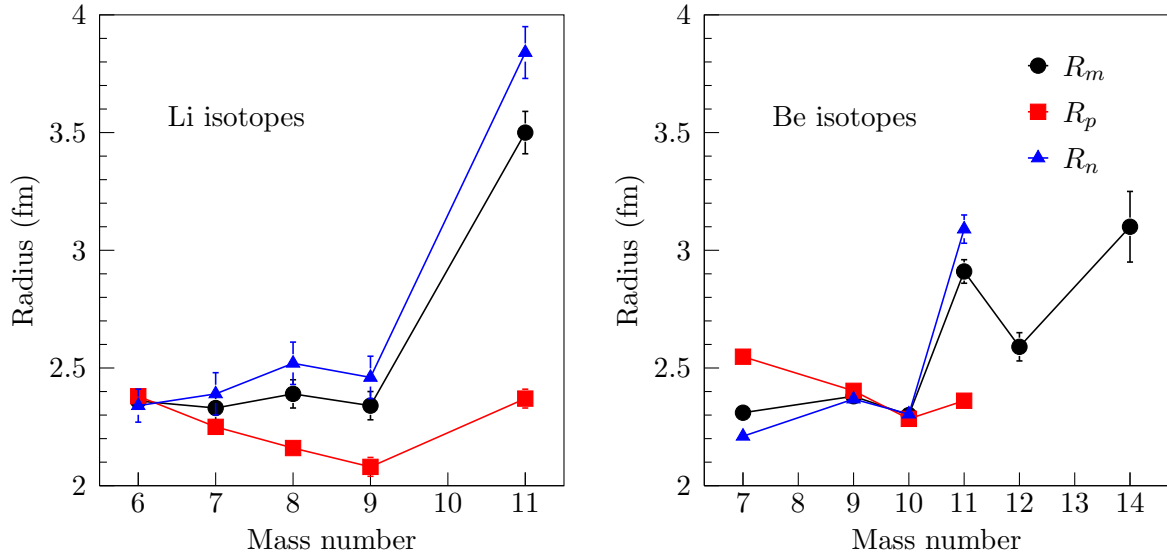


Figure 1.6: Deduced neutron (blue), proton (red), and matter (black) radii of lithium and beryllium isotopes. Data from [19].

measurements of large reaction cross-section, small neutron (or proton) separation energies, narrow momentum distributions, and a soft E1 mode of excitation [19]. Figure 1.7 shows the locations of the identified and potential halo nuclei in the chart of the nuclides.

The first identified halo system was ^{11}Li [20, 21]. Tanihata *et al.* calculated the radii of a chain of lithium isotopes by measuring the interaction cross-sections and noticed a significant increase in radius at $A = 11$ [20]. Kobayashi *et al.* later confirmed the halo identification by measuring the transverse momentum distribution of a ^9Li fragment after a $2n$ removal from ^{11}Li [22]. The measured distribution was fit by a combination of two Gaussians: one Gaussian whose width was similar to the transverse momentum distributions measured from bound nuclei, and another narrower one which indicated “the weak binding of the two outer neutrons in the ^{11}Li system” [22]. The first measurement of an electromagnetic dissociation (EMD) enhancement, predicted by Hansen and Jonson [23] was reported by Kobayashi *et al.* [24]. When comparing interaction cross-sections on targets of differing Z , they wrote that “a large enhancement due to the EMD process was found for high- Z targets” [24].

All presently known two-neutron halo nuclei are also identified as Borromean systems [25, 26]. A Borromean system is a three-body system in which each two-body subsystem is unbound. For a two-neutron halo nucleus of mass A , those systems include the dineutron and the $A - 1$ system. Due to pairing effects (in which a pair of nucleons is more bound than a single nucleon), all the identified two-neutron halo nuclei have an even number of neutrons.

1.5 Three-body correlations and decays

The properties of a three-body system, such as a Borromean nucleus, depend on the correlations between the three bodies. These correlations can be extracted using a variety of methods: radii measurements, correlation measurements based on intensity interferometry, Coulomb excitation, and reaction measurements [19]. Radii measurements, only able to be performed on bound nuclei, use charge and matter radii measurements to calculate the average distance between the two

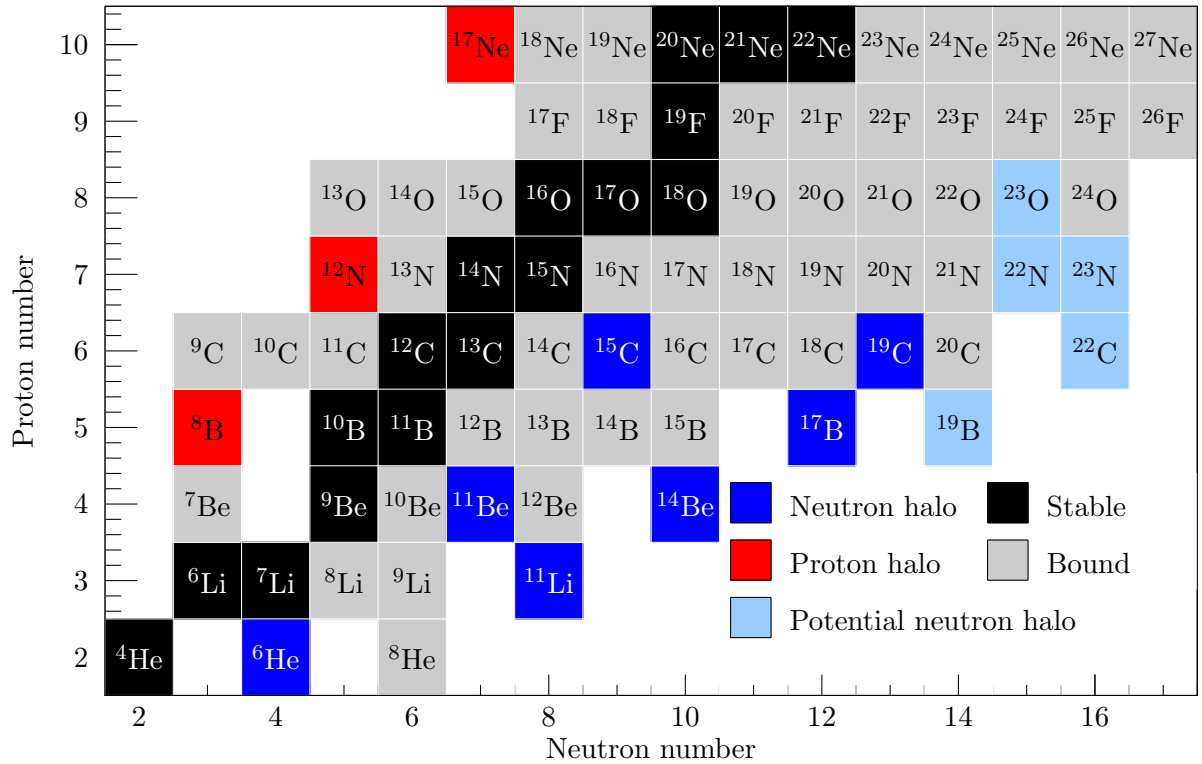


Figure 1.7: Chart of the nuclides, showing the known neutron and proton halo nuclei and the suspected neutron halo nuclei as reported by Tanihata, Savajols, and Kanungo [19]. Red squares indicate confirmed proton halo nuclei, dark blue squares indicate confirmed neutron halo nuclei, and light blue squares indicate potential neutron halo nuclei. Black squares indicate stable nuclei and the gray squares indicate bound nuclei.

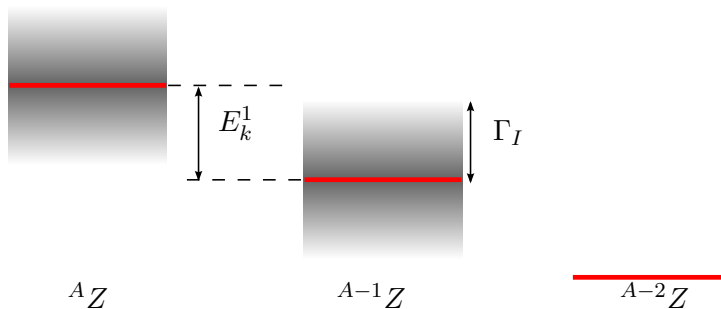


Figure 1.8: Level diagram for two-neutron decay labeling E_k^1 and Γ_I .

neutrons as well as their distance from the core. Correlation measurements look at the intensity correlation of two observed particles after they have been emitted from a bound state. The correlation function, which is a function of the difference of momenta between two neutrons, is fit and from that fit, a source size is extracted [27]. Coulomb excitation is used to excite a collective soft dipole mode in halo nuclei [23]. These measurements excite a bound nucleus and measure the strength of the E1 transition. From the integral of that strength, one can extract the distance between the core and the center-of-mass of the two neutrons in the ground state. Reaction measurements measure the kinematic properties of the fragments after break-up or decay and compare these to model predictions. These measured values include perpendicular and parallel momentum distributions, energy ratios, and angles between fragments. The work in this dissertation uses reaction measurements to investigate the correlations from the decay of excited states of ^{11}Li .

The kinematics of a two-body decay, such as the emission of a single neutron or proton, are very clear: in order to conserve momentum, the two particles are emitted back-to-back in the center-of-mass frame. The inclusion of a third particle makes this more complex. Conserving momentum in a three-body decay means all three particles must be emitted in the same plane. Within that plane, however, there are opportunities for various correlations between the three particles. In addition, there is the additional factor of timing: could this three-body decay be two sequential two-body decays?

Much more work has been done with two proton decays than with two neutron decays. Goldansky was the first to predict two-proton radioactivity [28]. Since this paper, the definitions have gotten a bit more nuanced. Goldansky defined a “true $2p$ ” decay as one where one-proton decay is energetically forbidden and all products are emitted simultaneously [28]. The first discovery of two-proton radioactivity like this was in ^{45}Fe [29, 30]. When there is an unbound intermediate state, the decay can be either sequential or democratic. A sequential decay is defined as one decay to an intermediate state followed by a second decay to a bound state. The decay of ^9B to $p + 2\alpha$ is a good example, although in this case, one of the two sequential steps is an alpha decay, not a proton decay [31]. In a democratic decay, there are no strong kinematic correlations between particles [32]. The decay of the ground state of ^6Be provides an example of this type of decay [31, 32]. The distinction between sequential and democratic is not cleanly defined, but Bochkarev suggested a ratio to quantify the difference [32]:

$$\text{Sequential: } \frac{\Gamma_I}{E_k^1} \ll 1$$

$$\text{Democratic: } \frac{\Gamma_I}{E_k^1} > 1$$

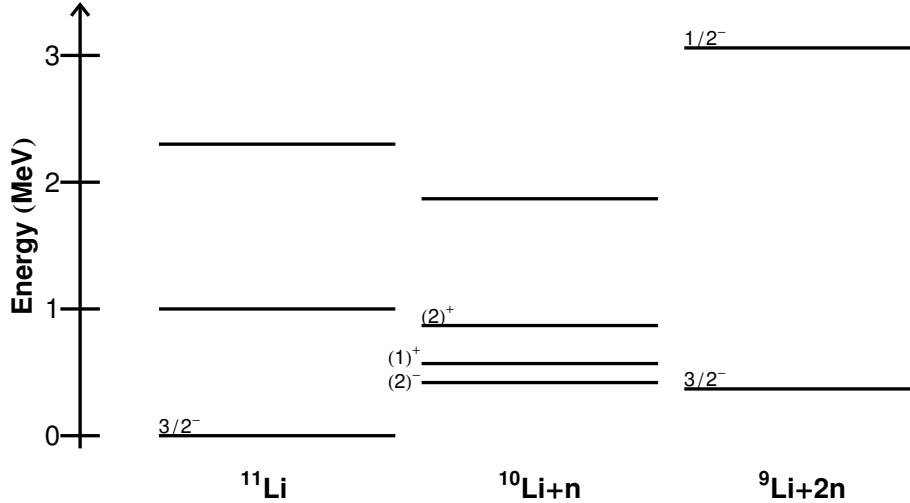


Figure 1.9: Level diagram of states in $^{11,10,9}\text{Li}$, relative to the ground state of ^{11}Li . Neutron separation energies are from Refs. [51–56]. Excited state energies and parities for $^{10,11}\text{Li}$ are general summaries of measurements presented in Tables 1.2 and 1.1. Ground state spin of ^{11}Li from Ref. [57]. Excited state spins in ^{10}Li are expected spins and parities based on $1s_{1/2}$ and $0p_{3/2}$ neutrons coupling with a $0p_{3/2}$ proton. Energy, spin, and parity of first excited state in ^9Li from Refs. [58–60]

where Γ_I is the width of the potential intermediate state and E_k^1 is the energy released when decaying to that intermediate state, shown in Figure 1.8. When the decay is through a narrow intermediate state, this ratio is much less than one and the decay is sequential. When the ratio is greater than or equal to one, the decay is democratic.

Though these definitions were mostly developed when discussing two-proton decays, they apply to two-neutron decays as well. For two-proton decays, the interaction between the two protons as they leave the nucleus (called a final state interaction) is repulsive, due to the Coulomb force. Without the Coulomb force, the potential between two neutrons is repulsive at very short ranges and attractive at longer distances, with the change-over distance being around 1 fm [33]. This attractive force can correlate the kinematics of the neutrons during the decay even if they were not correlated while in the nucleus [34]. The decay of strongly-correlated neutrons is sometimes called a dineutron model.

Experimentally, identification of these decay types is performed by measuring different energy and kinetic distributions. Dalitz plots were introduced in the 1950s [35, 36], have continued to be used in high-energy physics, and exist in a slightly modified form in nuclear physics [37, 38]. Jacobi plots of radii, energies, and kinematic variables have been used in understanding correlations in three-body decays, both proton and neutron [26, 31, 39–49]. When identifying a sequential decay of an unbound state in ^{24}O to ^{22}O , Hoffman *et al.* took a slightly different approach and plotted two different two-body decay energies against each other [50].

1.6 Previous experiments

1.6.1 Lithium isotopes: $A = 11, 10, 9$

The first halo nucleus, ^{11}Li , has been the subject of many experiments and many more papers. The review of previous work presented here will focus on measurements of the energies, spin, and parities of low-lying unbound states as well as measurements or calculations regarding correlations between the neutrons and the decay mode. In addition, some details of previous measurements and calculations of $^{10,9}\text{Li}$ will be discussed.

Table 1.1: Previous measurements of unbound states in ^{11}Li below 5 MeV. The energy shown here is the excitation energy. When papers reported a decay energy, the two-neutron separation energy $S_{2n} = 369.15$ keV [51] was added to produce the excitation energy.

Reaction	Energy (MeV)	Width (MeV)	Ref.
$^{11}\text{Li}(p,p)^{11}\text{Li}$	1.25 ± 0.15		Korshennikov96 [61]
$^{11}\text{Li}(p,p)^{11}\text{Li}$	3.0 ± 0.2		Korshennikov96 [61]
$^{11}\text{Li}(p,p)^{11}\text{Li}$	4.9 ± 0.25		Korshennikov96 [61]
$^{11}\text{Li}(p,p)^{11}\text{Li}$	1.3 ± 0.1	0.75 ± 0.6	Korshennikov97 [62]
$^{11}\text{Li}(\text{Pb},\text{X})^9\text{Li}+2n$	1.1	0.8	Sackett93 [63]
$^{11}\text{Li}(\text{Pb},\text{X})^9\text{Li}+2n$	1.2 ± 0.1	0.7 ± 0.2	Zinser97 [64]
$^{11}\text{Li}(\text{Pb},\text{X})^9\text{Li}+2n$	2.4 ± 0.2	2.1 ± 0.6	Zinser97 [64]
$^{11}\text{Li}(\text{C},\text{X})^9\text{Li}+2n$	1.24 ± 0.05	0.26 ± 0.24	Simon07 [55]
$^{11}\text{Li}(\text{C},\text{X})^9\text{Li}+2n$	2.45 ± 0.27	2.91 ± 0.72	Simon07 [55]
$^{14}\text{C}(\pi^-,pd)^{11}\text{Li}$	1.02 ± 0.07		Gornov98 [65]
$^{14}\text{C}(\pi^-,pd)^{11}\text{Li}$	2.07 ± 0.12		Gornov98 [65]
$^{14}\text{C}(\pi^-,pd)^{11}\text{Li}$	3.63 ± 0.13		Gornov98 [65]
$^{14}\text{C}(\pi^-,pd)^{11}\text{Li}$	0.92 ± 0.15	≈ 0.3	Gurov10 [66]
$^{14}\text{C}(\pi^-,pd)^{11}\text{Li}$	2.29 ± 0.25	≈ 0.7	Gurov10 [66]
$^{14}\text{C}(\pi^-,pd)^{11}\text{Li}$	3.9 ± 0.25	< 0.2	Gurov10 [66]
$^{11}\text{B}(\pi^-,\pi^+)^{11}\text{Li}$	1.2 ± 0.1	0.3 ± 0.9	Kobayashi93 [67]
$^{10}\text{Be}, ^{14}\text{C}(^{14}\text{C},\text{X})^{11}\text{Li}$	2.47 ± 0.10	1.2 ± 0.2	Bohlen95 [68]
$^{10}\text{Be}, ^{14}\text{C}(^{14}\text{C},\text{X})^{11}\text{Li}$	4.85 ± 0.3	< 0.1	Bohlen95 [68]

After the first detection of ^{11}Li [20, 21], Arnold *et al.* measured the $3/2^-$ spin and parity of the ground state [57], attributed to a single, unpaired proton in the $0p_{3/2}$ orbital. Kobayashi *et al.* then measured the parallel momentum distribution of the daughter ^9Li fragment after impinging a ^{11}Li beam on carbon and lead targets [22]. Expanding the targets used to include beryllium, aluminum, and copper allowed the same group to measure an EMD enhancement, cementing its halo status [24].

Most of the experimental work of ^{11}Li has focused on the properties of the bound ground state. The ground state wave-function is known to consist of an admixture of $0p_{1/2}^2$ and $1s_{1/2}^2$ configurations for the valence neutrons (see, for example, Refs. [69–71]). This reflects the level inversion that breaks the $N = 8$ magic number, which was also seen in $^{11,12}\text{Be}$.

With a two-neutron separation energy of 369.15 ± 0.65 keV [51], all the excited states of ^{11}Li are unbound. A compilation of previous measurements of the energies and widths of unbound states, organized by reaction mechanism, are presented in Table 1.1. A plurality of the measurements have used a ^{11}Li radioactive beam on stationary targets [55, 61–64] and two experiments have utilized the

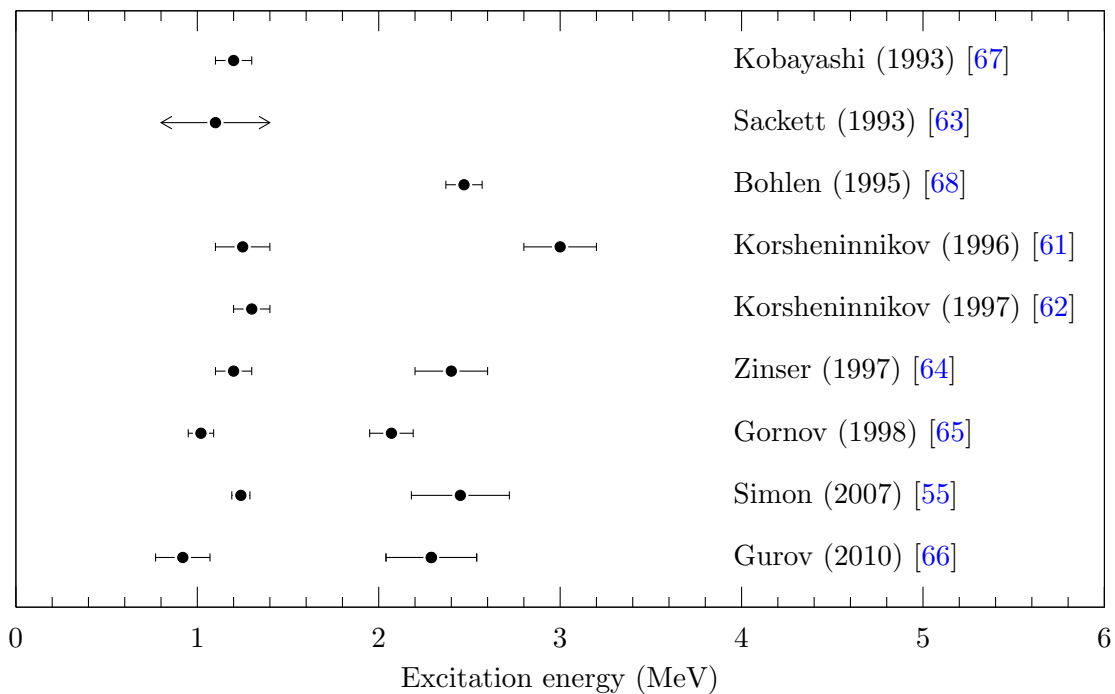


Figure 1.10: Previous measurements of ^{11}Li with excitation energies less than 3.5 MeV.

pions from the Los Alamos Meson Physics Facility [65,66,72]. One measurement used a pion double charge exchange reaction [67,73] and another used both the $^{10}\text{Be}(^{14}\text{C},^{13}\text{N})^{11}\text{Li}$ and $^{14}\text{C}(^{14}\text{C},^{17}\text{F})^{11}\text{Li}$ reactions [68]. Besides a state seen at roughly 1.1 MeV in every experiment except [68], there is little consistency. Even the possible values for that 1.1 MeV state range from 0.92 to 1.3 keV. Most of the measured widths have large errors bars, if the authors attempted to place any at all. A compilation of the previously measured energies is shown in Figure 1.10.

Beyond the spectroscopy of ^{11}Li , considerable interest has been shown in understanding the correlation between the two valence neutrons. Experimentally, consensus on the correlation between the two neutrons is difficult to find. Refs. [19] and [27] do agree on the average distance between the two-neutrons in the ground state. Kobayashi *et al.*'s 1992 pion charge exchange reaction showed “hints of a sequential decay process”, but had no firm conclusions regarding the correlation [67,73]. An experiment at Michigan State University compared data from a Coulomb excitation to models using a phase space decay as well as a dineutron decay and found that the data was fit with a three-body phase space decay and not with the dineutron model [63,74]. Shimoura *et al.* performed the same experiment and found that they could fit their data with a “direct Coulomb breakup mechanism with an extended ‘dineutron’ model” [75]. Ieki *et al.* fired back with the first publication of a spectrum of the cosine of the angle between the two neutrons and claimed it was fit with a phase-space decay. Zinser *et al.* also used a Coulomb excitation reaction and could not fit their neutron-neutron kinetic energy spectrum with a very simple dineutron model [64]. Gornov *et al.* found that they required break-up to ^9Li and a dineutron to fit the continuum portion of their missing mass spectrum but found it difficult to pin down a stronger conclusion because the “reaction mechanism operative in [their] pion absorption measurements is not known” [65]. This assessment was completely based on decay energy spectra, with no correlation spectra presented. Nakamura

et al. were able to fit their $B(E1)$ distribution with a three-body model that included two-neutron correlations in the initial and final states [76], which implied a two-neutron correlation in the ground state of ^{11}Li . Finally, in 2007, Simon *et al.* found evidence for sequential decay through ^{10}Li by constructing “mixed-event” spectra and seeing an enhancement after their Coulomb excitation [55]. It is important to note that the correlation results from Refs. [55,63,64,74,76,77] all used Coulomb excitation of a ^{11}Li . Since the $E1$ operator only acts on the center-of-mass coordinate of the dineutron, all their correlation measurements investigated the ground-state correlations. So far, no detailed Jacobi analysis as a function of decay energy (like those performed for ^6Be in Ref. [47] or for ^{14}Be in Ref. [78]) has been performed for ^{11}Li .

Most of the theoretical work regarding ^{11}Li has been devoted to understanding the properties of the ground state and describing both ^{10}Li and the ^{11}Li ground state in a consistent manner. There have been three main strategies for calculating these properties: large basis shell model calculations [23,79], three-body calculations in hyper-spherical coordinates usually achieved by solving the Faddeev equations [26,80–84], and by using a two-particle Green’s function [85–89]. Most calculations predict a dineutron correlation in the ground state of ^{11}Li . Reproduction of the $0p_{1/2}$ and $1s_{1/2}$ percentages in the ground state has proven sensitive to coupling to the continuum and the presence of a low-lying $\ell = 0$ state in ^{10}Li [80], but not to core excitation [83].

There have been few predictions of the unbound level structure of ^{11}Li . One $3/2^-$ excited state was predicted by Aoyama *et al.* [90]. Garrido and collaborators predicted 13 unbound states below 2 MeV [82]. Predictions of the correlations of neutrons beyond the bound ground state have also been rare. In 1992, Esbensen and Bertsch predicted that the neutrons released from the $E1$ excitation of the soft dipole mode would be emitted with an anti-correlation in the opposite directions, as did Hagino in 2009, using the same method [86,89]. The data have not shown this anti-correlation though. Sackett and Ieki argued there was no correlation while the data from Shimoura showed a correlation between the two neutrons emitted in the decay [63,75,77]. As one of the two sub-systems in the Borromean nucleus ^{11}Li , an understanding of ^{10}Li is essential for three-body calculations. The locations of states in ^{10}Li are used to create the $n+^9\text{Li}$ potential used in those calculations [18,87,91]. As an example, the inclusion of a low-lying $\ell = 0$ state in ^{10}Li significantly increased the percentage of $2s_{1/2}^2$ configuration in the ground state of ^{11}Li in a three-body calculation by Esbensen, Bertsch, and Hencken [87].

The ^{10}Li nucleus was confirmed as unbound by Poskanzer *et al.* in 1966 [104]. The first measurement of the mass was performed almost a decade later by Wilcox *et al.* who measured the neutron separation energy at -0.81 ± 0.25 MeV [92]. Fifteen years later, Amelin *et al.* used the $^{11}\text{B}(\pi^-,p)^{10}\text{Li}$ reaction to measure the energy of ^{10}Li and measured a lower separation energy of -0.15 ± 0.15 MeV. This figure has since been revised to approximately -50 keV based on many measurements of a lower-lying $\ell = 0$ virtual state [52–56]. A compilation of previous measurements of low-lying states in ^{10}Li is given in Table 1.2. Many of the measured energies disagree with one another and the spins have only been tentatively assigned by one experiment where they were based on expected doublets from coupling a $1s_{1/2}$ or $0p_{1/2}$ neutron to the unpaired $0p_{3/2}$ proton [99]. A review of the ^{10}Li picture generates the following two conclusions: the ground state decays by the emission of an $\ell = 0$ neutron and a state around 580 keV decay energy decays by the emission of an $\ell = 1$ neutron. This puts the ground state as a negative parity state and at least one excited positive parity state around 580 keV decay energy.

Some measurements have indicated another state between the negative parity ground state and the state around 580 keV [19,64,99,101], but such a state hasn’t been measured since 2003. Figure 1.11 shows previous measurements of low-lying positive parity states. Zinser *et al.* asserted that this low-lying state was an $\ell = 0$ decay based on the trend of the first four data points in the decay

Table 1.2: Previous measurements of low-lying unbound states in ^{10}Li under 2 MeV. The energy shown here is the decay energy.

Reaction	Energy (MeV or fm)	Width (MeV)	ℓ	Ref.
$^9\text{Be}(^9\text{Be}, ^8\text{B})^{10}\text{Li}$	0.8 ± 0.25	1.2 ± 0.3		Wilcox75 [92]
$^{11}\text{B}(\pi^-, \text{p})^{10}\text{Li}$	0.15 ± 0.15	< 0.4	0	Amelin90 [93]
$^{11}\text{B}(^7\text{Li}, ^8\text{B})^{10}\text{Li}$	≥ 0.1	< 0.23	0,1	Young94 [94]
$^{11}\text{B}(^7\text{Li}, ^8\text{B})^{10}\text{Li}$	0.538 ± 0.062	0.358 ± 0.023	1	Young94 [94]
$^{11}\text{Li}(\text{C}, \text{X})^{10}\text{Li}$	< -20 fm		0	Zinser95 [95]
$^{11}\text{Li}((\text{Pb}, \text{C}), \text{X})^{10}\text{Li}$	0.21 ± 0.05	$0.12^{+0.1}_{-0.05}$	0	Zinser97 [64]
$^{11}\text{Li}((\text{Pb}, \text{C}), \text{X})^{10}\text{Li}$	0.62 ± 0.1	0.6 ± 0.1	1	Zinser97 [64]
$^{11}\text{Li}(\text{p}, \text{pn})^{10}\text{Li}$	0.42		1	Kobayashi97 [96]
$^{11}\text{Li}(\text{p}, \text{n})^{11}\text{Be}^*$	-16^{+4}_{-7} fm		0	Shimoura98 [52]
$^{11}\text{B}(\pi^-, \text{p})^{10}\text{Li}$	0.48 ± 0.1^a	0.5 ± 0.1	0	Gornov98 [97]
$^{11}\text{B}(\pi^-, \text{p})^{10}\text{Li}$	0.1 ± 0.1	0.4 ± 0.1	0	Gornov98 [97]
$^{11}\text{B}(\pi^-, \text{p})^{10}\text{Li}$	0.7 ± 0.2	0.1 ± 0.1	1	Gornov98 [97]
$^{14}\text{C}(\pi^-, \text{dd})^{10}\text{Li}$	0.4 ± 0.07	0.3 ± 0.07		Gornov98 [97]
$^9\text{Be}(^9\text{Be}, ^8\text{B})^{10}\text{Li}$	0.5 ± 0.06	0.4 ± 0.06	1	Caggiano99 [98]
$^{18}\text{O}(^9\text{Be}, \text{X})^{10}\text{Li}$	< -20 fm		0	Thoennessen99 [53]
$^{10}\text{Be}(^{12}\text{C}, ^{12}\text{N})^{10}\text{Li}$	0.24 ± 0.04	0.1 ± 0.07	1	Bohlen99 [99]
$^9\text{Be}(^{13}\text{C}, ^{12}\text{N})^{10}\text{Li}$	0.53 ± 0.06	0.35 ± 0.08	1	Bohlen99 [99]
$^{9,10}\text{Be}(^{13,12}\text{C}, ^{12}\text{N})^{10}\text{Li}$	1.4 ± 0.08	0.2 ± 0.07	0,2	Bohlen99 [99]
$^{11,12}\text{Be}(^9\text{Be}, \text{X})^{10}\text{Li}$	< -20 fm		0	Chen01 [100]
$^9\text{Li}(\text{d}, \text{p})^{10}\text{Li}$	0.35 ± 0.11^b		1	Santi03 [101]
$^9\text{Li}(\text{d}, \text{p})^{10}\text{Li}$	0.77 ± 0.24			Santi03 [101]
$^9\text{Li}(\text{d}, \text{p})^{10}\text{Li}$	< 0.2			Santi03 [101]
$^{11}\text{Li}(\text{C}, \text{X})^{10}\text{Li}$	0.68 ± 0.1	0.87 ± 0.15	1	Simon04 [102]
$^{11}\text{Li}(\text{C}, \text{X})^{10}\text{Li}$	< -40 fm		0	Simon04 [102]
$^9\text{Li}(\text{d}, \text{p})^{10}\text{Li}$	0.38	0.2	1	Jeppesen06 [54]
$^9\text{Li}(\text{d}, \text{p})^{10}\text{Li}$	-13 to -24 fm		0	Jeppesen06 [54]
$^{11}\text{Li}(\text{C}, \text{X})^{10}\text{Li}$	-30^{+12}_{-31} fm		0	Simon07 [55]
$^{11}\text{Li}(\text{C}, \text{X})^{10}\text{Li}$	0.51 ± 0.044	0.54 ± 0.16	1	Simon07 [55]
$^{11}\text{Li}(\text{C}, \text{X})^{10}\text{Li}$	1.486 ± 0.088	< 2.2		Simon07 [55]
$^{11}\text{Li}(\text{p}, \text{pn})^{10}\text{Li}$	0.566 ± 0.014	0.548 ± 0.03	1	Aksyutina08 [56]
$^{11}\text{Li}(\text{p}, \text{pn})^{10}\text{Li}$	-22.4 ± 4.8 fm		0	Aksyutina08 [56]
$^{14}\text{C}(\pi^-, (\text{dd}, \text{pt}))^{10}\text{Li}$	0.7 ± 0.05	< 0.2		Gurov11 [103]
$^{12}\text{C}(\pi^-, \text{pt})^{10}\text{Li}$	0.7 ± 0.05	< 0.2		Chernyshev13 [72]
$^{12}\text{C}(\pi^-, \text{dd})^{10}\text{Li}$	0.78 ± 0.15	0.5		Chernyshev13 [72]

^aA single resonance at 0.48 ± 0.1 MeV and two resonances at 0.1 ± 0.1 and 0.7 ± 0.2 MeV were both used to fit the data.

^bA single resonance at 0.35 ± 0.11 MeV and a pair of resonances at 0.77 ± 0.24 and < 0.2 MeV fit the data equally well.

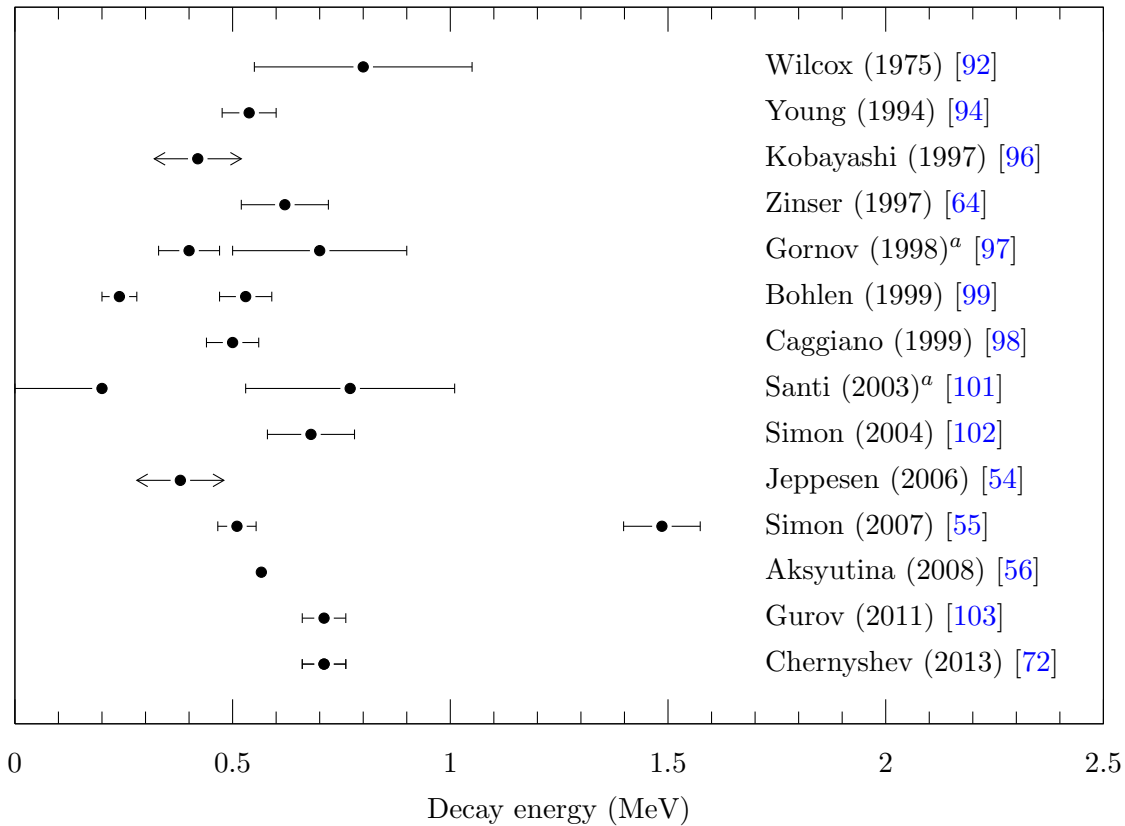


Figure 1.11: Previous measurements of unbound, positive-parity states in ^{10}Li . Measurements reported without error have arrows for error bars. Two different measurements in Chernyshev’s 2013 paper produced two different measurements of 0.7 ± 0.05 and 0.78 ± 0.15 MeV, here the weighted average is used [72].

^aBoth Gornov’s 1998 paper [97] and Santi’s 2003 paper [101] found two possible fits for the data. Details are in Table 1.2 and footnotes within.

energy spectrum but then used an $\ell = 1$ lineshape to fit the data, remarking “We are aware that this may not be the ideal parametrization of a virtual s state ... but have done so to be consistent with other papers on the subject” [64]. Other measurements in this energy region may not have seen this state because of poor statistics, overwhelming background, or significant population of the nearby (and broad) ground state.

If there were a positive parity state around 200 keV, it and the 580 keV state would likely correspond to the $1^+, 2^+$ doublet that arises from coupling a $p_{3/2}$ proton with a $p_{1/2}$ neutron. Only one experiment has assigned spins and parities to these states [99]. These assignments were based on expected spins and parities due to coupling and the selectivity of the reaction mechanisms used and assigned the states at 240 and 530 keV with spins and parities of 1^+ and 2^+ , respectively. Although this experiment was not expected to populate the wide ground state that could overshadow the low-lying positive parity state, the statistics were quite low and had significant background.

The ground state of ${}^9\text{Li}$ has been identified as $3/2^-$ [59] while the first excited state, at 2.69 MeV has a spin and parity of $1/2^-$ [58–60].

1.6.2 Beryllium isotopes: $A = 12, 11, 10$

The isotope ${}^{12}\text{Be}$ is located in the same island of inversion as ${}^{11}\text{Li}$ [10, 17, 105–110]. The ground state is expected to have a significant contribution from two neutrons in the $1s_{1/2}$ orbital. A low-lying 2^+ state and a low-lying isomeric 0^+ state confirm a nearby $1s_{1/2}$ orbital and high spectroscopic overlap with the ground state of ${}^{11}\text{Be}$ confirms a significant contribution from a $1s_{1/2}^2$ configuration [10, 108, 111]. In addition to the ground state structure, studies have been performed on the three bound states: 2^+ , 0^+ , and 1^- [107, 108, 111]. A 0^- state is expected to complete the $0^-, 1^-$ doublet from a valence neutron configuration of $0p_{1/2}^1 1s_{1/2}^1$, but a bound 0^- has not yet been found [112]. Very little is known about the higher-lying states, only two of which have been observed [113–116]. Both of those observed states have been above the one and two-neutron separation energies. A level diagram of all the measured ${}^{12}\text{Be}$ states and their relation to states in ${}^{11}\text{Be}$ and ${}^{10}\text{Be}$ is shown in Figure 1.12.

The lower of the two unbound states was first measured at 4559 ± 25 keV with a (t, p) reaction [119]. More than 15 years later, Fortune *et al.* repeated the reaction and reported a resonance energy and width of 4580 ± 5 keV and 107 ± 17 keV, respectively [114]. Since 1994, the state has been identified in four different reactions: ${}^{10}\text{Be}({}^{14}\text{N}, {}^{12}\text{N}){}^{12}\text{Be}$, ${}^9\text{Be}({}^{12}\text{C}, {}^9\text{C}){}^{12}\text{Be}$, ${}^{14}\text{C}({}^{12}\text{C}, {}^{14}\text{O}){}^{12}\text{Be}$, and ${}^{11}\text{Be}(d, p){}^{12}\text{Be}$ [120].

Although the state has been identified in multiple reactions, the assigned spin and parity have changed since the first measurement and have stirred recent debate. At the time of the first measurement, Fortune *et al.* assigned this state a spin and parity of 2^+ based on a comparison of angular distributions to theoretical Distorted Wave Born Approximation (DWBA) calculations [114]. More than fifteen years later, however, Fortune and Sherr revised that assignment to 3^- based on a private communication from J.D. Millener, who suggested that the population of the state was too strong to be a second 2^+ state [121]. After that re-assignment, Garrido *et al.* performed three-body calculations which suggested that the spin and parity were 0^+ , though both 1^- and 3^- assignments also could fit [122, 123]. Those three-body calculations were an extension of previous calculations that had been performed for the bound structure of ${}^{12}\text{Be}$ [84].

Since all these unbound states are unbound to both one and two neutron decay, some understanding of ${}^{11}\text{Be}$ and ${}^{10}\text{Be}$ is needed. As mentioned previously, ${}^{11}\text{Be}$ is also located in the island of inversion. Its ground state is $1/2^+$ [8, 124] with a dominant configuration of $1s_{1/2}$ for the valence neutron [125, 126]. The only bound excited state, at 320 keV, is the $1/2^-$ state [124], when the valence neutron is primarily in the $0p_{1/2}$ state. There have also been measurements of several

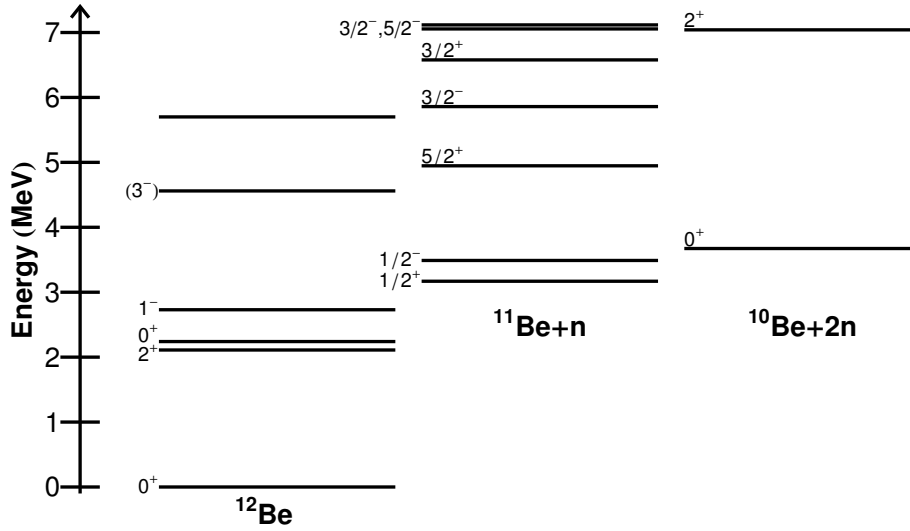


Figure 1.12: Level diagram of states in $^{12,11,10}\text{Be}$, relative to the ground state of ^{12}Be . Neutron separation energies are from [117, 118]. Bound and resonant state energies are from [107, 108, 111, 113–116].

unbound states [115, 116], shown in Figure 1.12. The ground state of ^{10}Be is 0^+ , while the first 2^+ state is located at an excitation energy of 3.37 MeV [115].

Chapter 2

Theoretical background

The decay of an unbound resonance is defined by a central energy and a width. Those can be measured directly from the data, but it can be difficult if not impossible to de-convolute the effects of resolutions and geometric acceptances to arrive at a spectrum that could be compared to other data sets. One solution to this is to perform a simulated experiment. This allows for the fitting of the energy and width through manipulation of an input decay energy distribution while properly accounting for experimental resolutions and acceptances. This chapter describes the theoretical background behind the lineshapes used to describe the single neutron and two neutron decays measured in this experiment.

2.1 Single neutron decay

Resonant decays, like those from neutron-unbound nuclei, can be described by a Breit-Wigner lineshape. Though the justification for the use of this lineshape takes many forms [127–130], the single neutron decay derivation here follows the R-matrix derivation presented in Thompson and Nunes [131]. A full derivation is beyond the scope of this document, but an outline of the derivation will be presented here. The reader is directed to Thompson and Nunes [131] as well as Lane and Thomas [129] for more detail.

2.1.1 R-matrix derivation

R-matrix theory is commonly used to describe nuclear scattering events. In this case, the one or two-proton knockout is assumed to be a direct reaction, populating the unbound state, which promptly decays. This is mapped onto R-matrix theory as inelastic scattering from one entrance channel to a different exit channel. Near the end, a simplification will be made to factor out dependence on the entrance channel.

R-matrix theory divides the calculation into two sections corresponding to physical regions: the interior and the exterior region. In the interior region, the particles interact with each other via the strong force and in the exterior region, they do not. The line of demarcation is the “channel radius” a , chosen at a distance where this can be assumed to be true. In the interior, the wavefunctions are constructed from the nuclear Hamiltonian. The R-matrix basis functions are constructed to have a fixed logarithmic derivative, β , at the radius a . The wavefunctions resulting from the diagonalization of the Hamiltonian in the R-matrix basis are matched at the radius a with the scattering wavefunctions in the exterior region. Here, R-matrix phenomenology is used to derive a resonance lineshape that will be fit to the data, rather than to make a prediction based on an assumed Hamiltonian. The lineshape will have pole energies E_p and reduced width amplitudes $\gamma_{p\alpha}$ as its fitted parameters.

The elements of the \mathbf{R} matrix at a scattering energy E for the uncoupled case are defined as:

$$R_{\alpha'\alpha}(E) = \sum_{p=1}^P \frac{\gamma_{p\alpha}\gamma_{p\alpha'}}{E_p - E} \quad (2.1)$$

where α indicates the entrance channel, α' is the exit channel, P is the number of poles, and the subscript p specifies a specific pole. The scattering S matrix is defined as:

$$\mathbf{S} = \frac{\mathbf{t}^{1/2}\mathbf{H}^- - a\mathbf{R}\mathbf{t}^{1/2}(\mathbf{H}^{-'} - \beta\mathbf{H}^-)}{\mathbf{t}^{1/2}\mathbf{H}^+ - a\mathbf{R}\mathbf{t}^{1/2}(\mathbf{H}^{+'} - \beta\mathbf{H}^+)} \quad (2.2)$$

Here, the matrix \mathbf{t} has diagonal elements $t_\alpha = \hbar^2/2\mu_\alpha$ where μ_α is the reduced mass of the channel α . \mathbf{H}^- and \mathbf{H}^+ are also diagonal matrices with elements $H_\alpha^{+/-} = G_\alpha \pm iF_\alpha$ where G_α and F_α are the irregular and regular solutions to the Coulomb wave equation and related to J -type Bessel functions. These functions are ℓ and E dependent, but the notation for those dependencies is included in the channel subscript α for simplicity. Equation 2.2 can be rewritten as

$$\mathbf{S} = (\mathbf{t}^{1/2}\mathbf{H}^+) \frac{1 - a\mathbf{R}(\mathbf{H}^{-'}/\mathbf{H}^- - \beta)}{1 - a\mathbf{R}(\mathbf{H}^{+'}/\mathbf{H}^+ - \beta)}. \quad (2.3)$$

Now define a diagonal ‘logarithmic’ matrix, \mathbf{L} , in terms of \mathbf{H}^+ as well as in terms of a shift matrix, δ , and a penetrability matrix, \mathbf{P} :

$$\mathbf{L} \equiv \mathbf{H}^{+'}/\mathbf{H}^+ - \beta = \frac{1}{a}(\delta + i\mathbf{P} - a\beta)$$

The diagonal shift and penetrability matrices have elements

$$\delta_\alpha = (\dot{F}_\alpha F_\alpha + \dot{G}_\alpha G_\alpha) P_\alpha$$

$$P_\alpha = \frac{k_\alpha a}{F_\alpha^2 + G_\alpha^2}$$

where the dot indicates a derivative with respect $\rho = k_\alpha r$ instead of r . Though the logarithmic matrix is defined in terms of \mathbf{H}^+ , its complex conjugate can be expressed in terms of \mathbf{H}^- :

$$\mathbf{L}^* = \mathbf{H}^{-'}/\mathbf{H}^- - \beta.$$

Using these definitions, the elements of the S matrix can be rewritten as

$$\mathbf{S} = \mathbf{\Omega}(\mathbf{t}\mathbf{H}^-\mathbf{H}^+)^{-1/2} \frac{1 - a\mathbf{R}\mathbf{L}^*}{1 - a\mathbf{R}\mathbf{L}} (\mathbf{t}\mathbf{H}^-\mathbf{H}^+)^{1/2} \mathbf{\Omega}$$

where the matrix $\mathbf{\Omega}$ has diagonal elements $\Omega_\alpha = e^{i\phi_\alpha}$ and ϕ_α are hard-sphere phase shifts. The product of diagonal matrices $\mathbf{t}\mathbf{H}^-\mathbf{H}^+$ can be rewritten in terms of the channel velocities \mathbf{v} , with elements $v_\alpha = \hbar k_\alpha/\mu_\alpha$:

$$(\mathbf{t}\mathbf{H}^-\mathbf{H}^+)_\alpha = \frac{\hbar v_\alpha a}{2P_\alpha}$$

The cross section for scattering from channel α_i to channel α is proportional not to the matrix \mathbf{S} , but the symmetric matrix $\tilde{\mathbf{S}}$, which is constructed with a similarity transformation $\tilde{\mathbf{S}} \equiv \mathbf{v}^{1/2}\mathbf{S}\mathbf{v}^{-1/2}$, and simplifies to

$$\tilde{\mathbf{S}} = \mathbf{\Omega}[1 + 2i\mathbf{P}^{1/2}(1 - a\mathbf{R}\mathbf{L})^{-1}\mathbf{R}\mathbf{P}^{1/2}]\mathbf{\Omega}.$$

This general equation simplifies with one assumption: a single pole (energy level, designated by E_0) and only two channels. Two channels *must* be considered because the desired description is one where the entrance and exit channels have the mass partitioned differently. This means that the final cross-section calculation will be performed with $\tilde{S}_{12} = \tilde{S}_{21}$:

$$\tilde{S}_{12} = e^{i\phi_1} \left[\frac{i\sqrt{2}\gamma_1 P_1^{1/2} \sqrt{2}\gamma_2 P_2^{1/2}}{(E_0 - E)(1 - aR_{11}L_1 - aR_{22}L_2)} \right] e^{i\phi_2} \quad (2.4)$$

The following definitions for formal width Γ_α , δ_α^0 , energy shift Δ_α , total energy shift Δ_T , and total formal width Γ_T can be substituted in Equation 2.4:

$$\begin{aligned} \Gamma_\alpha &= 2\gamma_\alpha^2 P_\alpha \\ \delta_\alpha^0 &= \delta_\alpha - a\beta \\ \Delta_\alpha &= -\gamma_\alpha^2 \delta_\alpha^0 \\ \Delta_T &= \Delta_1 + \Delta_2 = -\gamma_1^2 \delta_1^0 - \gamma_2^2 \delta_2^0 \\ \Gamma_T &= \Gamma_1 + \Gamma_2 = 2\gamma_1^2 P_1 + 2\gamma_2^2 P_2. \end{aligned}$$

The value of $-a\beta$ can be set at any constant value and in this work it has been set to $-a\beta = \delta_\alpha(E_0)$ as suggested by Lane and Thomas [129]. Once those definitions have been included, the expression for \tilde{S}_{12} is much simpler and already looks like a Breit-Wigner:

$$\tilde{S}_{12} = e^{i\phi_1} \left[\frac{i\Gamma_1^{1/2} \Gamma_2^{1/2}}{(E_0 - E + \Delta_T) + i\Gamma_T/2} \right] e^{i\phi_2}. \quad (2.5)$$

All that remains is to substitute Equation 2.5 into the following equation for the cross-section to go from entrance channel α_i to exit channel α :

$$\sigma_{\alpha\alpha_i}(E) = \frac{\pi}{k_i^2} \frac{2J_t + 1}{(2I_{p_i} + 1)(2I_{t_i} + 1)} |\tilde{S}_{12}|^2 \quad (2.6)$$

$$= \frac{\pi}{k_i^2} \frac{2J_t + 1}{(2I_{p_i} + 1)(2I_{t_i} + 1)} \frac{\Gamma_{\alpha_i} \Gamma_\alpha}{(E - E_0 + \Delta_T)^2 + \Gamma_T^2/4} \quad (2.7)$$

In this equation, k_i is the wavenumber of the entrance channel, J_t is the total spin of the populated state, and I_{p_i} and I_{t_i} are the spins of the projectile- and target-like fragments in the entrance channel.

The process of interest here is the decay of an unbound state. The population mechanism is unimportant. Equation 2.7 can be rearranged to clearly display a factorization of these two components, the population and the subsequent decay:

$$\sigma_{\alpha\alpha_i}(E) = \left(\frac{\pi}{k_i^2} \frac{(2J_t + 1)\Gamma_{\alpha_i}}{(2I_{p_i} + 1)(2I_{t_i} + 1)} \right) \left(\frac{\Gamma_\alpha}{(E_0 - E + \Delta_T)^2 + \Gamma_T^2/4} \right)$$

When all that is desired is a lineshape of the E dependence, the first grouping related to the population can be treated as a constant. In addition, during the decay process, the probability for decay through the entrance channel is small. As a consequence, $\Gamma_\alpha \gg \Gamma_{\alpha_i}$ and $\Gamma_T \approx \Gamma_\alpha$ and $\Delta_T \approx \Delta_\alpha$. The lineshape for the decay of a neutron-unbound state then is:

$$\sigma(E; E_0, \Gamma_0)_\ell = A \frac{\Gamma_\ell(E; E_0, \Gamma_0)}{[E_0 - E + \Delta_\ell(E; E_0, \Gamma_0)]^2 + \frac{1}{4}[\Gamma_\ell(E; E_0, \Gamma_0)]^2} \quad (2.8)$$

where the channel subscripts have been dropped and the dependences on the angular momentum of the neutron, the decay energy, the central resonance energy, and the energy-dependent width at E_0 (Γ_0) have been explicitly stated. Γ_0 , the width of the decay at E_0 is used as a substitute parameter for the reduced partial width γ^2 :

$$\Gamma_0 = 2\gamma^2 P_\ell(E_0)$$

which means that Γ_α (or Γ_ℓ in the case of Equation 2.8) is now:

$$\Gamma_\ell(E; E_0, \Gamma_0) = 2P_\ell(E) \left(\frac{\Gamma_0}{2P_\ell(E_0)} \right). \quad (2.9)$$

2.1.2 Saturation of resonance lineshape

The energy-dependent Breit-Wigner has as its input parameters a central energy, a width at that central energy, and an angular momentum index. One peculiar feature of just using the lineshape and ignoring the magnitude of the prefactor A from Equation 2.8 is that as the width Γ_0 increases, the lineshape becomes saturated. This can be seen by explicitly expanding the dependence of Δ_ℓ on Γ_0 :

$$\Delta_\ell(E; E_0, \Gamma_0) = -[\delta_\ell(E) - \delta_\ell(E_0)] \left(\frac{\Gamma_0}{2P_\ell(E_0)} \right)$$

and referring to a similar expansion in Equation 2.9. Substituting these into Equation 2.8 produces:

$$\sigma(E; E_0, \Gamma_0, \ell) = \frac{A}{\Gamma_0} \frac{P_\ell(E)/P_\ell(E_0)}{\left[\frac{E_0 - E}{\Gamma_0} - \frac{1}{2P_\ell} (\delta_\ell(E) - \delta_\ell(E_0)) \right]^2 + \frac{1}{4} [P_\ell(E)/P_\ell(E_0)]^2}$$

where Γ_0 is present only twice. Once in the denominator of the prefactor, where it has a solely multiplicative impact, and once when dividing the quantity $(E_0 - E)$. When the width increases, $\Gamma_0 \gg E_0 - E$ and that term becomes small. Far from the peak, the $\delta_\ell(E) - \delta_\ell(E_0)$ term is large and so the $\Gamma_0/(E_0 - E)$ term is negligible.

When that term can be neglected, the only effect of increasing the width of the Breit-Wigner distribution is to decrease the overall magnitude of the calculation. When the lineshape itself changes very little, then the sensitivity to the width Γ_0 is lost. An example of this saturation can be seen in Figure 2.1. Especially once experimental resolutions and acceptances are applied, the difference between the $\Gamma_0 = 10.0$ and $\Gamma_0 = 100.0$ distributions, for example, is small.

2.2 Two neutron decay

A single-neutron, two-body decay is entirely determined by the masses of the two particles and the decay energy of the system. The addition of a third-particle in the decay process increases the number of degrees of freedom as well as the complexity and options of the simulations. The three-body decays in this work were modeled by three different types of a decays: a phase space decay, a sequential decay, and a dineutron decay. Each uses a different method for constraining these extra degrees of freedom. Details of the implementation of the models in the simulations can be found in Section 4.4.6.2.

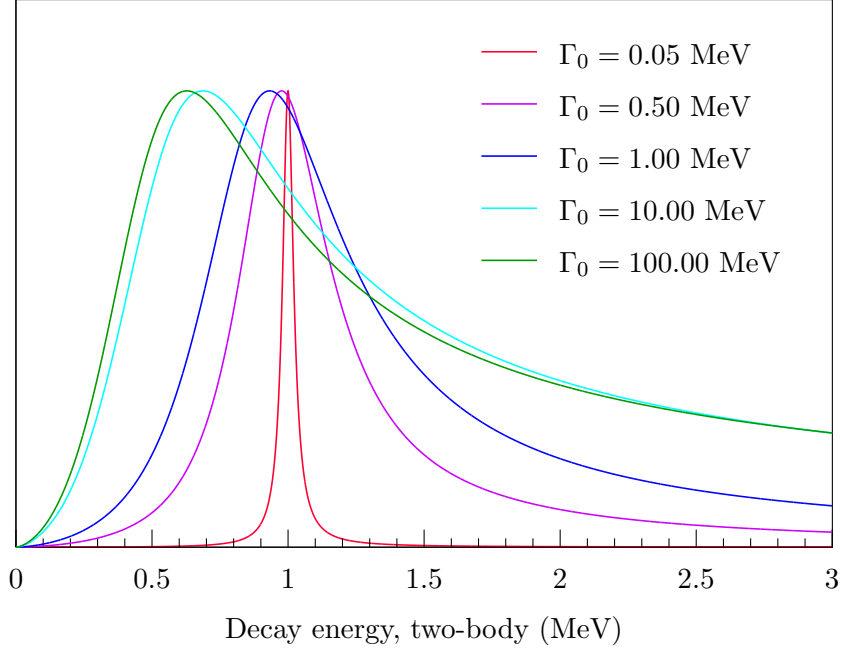


Figure 2.1: Energy-dependent Breit-Wigner lineshapes with varying Γ_0 . For all lineshapes, $\ell = 1$ and $E_0 = 1.0$ MeV. All lineshapes have been normalized to the same peak height.

2.2.1 Phase space decay

Just as an isotropic distribution uniformly fills the spherical surface elements, in a phase space decay of one particle into three daughter particles, the kinematics of the decay uniformly fill the three-body phase space. The three-body phase space integral, R_3 is defined as:

$$R_3 = \int \delta^4(P_0 - \sum_{j=1}^3 P_j) \prod_{i=1}^3 \delta(P_i^2 - m_i^2) d^4 P_i$$

where P_0 is the four-momentum of the initial state, P_i are the four-momenta of the three particles, and m_i are the rest masses of the three particles. This description includes kinematic factors such as the conservation of energy and momentum with the first delta function. The products of the second delta function and the infinitesimals also incorporate the density of states:

$$\begin{aligned} \delta(P_i^2 - m_i^2) d^4 P_i &= \delta(E_i^2 - (p_i^2 + m_i^2)) dE_i p_i^2 dp_i d(\cos \theta_i) d\phi_i \\ &= \frac{p_i^2}{2E_i} dp_i d(\cos \theta_i) d\phi_i \end{aligned}$$

where p_i is the magnitude of the three-momentum, E_i is the energy, and θ_i and ϕ_i are the angular coordinates of the daughter particles. When the momentum of a particle is large, there are more kinematic options for its arrangement, as reflected in the factor of $p_i^2/(2E_i)$. Energies and angles of the three decay products are constrained by distributions that uniformly fill this three-body phase space.

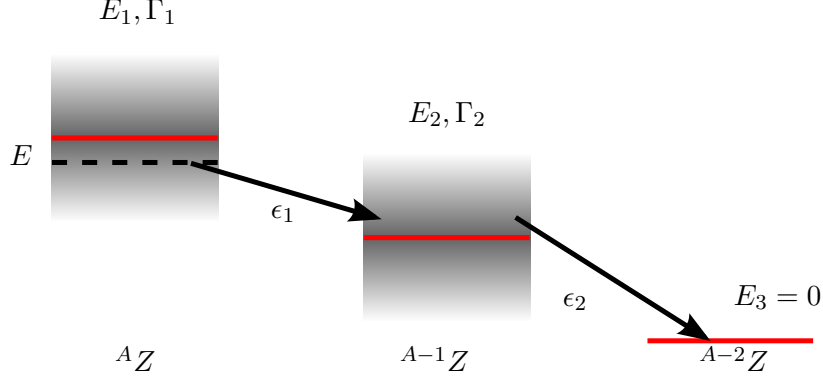


Figure 2.2: A diagram of the sequential decay described.

2.2.2 Sequential decay

The sequential decay model used in this document is based on previously published work by A. Volya [132,133]. The goal of the continuum shell model is to naturally integrate both the continuum and shell model descriptions of the nucleus, essential for accurately describing neutron decays which connect the two spaces. Details beyond this outline are available in Refs. [132,133].

A diagram of a sequential decay is shown in Figure 2.2. An unbound initial state in a nucleus of mass A has a distribution defined by a central energy E_1 and a width, Γ_1 . One neutron, with kinetic energy ϵ_1 is emitted in the decay to the intermediate state, defined by another central energy and width pair, E_2 and Γ_2 . A second neutron with kinetic energy ϵ_2 is then emitted in a decay to a bound state in the $A - 2$ nucleus. Here, the continuum shell model is used to calculate a distribution for the relative energy of the two neutrons $E_r = \epsilon_1 - \epsilon_2$ as a function of total decay energy E (note that E is the continuous variable indicating the total decay energy, as opposed to E_1 , which is the central value of the initial state distribution). This explicitly comes down to calculating $d\sigma(E)/dE_r$. The energy-dependent Breit-Wigner approximation for the cross-section due to a single resonance is

$$\frac{d\sigma}{dE_r} \propto \frac{1}{(E - E_1)^2 + \Gamma_T^2(E)/4} \frac{d\Gamma(E)}{dE_r}$$

and the total width due to a sequential decay is

$$\Gamma_T(E) = \int dE_r \frac{d\Gamma(E)}{dE_r}. \quad (2.10)$$

The Fermi Golden Rule gives the partial decay width distribution for the sequential process as:

$$\frac{d\Gamma(E)}{d\epsilon_1 d\epsilon_2} = 2\pi \delta(E - \epsilon_1 - \epsilon_2) |A_T(\epsilon_1, \epsilon_2)|^2 \quad (2.11)$$

where A_T is the total amplitude for the decay. Assuming a spin anti-symmetric pair of neutrons, the spatial part of A_T should be symmetric. Define that total amplitude as

$$A_T(\epsilon_1, \epsilon_2) = \frac{1}{\sqrt{2}} \left(\frac{A_1(\epsilon_1)A_2(\epsilon_2)}{\epsilon_2 - (E_2 - \frac{i}{2}\Gamma_2(\epsilon_2))} + \frac{A_1(\epsilon_2)A_2(\epsilon_1)}{\epsilon_1 - (E_2 - \frac{i}{2}\Gamma_2(\epsilon_1))} \right) \quad (2.12)$$

where A_1 and A_2 are the single-particle decay amplitudes for the two decays. This assumes that the two neutrons are in a spin-antisymmetric singlet state with a symmetric position component.

Specifically, the implementation included here assumes that the two neutrons came from the same orbital and are coupled to a J^π of 0^+ .

With a substitution of $E = \epsilon_1 + \epsilon_2$ and $E_2 = E + S$, where S is the difference between the energy of the intermediate state and the initial energy, Equation 2.12 can be rewritten as

$$A_T(\epsilon_1, \epsilon_2) = \frac{1}{\sqrt{2}} \frac{A_1(\epsilon_1)A_2(\epsilon_2)[S + \epsilon_2 - \frac{i}{2}\Gamma_2(\epsilon_1)] + A_1(\epsilon_2)A_2(\epsilon_1)[S + \epsilon_1 - \frac{i}{2}\Gamma_2(\epsilon_2)]}{[S + \epsilon_1 - \frac{i}{2}\Gamma_2(\epsilon_2)][S + \epsilon_2 - \frac{i}{2}\Gamma_2(\epsilon_1)]} \quad (2.13)$$

At this point, it is useful to know the energy dependence of A_1 and A_2 . The energy dependence can be understood in the following way. Γ_i is defined as 2π times the square of the single-particle amplitude and it can also be defined as an energy-dependent single-particle decay width, $\gamma_\ell(\epsilon)$, multiplied by a spectroscopic factor, \mathcal{S}_i . Put another way,

$$\Gamma_i = 2\pi|A_i(\epsilon)|^2 = \gamma_\ell(\epsilon)\mathcal{S}_i. \quad (2.14)$$

The single-particle decay width can be approximated with the calculated width for a neutral particle in a square well [134]. This width has a slight mass dependence, so the decay for mass A to mass $A - 1$ will be slightly greater than that for the decay of $A - 1$ to $A - 2$. In this work, however, that difference is small, so the energy dependence (in γ_ℓ) is separable from the index dependence (in \mathcal{S}_i). Equation 2.14 can be used then to simplify 2.13:

$$A_T(\epsilon_1, \epsilon_2) = \frac{-1}{\sqrt{4\pi}} \frac{\sqrt{\gamma_\ell(\epsilon_1)\gamma_\ell(\epsilon_2)\mathcal{S}_1\mathcal{S}_2}[2S + E - \frac{i}{2}(\Gamma_2(\epsilon_1) + \Gamma_2(\epsilon_2))]}{[S + \epsilon_1 - \frac{i}{2}\Gamma_2(\epsilon_2)][S + \epsilon_2 - \frac{i}{2}\Gamma_2(\epsilon_1)]}$$

Finally, substitute this into Equation 2.11 and write the differential in terms of the relative energy E_r :

$$\frac{d\Gamma(E)}{dE_r} = \frac{1}{8\pi} \gamma_\ell(\epsilon_1)\gamma_\ell(\epsilon_2)\mathcal{S}_1\mathcal{S}_2 \left| \frac{2S + E - \frac{i}{2}(\Gamma_2(\epsilon_1) + \Gamma_2(\epsilon_2))}{[S + \epsilon_1 - \frac{i}{2}\Gamma_2(\epsilon_2)][S + \epsilon_2 - \frac{i}{2}\Gamma_2(\epsilon_1)]} \right|^2 \quad (2.15)$$

This defines the relative energy of the two neutrons for a sequential decay.

2.2.3 Dineutron decay

Like the sequential decay theory, the dineutron decay theory is also based on work previously published by A. Volya [132, 133]. The amplitude for the decay is:

$$A_T(\epsilon_K, \epsilon_I) = \frac{A_1(\epsilon_K)A_2(\epsilon_I)}{\epsilon_I - (E_2 - \frac{i}{2}\Gamma_2(\epsilon_I))}$$

Instead of ϵ_1 and ϵ_2 for the energies of the neutrons, let ϵ_K be the kinetic energy of the dineutron and ϵ_I be its intrinsic energy. The initial state energy, E_1 is the sum of those energies: $E_1 = \epsilon_K + \epsilon_I$. A_1 and A_2 are the amplitudes of the emission of the dineutron (the first step) and the separation of the dineutron (second step). Putting this directly in the Fermi Golden Rule (Equation 2.11) produces

$$\frac{d\Gamma}{d\epsilon_K d\epsilon_I} = \frac{1}{2\pi} \delta(E_1 - \epsilon_K - \epsilon_I) \frac{\Gamma_1(\epsilon_K)\Gamma_2(\epsilon_I)}{(\epsilon_I - E_2)^2 + \Gamma_2^2(\epsilon_I)/4}. \quad (2.16)$$

Assume that both the decay of the dineutron from the fragment and the decay of the dineutron itself can be parametrized as an s-wave decay. The decay width of a neutral $\ell = 0$ particle in a

square well derived by Bohr and Mottelson [134] is used then to define Γ_1 and Γ_2 :

$$\Gamma_1(\epsilon_K) = \frac{2\hbar^2}{m_D R} k_K \quad (2.17)$$

$$\Gamma_2(\epsilon_I) = \frac{2\hbar^2}{\mu r} k_I \quad (2.18)$$

where m_D is the mass of the dineutron ($2m$), μ is the reduced mass ($m/2$), R is the channel radius for the dineutron separating from the $A-2$ daughter fragment defined by $R = r_0[(A-2)^{1/3} + 2^{1/3}]$, r is the channel radius for the breakup of the dineutron, defined by $R = r[1^{1/3} + 1^{1/3}]$, and r_0 is the scaling factor that parametrizes that radius, here set to 1.4 fm.

The value for the “intermediate” state energy E_2 is not as obvious as in the sequential decay. As the intrinsic energy ϵ_I goes to zero though (or in this case gets very small relative to E_2), the denominator must be proportional to $1/a_s + ik_I$ where a_s is the s-wave neutron-neutron scattering length to satisfy the effective range approximation. Associated with this scattering length is an energy, ϵ_0 , defined as:

$$\epsilon_0 = \frac{\hbar^2}{2\mu a_s^2}.$$

To make the denominator proportional, the width $\Gamma_2(\epsilon_I)$ should be equal to $-2k_I a_s E_2$, which defines the “intermediate” state energy E_2 as:

$$E_2 = -\frac{\hbar^2}{\mu r_0 a_s} = -\epsilon_0 \frac{2a_s}{r_0}.$$

Using the definition for ϵ_0 and the following definitions for ϵ_I and ϵ_K ,

$$\epsilon_K = \frac{\hbar^2 k_K^2}{2m_D}$$

$$\epsilon_I = \frac{\hbar^2 k_I^2}{2\mu}$$

Equations 2.18 and 2.17 can be re-written as

$$\Gamma_1(\epsilon_K) = 2 \frac{|a_s|}{R} \sqrt{\epsilon_0 \epsilon_K} \quad (2.19)$$

$$\Gamma_2(\epsilon_I) = 4 \frac{|a_s|}{r} \sqrt{\epsilon_0 \epsilon_I} \quad (2.20)$$

Substituting Equations 2.19 and 2.20 into Equation 2.16 produces:

$$\frac{d\Gamma(E_1)}{d\epsilon_I} = \frac{1}{\pi} \frac{\sqrt{(E_1 - \epsilon_1)\epsilon_1}}{\left(1 + \frac{r\epsilon_I}{2a_s\epsilon_0}\right)^2} \frac{r}{\epsilon_0 + \epsilon_1} \frac{1}{R}$$

which defines the distribution of the intrinsic energy of the dineutron.

Chapter 3

Experimental techniques

3.1 Beam production

The experiment was performed at the National Superconducting Cyclotron Laboratory (NSCL) in July and August of 2012. A ^{13}B beam was provided by the Coupled Cyclotron Facility (CCF) [135] and the A1900 Fragment Separator [136] using the process of projectile fragmentation [137]. A schematic of the CCF and A1900 is shown in Figure 3.1. Ions of $^{18}\text{O}^{3+}$ were injected into the K500 cyclotron, where they were accelerated to an energy of 10.91 MeV/u. They then traveled to the K1200 cyclotron where they immediately passed through a stripper foil that stripped off the rest of their electrons. These fully ionized nuclei were accelerated through the K1200 and emerged fully stripped at an energy of 120 MeV/u.

After the K1200 cyclotron, the oxygen beam impinged on a Be production target (2491 mg/cm^2), creating a wide variety of fragments. All these fragments entered the A1900 Fragment Separator, which was set to the magnetic rigidity of the desired ^{13}B secondary beam to filter out most other fragments. A 300 mg/cm^2 aluminum wedge was included at the dispersive midplane of the A1900 to separate nuclei of different charge that entered the wedge with the same magnetic rigidity. Energy loss through the aluminum wedge is proportional to Z^2 where Z is the charge of the nucleus. Different elements that entered the wedge with the same magnetic rigidity left with different rigidities, allowing them to be filtered out by the magnets after the wedge. The ^{13}B beam was delivered to the experimental vault with an energy of 71 MeV/u, corresponding to a magnetic rigidity of 3.2271 Tm.

In addition to the ^{13}B beam, the CCF and A1900 also provided a ^{12}B beam. The primary beam, target, and degrader were all the same in the production of the ^{12}B beam, but the magnet settings were different. The ^{12}B beam arrived at the experimental vault with an energy of 71 MeV/u and a magnetic rigidity of 2.97720 Tm.

3.2 Beam detector and target

As it left the A1900, the beam passed through a timing scintillator (named the A1900 scintillator) that was optically coupled to a photomultiplier tube (PMT). Ten meters downstream, upon entering the experimental area (shown in Figure 3.2), the beam hit a thin plastic timing scintillator, called the target scintillator. The 0.254 mm thick target scintillator was made of BC-404 and optically coupled to one PMT. At a location 1.04 m downstream of the timing scintillator, the beam impinged upon a 51.37 mg/cm^2 beryllium target. Such a thin target was able to be used because of the high beam rate, which was approximately 800,000 Hz on target.

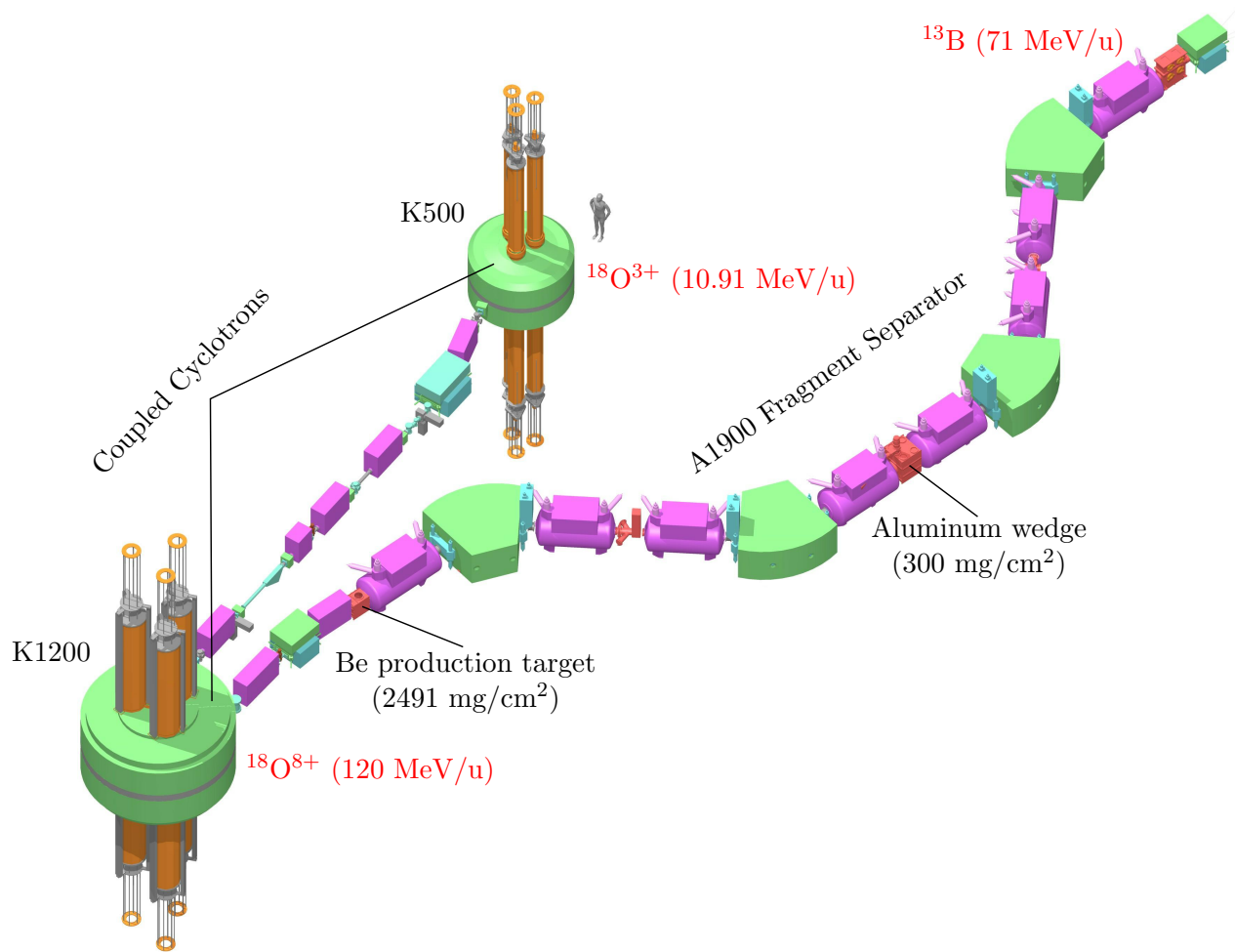


Figure 3.1: Schematic of the Coupled Cyclotron Facility and A1900 Fragment Separator with the production setting for this experiment.

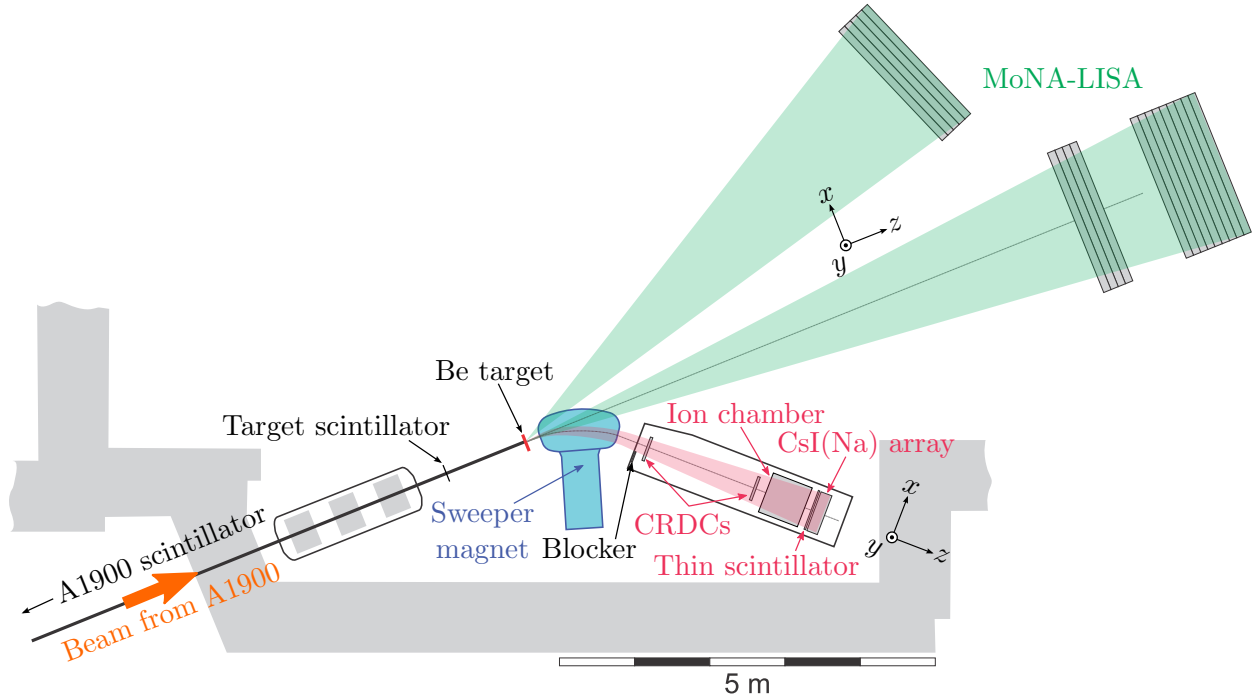


Figure 3.2: Schematic of the experimental area.

3.3 Sweeper magnet

Unreacted beam, charged reaction fragments and neutrons leaving the target entered the Sweeper magnet [138]. This large-gap dipole magnet had a bending angle of 43.3 degrees and a radius of 1 meter. The Sweeper magnet bent the trajectories of the unreacted beam and charged reaction fragments into a suite of charged particle detectors while the neutrons, unaffected by the magnetic field, continued straight through a vertical gap of 14 cm into the neutron detectors MoNA and LISA, detailed later in Section 3.5. The maximum magnetic rigidity for the Sweeper magnet is 4 Tm. For reactions with the ^{13}B beam, the magnetic rigidity of the Sweeper was set to 3.76 Tm. For reactions with the ^{12}B beam, it was set to 3.71 Tm. Both settings were set to center the ^9Li fragments in the detectors and minimize the amount of unreacted beam interacting in CRDC1.

3.4 Charged particle detectors

After the Sweeper magnet was a large vacuum box containing a suite of detectors for the charged fragments. The positions of the particles was measured with Cathode Readout Drift Counters (CRDCs), the energy loss was measured in an ion chamber, the time of flight was measured with a plastic timing scintillator, and the total remaining energy was measured with a CsI(Na) scintillator array.

3.4.1 Blocker

A 25.4 cm x 13 cm x 9.5 mm tungsten blocker was located at the entrance to the Sweeper detector box. In this experiment it sat just off the entrance of the beamline into the box, not blocking the active area of any detector. Most of the unreacted beam was bent into the blocker.

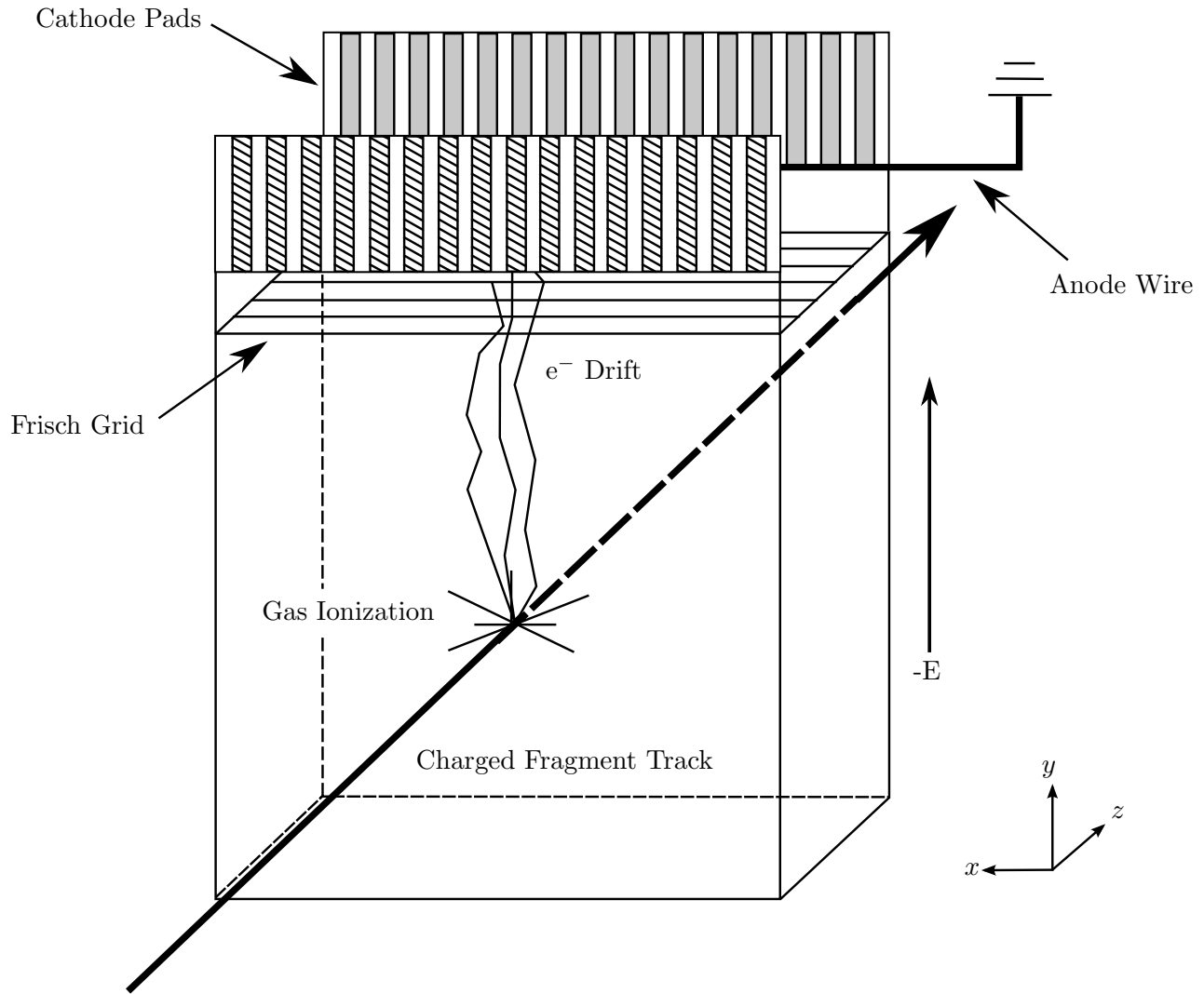


Figure 3.3: Schematic of CRDC operation modified from [139] where the z -direction has been expanded for detail. The field shaping wires mentioned in the text are not included for visibility and simplicity.

3.4.2 Cathode Readout Drift Counters

Two CRDCs were positioned along the beam line. The first CRDC was positioned immediately after the blocker (1.72 m from the target) and the second was located 1.55 m downstream from the first. The active area of each CRDC was 30 cm x 30 cm in the xy -plane. Each detector was filled with a gas mix of 20% isobutane and 80% CF_4 at an operating pressure of 300 Torr.

Each CRDC operated similarly to a two-dimensional ion chamber optimized for position. A schematic of the operation is shown in Figure 3.3. The passage of charged particles through the detector created ionization pairs in the gas, which drifted apart due to an applied electric field. In this experiment, the field was created by the application of a 1000 V drift voltage between a plate at the top of the detector and the Frisch grid near the bottom of the detector. Field shaping wires were placed at regular intervals on the two faces of the detector and parallel to the x -direction. Above the Frisch grid was a charged anode wire (parallel to the x -axis) and a series of 116 aluminum

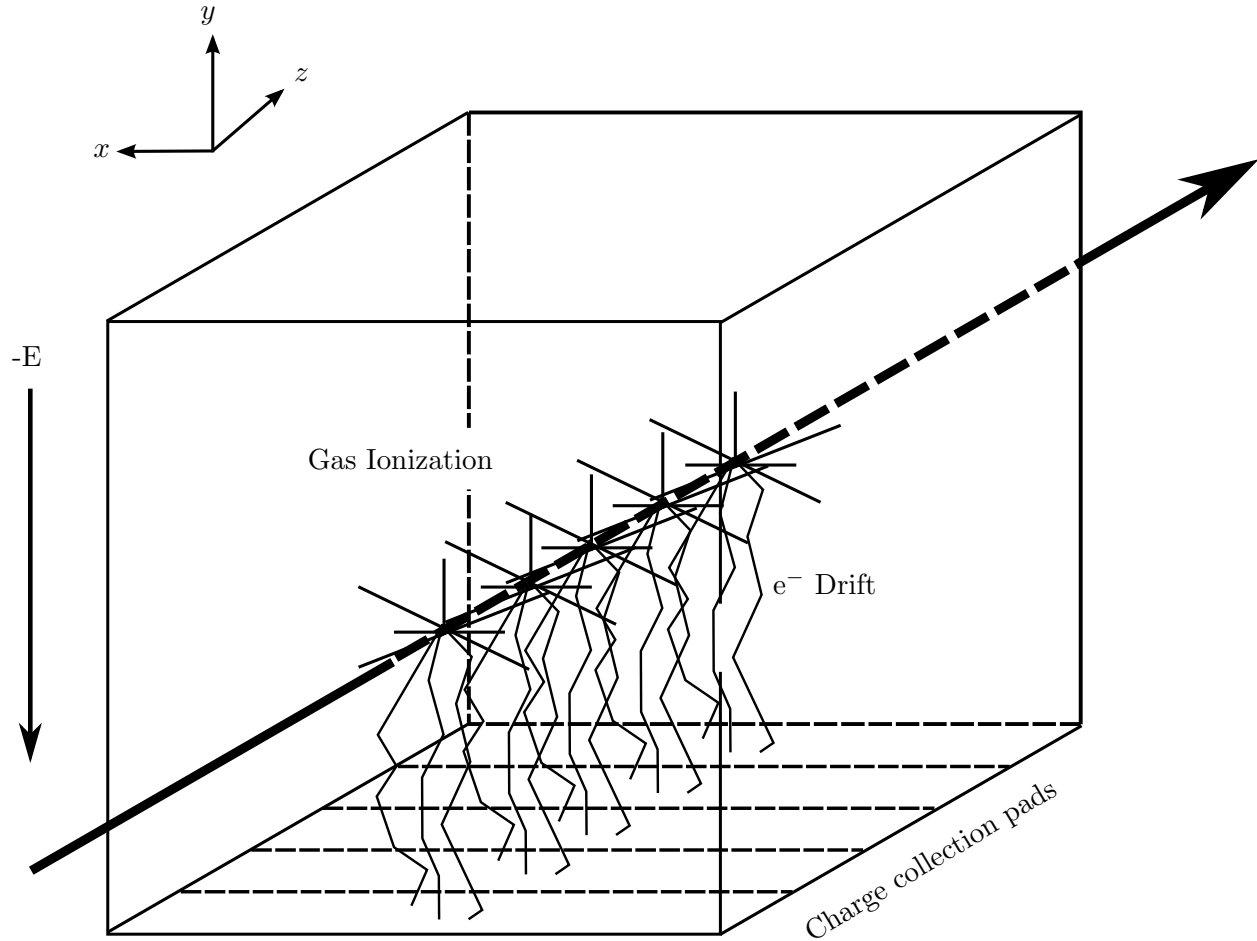


Figure 3.4: Schematic of ion chamber.

cathode pads with a pitch of 2.54 mm in width, segmented along the x -axis. Once the electrons drifted through the Frisch grid, they felt the strong field created by the anode wire. This field caused an avalanche of electrons, increasing the number available for detection. The y -position of the particle was determined by the drift time of the electron, measured as the time difference between the thin timing scintillator near the end of the beam line and the detection of charge along the anode wire. The x -position of particle was determined with induced cathode readout [140]. In this method, a charge distribution is induced upon the cathode pads by the avalanche electrons. The peak of this distribution gives the x -position of the particle.

3.4.3 Ion chamber

A schematic of the ion chamber is shown in Figure 3.4. The active area of the ion chamber was 40 cm x 40 cm and its length was 65 cm. It was filled with P-10 gas (90% argon and 10% methane) at 300 Torr. Windows made of Kevlar filament, 12 μm PPTA (an aramid plastic), and epoxy allowed the particles to pass in and out of the detector with little energy loss. The upstream window had an area of 30 cm x 30 cm to match the geometric acceptance of the second CRDC, while the downstream window had an area of 40 cm x 40 cm, to allow for the spread of the beam. A large plate at the top of the ion chamber and 16 charge collection pads at the bottom were biased to

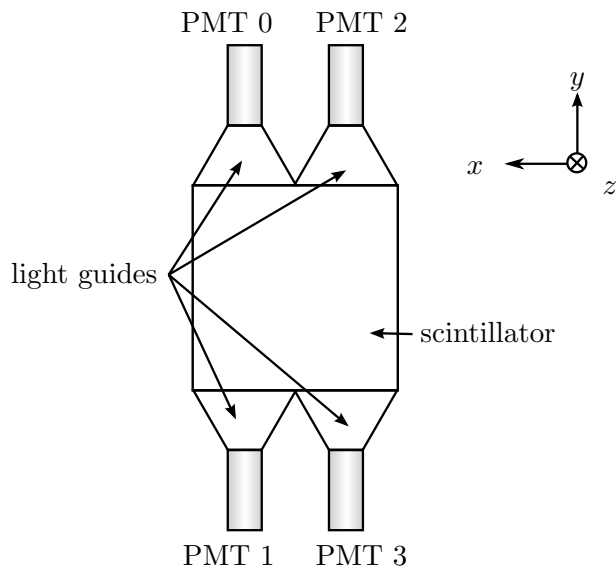


Figure 3.5: A schematic of the thin scintillator, as seen from upstream of the detector.

create a drift voltage of 10 V. As charged particles passed through, they created ion pairs. The electrons drifted down and were collected on the 16 collection pads which discretized the z -direction and extended along the x -direction. The charge collected on all 16 pads was used as a measurement of the energy loss in the ion chamber.

3.4.4 Timing scintillator

A thin timing scintillator sat immediately after the ion chamber to serve as the charged fragment trigger as well as to measure the time of flight of the particles. The 55 cm x 55 cm x 5 mm scintillator was made of EJ-204, an equivalent to BC-404, both types of plastic from Eljen and Bicon, respectively. Two trapezoidal light guides were attached to the top edge of the scintillator and another two were attached on the bottom. Each light guide was optically coupled to the thin scintillator and a PMT as shown in Figure 3.5.

Organic scintillators such as this one take advantage of the π -electron structure of the dopant molecules within the plastic. The electronic energy levels consist of singlet states and vibrational states which are associated with those singlet states. The spacing between vibrational states that correspond to a singlet state is much smaller than the spacing between singlet states. At room temperature, due to thermalization, most of the molecules are in the ground state. As a charged particle passes through, kinetic energy from the passage of the particle is absorbed by the molecules, exciting them. Higher excitations are quickly de-excited to the first excited singlet state through internal conversion. Any vibrational energy is thermalized and most of the affected molecules are now in the first excited singlet state. This state then decays and emits scintillation light to any of the states associated with the ground singlet state. This light propagates to the light guides on either end of the detector. For a timing scintillator, the decay constant associated with this decay should be small - for EJ-204 this constant is 1.8 ns.

3.4.5 CsI(Na) array

At the end of the beamline, charged fragments were stopped in a CsI(Na) array. A mechanical design of the array is shown in Figure 3.6. The array consists of twenty-five 3.25" x 3.25" x 2.16"

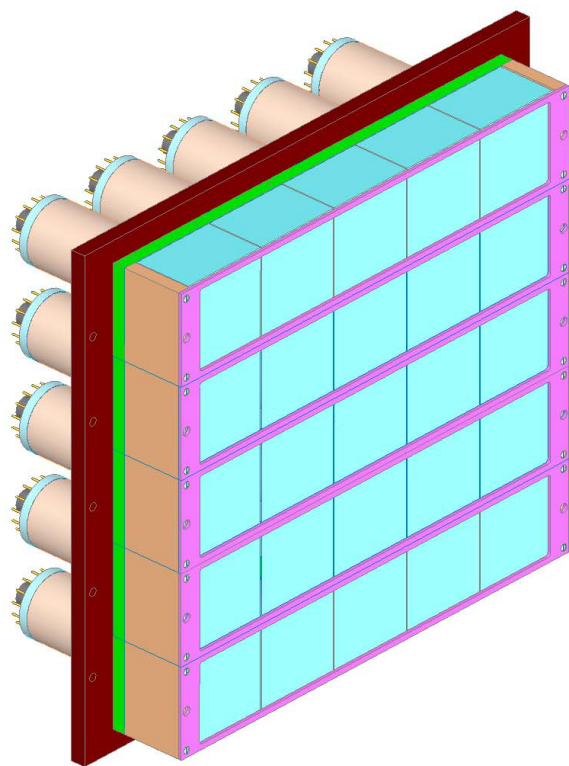


Figure 3.6: A mechanical design drawing of the CsI(Na) array.

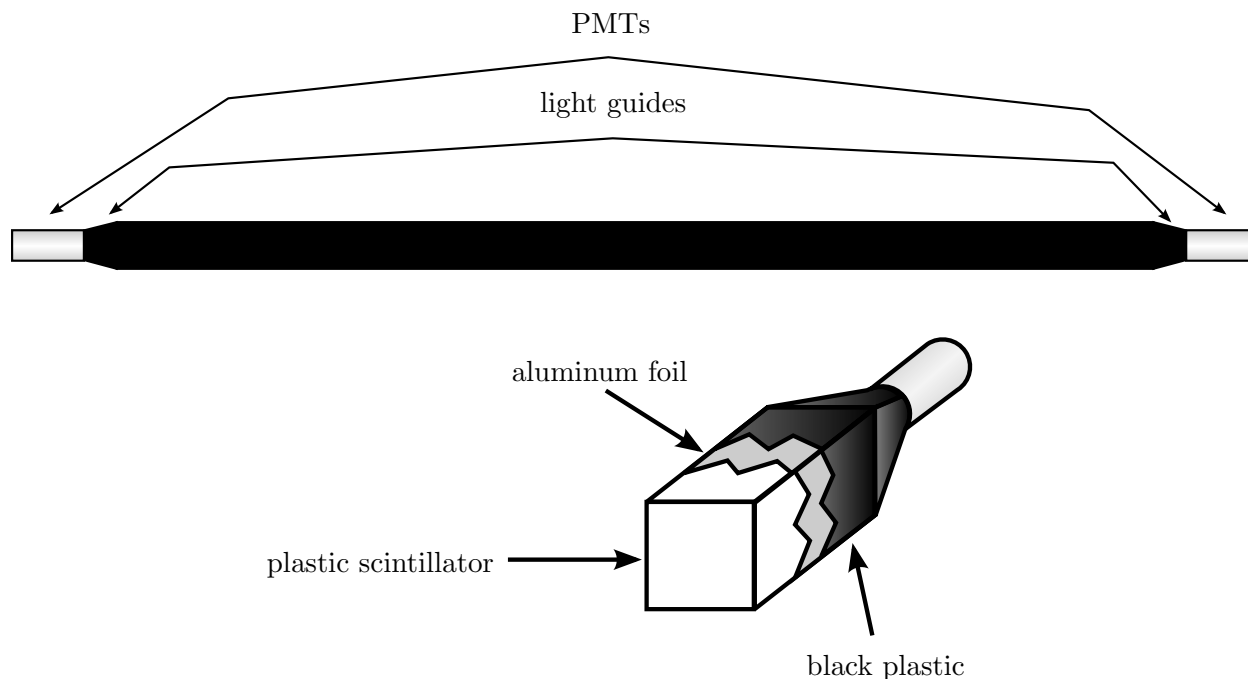


Figure 3.7: A schematic of a MoNA LISA bar.

CsI(Na) crystals. There were five assemblies, each of which consisted of one row of five crystals. When these assemblies were stacked, it produced a 5x5 array. Since the array was centered on the beamline, the cross-sectional area seen by the beam was 16.25" x 16.25" or 41 cm x 41 cm. For optical separation and to maximize internal reflection, each crystal was wrapped in reflective material 0.2 mm thick. Each crystal was optically coupled on its downstream side to a Hamamatsu PMT R1307 with magnetic shielding. Each PMT was powered by a voltage divider which also provided a single signal output.

Each assembly was fitted into a stainless steel frame which was bolted to a stainless steel support structure. This structure sat on the rails of the Sweeper detector box, enabling the CsI(Na) array to move along the full length of the box. The crystals themselves were hygroscopic and easily damaged by moisture in the air. To deal with this, a four sided gas cover surrounded the crystals. When the thin scintillator was pushed up against the cover, it created a five sided box. A gas inlet allowed the flow of dry air along the face of the crystals without requiring the dry air to fill a large space. This air flowed over the face of the crystals whenever the detector box was not under vacuum.

3.5 MoNA-LISA

Both the Modular Neutron Array (MoNA) and the Large-area multi-Institutional Scintillator Array (LISA) consisted of 144 2 m x 10 cm x 10 cm plastic scintillator bars. The MoNA bars were BC-408 and the LISA bars were EJ-200. Each bar (shown in Figure 3.7) was wrapped in reflective material to reduce light lost as well as black plastic to prevent ambient light from entering the detector. When a nuclear interaction occurred between the neutron and the hydrogen or carbon atoms in the plastic, the kinetic energy of that hydrogen or carbon atom was converted to prompt fluorescence in the same manner as described in Section 3.4.4. Because the neutron to hydrogen mass ratio is so much larger than the neutron to carbon mass ratio and the recoil is therefore much greater, most

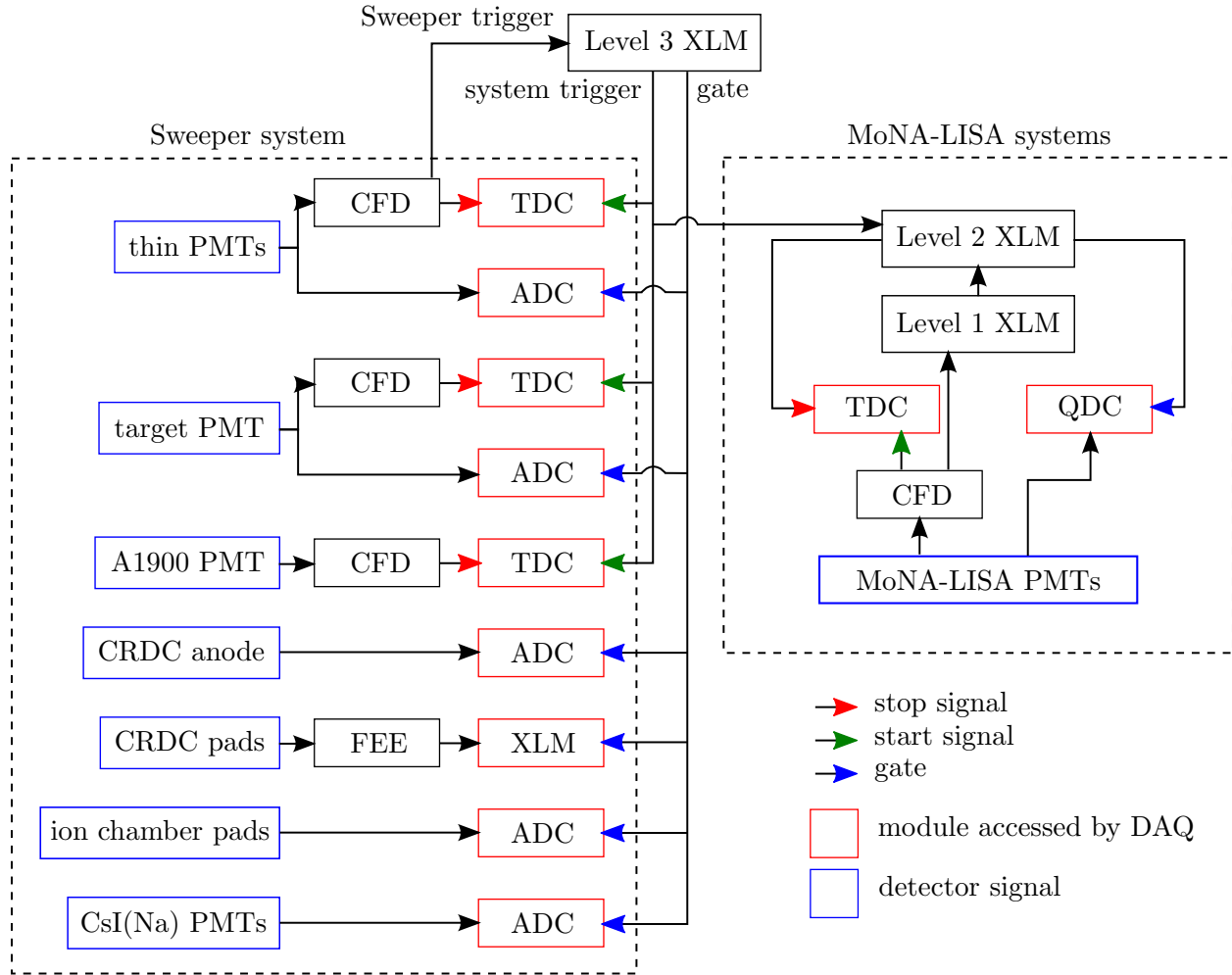


Figure 3.8: Schematic of the MoNA-LISA-Sweeper electronics set-up.

of the light output came from neutron on hydrogen reactions. The emitted light was funneled to the ends of the bars via total internal reflection and reflection off the foil wrapping. A shielded PMT at each end of the bar collected the light and turned it into an electronic signal. MoNA used Photonis XP2262/B PMTs and LISA used Hamamatsu R329-02 PMTs.

3.6 Electronics and Data Acquisition

The electronics and data acquisition (DAQ) systems have been described in detail in [139,141,142], but a short overview is provided here and an abbreviated schematic of the systems is shown in Figure 3.8.

MoNA, LISA, and Sweeper each operated as independent data acquisition subsystems connected by a “Level 3” system that generated a system trigger and “timestamp” that was relayed to each system. The system trigger in this experiment was generated solely based on the arrival of a signal in the left upper (0) PMT of the thin scintillator. The “timestamp” was a unique 64-bit word generated by a clock in the “Level 3” system. Upon the generation of a system trigger, that trigger and the “timestamp” were relayed to the three subsystems, which proceeded to read out the data independently.

MoNA and LISA had independent but identical electronics set-ups. Each PMT had two outputs, an anode and a dynode. The negative signal from the anode was used for a local trigger and for timing. The positive signal from the dynode was used to measure the charge collected in each PMT. The timing and triggering branch signal went from the anode to a constant fraction discriminator (CFD). Two outputs from the CFD went to a time-to-digital converter (TDC) and to a Xilinx Logic Module (XLM) for the subsystem trigger logic. The TDC modules were operated in common stop mode, where a signal from the detector triggered the start of measurement and the System 3 trigger ended the measurement. The charge branch signal went from the dynode through a passive inverter to a charge-to-digital converter (QDC) module. This process was duplicated for all 288 PMTs in each subsystem. Charge and timing information for each PMT was read out by the DAQ computer directly from the QDCs and TDCs.

The electronics set-up for the Sweeper included electronics for each of the three timing scintillators, CRDCs, ion chamber and CsI(Na) array. The A1900 timing scintillator signal was sent to a time-to-amplitude converter (TAC). The output from the TAC was then sent to an amplitude-to-digital converter (ADC). The output from the PMT attached to the target scintillator as well as the output from the four PMTs attached to the downstream thin scintillator were sent through a CFD into a TDC. All TDCs in the Sweeper DAQ operated in common start mode, where the Level 3 trigger began the measurement and the signal from each individual PMT stopped the measurement. The pad signals from the CRDCs were digitized by Front-End-Electronics (FEE) modules which sampled the pad pulse and sent the information into an XLM for readout. The signal from each pad in the ion chamber was sent through a shaper and into an ADC. The output from the four PMTs attached to the thin scintillator were split to allow for the time measurement described previously and a charge measurement by delivering the signals directly to a QDC. The signals from each PMT in the CsI(Na) array were sent through a shaping amplifier and into an ADC. Each time the system was triggered, all ADCs, TDCs, QDCs, and XLMs were read out by the Sweeper DAQ computer.

3.7 Invariant mass spectroscopy

Neutron unbound states typically have decay widths on the order of 10-1000 keV with mean lifetimes ranging from 7×10^{-20} to 7×10^{-22} seconds. At a beam velocity of approximately 11 cm/ns, these nuclei travel 7000-70 fm before decaying. In comparison, the radius of the ^9Be target nucleus is approximately 2.5 fm and the target was 278 μm thick. The short time scale makes direct measurement impossible. Invariant mass spectroscopy was used to reconstruct the energy released in the decay, also known as the decay energy.

Assume particle A decays into m daughter particles. Momentum and energy must be conserved and the cleanest way to do this is by utilizing four-vectors. We equate the four-vector of the original particle, P_A^μ , with the sum of the four-vectors of the decay products, P_i^μ and then can calculate the

invariant mass M_A of the original particle

$$\begin{aligned}
P_A^\mu &= \sum_{i=1}^m P_i^\mu \\
(P_A^\mu)^2 &= \sum_{i=1}^m \sum_{j=1}^m P_i^\mu P_{j\mu} \\
M_A^2 &= \sum_{i=1}^m M_i^2 + 2 \sum_{i=1}^{m-1} \sum_{j=i+1}^m (E_i E_j - 2\vec{p}_i \cdot \vec{p}_j) \\
M_A &= \sqrt{\sum_{i=1}^m M_i^2 + 2 \sum_{i=1}^{m-1} \sum_{j=i+1}^m (E_i E_j - 2\vec{p}_i \cdot \vec{p}_j)}
\end{aligned}$$

where $M_{i,j}$ are the masses of the decay products and $E_{i,j}$ and $\vec{p}_{i,j}$ are the energies and three-momenta of the decay products.

The decay energy is defined as the difference in mass between the initial and final products, so we subtract the final product masses to get the equation for the decay energy:

$$E_{decay} = \sqrt{\sum_{i=1}^m M_i^2 + 2 \sum_{i=1}^{m-1} \sum_{j=i+1}^m (E_i E_j - \vec{p}_i \cdot \vec{p}_j)} - \sum_{i=1}^m M_i \quad (3.1)$$

For a single neutron decay, this simplifies to:

$$E_{decay} = \sqrt{M_f^2 + M_n^2 + 2E_f E_n - 2\vec{p}_f \cdot \vec{p}_n} - M_f - M_n.$$

For a two-neutron decay, Equation 3.1 reduces to:

$$E_{decay} = \sqrt{M_T^2 + 2(E_T^2 - \vec{p}_T^2)} - M_f - 2M_n.$$

where

$$M_T^2 = M_f^2 + 2M_n^2$$

$$E_T^2 = E_f E_{n_1} + E_f E_{n_2} + E_{n_1} E_{n_2}$$

and

$$\vec{p}_T^2 = \vec{p}_f \cdot \vec{p}_{n_1} + \vec{p}_f \cdot \vec{p}_{n_2} + \vec{p}_{n_1} \cdot \vec{p}_{n_2}.$$

It is important to note that when there are more than two decay products, the invariant mass and decay energy are accurate calculations regardless of decay mechanism (sequential, democratic, etc.).

3.8 Particle correlation techniques

The mode of decay is primarily illuminated in this work by observing correlations between the particles through Jacobi and Dalitz plots.

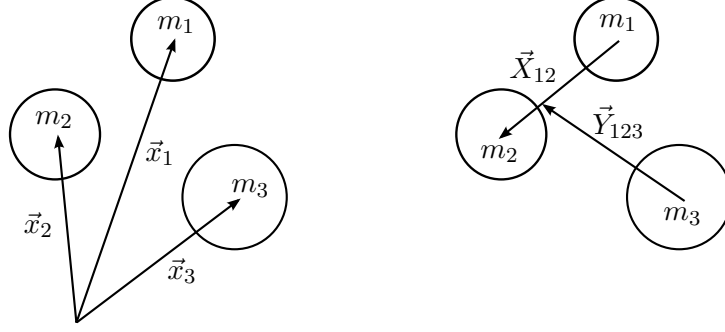


Figure 3.9: Three possible coordinate definitions for a three-body system.

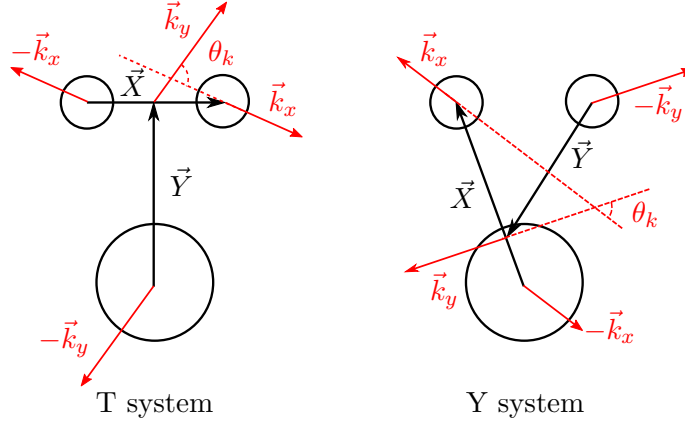


Figure 3.10: T and Y systems and associated Jacobi coordinates for fragment+ $n + n$ system.

3.8.1 Jacobi coordinates

To construct the Jacobi coordinates, we begin with a three body system, as illustrated on the left side of Figure 3.9. Each mass m_n has a coordinate vector \vec{x}_n . By eliminating the center of mass motion, the system can be redefined with only two relative coordinate vectors \vec{X}_{ij} and \vec{Y}_{ijk} (shown on the right side of Figure 3.9). The first Jacobi coordinate, \vec{X} is the vector between two particles. The second vector, \vec{Y} , begins at the third particle and ends at the center of mass of the system defined by the first two particles. Mathematically,

$$\vec{X}_{ij} = \vec{x}_j - \vec{x}_i$$

$$\vec{Y}_{ijk} = \frac{m_i \vec{x}_i + m_j \vec{x}_j}{m_i + m_j} - \vec{x}_k$$

where i , j , and k are the indices of particles. An example of this in the general three-body case is shown on the right side of Figure 3.9.

The rotation of particles through the three indices gives us three different coordinate systems: \vec{X}_{12} and \vec{Y}_{123} , \vec{X}_{23} and \vec{Y}_{231} , and \vec{X}_{31} and \vec{Y}_{312} . For three-body systems with two identical particles, these three systems, shown in Figure 3.10, are called the T system and the Y systems. The momentum vectors associated with \vec{X} and \vec{Y} are:

$$\vec{k}_x = \frac{m_j \vec{k}_i - m_i \vec{k}_j}{m_i + m_j}$$

$$\vec{k}_y = \frac{m_k(\vec{k}_i + \vec{k}_j) - (m_i + m_j)\vec{k}_k}{m_i + m_j + m_k}$$

where \vec{k}_i is the momentum vector of particle i .

The specific Jacobi variables used in this analysis are the cosine of the angle θ between the vectors \vec{k}_x and \vec{k}_y and the ratio of the energies (E_x/E_T) of the two-body system defined by \vec{X} and the total three body system:

$$E_x = \frac{(m_i + m_j)k_x^2}{2m_i m_j}$$

$$\cos \theta_k = \frac{\vec{k}_x \cdot \vec{k}_y}{k_x k_y}$$

These variables can be used in one and two-dimensional plots for analysis purposes. Although each system (T and Y) fully defines the correlations between the particles, sometimes it is easier to see specific correlations in one or the other. Some example Jacobi plots for phase-space, sequential, and dineutron decays calculated using the models described in Section 2.2 are shown in Figure 3.11. For the T-system, the energy ratio shows how the energy is split between the decay of the neutron pair and the decay between that two-body system and the core. For a dineutron decay, this would show the energy ratio between the dineutron scattering state and the total decay energy. A large total decay energy would skew the system toward the “zero” end of the energy ratio spectrum, while a small decay energy would skew the plot toward the “one” end of the spectrum. The energy ratio, E_x/E_T , in the Y-system is ideal for showing how the energy is shared between the neutrons. Unequal sharing of the energy is indicative of a sequential decay through a narrow state that is much closer to the initial(final) state than it is to the final(initial) state. In Figure 3.11, the equally shared sequential decay line has shoulders which indicate unequal sharing of the energy between the neutrons. These shoulders are correlated with a long, high-energy tail in the three-body decay energy distribution. Though the intermediate central energy is half the initial state’s central energy, neutrons decaying from that high-energy tail are more likely to share the total energy unequally. The $\cos(\theta)$ plot for the T-system should, by definition, be symmetric and can also discriminate between types of sequential decays. The $\cos(\theta)$ plot for the Y-system shows how correlated the neutrons are in space: if the angle is large (and $\cos(\theta) \sim -1$), the system has a dineutron-like structure and if the angle is small (and $\cos(\theta) \sim 1$), the system has a cigar-like structure, with the neutrons on either side of the core.

3.8.2 Dalitz plots

Dalitz plots are two-dimensional graphs commonly used in high-energy physics to study correlations in three-body decays. Introduced by R.H. Dalitz in the early 1950s [35, 36], their primary feature is that they are uniformly filled for a simple phase-space decay. Any correlations or resonances between the three bodies will show up as an enhancement within a uniformly filled section.

The plots utilize the fact that two coordinates define the kinematics of a three-body system (as in the Jacobi systems). When Dalitz introduced the plots, he chose two variables constructed from kinetic energies of the particles [35]. Another option is to plot pairs of squared invariant masses against each other. If mass A decays to masses i, j , and k , the axes of the Dalitz plot would be m_{ij}^2 and m_{jk}^2 . This approach is more commonly used now than the kinetic energy coordinates used by Dalitz.

The boundary of the uniformly filled area is defined by the kinematics and decay energy of the system. In Dalitz’s original paper, the boundary was circular [35]. When invariant masses are used,

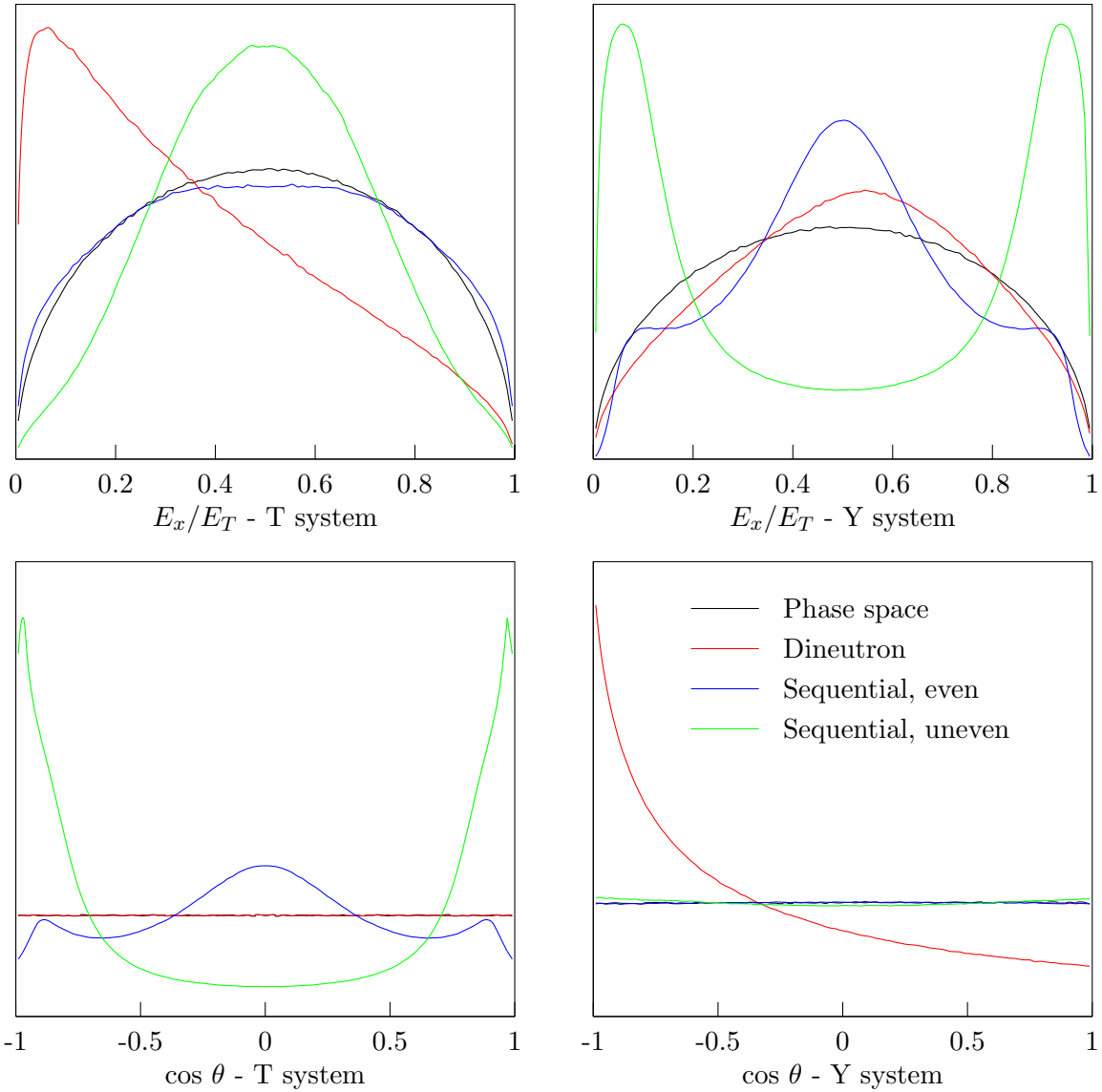


Figure 3.11: Example Jacobi plots for a phase space decay (black), a dineutron decay (red), and a sequential decay (blue). The left column shows Jacobi coordinates from the T-system and the right column shows Jacobi coordinates from the Y-system. The energy ratios are shown on the top row and the angular distributions are shown in the bottom row. All distributions are without any acceptances or resolutions applied. In the $\cos \theta$ -T system plot, the dineutron and phase space lines overlap.

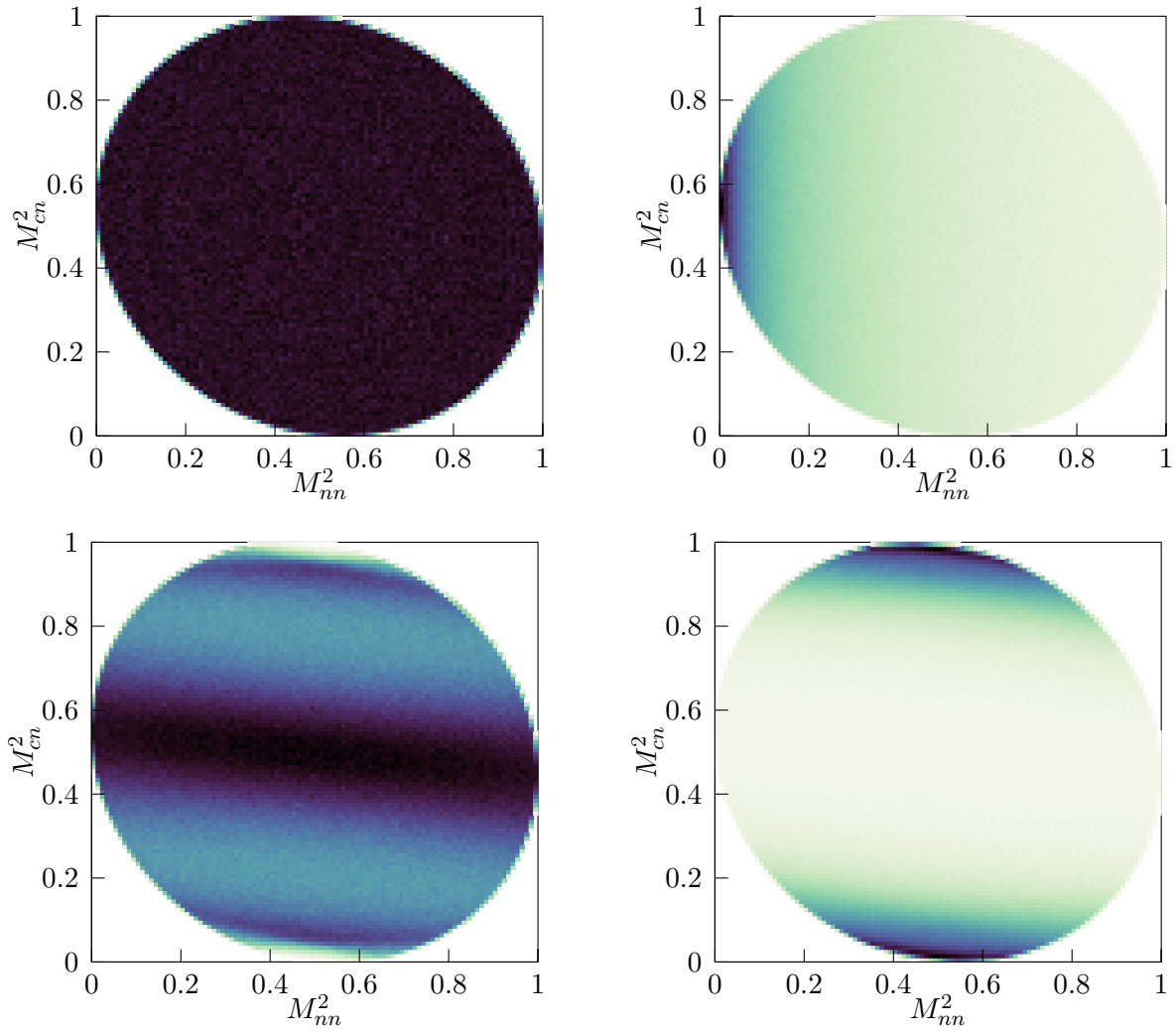


Figure 3.12: Example Dalitz plots for a phase space decay (upper left), a dineutron decay (upper right), and two sequential decays (bottom row). The sequential decay in the bottom left panel shows a decay through an intermediate state approximately halfway between the initial and final states, while the sequential decay shown in the bottom right has a more asymmetric energy distribution. All distributions are without any acceptances or resolutions applied.

the shape more often resembles a rounded, skewed triangle. Different total decay energies lead to different boundaries for the Dalitz plots. When a wide decay energy range is considered, though, these different boundaries reduces the efficacy of the plot. To restore the uniformity of the filled area, Marqués and collaborators introduced a normalized invariant mass [37]:

$$m_{ij}^2 = \frac{M_{ij}^2 - (m_i + m_j)^2}{(m_i + m_j + E_d)^2 - (m_i + m_j)^2}$$

where $m_{i,j,k}$ are the masses of the individual decay products, $M_{i,j}^2$ is the squared invariant mass of the two-body system i, j , and E_d is the decay energy. This normalization creates two coordinates that range from 0 to 1 and which create a circular boundary when plotted against each other.

Just like the Jacobi plots, the Dalitz plots can be used in two-dimensional form or one-dimensional form, where the one-dimensional plots are simply projections of the two-dimensional plot. Some example two-dimensional plots are shown in Figure 3.12. The physical intuition and understanding that can be gained from these plots is similar to that from the Jacobi plots. A dineutron-like correlation between the neutrons will produce an enhancement near $m_{nn}^2 = 0$ and $m_{cn}^2 \approx 0.5$ that will steadily decrease as $m_{nn}^2 \rightarrow 1$. The decay through a narrow resonance in an intermediate system will produce a pair of enhancements in m_{cn}^2 that will show up as bands in the two-dimensional plot. The location and widths of those bands will be indicative of the energies released in the two sequential decays and their widths.

Chapter 4

Data Analysis

This chapter discusses the steps taken to transform electronic signals to a set of meaningful data spectra and the simulation used to interpret those spectra.

4.1 Calibrations and corrections

The electronic signals recorded in the data stream were extracted, calibrated and corrected before they were used in calculations of any sort. This section details the calibration of the individual detectors.

4.1.1 Charged particle calibrations and corrections

4.1.1.1 CRDCs

The signals from the CRDCs went through a significant amount of processing on their way to producing a position spectrum. The raw signals included samples of charge found on each pad, the total charge collected on the anode wire, and the drift time of the electron. The drift time was measured as the time difference between the collection of charge on the anode and the arrival of the particle downstream in the thin scintillator. The samples on each pad were combined to give a raw total charge for each pad and the distribution of charge over the pads was fit to give a pad position of the particle's interaction location. Finally, this pad position was converted to an x -position and the drift time was converted to a y -position.

Certain pads in the CRDCs displayed abnormal behavior. For a good position spectrum, the behavior of the pads should be as uniform as possible across the entire detector. Pads with abnormal charge collection, identifiable by comparing raw charge spectra, were eliminated from further calibrations, corrections, and calculations. Examples of charge spectra from good and bad pads are shown in Figure 4.1. Only one pad, pad 69, was identified as bad in CRDC1, while three, pads 24, 73, and 89, were identified as bad in CRDC2.

Instead of integrating the entire charge collection, each pad in the CRDCs took 0-4 samples in a Riemann sum approximation to the full integral (Figure 4.2). The samples were counted and then summed as an approximation of the total charge deposited on that pad.

In this experiment, the number of samples collected varied regularly as a function of y -position for both CRDCs (Figure 4.3). More specifically, for events near evenly spaced y -positions (approximately 65 mm spacing), the number of samples collected for each pad was less than four. This spacing was the same as the y -spacing of the electric field shaping wires along the faces of the detector. To correct for this, the total charge collected on each pad was normalized by the number of samples collected by that pad for a given event. This allowed accurate comparison of the total charge collected in each CRDC, known as the pad sum.

After the raw signal from each pad had been normalized to the number of samples, the next step was to subtract the pedestal, the small current that always ran through the cathode pads of

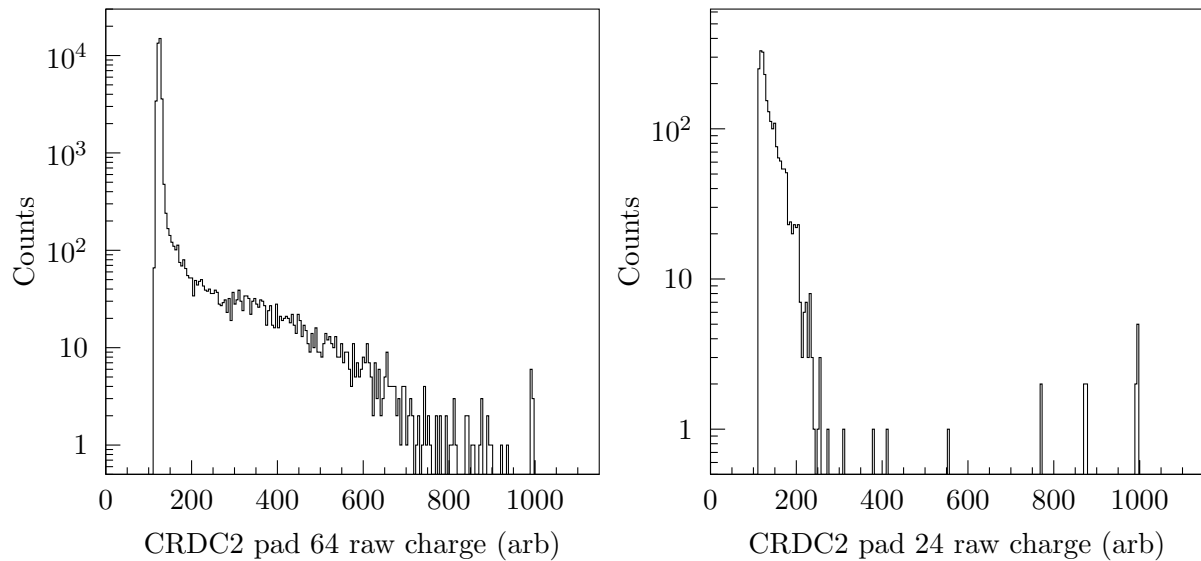


Figure 4.1: Examples of total charge spectra for two pads in CRDC2. Pad 64 (left) is an example of a good total charge spectrum and pad 24 (right) is an example of a bad total charge spectrum.

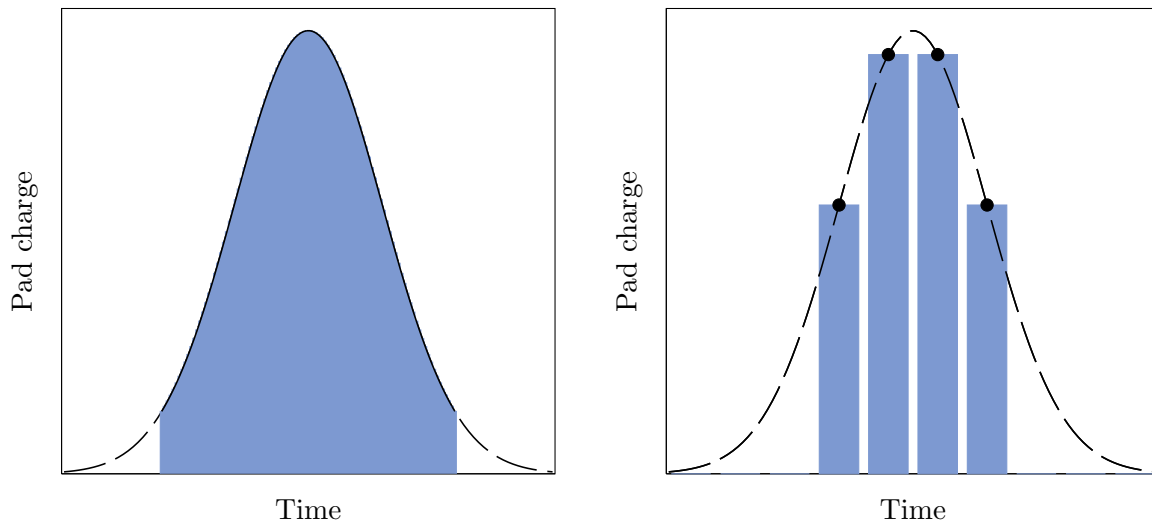


Figure 4.2: Example charge distribution on CRDC pads as a function of time. A full charge integration measurement would integrate the shaded area on the left. The sampling method adds the values of a discrete number of points, as shown on the right.

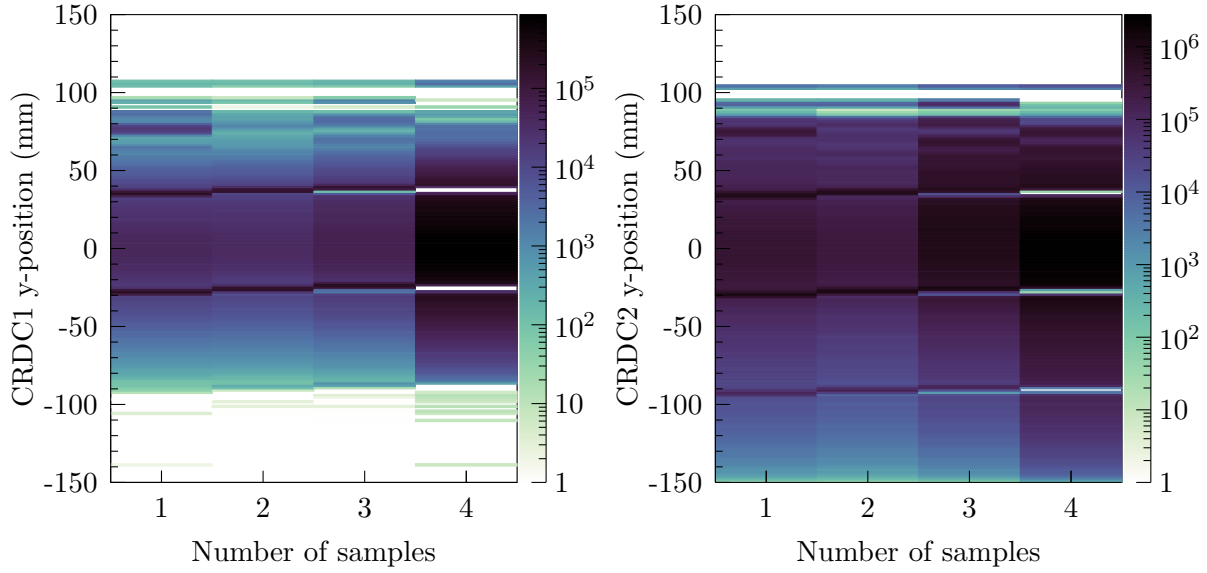


Figure 4.3: CRDC y -position versus number of samples collected for each pad (left: CRDC1, right: CRDC2). Both plots are shown with the z -axis on a log scale. Each CRDC collects fewer samples at certain regularly spaced intervals along the y -direction, visible in these plots as enhancements at lower numbers of samples and vacancies at the spectra for four samples.

the CRDCs. When a charged particle traveled through the detector, the charge read out by the electronics was the sum of the pedestal and the charge generated by the particle's passage.

To measure the pedestal value of each CRDC pad, the charge in each pad was measured when no particles were passing through. The distribution of charge collected on the pads was normalized to the number of samples and then fit with a Gaussian lineshape to extract the centroid - the pedestal value.

Event by event and pad by pad, the total charge on each pad was determined with the following equation:

$$Q_{pad} = \frac{1}{n_{samples}} \sum_{i=0}^{n_{samples}} q_i - q_{ped}$$

where Q_{pad} was the total charge deposited on the pad, $n_{samples}$ was the number of samples on that pad for that event, q_i were the individual samples collected and q_{ped} was the measured pedestal charge.

Once the total charge collected on each pad was calculated, the charge distribution across all the pads was used to find the pad position. A Gaussian lineshape was fit to each distribution, as shown in Figure 4.4. The central value of the fit was taken as the position of the particle relative to the set of pads.

The final step was to convert this pad position to an x -position in the lab frame and convert the drift time to a y -position. Both of these conversions were performed at the same time by utilizing the tungsten masks in front of each detector and a ^{17}N beam. The masks had a known pattern of holes and lines. When the beam passed through each hole, that known location was associated with a pad position and drift time. With enough of these holes and lines illuminated, linear transformations from pad position to x -position and drift time to y -position were calculated.

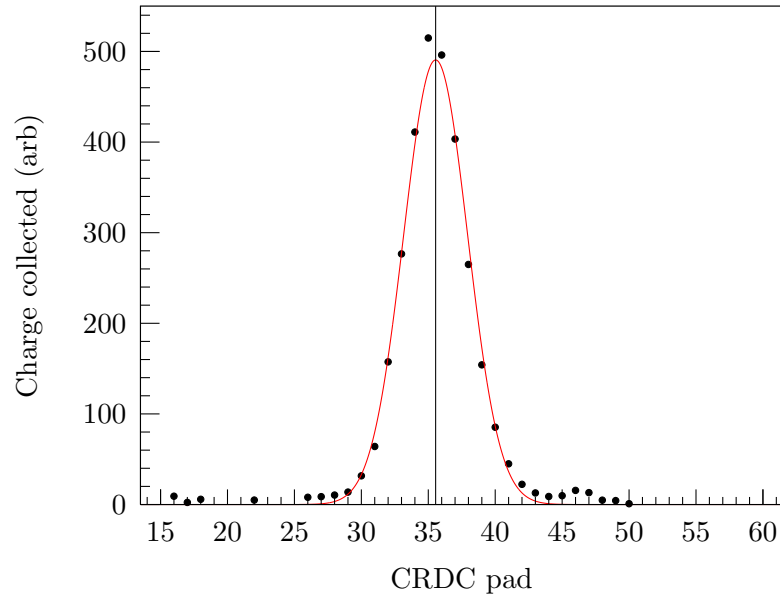


Figure 4.4: An example of a charge distribution fit for CRDC2. The centroid of the Gaussian fit, shown here by the vertical line, would be used as the position of the particle in this detector.

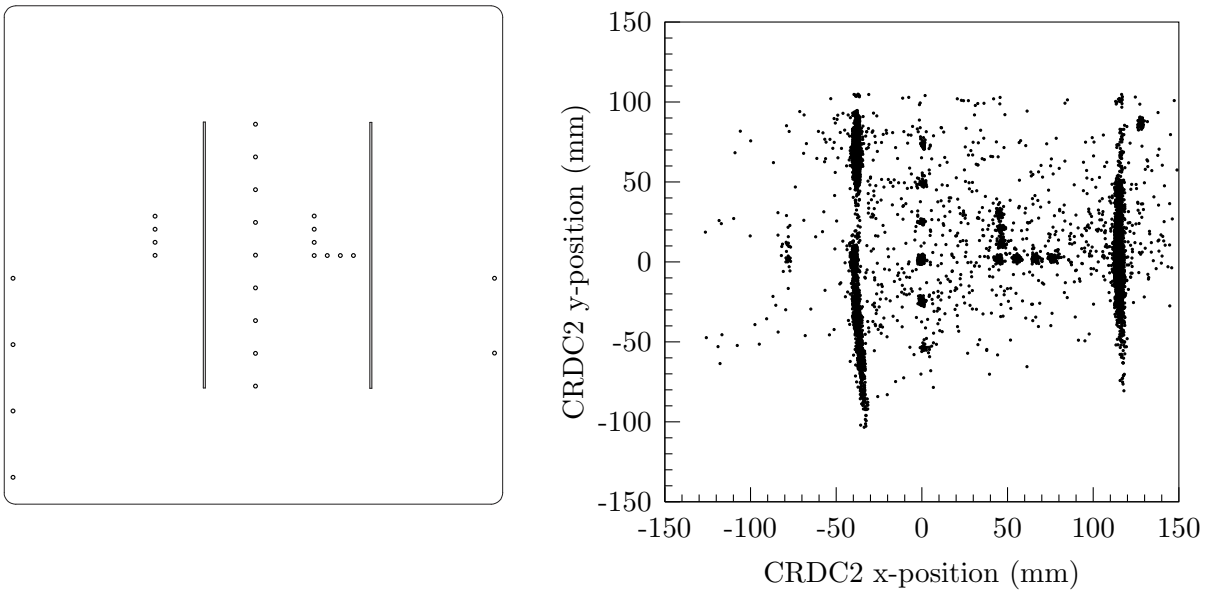


Figure 4.5: Left: mechanical design drawing of the CRDC mask. Right: Example of CRDC mask data from run 157.

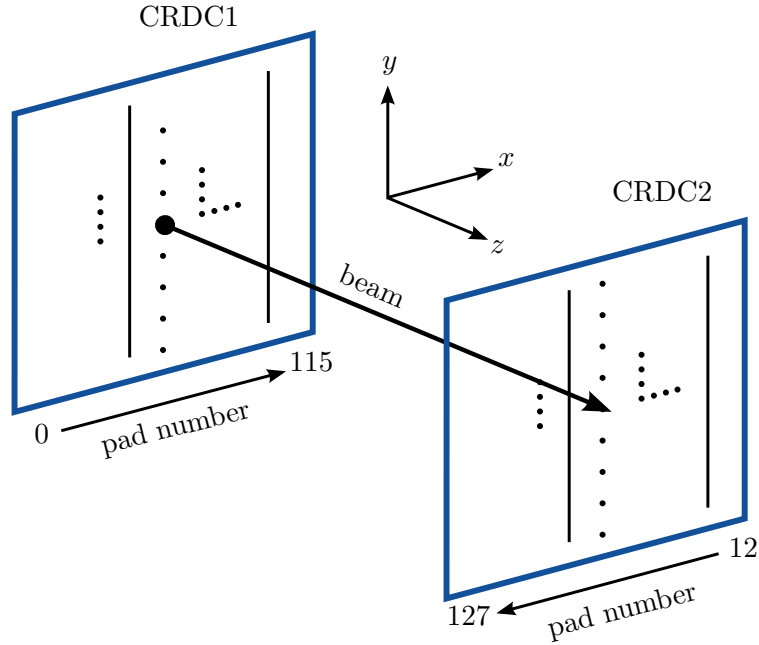


Figure 4.6: A schematic of the CRDC masks and their relation to the lab coordinate frame, the beam, and the pads in each detector.

An example of the data collected for this calibration is shown in Figure 4.5.

A schematic of the masks and their relations to the lab frame, beam direction, and pad numbers is shown in Figure 4.6. The magnitude of the slope of the x -position linear fit was defined by the pitch of the pads - $1/10''$. The sign of the slope depended on the orientation of the pad electronics - CRDC1 had a positive slope, while CRDC2 had a negative slope. Since the collected electrons drifted upward to the anode of the detector, the sign of the y -position slope was negative. An additional offset was included in the y -direction to place the central path of the beam along the $y = 0$ axis. The offsets for the x -position fit were determined by the mask.

The masks were located 45 mm in front of the detector [141]. Because of this z -offset, particles going through the same hole at different angles could pass through the detector at different positions. This effect was corrected by iterating the calibration process. After performing position calibrations for both CRDCs (and assuming no z -offset), the angle of the particle was calculated and the position calibrations were performed again, this time accounting for the z -offset. This process was repeated until the slopes and offsets converged.

Mask data was collected approximately every 48 hours to account for possible drifts in the detectors. The final slopes and offsets from each pair of calibration runs are shown in Tables 4.1 and 4.2. Since the spread was fairly small and exhibited no drift in positions for the production data, an average was used for each slope and offset (included in Tables 4.1 and 4.2).

4.1.1.2 Ion chamber

The ion chamber was segmented in 16 pads along the beam direction, each of which registered a charge collected for each event. While the charge collected in the ion chamber can be used almost without any calibrations, the data can be cleaned up significantly by removing bad pads, gain-matching the remaining pads, and applying position and time corrections.

Table 4.1: CRDC1 mask calibration slopes and offsets from all CRDC1 mask runs. Because there were so few holes in the y -direction (typically only 3), errors were unreasonably small. Slopes and offsets have been truncated at the same significance as their CRDC2 counterparts (Table 4.2).

CRDC1 mask run	x slope (mm/pad)	x offset (mm)	y slope (mm/ns)	y offset (mm)
25	2.54	-178.0 ± 0.2	-0.19	101
96	2.54	-178.7 ± 0.2	-0.19	99
156	2.54	-178.5 ± 0.1	-0.19	101
240	2.54	-178.7 ± 0.2	-0.19	101
average	2.54	-178.49 ± 0.08	-0.19	101

Table 4.2: CRDC2 mask calibration slopes and offsets from all CRDC2 mask runs.

CRDC2 mask run	x slope (mm/pad)	x offset (mm)	y slope (mm/ns)	y offset (mm)
26	-2.54	186.8 ± 0.2	-0.19 ± 0.01	113 ± 2
97	-2.54	186.2 ± 0.2	-0.19 ± 0.01	112 ± 3
157	-2.54	186.7 ± 0.1	-0.19 ± 0.02	112 ± 3
241	-2.54	187.0 ± 0.2	-0.19 ± 0.02	112 ± 3
average	-2.54	186.68 ± 0.08	-0.19 ± 0.01	112 ± 1

Pad 1, the second pad from the front, was removed from further calibrations and calculations because it registered almost a factor of 5 less charge than any other pad during the experiment.

Approximating the ion chamber as 65 cm of argon gas (instead of the P-10 mixture it was), the incoming ^{13}B beam should have lost approximately 36 MeV in the first half of the detector and 37 MeV in the second half of the detector. This indicates that the beam did not slow down significantly as it passed through the detector and that each pad should have collected the same amount of charge.

To gain match the ion chamber pads, the beam was sent down the center of the ion chamber and the charge on each pad was measured. One pad, pad 8, was chosen as the ideal pad to which all others would be gain matched. Each charge distribution was fitted with a Gaussian (see Figure 4.7). Those centroids, q_{pad} , were then compared to calculate a slope, m_{pad} , for each pad:

$$m_{pad} = \frac{q_{ref}}{q_{pad}} \quad (4.1)$$

where q_{ref} was the centroid of pad 8.

For each event, the calibrated charge on each pad was calculated by multiplying the charge collected on each pad by that pad's slope to produce a calibrated charge value. The total energy loss through the detector, referred to as the ion chamber sum, was calculated on an event-by-event basis by summing together the calibrated charge values of all good pads.

The ion chamber exhibited a slight position dependence in the x -direction. In the data shown in Figure 4.8, a cocktail beam with many different fragments was swept across the entire face of the ion chamber. The position dependence here was likely caused by inefficient charge collection. Inefficient charge collection was much more apparent in the cases of a high Z fragment when more ionization was created and the difference was greater than the resolution of the detector. To correct this position dependence, the highest Z component of Figure 4.8 (nitrogen) was fit with a second-degree polynomial with coefficients (a_0 , a_1 , and a_2) and each summed signal, $Q_{ic,sum}$, was divided by the value of that polynomial at that x -position to produce the position-corrected value,

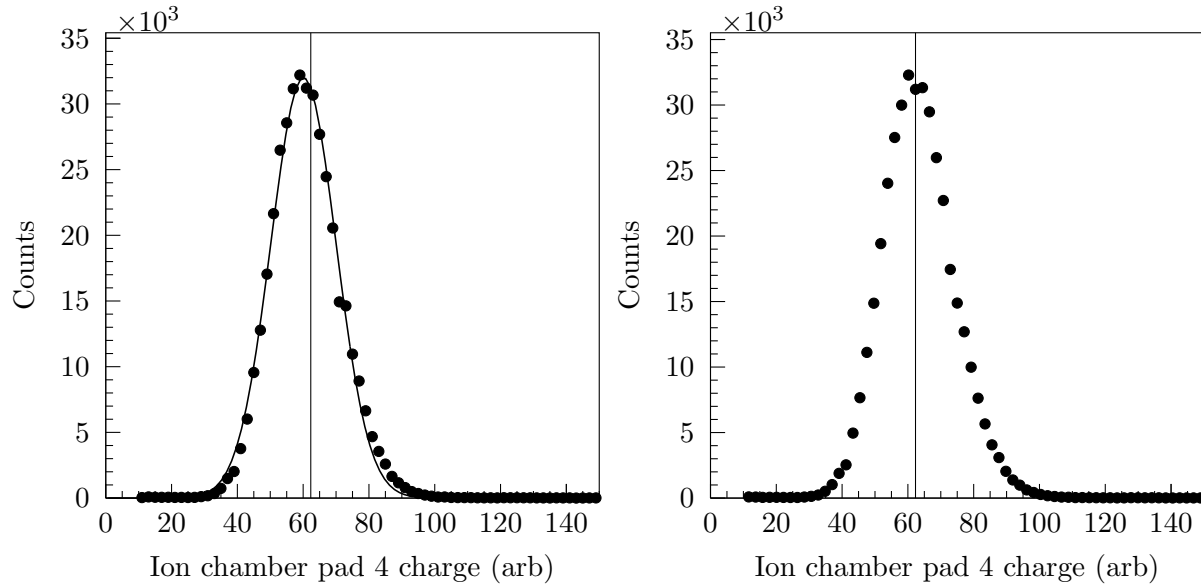


Figure 4.7: An example of fitting used in gain-matching the ion chamber. Left: points show raw charge signal from pad 4, thick solid line is Gaussian fit to data, and thin vertical line indicates centroid of “ideal” pad 8. Right: points show gain-matched charge signal from pad 4 and thin vertical line indicates centroid of “ideal” pad 8.

Table 4.3: Ion chamber position and time correction coefficient values.

Position correction		Time correction	
Coefficient	Value	Coefficient	Value
a_0	129.728	b_0	8.93895
a_1	-0.01787	b_1	119.669
a_2	-0.00034	b_2	0.460586

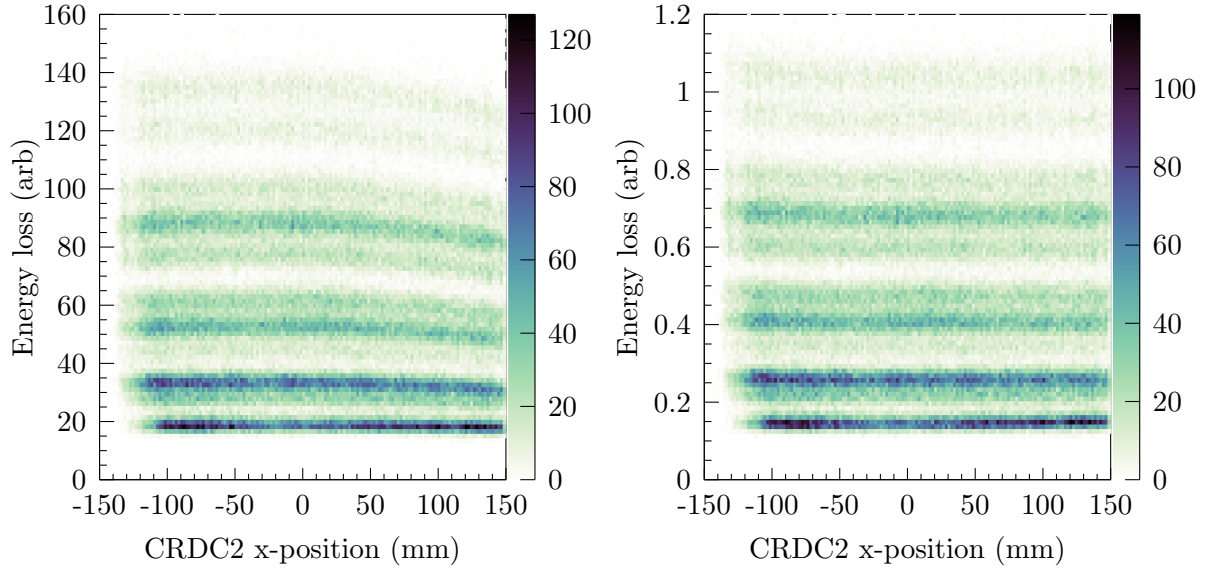


Figure 4.8: Position dependence of the ion chamber. The left panel shows the summed signal from the ion chamber as a function of CRDC2 x -position when using a cocktail beam. The right panel shows the position-corrected summed signal from the ion chamber.

$Q_{ic, poscorr}$:

$$Q_{ic, poscorr} = \frac{Q_{ic, sum}}{a_0 + a_1x + a_2x^2} \quad (4.2)$$

The fitted coefficients are shown in Table 4.3 and the results are shown on the right side of Figure 4.8.

A slow drift of the signal in the ion chamber over time was noticed during the production runs (Figure 4.9). This drift did not positively correlate with drift of signals in any other detector. The position-corrected energy loss was observed to have the following functional form:

$$\frac{b_0}{t + b_1} + b_2 \quad (4.3)$$

where t was the run number. The coefficients b_0 , b_1 , and b_2 were all coefficients to be fitted. The time dependence was removed by dividing $Q_{ic, poscorr}$ by the fit to create a new parameter, $Q_{ic, corr}$:

$$Q_{ic, corr} = \frac{Q_{ic, poscorr}}{b_0/(t + b_1) + b_2}. \quad (4.4)$$

The fitted coefficients for the drift in the ion chamber are shown in Table 4.3 and the results are shown on the right side of Figure 4.9.

4.1.1.3 Thin scintillator

The thin scintillator was located near the end of the beam line and had four PMTs, attached as in Figure 3.5. The four PMTs were labeled by a number and a description of their location (Table 4.4). The signal from each PMT was split to measure both total charge collected and the time of collection. Those raw signals were combined for a measurement of the total energy loss in the

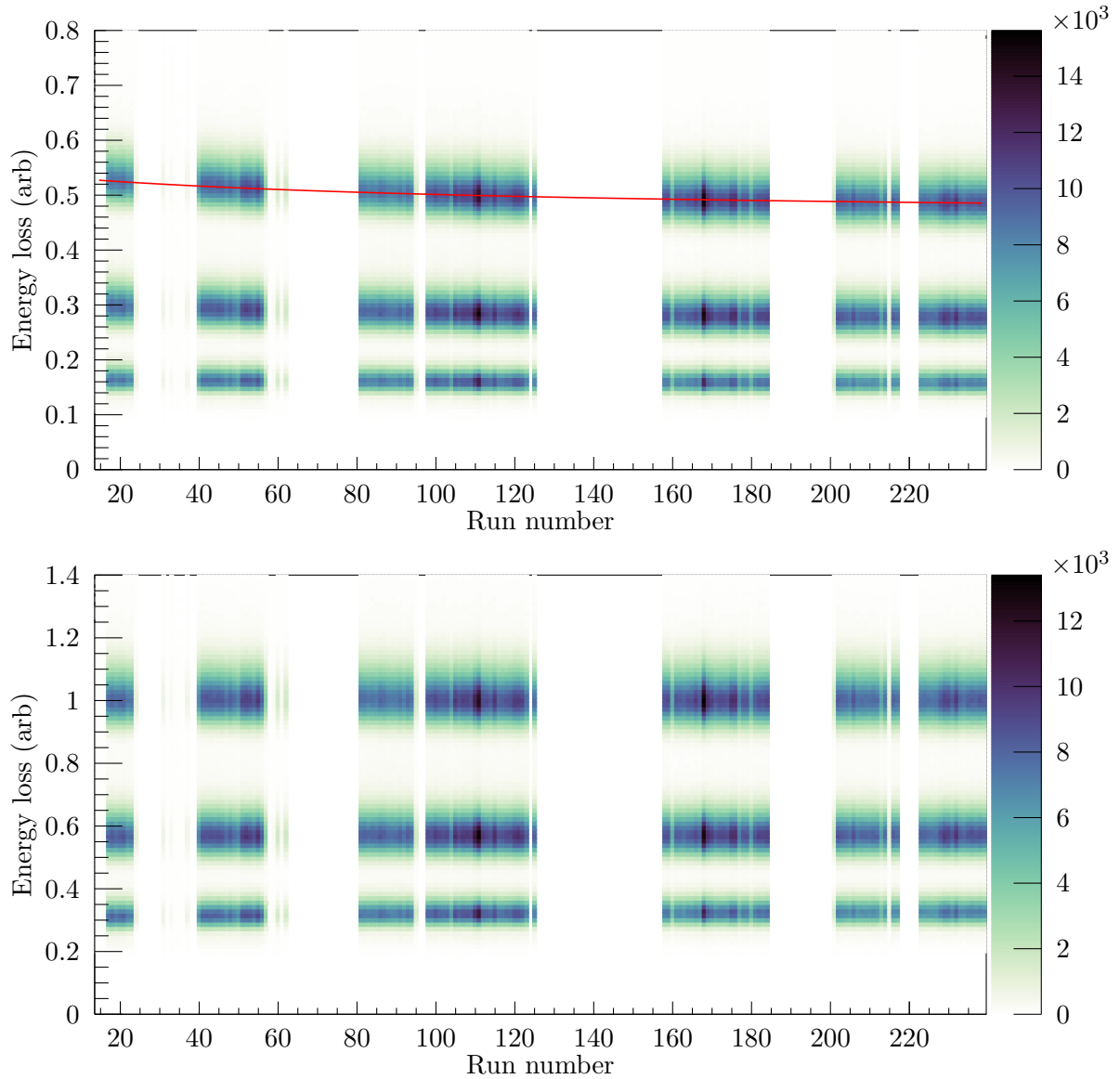


Figure 4.9: Time dependence of the summed ion chamber signal. The top panel shows the summed, position-corrected ion chamber signal as a function of run number. The red line is the fitted function 4.3 using parameters from Table 4.3. The bottom panel shows the summed, position-corrected, and time-corrected ion chamber signal as a function of run number.

Table 4.4: Thin scintillator locations and gain-matching slopes and offsets.

Location	Number	Slope	Offset	Time offset (ns)
Left upper	0	1	0	37
Left lower	1	1	349.819	44.8542 ^a , 11.7117 ^b , 10.8104 ^c
Right upper	2	1.22494	12.0517	-8.46805
Right lower	3	1.68587	-155.151	25.2282

^aruns 1-31

^bruns 32-75

^cruns 76-245

detector and the time of interaction in the detector. As with the ion chamber, inhomogeneities in position and time were corrected.

The time and charge signals in each of the thin scintillator's four PMTs had an inherent position dependence due to the attenuation through the plastic. In order to construct correct time and charge measurements, the information from all four PMTs was gain-matched and combined. To gain-match the four thin scintillator PMTs, the ^{13}B beam was sent down the center of the detector. Events at the very center of the detector were selected because the light from these events traveled similar distances to each PMT, so the signals arriving at the PMT would have been equal in magnitude and travel time.

The charge signals from each PMT were fit with a Gaussian lineshape. The left lower, right upper, and right lower signals were all gain-matched to the signal from the left upper PMT. For the linear gain-matching, the slope was determined by the ratios of the widths of the Gaussian fits while offsets were chosen to put all of the centroids at the same location. Slopes and offsets from the gain-matching are shown in Table 4.4. An absolute measurement of energy loss was not required, so calibrations to convert from QDC channels to total MeV were not needed.

Once all four PMTs were gain-matched, their signals were combined to provide a measurement of the total charge (e) deposited in the detector:

$$e_{top} = \frac{q_{LU} + q_{RU}}{2}$$

$$e_{bottom} = \frac{q_{LD} + q_{RD}}{2}$$

$$e = \frac{\sqrt{e_{top}^2 + e_{bottom}^2}}{2}$$

where $q_{LU,RU,LD,RD}$ are the gain-matched signals from the left upper, right upper, left lower, and right lower PMTs, respectively.

The total charge from the thin scintillator exhibited both position and time dependence. The corrections for both were similar to those for the ion chamber described in Section 4.1.1.2, except the position dependence was fit with a sixth-order polynomial:

$$e_{poscorr} = \frac{e}{\sum_{i=0}^6 a_i x^i}. \quad (4.5)$$

Figure 4.10 shows the energy loss in the thin scintillator before and after the position correction. The time drift in the total energy signal was corrected using Equation 4.3 and before and after spectra are shown in Figure 4.11. Correction parameters for both are shown in Table 4.5.

Table 4.5: Thin scintillator position and time correction coefficient values.

Position correction		Time correction	
Coefficient	Value	Coefficient	Value
a_0	1053.34	b_0	-6.064
a_1	0.235699	b_1	88.6789
a_2	-0.00802787	b_2	0.861741
a_3	-2.7786e-05		
a_4	2.30353e-07		
a_5	3.19837e-10		
a_6	-2.0901e-12		

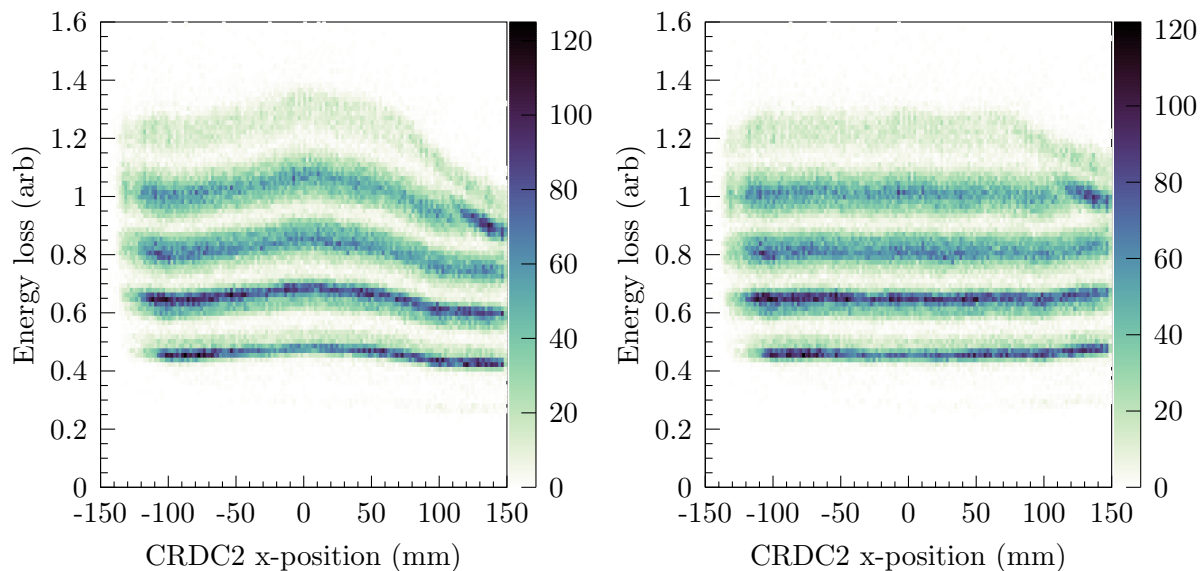


Figure 4.10: Position dependence of the charge signal from the thin scintillator. The left panel shows the total signal from the thin scintillator as a function of CRDC2 x -position when using a cocktail beam. The right panel shows the position-corrected summed signal from the thin scintillator. The correction was chosen so that the isotopes of interest (lithium and beryllium) had no position dependence. The remaining position dependence was primarily for the heavier isotopes, nitrogen and carbon.

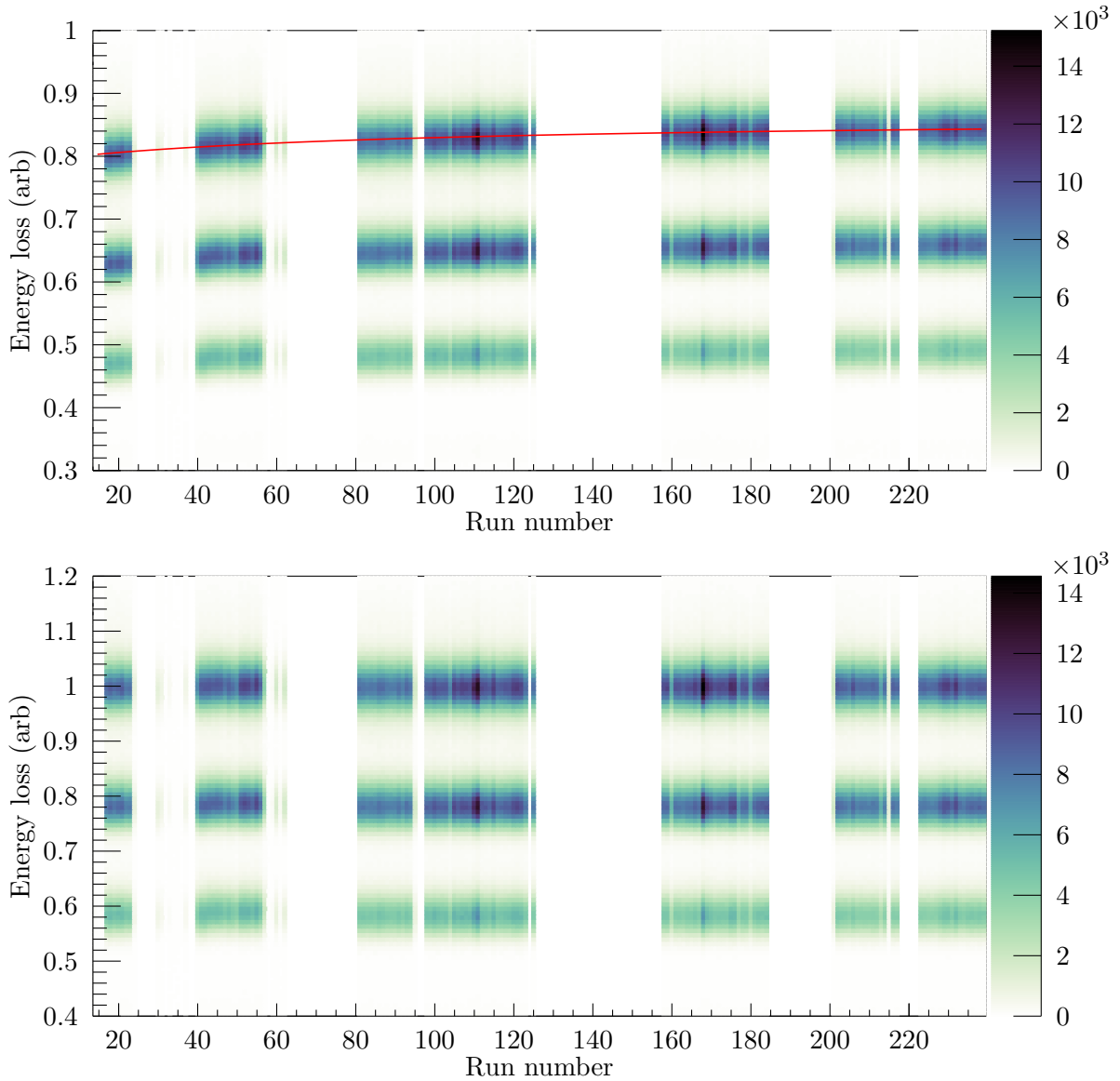


Figure 4.11: Time dependence of the total thin scintillator charge signal. The top panel shows the summed, position-corrected thin scintillator charge signal as a function of run number. The red line is the fitted function 4.3 using parameters from Table 4.5. The bottom panel shows the summed, position-corrected, and time-corrected charge signal as a function of run number.

Table 4.6: Calibration parameters for the timing signals from the A1900 and target scintillators.

Parameter	Value
A1900 slope	0.1 ns/channel
A1900 offset	-134.57 ns
Target slope	0.1 ns/channel
Target offset (run number < 72)	-40.4 ns
Target offset (run number \geq 72)	-24.1 ns
c_0	4.698 ns
c_1	128.9 channels
c_2	-1.5 ns

To calibrate the time signals from each PMT, only an offset was used, since a slope of 0.1 ns/channel was fixed by the range of the TDC. A 20 ns jitter was included in the timing by the use of a Field Programmable Gate Array (FPGA). All TDC channels received a start command from the individual timing detectors and the stop signal was generated by the FPGA. The amount of jitter varied on an event-by-event basis but since the same stop signal was used for all TDCs, the jitter was the same for each timing signal within an event. To eliminate the jitter, one timing signal (the thin left upper PMT) was subtracted from all other timing signals to create a time spectrum for that detector. This subtraction was done after the slopes were applied to allow for different TDC ranges.

After the jitter was subtracted, the time calibration was performed using the same event selection for the charge calibration. The timing signals from the other three thin scintillator PMTs were fit with Gaussians. The timing offset was calculated to align the mean values of all the Gaussian fits. Time calibration offsets for the thin PMTs are shown in Table 4.4. The calibrated timing signals from each PMT were then averaged to form one timing signal from the device:

$$t_{thin} = \frac{t_{LU} + t_{LD} + t_{RU} + t_{RD}}{4} \quad (4.6)$$

where t_{thin} is the final timing signal and $t_{LU,RU,LD,RD}$ are the timing signals from the individual PMTs.

Faulty electronics caused some signals to drop out or shift during the experiment. During the experiment the signal from the left lower PMT jumped twice. The first time was due to a loss of signal in the middle of run 14 and was not fixed until after run 31. The second was a shift that was correlated with fixing a double peaking problem in the target scintillator immediately after run 75. Different offsets, shown in Table 4.4, were applied for each of these sections. In addition, for a short time during the beginning of the experiment, that same time signal disappeared. For those events, the time signals from the three remaining PMTs are averaged. This slightly worsens the timing resolution but allows the inclusion of many more events.

4.1.1.4 Other timing scintillators

Two other timing scintillators were used, one immediately after the A1900 (the A1900 scintillator) and another approximately one meter upstream from the target (the target scintillator). The target scintillator had one attached PMT whose signal was split to record both the charge and time. The A1900 scintillator was located approximately 11 m upstream from the target and the signal from its one PMT recorded only the time of interaction in the scintillator.

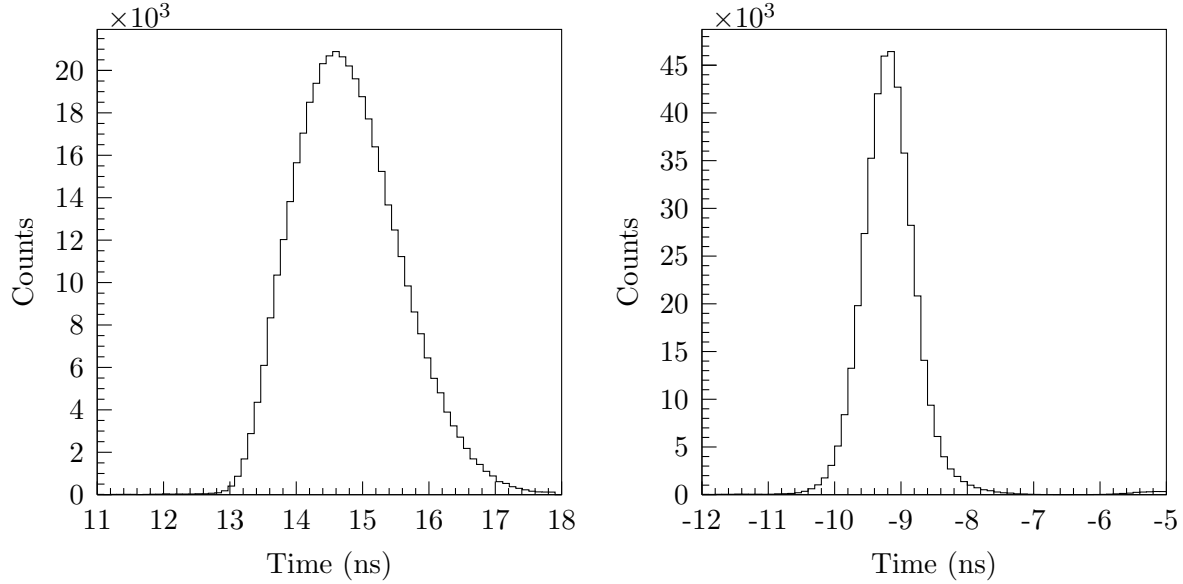


Figure 4.12: Timing signal from the target scintillator before (left) and after (right) the walk correction.

Since an absolute value of energy loss through the scintillator was not necessary, the charge signals were always displayed as raw QDC channel values. The basic time calibrations for both the target and A1900 scintillators were performed in the same way and used a calibration similar to that for the thin scintillator PMTs. First, the TDC channel value was multiplied by a slope of 0.1 ns/ch to convert it to nanoseconds. Second, the FPGA jitter was removed by subtracting the signal from the left upper PMT of the thin scintillator. Third, an offset was applied so that the time difference between scintillators reflected the calculated speed of an unreacted beam sent through the system. Calibration values are shown in Table 4.6.

For events with low charge deposition in the target scintillator, a shift in timing (a “walk”) was observed (see Figure 4.12). To fix this and improve the timing resolution of the detector the charge dependence of the timing signal was fit with an exponential function and corrected. The final correction took the form:

$$t_{targ.} = t_{ns} - c_0 e^{-q/c_1} - c_2, \quad (4.7)$$

where $t_{targ.}$ was the walk-corrected time, t_{ns} was the calibrated but uncorrected time, q was the charge collected by the PMT, and c_0 , c_1 , and c_2 were correction parameters. The final calibration parameters for the target calibration are shown in Table 4.6 and the result is shown in Figure 4.12.

In the first few days of the experiment, the target scintillator exhibited a double peaking as shown by the black line in Figure 4.13. This was attributed to faulty electronics and fixed approximately two days into the experiment. Due to the change in electronics required to fix the double-peaking, the target timing signal required different offsets before and after the change. Values before and after the change are shown in Table 4.6. The double peaking had a minimal effect on the beam identification, but if used for the particle identification, would significantly worsen the resolution. To avoid this, the time of flight from the A1900 scintillator to the thin was used as the timing signal for the particle identification.

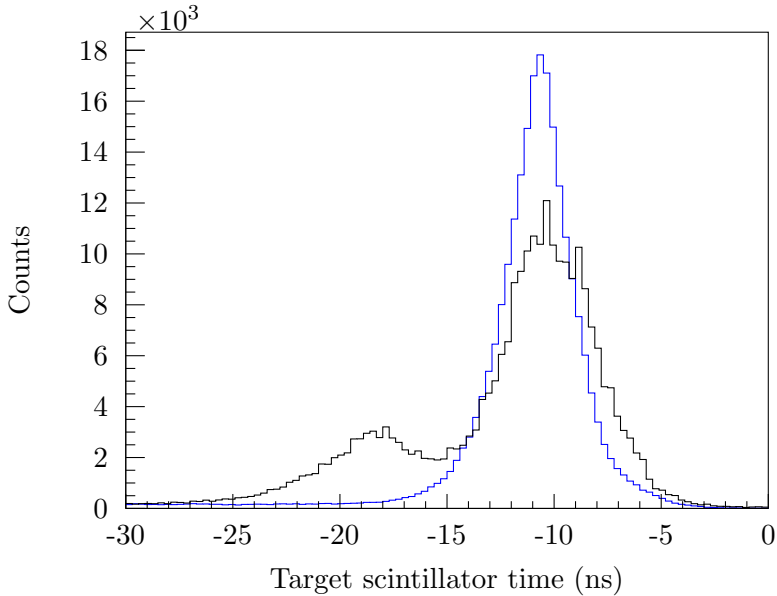


Figure 4.13: Target scintillator timing spectra from run 41 (black), taken while the target exhibited double peaking, and from run 90 (blue), taken after the double peaking was fixed.

4.1.1.5 CsI(Na) array

The CsI(Na) array was used sparingly in this analysis because particle identification was achieved through a corrected time of flight, so extensive calibration of the detector was not required. A peak-sensing ADC was used to read out the charge collected in each PMT. More extensive calibrations were carried out by collaborators at Augustana College but were not used in the current analysis.

4.1.2 MoNA-LISA calibrations and corrections

Raw output from each MoNA-LISA PMT (576 total) included a charge measurement that reflected the total light collected by the PMT and a time measurement of the light's arrival at the PMT. A series of calibrations converted these signals to a calibrated deposited charge measurement, a time of interaction in the bar, and a position of interaction along the length of the bar.

Cosmic ray data taken before the experiment was used for most MoNA-LISA calibrations. Muons from cosmic rays deposit roughly 2 MeV/cm of energy in each detector [143] as they pass through the detectors at roughly the speed of light [144]. This will deposit approximately 20 MeV electron equivalent of light into the bar. One MeV electron equivalent (MeVee) is equivalent to the light deposited by a 1 MeV electron.

4.1.2.1 Charge calibration

The first step in charge calibrations for MoNA-LISA was to roughly gain-match the PMTs by changing the applied high voltage. Each high voltage was adjusted until the cosmic-ray peak from each PMT showed up in roughly the same channel. Final high voltage values ranged from 1298.5 to 1951.5 V.

When the detectors were off and the electronics were on, a small current ran through every QDC channel. When the detectors were on and collecting data, this small current, called a pedestal, had

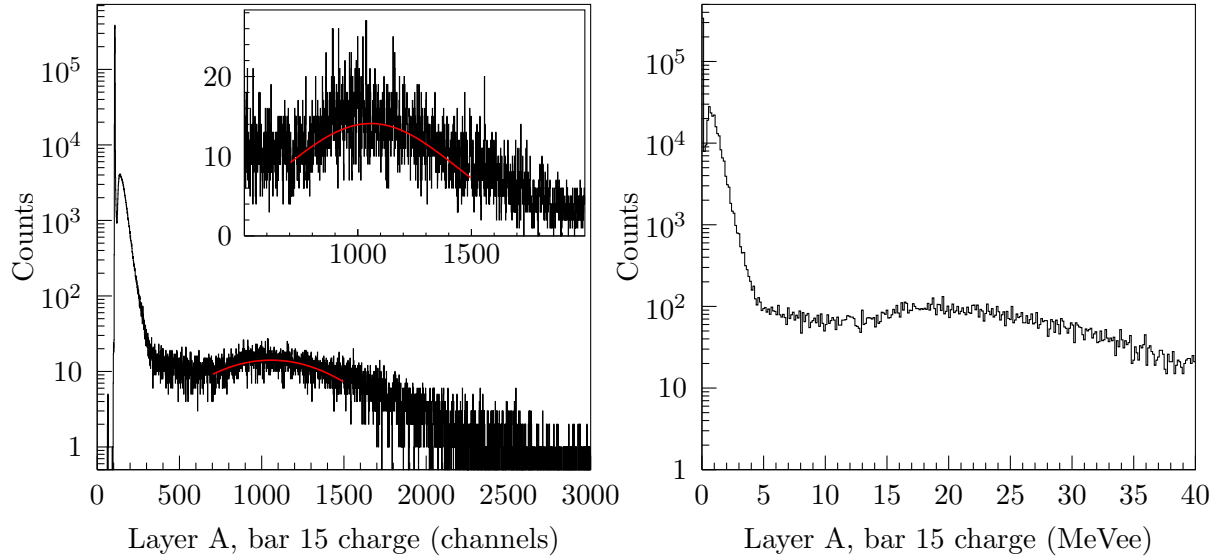


Figure 4.14: An example of MoNA-LISA’s charge calibration procedure. The raw charge from each QDC channel is plotted (left). The cosmic peak around channel 1200 is fit with a red Gaussian line. The inset shows channels 500 to 2000 with a linear scale on the y-axis. Those values are used to construct a linear fit whose slope and offset are applied to produce a calibrated charge signal in MeVee (right).

two consequences. The first was that it offset the true charge collected so that channel 0 did not correspond to zero energy. The second was that it caused every QDC channel to be read out for every triggered event, regardless of how many bars registered a real interaction. This deluge of data to be read-out would cause significant dead time.

The solution to the first problem was to apply a linear calibration to translate the channel number to a light measurement where the offset value was the same as the peak of the pedestal. Using the pedestal and muon peak as known values (0 and 20 MeVee, respectively), a linear fit for each PMT was found. An example of this procedure is shown in Figure 4.14.

The solution to the second problem was to apply a hardware threshold so that channels without a signal greater than the threshold were not included in the data readout. The thresholds, which should be above most of the pedestal peak, not at its peak, can only be set in multiples of 16 channels. In this experiment, a mistake in the code for calculating the thresholds set the thresholds higher than they needed to be; the thresholds for this experiment ranged from 0.4 to 0.9 MeVee.

4.1.2.2 Position calibration

Two of the spatial coordinates (roughly y and z for the array at zero degrees from the incoming beam) of each interaction were given by the discretization of the bars. The third spatial dimension, the measurement of the interaction along the bar, was given by the time difference between the light’s arrival at the PMTs on either end of the detector (see Figure 3.7).

The first step in this process was to convert the channel readout of the TDCs to a time. An absolute time was not possible, but a slope was applied to convert channels to nanoseconds. This slope was roughly given by the set range of the TDC (350 ns over 4096 channels is approximately 0.085 ns/channel), but since time resolution was essential, the TDC calibration slope was also

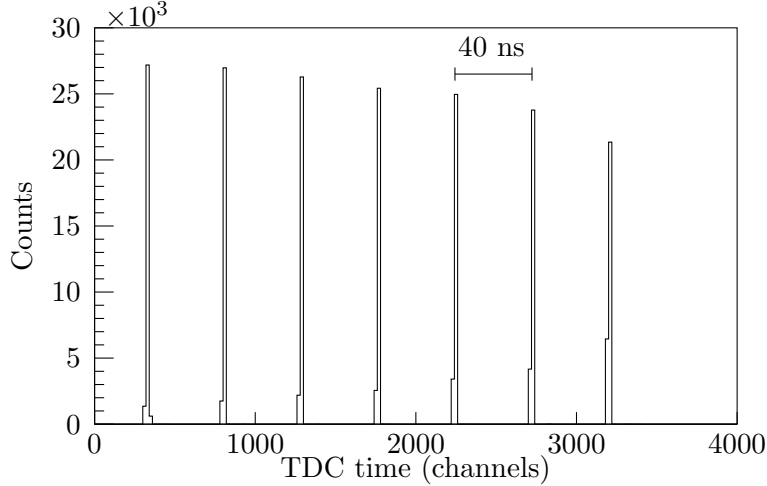


Figure 4.15: An example of the raw time spectrum during MoNA-LISA’s TDC calibration procedure. A pulser pulses the system every 40 ns, creating a spectrum with peaks at intervals that correspond to 40 ns.

measured with a pulser that pulsed the system every 40 ns, generating a pulse structure as seen in Figure 4.15. The peaks were fitted and the difference between various peaks was used to generate a linear fit to convert channel difference to time difference. In MoNA, those slopes centered around 0.083 ns/channel with a full range between 0.08 and 0.09 ns/channel (Figure 4.16). In LISA, those slopes centered around 0.089 ns/channel with a full range between 0.081 and 0.092 ns/channel (Figure 4.16).

With the PMT times calibrated, the next step was to convert the time difference between the two PMTs to a position along the bar. Cosmic-ray data was used to illuminate the entire length of the bar uniformly. An example of the raw data is shown in Figure 4.17. The edges of the step-like distribution are the edges of the bar, designated as -100 and 100 cm. To set the position calibration, a linear slope was calculated from those two points and then an offset was used to place the center of the bar at 0 cm.

4.1.2.3 Time calibrations

The measurement of a time difference between the interaction at the target and the interaction of the neutron in MoNA-LISA was crucial to the operation of the device. While the position along the bar was determined by the time difference between the two PMTs, the time of the interaction was determined by an average of the two times and then an offset to appropriately place the time of the interaction within the time of all the other interactions in the detector.

The known velocity of the cosmic-ray muons, v , was utilized to calibrate the timing of each bar relative to the bottom bar of its vertical layer. Only events that triggered a majority of the bars in the layer and deposited approximately 20 MeV in each bar were used. Then, for each bar, a time difference, Δt_{a0} , and path distance, Δd_{a0} , between the interaction point in that bar (a) and the bottom bar (0) were calculated. The value of

$$\Delta t_{a0} - \Delta d_{a0}/v \quad (4.8)$$

was plotted, which should be centered at zero if the time offsets for bar a are correct. If the Gaussian distribution was not centered at zero, an offset was added to the time calibration of bar a

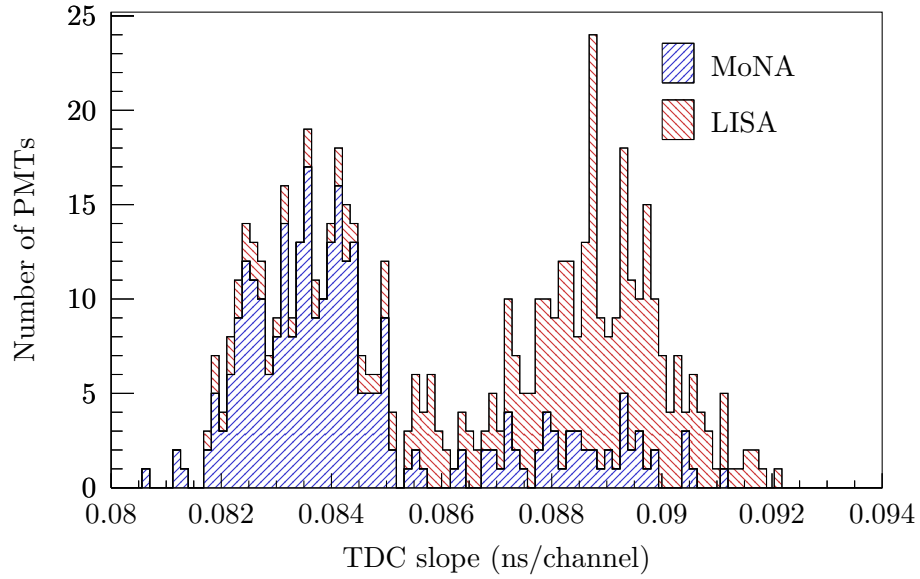


Figure 4.16: TDC slope values for MoNA and LISA.

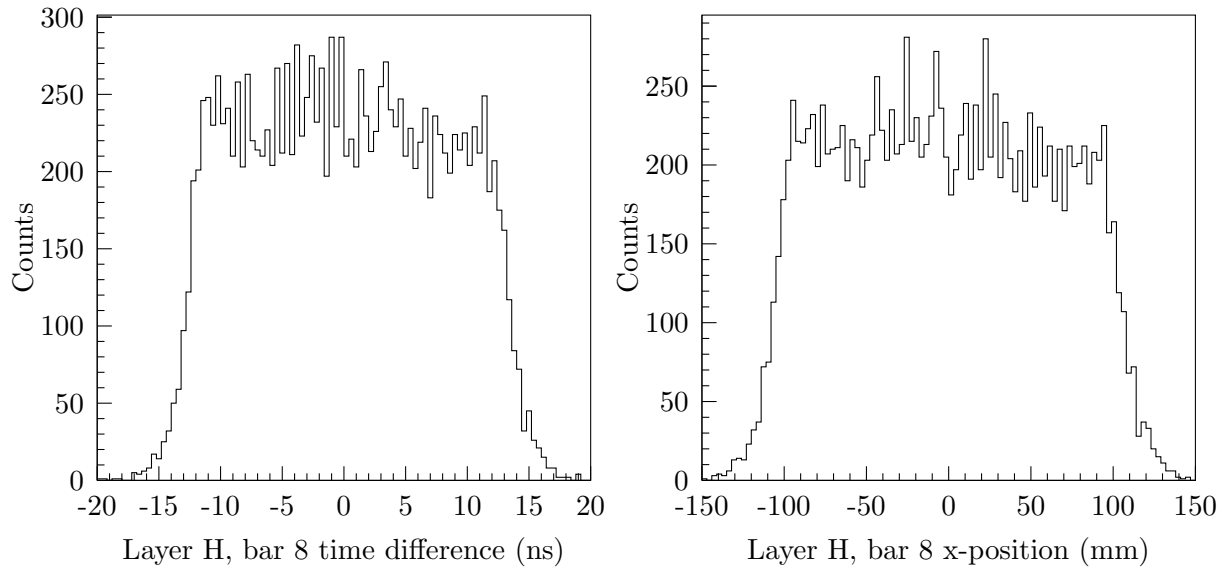


Figure 4.17: X-position calibration example. The final x -position spectrum (right) for one bar was calculated based on the time difference between the two PMTs (left).

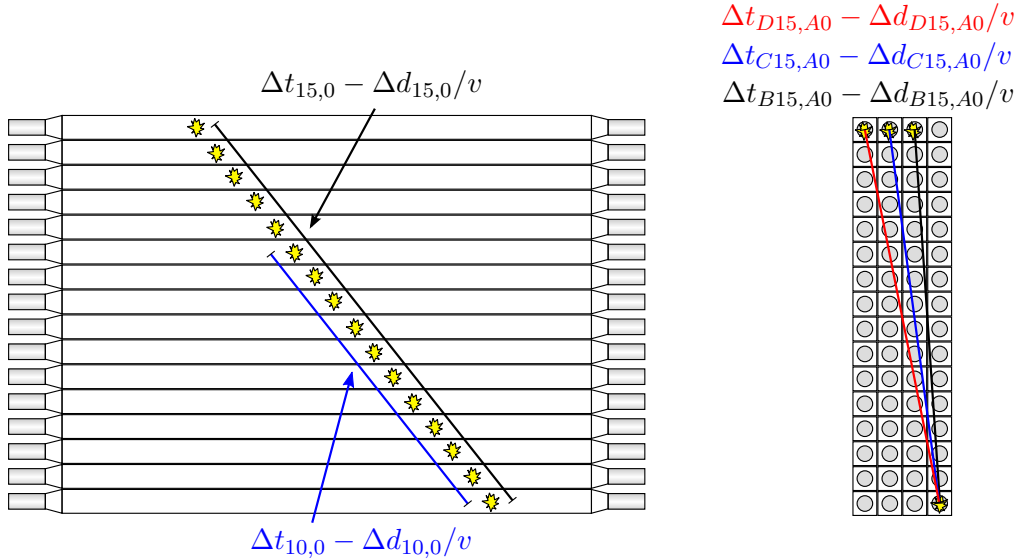


Figure 4.18: Schematics showing the differences used to calibrate the time measurement in MoNA-LISA. The view on the left is from the front of the array and the schematic on the right shows the side view of the array, looking head-on at the PMTs.

Table 4.7: Final time offsets for each table of MoNA-LISA, before and after the electronics change.

Time period	MoNA offset (ns)	LISA at 0° offset (ns)	LISA at 30° offset (ns)
Before run 76	433.83	411.295	409.901
Run 76 and after	429.103	406.392	405.25

so that it was. At this point, the velocity of the muon, when calculated using the time and position of interactions within a single vertical layer, should be measured accurately. The left diagram of Figure 4.18 shows these interactions and the differences used.

Once each vertical layer was “tied together in time”, the next step was to link layers on the same table (right diagram of Figure 4.18). Specifically, the time of each vertical layer needed to be calibrated relative to the time of the bottom bar in the front layer. The same process was used, but this time utilizing events that had interacted in the bottom bar of the front layer as well as in the top bar of other layers. From this, each vertical layer received an additional time offset that was applied to all its bars.

At this point, each table of bars (1 table for MoNA and 2 for LISA) are time calibrated relative to all other bars on that table. The final step was to place each table appropriately in time relative to interactions in the target. This required data from the experiment where a thick target was placed in the target position. The ^{13}B collided with the thick target, creating many gamma rays. Based on the locations of the bars relative to the target, a final offset was applied to all bars in each table such that the velocity of the gamma rays was 29.98 cm/ns. Two different sets of offsets were applied because the electronics that created the start signal for MoNA-LISA changed part of the way through the experiment. Both sets of final offsets are shown in Table 4.7. As a final check, Figure 4.19 shows the timing spectra for all three tables as well as vertical lines to indicate the expected arrival times of γ -rays and neutrons from the thick target.

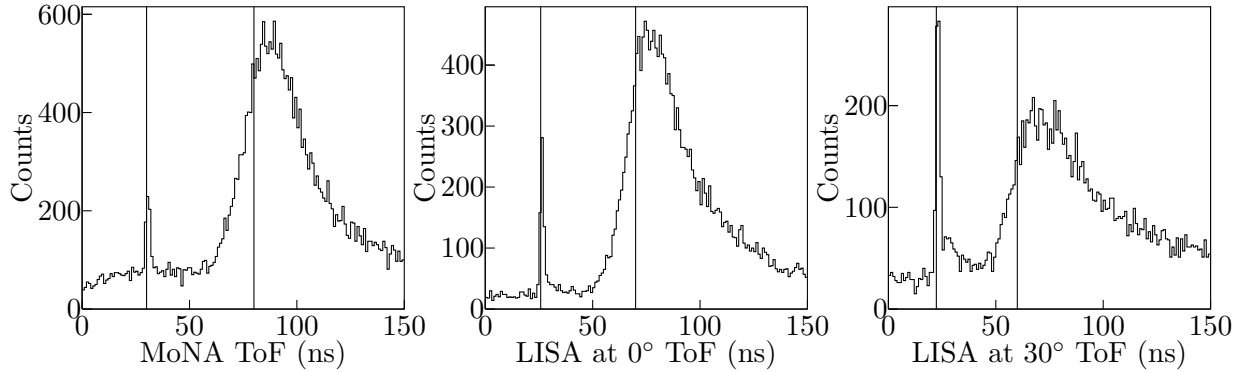


Figure 4.19: Calibrated timing spectra for each table. Impinging the beam on a thick target produced many γ -rays and neutrons. Vertical lines indicating the expected arrival of γ -rays and neutrons at the front of that table. The left panel shows the time-of-flight to the MoNA table, the center panel shows the time-of-flight to the first LISA table, and the right panel shows the time-of-flight to the second LISA table.

4.2 Event selection

Once the information from each detector was calibrated, information from different detectors was combined to make a specific measurement. Essential to each specific measurement is the selection of data events with the necessary information. This section details how almost 200 hours of data was reduced to roughly 3 hours of useful events.

4.2.1 Beam identification

Event selection began by identifying the ^{13}B component of the incoming beam. Components of the beam were identified by removing the target and allowing the beam to enter the Sweeper detector box. The magnetic rigidity of the beam as it entered the vault was 3.2271 Tm. At this rigidity, the velocity of the desired ^{13}B beam was 11.1 cm/ns. A ^{14}C contaminant traveled the distance between the A1900 and target scintillators 8 ns faster than the ^{13}B and was identifiable in a plot of energy loss in the ion chamber against the time-of-flight between the two detectors (Figure 4.20). Separation of the ^{13}B from the ^{14}C contaminant was achieved with a time-of-flight gate between 85 and 92 ns, as shown in Figure 4.20.

A similar process was repeated to identify and isolate the ^{12}B beam, which arrived in the vault with a rigidity of 2.9772 Tm. A ^{13}C contaminant was clearly visible in the energy loss vs. time-of-flight spectrum. The velocity of the ^{12}B beam was also 11.1 cm/ns, so the same time-of-flight was used to separate the ^{12}B beam from the contaminant as was used for the ^{13}B beam.

4.2.2 Event quality gates

The detectors did not always behave in a uniform and expected manner. Events in which the experimental system behaved abnormally could lack information from a detector or contain incorrect information. The gates described in this section were used to remove those events from the data stream.

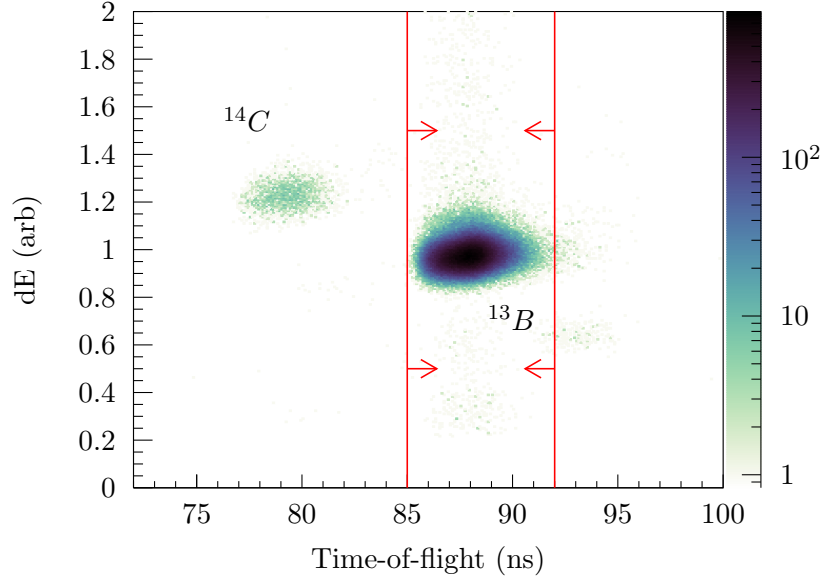


Figure 4.20: Beam component identification using energy loss through the ion chamber (y -axis), and time-of-flight from the A1900 scintillator to the target scintillator (x -axis).

The incoming beam rate was approximately 800 kHz, slightly less than one beam particle every microsecond. Within the approximately 400 ns range of the TDCs then, there was a possibility that another particle could go through the beamline, cause scintillation, and record a time. In this case separate detectors would have measured the time for different beam particles, resulting in a different time-of-flight than expected.

The frequency of the cyclotron was 21.8259 MHz, so these events with erroneous time measurements should show up as smaller “echos”, separated by 46 ns, as seen in Figure 4.21. This figure shows the time difference between the A1900 scintillator, 11 m upstream from the target, and the thin scintillator near the end of the beamline. The echos were eliminated by a time-of-flight gate as indicated by the vertical lines in Figure 4.21.

In other events, the position information from the CRDC was not considered reliable. The y -position was measured by the time difference between the particle interacting in the thin scintillator and the collection of the charge carrier at the anode of the CRDC. In some events, the charge carrier wasn’t collected at the anode and the y -position measurement was unable to be made.

The x -position measurement was also compromised in some events. To calculate the position accurately, charge needs to be induced on multiple pads. Some events showed abnormally low total charge across the pads. In addition, some events showed an abnormally high charge collection, possibly in connection to multiple particles passing through the detector. These events were eliminated by gating on the total charge summed over all the pads (the pad sum). Those gates are shown in Figures 4.22 and 4.23.

When the x -position was calculated by fitting the charge distribution across the pads with a Gaussian, several variables were stored, including the centroid, the width, and the χ^2 value for the fit. A limit on the maximum χ^2 value removed events with bad x -position fitting and is shown in Figure 4.23.

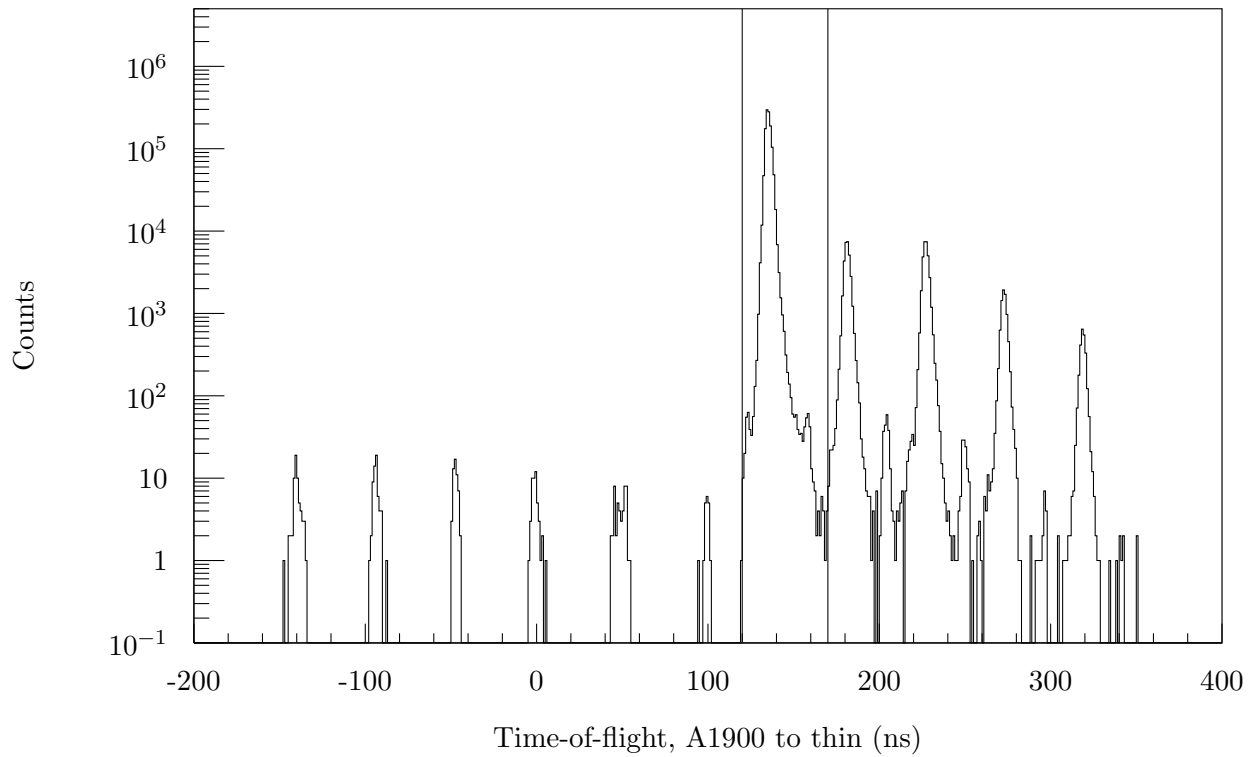


Figure 4.21: Time difference between the A1900 and thin scintillators, showing “echos” from events in which the A1900 scintillator recorded the time of a different particle than the thin scintillator. The vertical lines indicate the limits of the gate used to eliminate these events.

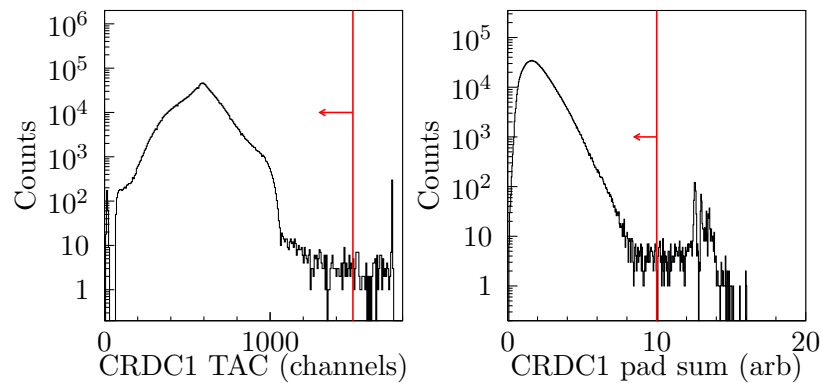


Figure 4.22: Event quality gates applied to the CRDC1 parameters TAC (left) and pad sum (right). Red vertical lines with arrows indicate the requirements for an event to pass through the gate.

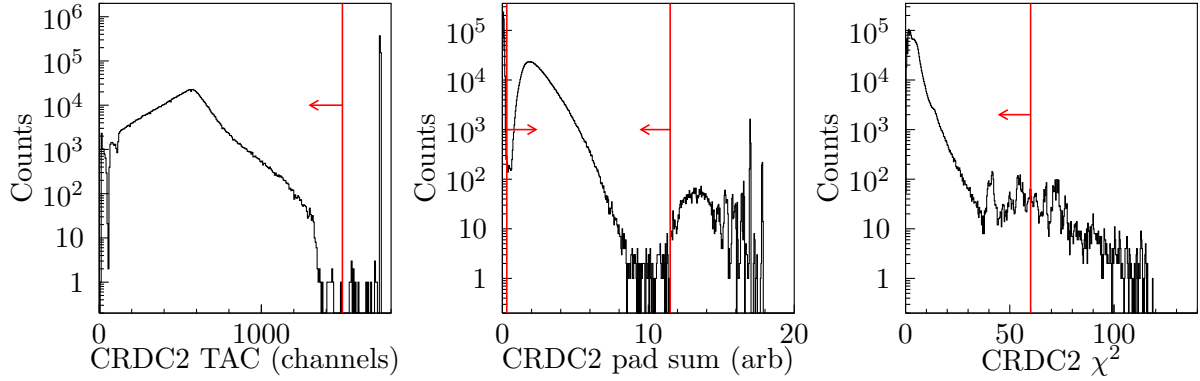


Figure 4.23: Event quality gates applied to the CRDC2 parameters TAC (left), pad sum (center), and χ^2 (right). Thick red vertical lines indicate the requirements for an event to pass through the gate.

4.2.3 Isotope identification

Many products were expected from the $^{13}\text{B}+^9\text{Be}$ reaction. Primarily, isotopes with a Z and A less than or equal to that of the beam were created. The magnetic rigidity of the Sweeper (3.76 Tm for ^{13}B) restricted the isotopes successfully traversing the magnet to those with magnetic rigidities within an acceptance window. For the Sweeper, this was roughly the rigidity of the magnet plus or minus 8%. For this experiment, nuclides within that range included $^{14,15}\text{B}$, $^{10,11,12}\text{Be}$, $^{7,8,9}\text{Li}$, and ^6He .

Element identification was achieved by measuring the energy losses through the ion chamber and the thin scintillator. Although elemental separation can be seen in the individual PMTs of the thin scintillator as well as the individual pads of the ion chamber, two-dimensional gates on the elements produced a cleaner identification (see Figure 4.24).

The next step was isotopic separation. Ideally, a dipole magnet should separate the isotopes by magnetic rigidity. In practice however, the distributions are broad enough that they overlap one another and make isotope separation more difficult. The Sweeper magnet convolutes x -position, x -angle, and time-of-flight. This convolution must be untangled for clean isotope identification. A detailed description of the process can be found in [139], but an overview as well as the final results are presented here.

The convolution can be seen using a three-dimensional plot of x -position, x -angle, and time-of-flight (Figure 4.25) gated on one element, in this case, lithium. The goal was to find a combination of parameters to correct the time-of-flight for variances in x -position and x -angle. To do this, this three-dimensional plot was projected down to the x -position- x -angle plane and the contours guided the convolution of x -position and x -angle into a new parameter. When this new parameter was plotted against time-of-flight, three two-dimensional groups of events were visible - isotope separation. The final goal was isotope separation from one single time-of-flight parameter, so the time-of-flight was corrected for this convoluted x -position- x -angle parameter.

The large gap in the magnet caused a dependency on the y -position and y -angle. The time-of-flight was corrected for both of these parameters as well as the energy loss through the ion chamber in a similar fashion to correcting for the x -position- x -angle convolution. Parameters and correction factors used to construct the final time-of-flight parameter are shown in Table 4.8. To create the

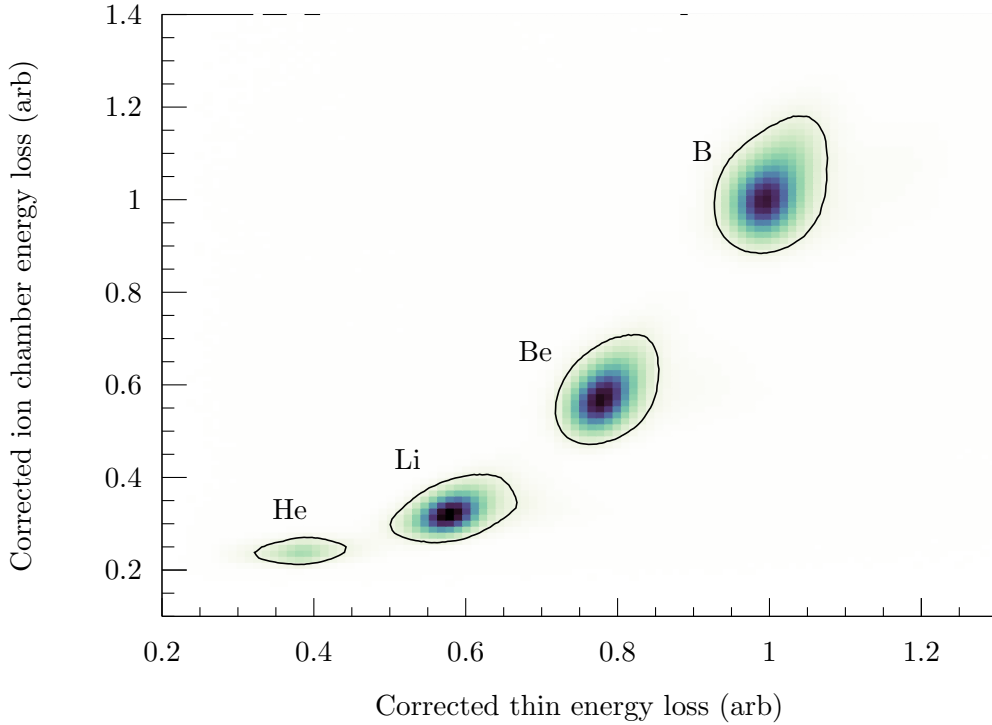


Figure 4.24: Element identification.

final separation parameter,

$$ToF_{corr} = ToF_{A1900-thin} + \sum_{i=0}^P c_i p_i$$

where c_i and p_i are the coefficients and correction factors noted in Table 4.8, ToF_{corr} is the corrected time of flight, and $ToF_{A1900-thin}$ is the time of flight from the A1900 to the thin scintillator.

This time-of-flight correction for lithium could be used to separate the beryllium isotopes as well, but the separation was better when a separate set of corrections were used. Those parameters are shown in Table 4.9. Separation of the lithium and beryllium isotopes in coincidence with an interaction in MoNA-LISA is shown in Figure 4.26. The ^{12}Be peak is small because creating ^{12}Be from the beam requires all the neutrons to remain in the fragment. The same plot for isotopes

Table 4.8: List of correction factors used to produce the lithium isotope separation parameter. The numbers in the right column were multiplied by the parameter on the left, summed, and added to the time-of-flight from the A1900 to the thin to produce a corrected time-of-flight parameter for the lithium isotopes from the ^{13}B beam. Both position parameters, x and y , were calculated 12.59 cm downstream of CRDC1.

Parameter	Correction factor	Parameter	Correction factor
x	-1.14×10^{-1}	θ_x	1.8×10^{-1}
x^2	-3.6×10^{-4}	θ_x^2	1.95932×10^{-4}
y	5.29126×10^{-3}	θ_x^3	-8.54275×10^{-6}
y^2	6.90292×10^{-4}	$\Delta E_{ic.corr}$	13.0485

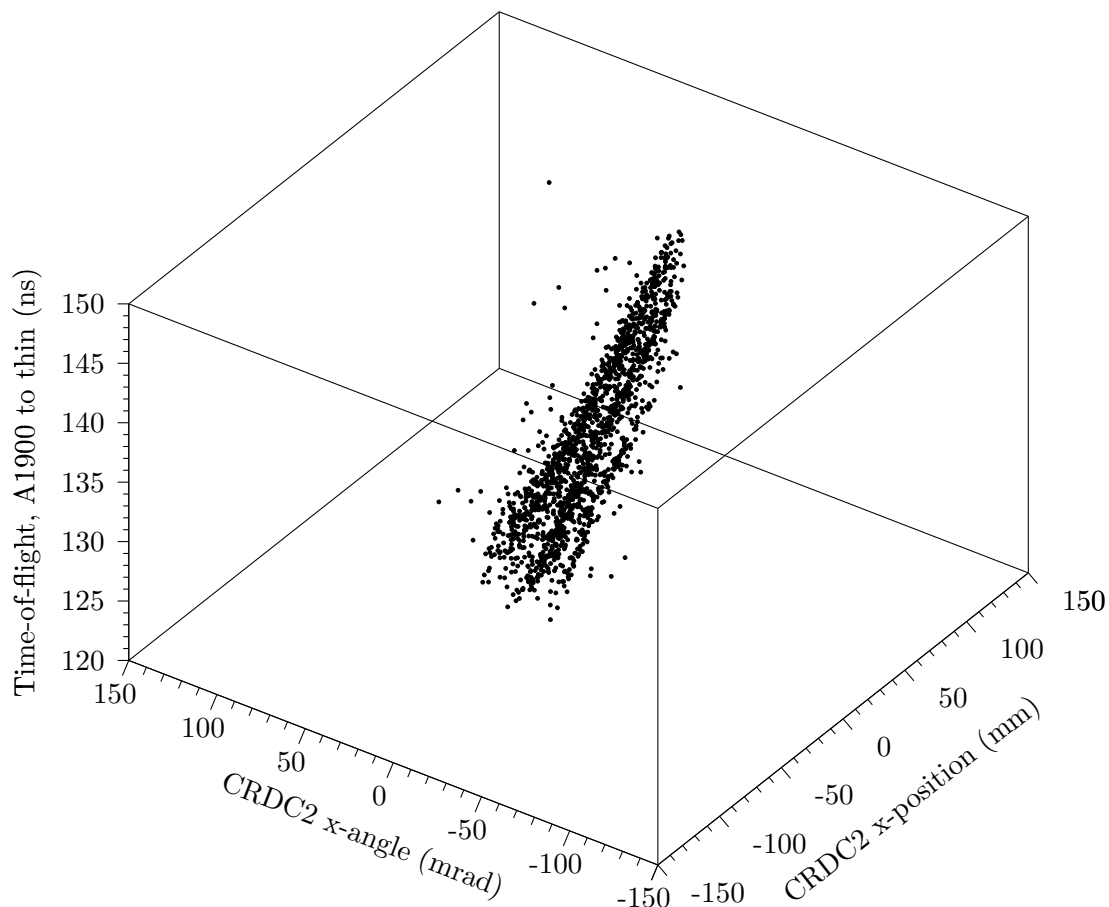


Figure 4.25: Three-dimensional plot showing lithium isotope identification by plotting x -position, x -angle, and time-of-flight.

Table 4.9: List of correction factors used to produce the beryllium isotope separation parameter. The numbers in the right column were multiplied by the parameter on the left, summed, and added to the time-of-flight from the A1900 to the thin to produce a corrected time-of-flight parameter for the lithium isotopes from the ^{13}B beam. Both position parameters, x and y , were calculated 12.59 cm downstream of CRDC1.

Parameter	Correction factor	Parameter	Correction factor
x	-6.5×10^{-1}	θ_x	1.00191851
x^2	-2×10^{-3}	θ_x^2	1.95932×10^{-3}
y	5.29126×10^{-3}	θ_x^3	-8.547275×10^{-6}
y^2	2.8×10^{-3}	$\Delta E_{ic.poscorr}$	60
$\text{ToF}_{A1900-thin}$	2.55		

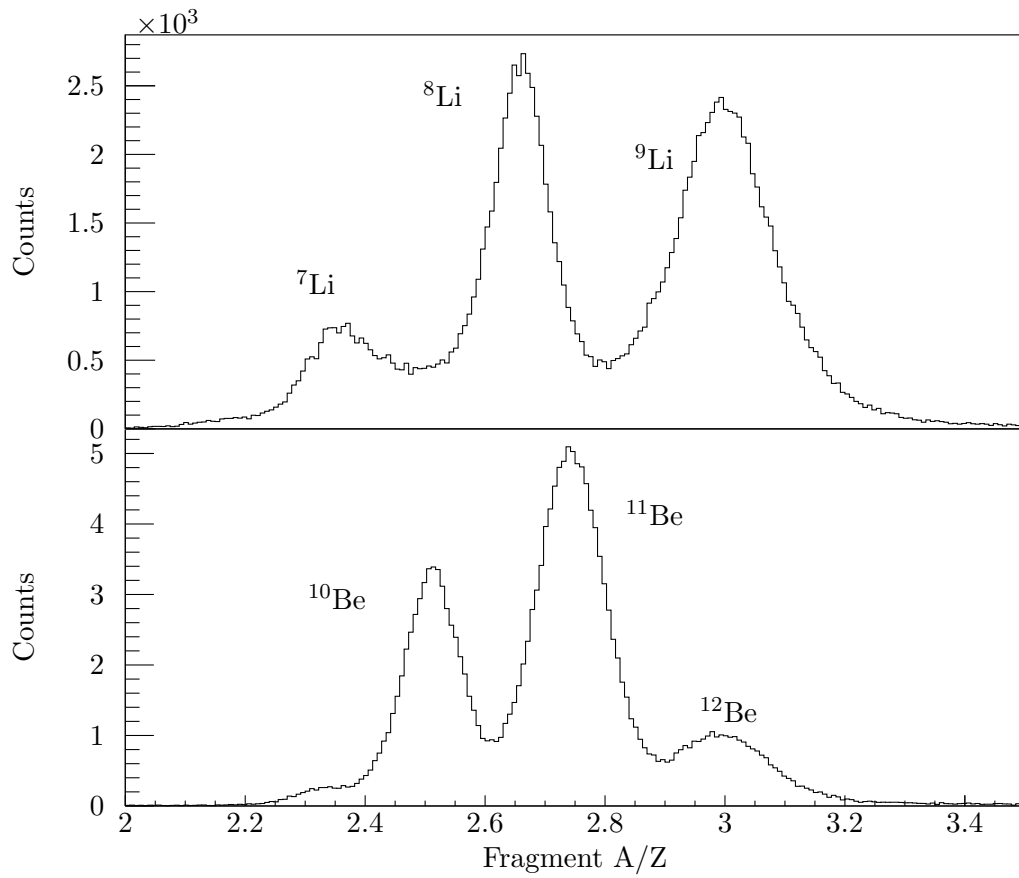


Figure 4.26: Lithium (top) and beryllium (bottom) particle identification from the ${}^{13}\text{B}$ beam and in coincidence with an interaction in MoNA-LISA.

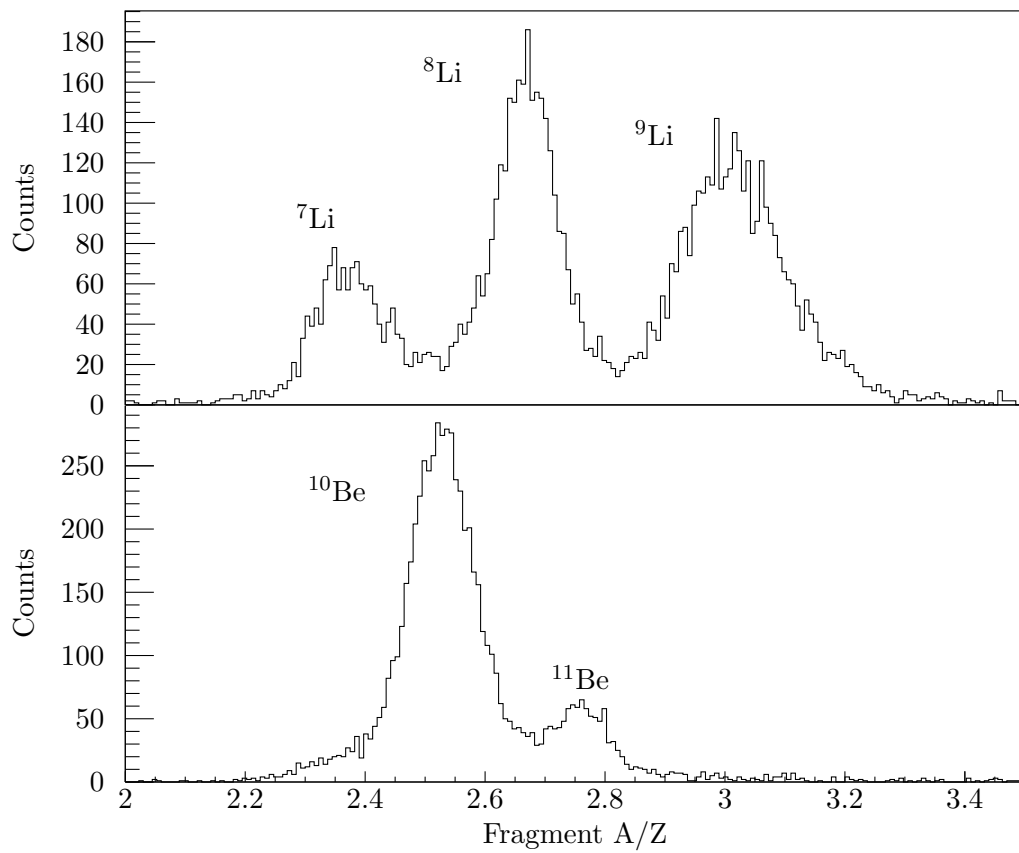


Figure 4.27: Lithium (top) and beryllium (bottom) particle identification from the ${}^{12}\text{B}$ beam and in coincidence with an interaction in MoNA-LISA.

created from the ^{12}B beam is shown in Figure 4.27. In this figure, ^{11}Be is the fragment created by removing a proton and leaving all the neutrons in the nucleus, so it is smaller than the ^{10}Be peak.

4.2.4 Neutron interaction selection

Though MoNA-LISA was designed to detect neutrons, it also detected some background radiation. This background consisted primarily of muons from cosmic rays and gamma rays from the surrounding environment or from reactions in the target. The neutron interactions needed to be separated from these interactions.

The raw neutron time-of-flight spectrum in coincidence with ^9Li is shown in the top panel of Figure 4.28. The bottom panel shows the charge versus time spectrum for the interactions in MoNA-LISA. For each event, there could be multiple interactions in MoNA-LISA; these histograms only show the first interaction in MoNA-LISA, sorted based on interaction time. The one-dimensional histogram has three main features: a sharp peak around 36 ns, a wider peak around 70 ns, and a large background component. The two-dimensional histogram shows that the peak around 70 ns deposited a lot of charge, the peak around 36 ns deposited a small amount of charge, and the background also deposited a small amount of charge. Not shown in the two-dimensional spectrum are all the first interactions in MoNA-LISA that generated a time measurement but whose total charge deposited was below the QDC threshold. These events constituted the majority of the background component and the sharp peak around 36 ns.

Cosmic ray background interactions would have deposited 20 MeVee of energy in the detector and appear as a horizontal band in the two-dimensional spectrum. Such a band is not visible, therefore any background from cosmic rays was negligible.

The shape of the background in the top panel Figure 4.28 was due to three factors: the staggering of the time ranges for the three sections of MoNA-LISA, the time ordering of the interactions, and the high beam rate.

The first interaction in MoNA-LISA could occur anywhere within the detector, so Figure 4.28 contains interactions from MoNA and both tables of LISA. The time window of each table, however, was slightly different. This softened the sharp edges expected of the background. Separating this spectrum into the individual spectra from each Table (Figure 4.29) shows that the perceived bump around 15 ns is the beginning of the background collected from the MoNA table. In addition, the γ -ray peaks and neutron peaks from each table become sharper.

The time-ordering process also skewed the time-of-flight spectrum, particularly the background. If the background was evenly distributed across time, then for events in which multiple interactions are registered, this spectrum only shows the time of the first interaction, which is guaranteed to be before the time of the second interaction. This is illustrated in Figure 4.30. The top panel breaks down the events with two interactions in the first table of LISA. The distributions for the first and second interactions are noticeably different, with the first interaction spectrum (the one that would be included in Figure 4.28) skewed toward smaller times-of-flight. The bottom panel shows the distribution of events with one interaction compared with the summed “two interaction” spectrum from the top panel.

The background before the γ -ray peak in Figure 4.30 is flat, while the background after it is not. The remaining gentle downward slope is likely due to the high rate of the beam and the abnormally large γ -ray peak (the γ -ray peak is often one-tenth the size of the neutron peak). The TDCs registered only the first interaction in each bar, so any background events occurring in the same bar after another are immediately discarded. The effect of this is to remove events predominantly from the higher end of the time-of-flight spectrum.

A zoomed-in spectrum of the peak at 36 ns is shown in Figure 4.31. The shape and charge

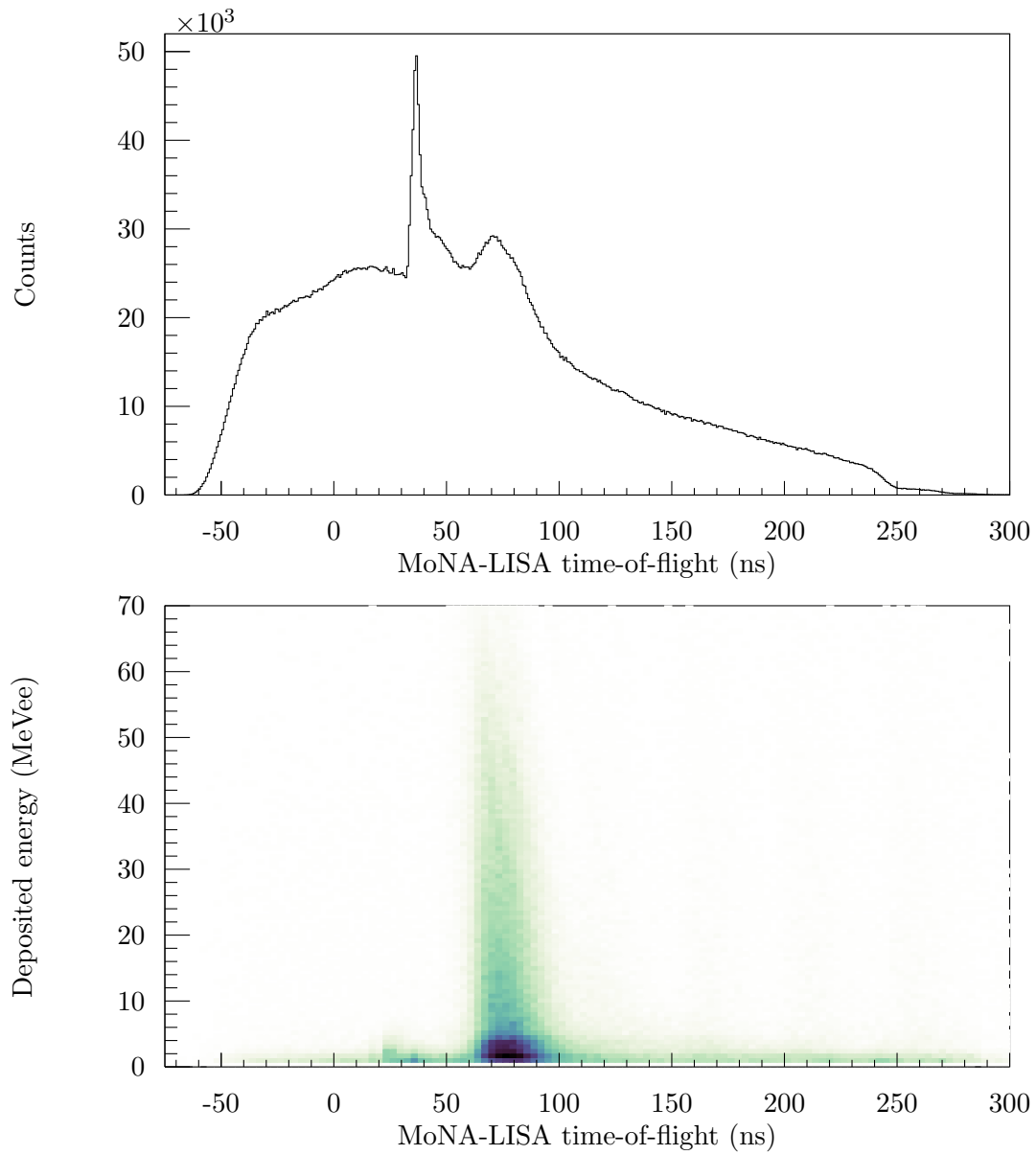


Figure 4.28: Top: Raw neutron time-of-flight spectrum. Bottom: Charge deposited vs. time-of-flight for the first interaction in MoNA-LISA.

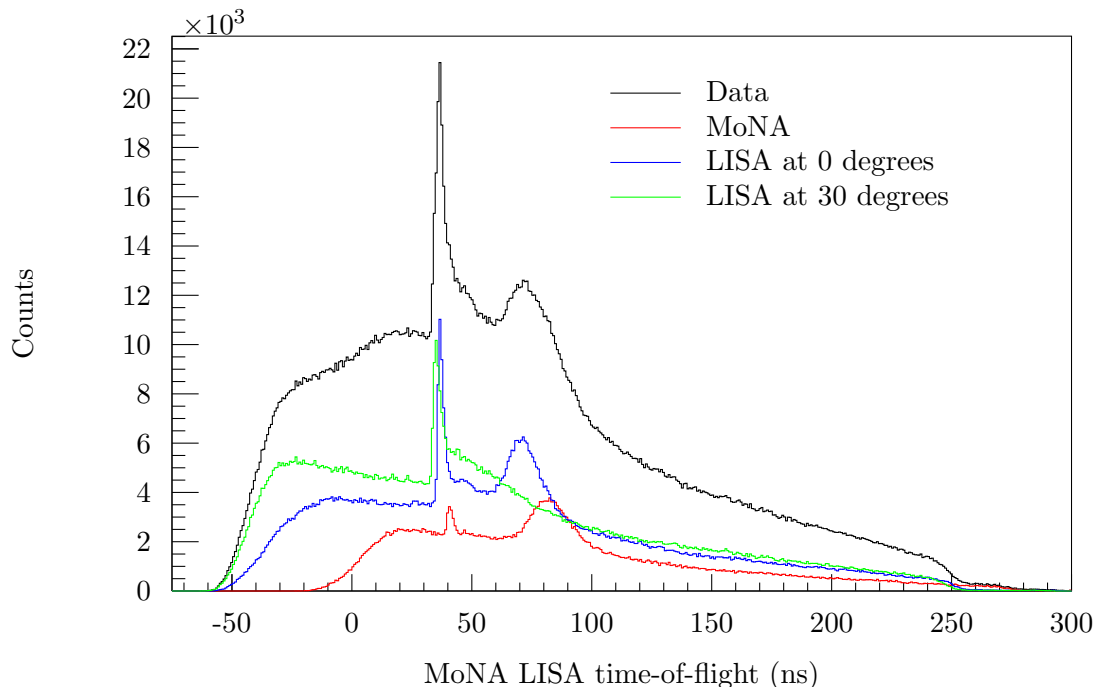


Figure 4.29: A breakdown of the time-of-flight spectrum of Figure 4.28 by sections (tables) of the detector.

deposition (mostly below threshold) are consistent with γ -ray interactions from a point source, but the time-of-flight is not - γ -rays from the target should arrive at approximately 26 ns. Separating the γ -ray peak into the constituent tables (Figure 4.32), shows that each table has a unique time difference between the expected arrival time and the measured arrival time of the γ -rays (10.9 ns for MoNA, 10.7 ns for LISA at 0° , and 13.0 ns for LISA at 30°). Assuming the source of these γ -rays was in the experimental area and that the difference in time-of-flight can be correlated with the distance from that source, these differences can be used to see where in the vault this source could be.

The expected time difference of gamma arrival at two different detectors was calculated for every point in the vault. The measured time difference was subtracted from this calculated time difference. This calculation was done for each pair of detectors and is shown in Figure 4.33. The source can be located anywhere along the line where this quantity is zero, delineated by the curved black lines.

Overlaying all of these zero-lines on the vault layout diagram (shown in Figure 4.34) can give some indication of where the gamma source could be located. In this case, it appears the γ -rays are coming from the negative x side of the Sweeper detector box, near the tungsten blocker. This is close to where the unreacted beam was dumped, so it seems likely that this large γ -ray peak was coming from unreacted beam being dumped on the tungsten blocker or the wall of the Sweeper detector box. The expected rate of two incoming beam particles arriving at the same time is small, but not negligible.

Accounting for the shape of the background is not enough - the neutrons still needed to be separated. The γ -ray peak was easily separated from the neutron peak by time-of-flight, but the continuous background underneath was not. It was separated, however, by requiring a certain amount of charge to be deposited in the bars. Since the QDC thresholds were set abnormally

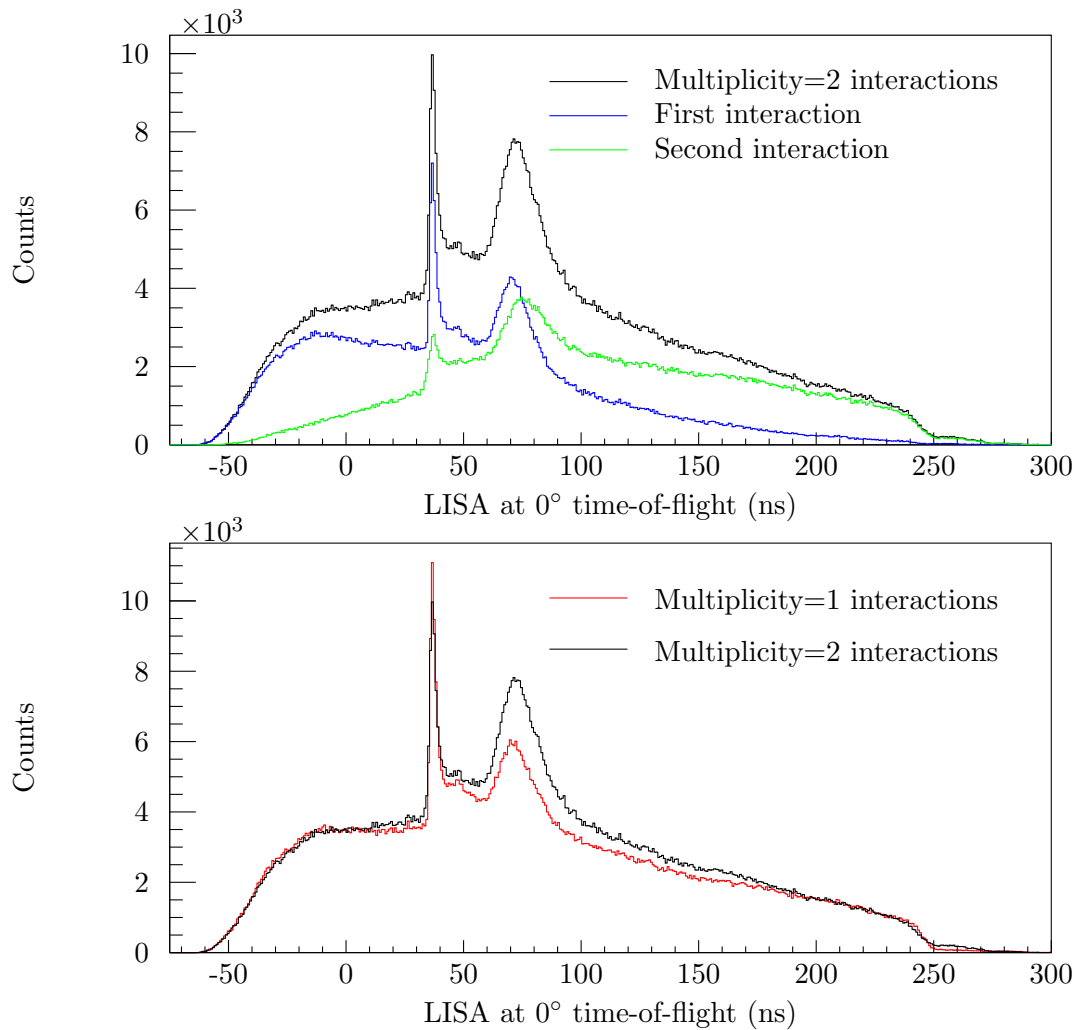


Figure 4.30: Top: Time-of-flight breakdown of events with two (and only two) interactions in the section of LISA at 0 degrees. The blue line shows the first interaction spectrum, while the green line shows the spectrum of the second interaction. The black line is the sum of those two components. Bottom: Comparison of the time-of-flight spectrum for events with one interaction (red line) and the summed spectrum from above (black line). The red line has been normalized to the flat background before the gamma peak of the black line.

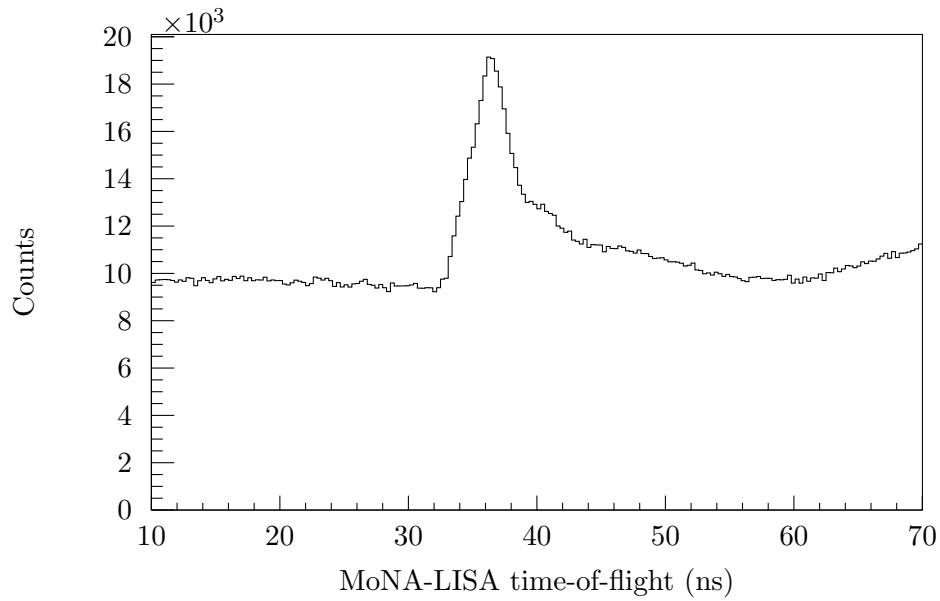


Figure 4.31: The γ -ray peak in MoNA-LISA during the ^{13}B production runs.

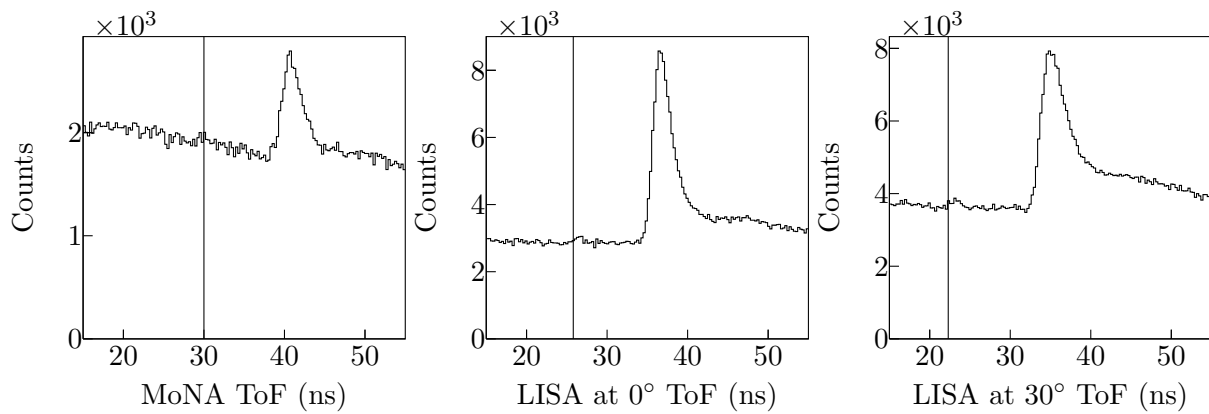


Figure 4.32: The arrival time of the large γ -ray peak, as observed by MoNA (left), the LISA table at 0 degrees (center), and the LISA table at 30 degrees (right). Vertical lines indicate expected arrival time of γ -rays from the target area.

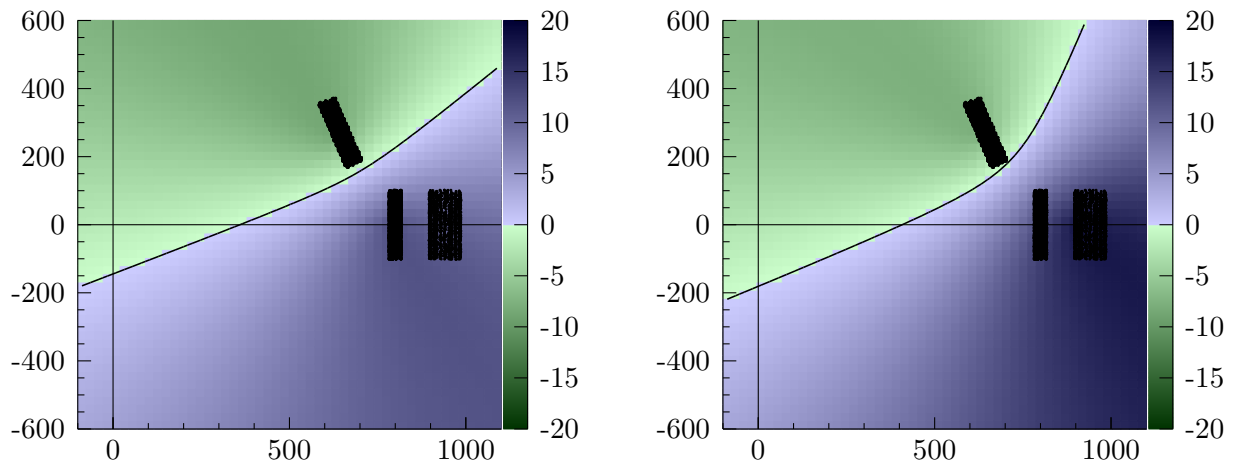


Figure 4.33: Difference of time differences between two of the three detectors. The left panel shows the comparison between LISA at 0° and LISA at 30° , and the right panel shows the comparison between MoNA and LISA at 30° . Black lines indicate the possible locations of a point gamma source to produce the measured time difference between the two detectors.

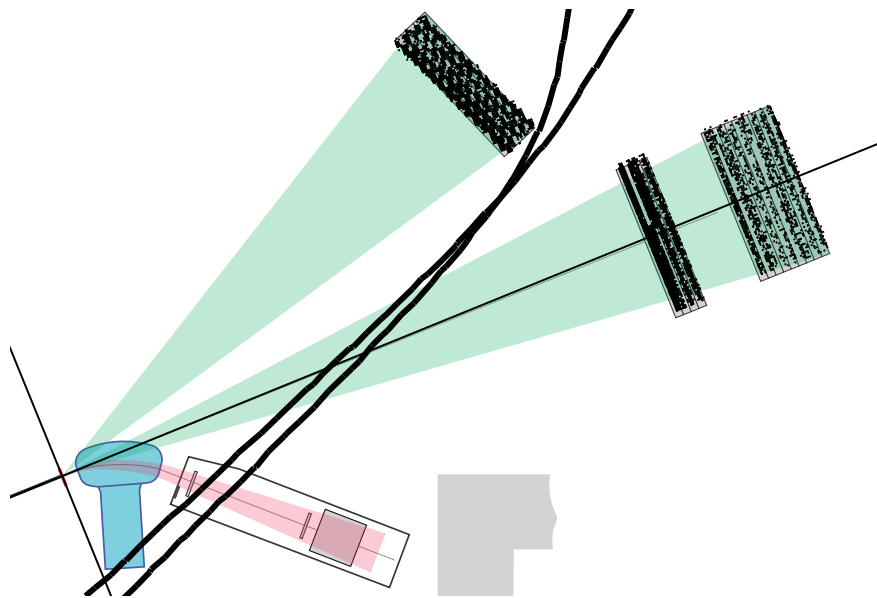


Figure 4.34: The two zero-lines from Figure 4.33 overlaid on the vault layout. The intersection of these lines indicates the likely location of a point gamma source. Within the error of the calculation, and given the layout of the experimental vault, a gamma source was identified inside the Sweeper box.

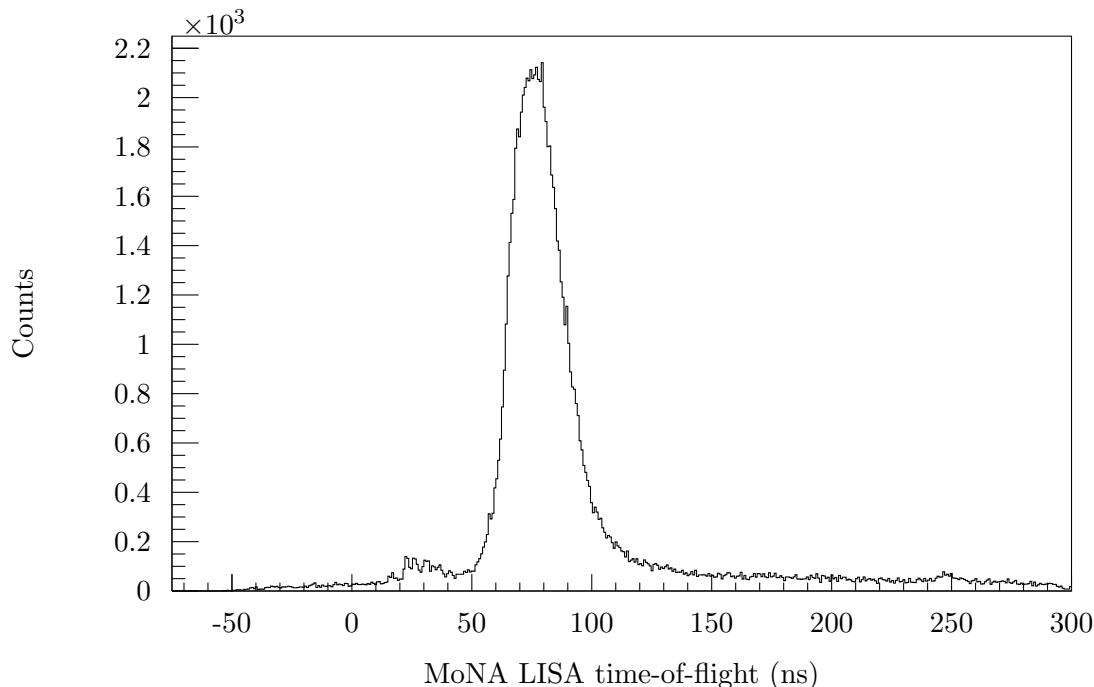


Figure 4.35: Final time-of-flight spectrum for MoNA-LISA. This spectrum requires that each interaction not only have a valid charge but also a valid time.

high for this experiment, the lowest requirement of this type that could be made was to simply have a charge measurement for the event. Including this requirement effectively eliminated the background.

One concern in requiring a charge measurement was the possibility that while the first interaction might not have had a valid charge and thus not be included as a neutron event, the second (or third or fourth) interaction might qualify. In this case, the second interaction should be considered the first, the third the second, and so on. This becomes especially important when looking for the interactions of multiple neutrons. In an attempt to count the neutron interactions more accurately, the interaction algorithm was modified. Whereas previously, interactions needed only a valid time signal to pass the calibration and be incorporated into the data, they now required valid time and charge signals. The raw data still included all of the information, but the calibrated neutron time-of-flight spectrum changed. The final time-of-flight spectrum, shown in Figure 4.35, eliminated the background and enhanced the statistics by mining the later interactions for interactions with valid charge signals.

4.3 Inverse tracking

All the position measurements were performed after the fragments had been bent by the Sweeper magnet. In order to retrieve the momentum and position information of the particles at the target, they needed to be tracked through the magnet. This reconstruction of particle trajectories before the magnet is fully described in [145], but a summary is presented here.

Ion-optical matrices are used to transform the coordinates of a particle before a magnet to the coordinates of the particle after it traverses the magnet. Specifically, the Sweeper ion-optical matrix relates the set of variables $(x, \theta_x, y, \theta_y, \delta)^{(T)}$ at the target to the variables $(x, \theta_x, y, \theta_y, \Delta L)^{(D)}$ at

the detector. In this case, x is the dispersive position, y is the non-dispersive position, and the θ variables are ratios of transverse momentum in that (x or y) direction over the total momentum:

$$\sin \theta_{(x,y)} = p_{(x,y)}/p_0.$$

The variable ΔL is the length difference between the path traveled by the particle and the central path. The variable δ is the relative energy deviation:

$$\delta = \frac{E - E_0}{E_0}$$

where E is the energy of the particle and E_0 is the energy of a particle following the central trajectory through the magnet. The value of E_0 can be determined by the magnetic field of the magnet.

The forward matrix M_f is defined such that:

$$\begin{pmatrix} x \\ \theta_x \\ y \\ \theta_y \\ \Delta L \end{pmatrix}^{(D)} = M_f \begin{pmatrix} x \\ \theta_x \\ y \\ \theta_y \\ \delta \end{pmatrix}^{(T)}$$

This matrix is useful given the incoming particle information, but that only happens during a simulation. For the data, this matrix needs to be transformed to one that takes in the measured variables and gives back the unknown variables at the target- an inverse mapping. There were measurements of $x^{(D)}, \theta_x^{(D)}, y^{(D)}$, and $\theta_y^{(D)}$ and the needed variables were $x^{(T)}, \theta_x^{(T)}, y^{(T)}, \theta_y^{(T)}$, and δ .

One way to fix this situation of four input variables and five output variables is to measure the incoming beam distribution with tracking CRDCs before the target. Then $x^{(T)}$ and $y^{(T)}$ are available and the reconstruction is overdetermined. In this experiment though, the use of tracking detectors was precluded by the high incoming beam rate.

In this case, the solution was to assume that every particle arrived at the target with $x^{(T)} = 0$. If the beam was centered at $x = 0$ (or close to it), this assumption will slightly worsen the resolution of the measurement, but should not shift it. If the beam were not centered, this would result in a reconstructed energy and x -angle that were also shifted from the input values [145]. A series of transformations then produce a matrix M_i , which transforms the measured variables to the variables needed to reconstruct the four-momentum of the fragment at the target:

$$\begin{pmatrix} \theta_x^{(T)} \\ y^{(T)} \\ \theta_y^{(T)} \\ \Delta L \\ \delta \end{pmatrix} = M_i \begin{pmatrix} x^{(D)} \\ \theta_x^{(D)} \\ y^{(D)} \\ \theta_y^{(D)} \\ x^{(T)} \end{pmatrix}$$

4.4 Modeling and simulation

The final step in the analysis was to create a simulation, compare it to the data, and use it to extract values of decay energy and width. An in-house Monte Carlo simulation took into account the incoming beam profile, reaction, and subsequent decay as well as the geometric acceptances

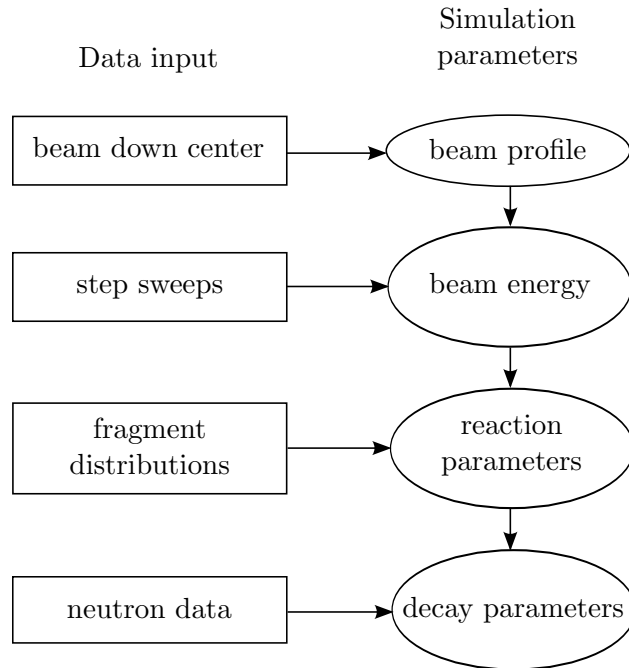


Figure 4.36: A flow chart of the simulation process and the various data that are used as input.

and intrinsic resolutions of the detectors. In addition, the simulation was able to reproduce cuts made on the data for a one-to-one comparison between data and simulation.

Various kinds of data were used as input to determine the parameters of the simulation. A flow chart is shown in Figure 4.36. During the experiment, the strength of the Sweeper magnet was measured with a Hall probe. Those values were used to create the ion-optical maps. Several runs of data were designed to help calibrate the simulation. Runs where the beam was sent down the central trajectory of the Sweeper magnet (“beam down center” runs) were used to fix the incoming beam profile. Next, the current running through the Sweeper magnet was changed to sweep the beam in discrete steps across the active area of the detectors (“step sweeps”). This data was used to fix the beam energy. The fragment distributions are primarily dominated by the reaction kinematics, so reproducing those distributions in the simulation sets the reaction parameters. Finally, the combination of fragment and neutron data was used to extract the decay parameters such as energy, width, and decay type.

The motion of the charged particles was simulated using an in-house simulation titled ST_MONA. Acceptances were applied by eliminating particles that did not hit the active area of the detectors and resolutions were applied by smearing the signals with Gaussians representative of the resolution. The interactions of the neutrons with MoNA-LISA was modeled with GEANT4 [146, 147] and the custom neutron interaction model MENATE_R [148].

4.4.1 Incoming beam parameters

The incoming beam parameters of the simulation were set by duplicating the distributions from sending the unreacted beam through the detectors. In this data set, the beryllium target was retracted and an attenuated beam was sent into the Sweeper magnet, which was set to direct the beam along the central trajectory of all detectors.

In this case, the goal was to duplicate the position and angular distributions at both CRDC

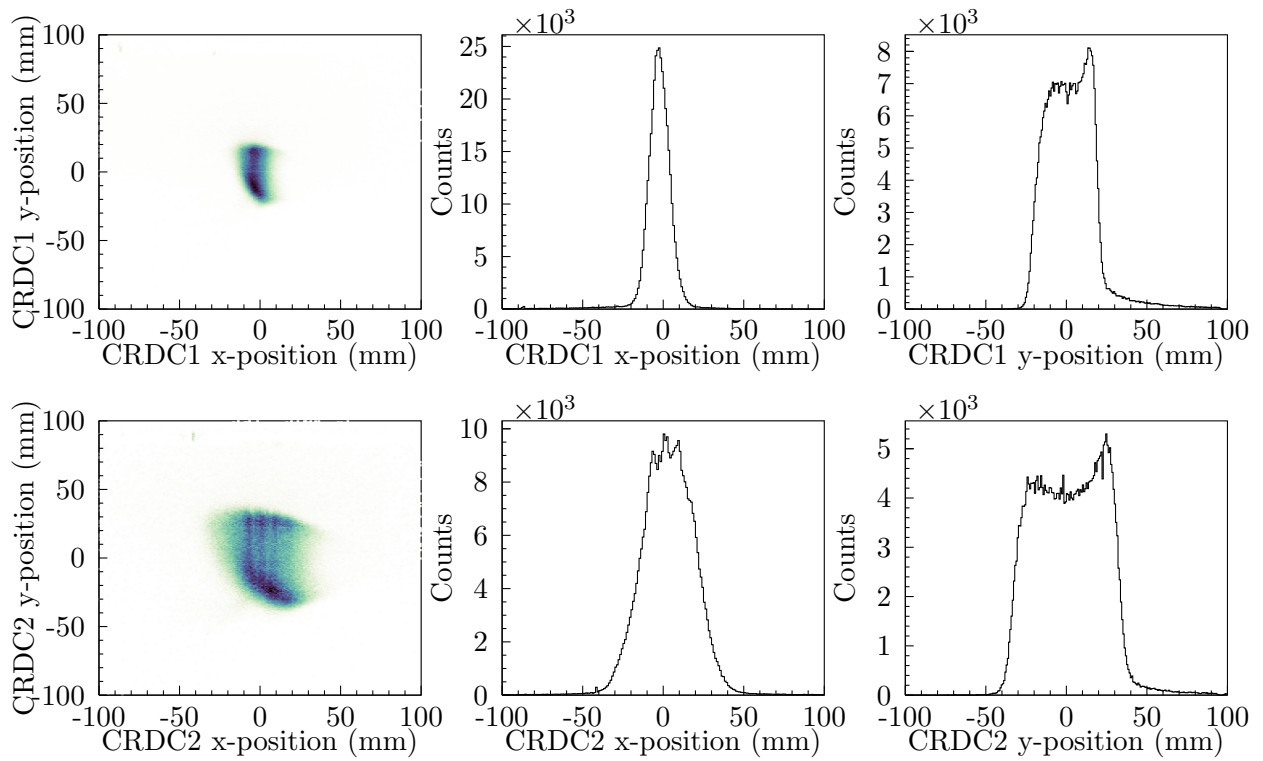


Figure 4.37: Incoming beam distributions in CRDC1 (top row) and CRDC2 (bottom row). The left column shows the two-dimensional positional profile, the middle column shows the x-projection, and the right column shows the y-projection.

Table 4.10: List of simulation parameters used to recreate the incoming ^{13}B beam profile. Part 1 recreated the horizontal peak around 30 mm in the y -position of CRDC2, Part 2 recreated the square background, and Part 3 recreated the slanted peak around -20 mm in the y -position.

Simulation flag	Part 1	Part 2	Part 3	Significance
cx	-0.001	-0.001	0.00	x -distribution centroid
dx	0.008	0.0075	0.004	x -distribution width
ctx	-0.004	-0.004	0.001	θ_x -distribution centroid
dtx	0.005	0.002	0.002	θ_x -distribution width
cy	0.005	0.00	-0.012	y -distribution centroid
dy	0.00	0.007	0.0005	y -distribution width
fy	-	20	-	y -distribution shape factor
cty	0.0055	0.00	0.00	θ_y -distribution centroid
dty	0.0015	0.0085	0.009	θ_y -distribution width
fty	-	20	-	θ_y -distribution shape factor
sctx	-0.82	-0.82	-0.82	Rotation angle between x and θ_x distributions
sxy	-	-	0.5	Rotation angle between x and y distributions
scale	20	100	7	Relative intensities of the components

detectors, CRDC1 and CRDC2. A first look at the beam profile in position space (Figure 4.37) shows that these were not simple Gaussian distributions. It looked like there were three components to this beam: a horizontal peak around 30 mm in the y -position of CRDC2, a square background and a slanted peak around -20 mm in the y -position.

Many different parameters were included in the duplication of the beam profile. A summary of them is shown in Table 4.10 and the final result is compared to the data in Figures 4.38 and 4.39. An initial estimate of the beam energy and spread was taken from the information from the A1900 group. Initial x , y , θ_x , and θ_y distributions were created and then tweaked. Most distributions were modeled as Gaussian and so were defined by a centroid and a width.

The exception to this were the y and θ_y distributions for the second component, the square background. These distributions were defined with a generalized normal distribution:

$$Ae^{-(|x-\mu|/\alpha)^\beta}$$

where μ , α , and β are parameters that can be varied. In this case, μ varies the location of the centroid, α scales the width of the distribution, and β is a shape parameter. When $\beta = 2$, this is a normal distribution with centroid μ and width α . In the limit that $\beta = \infty$, this is a uniform density from $\mu - \alpha$ to $\mu + \alpha$.

A correlation between x and θ_x was necessary to reproduce the beam profile. The correlation was imposed on an event-by-event basis. A random value was picked for each of the two independent distributions and then a rotation was imposed upon that coordinate pair.

The same process was used to reproduce the ^{12}B beam. Those beam parameters are given in Table 4.11 and a comparison between data and simulation is shown in Figures 4.40 and 4.41.

4.4.2 Beam energy

The energy of the incoming beam was determined by the magnetic rigidity of the last magnet before the target and the energy spread was set by momentum slits located upstream of the experimental setup. The use of the slits created an energy distribution that was similar to a step function, so

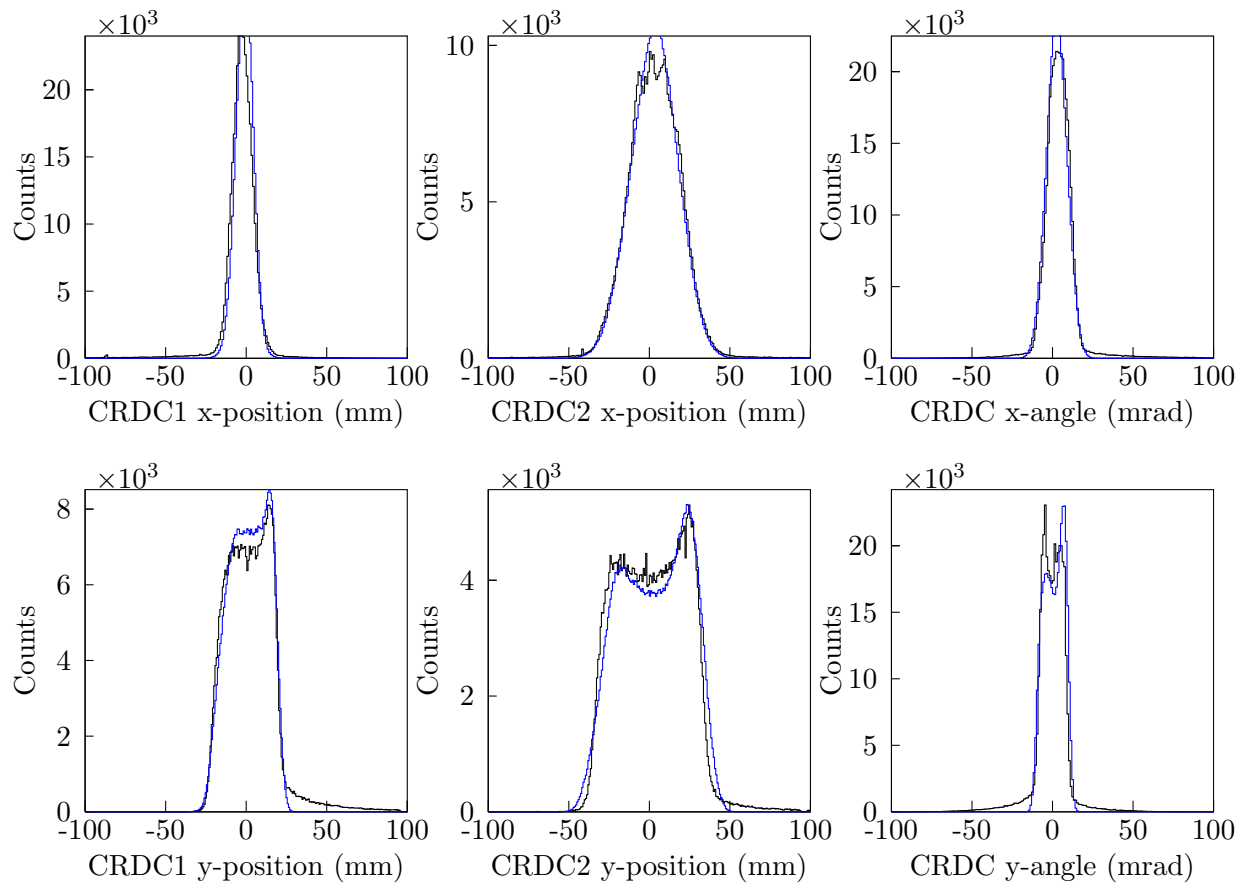


Figure 4.38: Simulated (blue) and data (black) position and angular spectra for the incoming ^{13}B beam profile. Top row: CRDC1 x -position, CRDC2 x -position, and x -angle. Bottom row: CRDC1 y -position, CRDC2 y -position, y -angle.

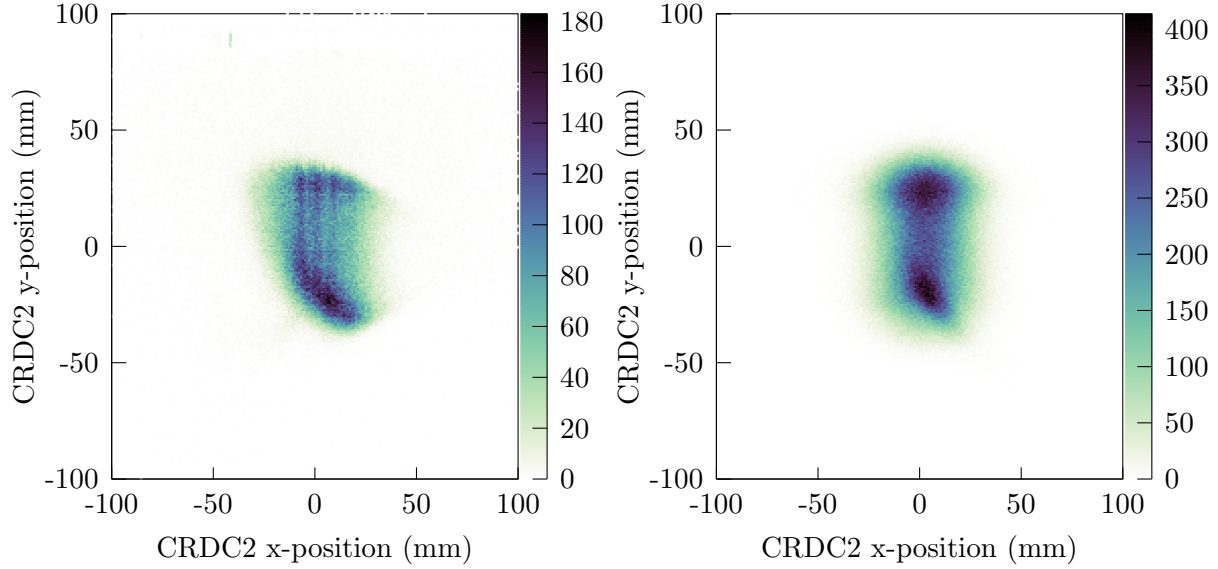


Figure 4.39: CRDC2 position spectra from data (left) and simulation (right) for the incoming ^{13}B beam.

Table 4.11: List of simulation parameters used to recreate the incoming ^{12}B beam profile. Part 1 recreated the horizontal peak around 30 mm in the y -position of CRDC2, Part 2 recreated the square background, and Part 3 recreated the slanted peak around -20 mm in the y -position.

Simulation flag	Part 1	Part 2	Part 3	Significance
cx	0.00	0.00	0.00	x -distribution centroid
dx	0.0055	0.0055	0.004	x -distribution width
ctx	-0.003	-0.003	0.003	θ_x -distribution centroid
dtx	0.002	0.002	0.002	θ_x -distribution width
cy	0.004	0.00	-0.012	y -distribution centroid
dy	0.005	0.007	0.0005	y -distribution width
fy	-	50	-	y -distribution shape factor
cty	0.004	0.00	0.00	θ_y -distribution centroid
dty	0.0015	0.0085	0.0009	θ_y -distribution width
fty	-	20	-	θ_y -distribution shape factor
sctx	-0.82	-0.82	-0.82	Rotation angle between x and θ_x distributions
sxy	-	-	0.25	Rotation angle between x and y distributions
scale	15	50	20	Relative intensities of the components

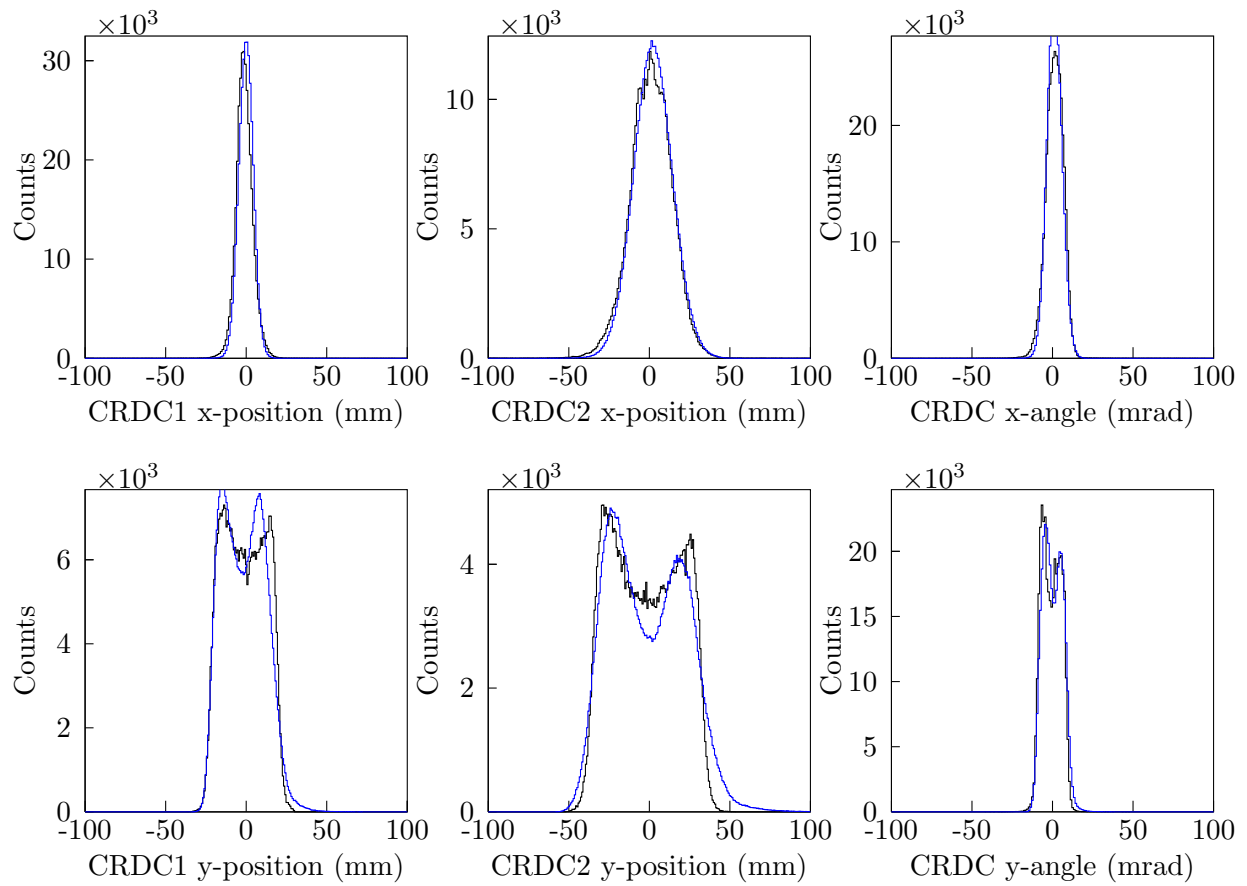


Figure 4.40: Simulated (blue) and data (black) position and angular spectra for the incoming ^{12}B beam profile. Top row: CRDC1 x -position, CRDC2 x -position, and x -angle. Bottom row: CRDC1 y -position, CRDC2 y -position, y -angle.

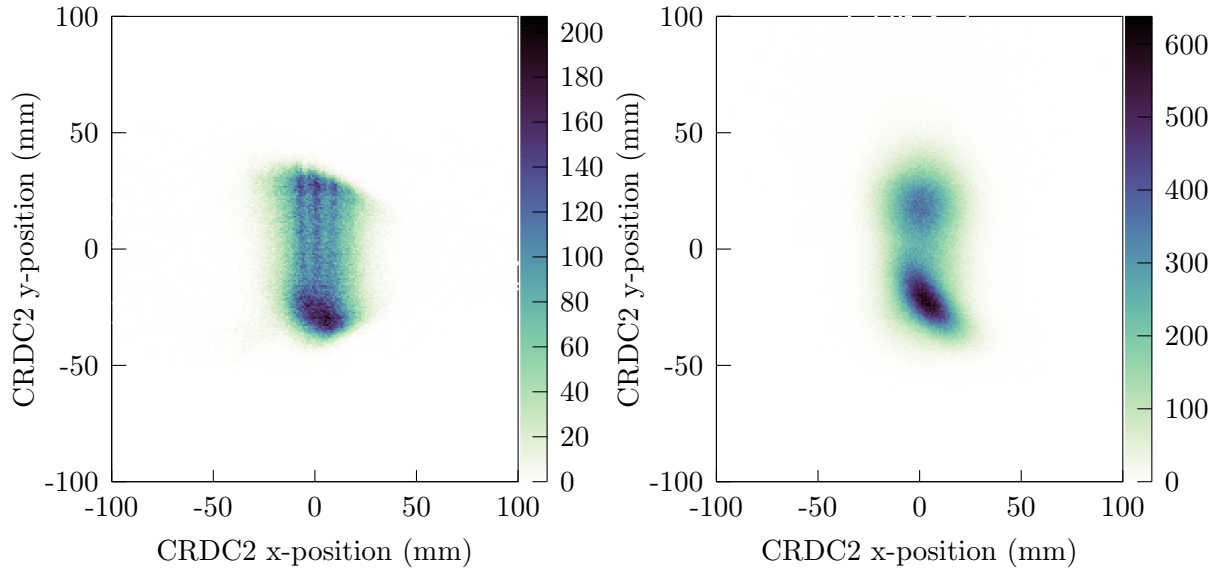


Figure 4.41: CRDC2 position spectra from data (left) and simulation (right) for the incoming ^{12}B beam.

the simulated beam energy distribution was defined by a centroid energy and a width which was the full width of a step function distribution.

The momentum slits were set at 0.2% dp/p , which corresponded to a 0.4% spread in energy. For the ^{13}B runs, the quadrupole magnet immediately before the magnet was set at 3.2271 Tm (71.38 MeV/u). For the ^{12}B runs, this was set at 2.9772 Tm (71.33 MeV/u). The centroid energy was tuned from these nominal values by comparing simulation to data sets in which the Sweeper was set to different magnetic rigidities, which moves the centroid of the beam in the dispersive (x) direction. These “step sweep” data sets (so called because the beam was swept across the detectors in discrete steps) were also used to confirm that the beam profile does not change as a function of the optics imposed by the Sweeper magnet. The final beam energy used in the simulation was 71 MeV/u.

4.4.3 Reaction parameters

The $1p$ - and $2p$ -knockout reactions were simulated by removing the nucleons from the beam and giving the unbound system a momentum “kick”. The momentum kick was parametrized based on the Goldhaber model [149] for parallel momentum distributions and the model proposed by Van Bibber [150] for perpendicular momentum distributions. In these models, the parallel and perpendicular momentum kicks are Gaussian in shape and defined by widths, σ_{\parallel} for the parallel distribution and σ_{\perp} for the perpendicular distribution. These widths were fixed by the observed position and angle distributions of the fragments and are given in Table 4.12. In addition, a friction term was included to reproduce the low-momentum tail observed in the data (Figure 4.43) and commonly attributed to dissipative interactions within the target [151]. This friction term was created by multiplying every negative parallel momentum kick by a constant factor. In this case, the factor 2 was chosen to reproduce the tail observed in the data. A comparison of simulation and data for the ^9Li fragments from the ^{13}B beam is shown in Figure 4.42.

Table 4.12: Widths of the parallel and perpendicular kicks used to reproduce the kicks of the knockout reaction.

Beam	Fragment	σ_{\parallel} (MeV/c)	σ_{\perp} (MeV/c)
^{13}B	^9Li	183	244
^{13}B	^{11}Be	90	180
^{13}B	^{10}Be	122	244
^{12}B	^9Li	121	243

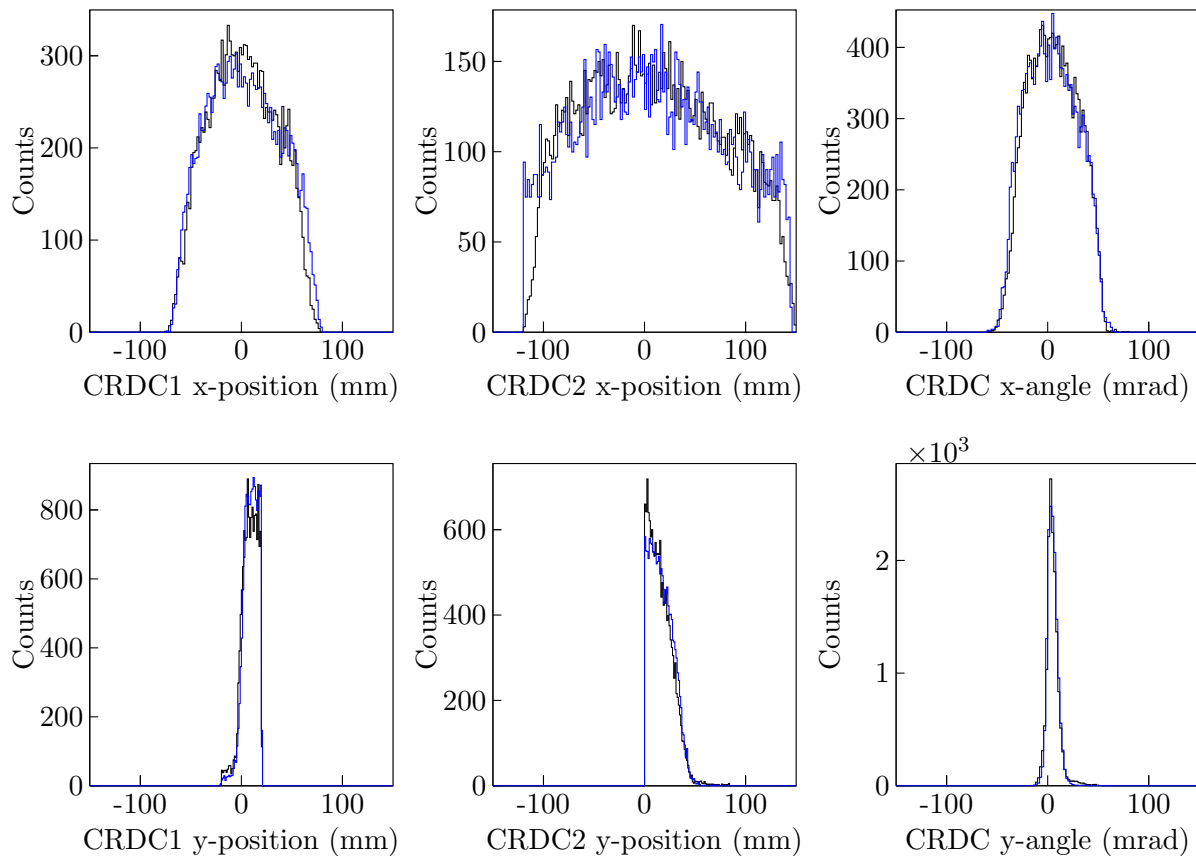


Figure 4.42: Simulated (blue) and data (black) position and angular spectra for the ^9Li fragments from the ^{13}B beam. Top row: CRDC1 x -position, CRDC2 x -position, and x -angle. Bottom row: CRDC1 y -position, CRDC2 y -position, y -angle. See Section 4.4.5 for information about the cut on CRDC2 y -position.

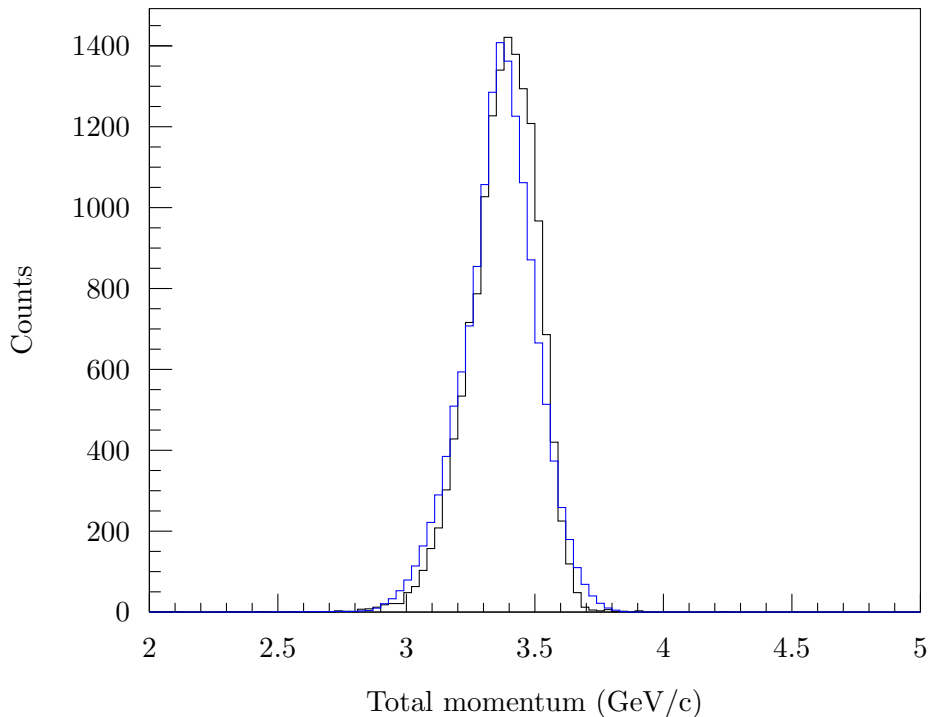


Figure 4.43: Total momentum of the ${}^9\text{Li}$ fragments in the data (black line) and simulation (blue line).

4.4.4 Other parameters

The target area density of 51.37 mg/cm^2 was fixed by measuring the thickness of the target (0.278 mm) with a pair of calipers and converting to area density, assuming natural beryllium composition. The magnetic field strength used to create the field maps for the Sweeper magnet was fixed by measurements by a Hall probe inserted in the field of the magnet. The geometric acceptances of the detectors were also included. Those were based on measurements made before and during the experiment. Resolutions for MoNA-LISA included a Gaussian resolutions for time measurements and position measurements along the length of the bar as well as discretization in the directions perpendicular to the length of the bar [142].

4.4.5 Additional cuts

For a consistent comparison of data to simulation, additional cuts had to be made to both the simulation and the data. As an example, intrinsic limits on the data due to the finite physical size of the detectors had to be explicitly imposed upon the simulations. Imposed detector limits included the x and y limits imposed by the windows in the front and back of the ion chamber, as well as the CRDCs. The simulated light threshold for PMTs in MoNA-LISA was raised to account for the high QDC thresholds (Section 4.2.4).

Other cuts were applied to both the simulation and the data. A “notch” of missing data was observed in the lower half of CRDC2. It was determined that this was an effect of the detector and not representative of the actual fragment distributions. To eliminate any bias due to this notch, both the data and simulation were restricted to events above the beam axis ($y > 0$). Due to the

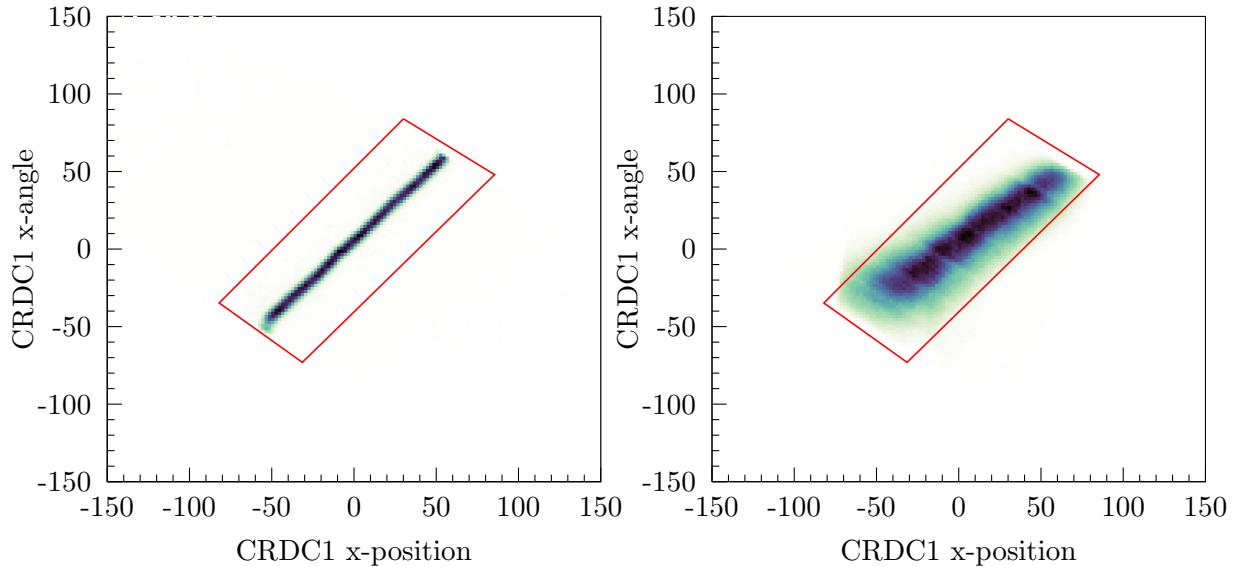


Figure 4.44: CRDC1 x-angle versus CRDC1 x-position for a beam sweep run with no target (left) and for production (right). The red polygon indicates the “sweep” gate.

known non-uniformity in the y -direction of the dipole field within the Sweeper magnet, events were also required to be within 20 mm of the dispersive plane when they reached CRDC1. Finally, events that were bent by the Sweeper magnet in a regular fashion had a strong correlation between x -position and x -angle after the magnet (Figure 4.44). A cut was applied (the “sweep” gate) to select only those events.

This experiment was not designed to measure the decay of ^{12}Be , so the ^{11}Be fragment was off-center. The x -position distribution of ^{11}Be fragments should be centered off the $-x$ side of CRDC2. The experimental spectrum, in contrast with the simulated spectrum in Figure 4.45, shows the x -position distribution covering the entire detector. This contamination was reduced by only analyzing ^{11}Be fragments arriving at a CRDC2 x -position of less than -50 mm.

4.4.6 Decay models

Once the fragment distributions were reproduced, the final step was to use the data, specifically the decay energy plots, to pin down the decay parameters such as energy, width, scattering length, and decay mode.

4.4.6.1 Single neutron decay

The decay energy for a single neutron decay was modeled as an energy-dependent Breit-Wigner, as described in Section 2.1.1:

$$\sigma_{\ell}(E; E_0, \Gamma_0) = A \frac{\Gamma_{\ell}(E; E_0)}{[E_0 - E + \Delta(E; \Gamma_0)]^2 + \frac{1}{4}[\Gamma_{\ell}(E; \Gamma_0)]^2}.$$

When using this model, the fitting parameters were the centroid energy, E_0 , the width, Γ_0 , the angular momentum of the neutron released, ℓ , and the relative intensity of the lineshape. In this analysis, this lineshape was used to model the decays of ^{12}Be , ^{11}Be , and ^{10}Li .

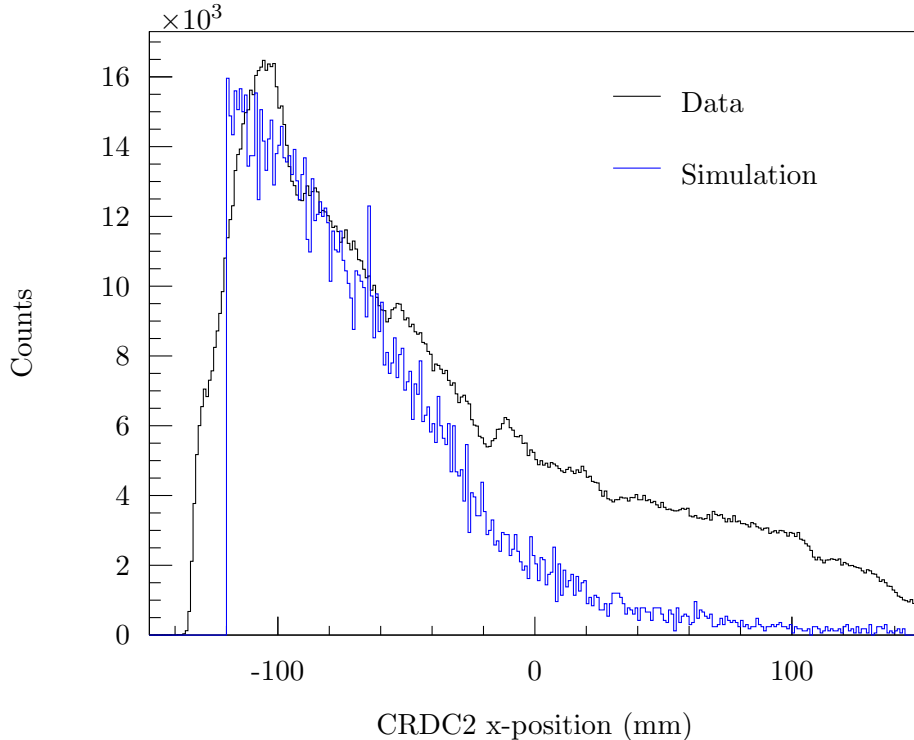


Figure 4.45: Full x -position spectrum for ^{11}Be , data (black line) and simulation (blue line).

4.4.6.2 Two neutron decay

The decays of ^{12}Be and ^{11}Li were modeled as two neutron decays to ^{10}Be and ^9Li , respectively. The decay of ^{12}Be was only modeled as a phase-space decay (Section 2.2.1), while the ^{11}Li was modeled as a phase-space decay, a sequential decay, and as a dineutron decay. In the two-neutron ^{12}Be , the energy was fixed by minimizing the one-neutron decay energy (from the $^{12}\text{Be} \rightarrow ^{11}\text{Be} + n$ decay) and then converting that to a two-neutron decay energy (for the $^{12}\text{Be} \rightarrow ^{10}\text{Be} + 2n$ decay). The width was fixed with a single-particle decay width calculation from Bohr and Mottelson [134]. For the ^{11}Li decay, the total decay energy, total decay width, intermediate decay energy, second decay width, and the relative intensity were all free fitting parameters.

The two-neutron phase space decays utilized the `TGenPhaseSpace` class as implemented in ROOT [152]. The four-vector of the decaying particle and the mass distribution of the decay products were input and the four-vectors of the three decay products were output. The sequential decay used the relative energy distribution as defined in Section 2.2.2 to set the energies of the two decays and then isotropically distributed the two decays. In the sequential decay, the energies and widths of the two unbound states as well as the angular momentum of each decay were the input used to create the lineshape. In a similar fashion, the dineutron decay simulation utilized the energy distribution defined in Section 2.2.3 to define the decay energies that separated the two neutrons from the charged fragment and the two neutrons. The two “decays” were isotropically distributed. The inputs for each dineutron lineshape were the central decay energy and the total two-neutron decay width.

4.5 Fitting and error analysis

Simulated spectra were compared to experimental spectra using the least-squares fitting method, commonly called a χ^2 analysis. For binned data and simulations, the following test statistic was constructed:

$$S = \sum_{i=1}^n \frac{(y_i^{exp} - y_i^{sim}(\alpha))^2}{\sigma_i^2} \quad (4.9)$$

where n is the number of bins, y_i^{exp} is the experimental number of events in bin i , $y_i^{sim}(\alpha)$ is the simulated number of events in bin i as a function of the parameter set α , and σ_i is the error of y_i^{exp} , which is taken to be the square root of y_i^{exp} . This test statistic was used for minimization of parameters and error estimation. This test statistic is commonly referred to as χ^2 , so for consistency, that is how it will be referenced throughout the document.

For each comparison of data to simulation, the parameter set α was varied until χ^2 was at a minimum. The least squares method assumes a Gaussian distribution of events within each bin, which cannot be assumed when the number of events in a bin is small. The inclusion of bins with very few events could also skew the minimization to place more importance on those events. To reduce this effect, only bins with more than 5 events were included in any fitting procedure. It is also possible to use this statistic to test many histograms at once, by simply expanding the sum to include bins from different histograms.

This test statistic also provides us with a way to estimate the statistical error in the parameter minimization. The most common way to determine a 1σ statistical uncertainty is by taking the values of α_j at which $\chi^2 = \chi_{min}^2 + 1$. This assumes that the χ^2 vs. α_j plot is parabolic in shape. Although the data is not always the perfect linear situation that generated this definition for the 1σ limit, for consistency with comparison to other data, this method has been used here to estimate the statistical uncertainty. The minimum of each χ^2 vs. α_j plot was fit with a parabola and limits corresponding to $\chi^2 + 1$ were extracted.

When multiple parameters were simultaneously minimized (say, α_0 and α_1), then each point in the χ^2 plot was constructed by fixing α_0 and varying all other parameters ($\alpha_1, \alpha_2, \dots$) until a minimum was found. This was repeated for multiple values of α_0 .

During the analysis, it was necessary to fit the same data set with different models. In this case, a reduced test statistic was used to compare models with different numbers of parameters. A reduced test statistic was constructed by dividing the original statistic, χ^2 , by the number of degrees of freedom. Here, the number of degrees of freedom was defined as the number of bins participating in the fit less the number of parameters in the set α . This comparison of reduced χ^2 was used to select a preferred model.

In addition to the statistical uncertainty in the measured values, the systematic error was established by varying potential sources of error within reasonable limits and re-fitting that new spectrum. Previous experience had shown that most sources of systematic error were primarily associated with the neutron measurements, so the following sources of experimental error were considered: MoNA-LISA global time offsets and measurements of MoNA-LISA detector positions. In addition, three values set in the simulation were also varied to fix a systematic error: the x -position resolution, the time-of-flight resolution, and the threshold set for light collection at the PMTs.

Some systematic error was also identified from fitting the entire χ^2 curve and not just choosing the parameter set with the lowest χ^2 . All three of the sources of systematic error in the simulation produced the same additional error for the ^{10}Li fit even though the histograms simulated with some error looked almost identical to those with no added error. The same systematic error measurement

was then generated by fitting a simulation with itself and determined to be due to the curve fitting, rather than either resolution or the threshold. This error is identified in the systematic error tables as “Error from fitting.”

Chapter 5

Results and Discussion

5.1 ^{11}Li

The three-body decay energy spectrum for the ^{11}Li system is shown in Figure 5.1. This spectrum uses the first two interactions in MoNA-LISA that pass a time-of-flight requirement and a charge threshold, as detailed in Section 4.2.4. These requirements, however, do not ensure that those first two interactions come from two different neutrons. Figure 5.1 has contamination from neutron scattering cross-talk: events in which a single neutron interacts in the detector, scatters, and then interacts again, creating two interaction sites from one neutron.

To eliminate this fake two-neutron signal and enhance the real two-neutron spectrum, a pair of requirements, known as causality cuts were applied to the data. The first requirement was placed on the velocity of a hypothetical neutron scattering from the first interaction site to the second (v_{12}). This velocity was compared to the velocity of the neutron that traveled from the target to the first interaction site (v_{01}). If $v_{12} < v_{01}$, then it is possible that the first two interactions were caused by the same neutron interacting twice. The first requirement, then, is that $v_{12} > v_{01}$. The second requirement was placed on the distance between the two interaction points. The probability that a second interaction was caused by the same neutron as the first decreases sharply with the distance between the interactions. In addition, the discretization in the y and z directions produces an uncertainty in the absolute position of ~ 10 cm, which corresponds to a large uncertainty in v_{12} . In contrast, the distribution of distances between interactions from two different neutrons is relatively flat. Figure 5.2 shows the number of real and fake two-neutron events that pass the causality cuts as a function of the distance used in the causality cut for a phase space decay from a 1.5 MeV state in ^{11}Li ($\Gamma = 2.0$). The cut was set at 50 cm for a combination of efficiency and purity. Though the efficacy of these causality cuts changes as a function of energy and decay mode, the events that make it through these causality cuts are approximately 90% real two-neutron events.

These causality cuts were applied to the three-body decay energy plot shown in Figure 5.1 and the resulting histogram is shown in Figure 5.3. The broad peak around 700 keV appears to be consistent with previous measurements, though the width appears larger than the measurements from Refs. [55, 62–64, 66, 67]. There is a suggestion of a state around 2.2 MeV decay energy, but the statistics are low.

Figure 5.4 shows the Jacobi plots for the ^{11}Li data below 1.6 MeV decay energy and with causality cuts applied. The most obvious feature is a peak near -1 of the Y-system $\cos\theta$ spectrum, indicating directional correlation of the two neutrons. This is supported by the asymmetric T-system energy ratio in the upper left panel. The lack of sharp peaks in either the Y-system energy ratio or the T-system angle suggest that the decay does not proceed sequentially through a narrow state in ^{10}Li .

To go beyond these initial qualitative conclusions requires comparison with the simulation. Figure 5.5 shows the potential decay paths through which an excited ^{11}Li nucleus could decay. It could decay sequentially through states in ^{10}Li (red, blue, green, and magenta), or it could decay

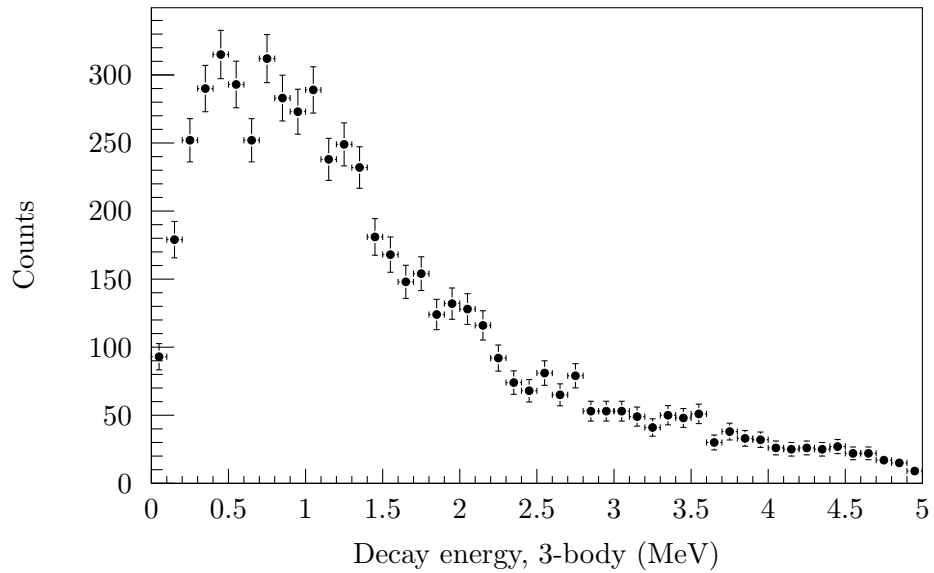


Figure 5.1: Decay energy for the ${}^9\text{Li}+n+n$ system. No causality cuts are applied.

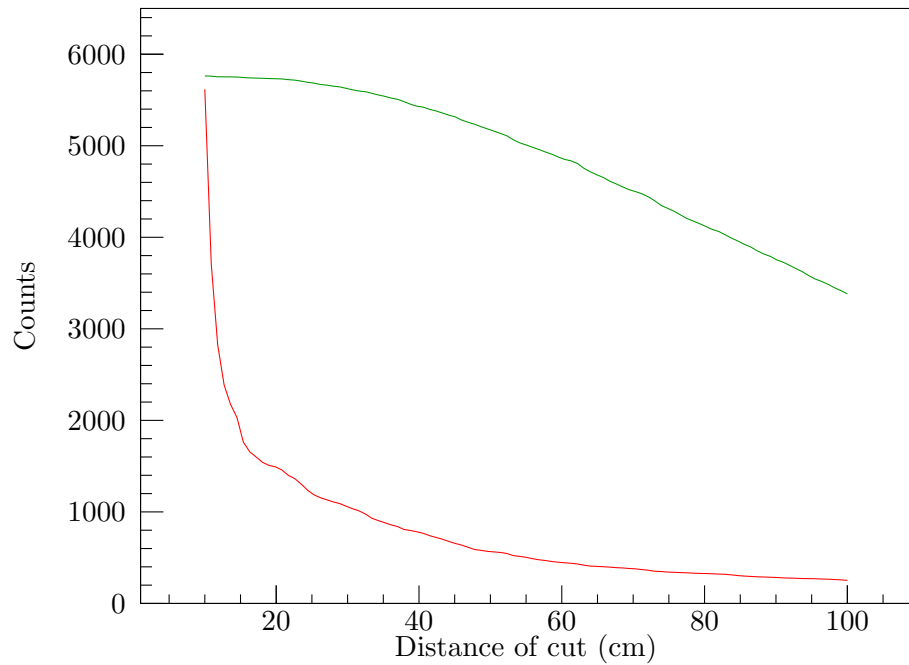


Figure 5.2: Number of real two neutron events (green, top line), and fake two neutron events (red, bottom line) that pass the causality cut as a function of the magnitude of the distance cut, based on a simulation of a phase space decay from ${}^{11}\text{Li}$.

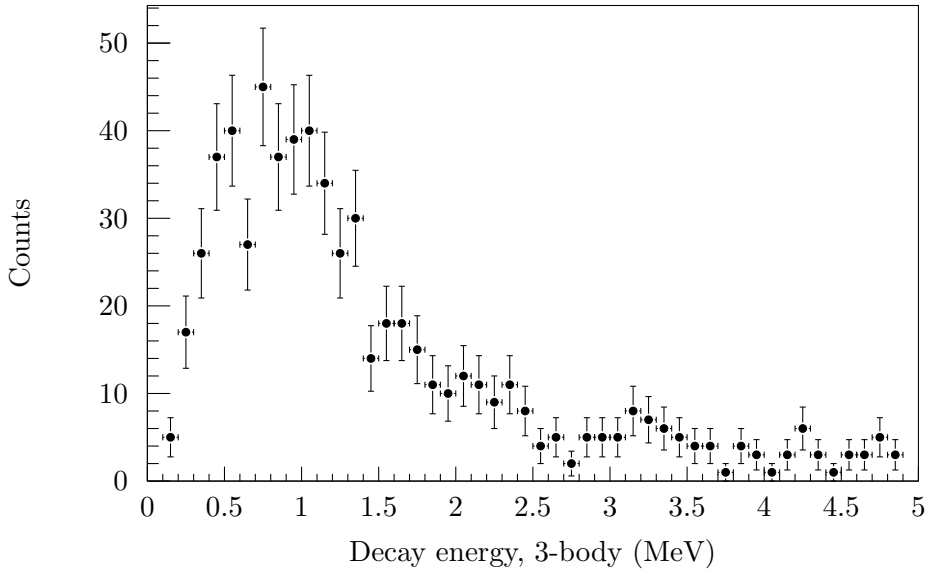


Figure 5.3: Decay energy for the ${}^9\text{Li}+n+n$ system. Causality cuts are applied.

in a three-body decay directly to ${}^9\text{Li}$ by emission of correlated neutrons (dineutron model, orange) or uncorrelated emission of neutrons (phase space or democratic model, cyan).

The qualitative analysis suggested that a dineutron model will fit best and that a sequential decay through a narrow state will not fit the Jacobi plots. There are four potential sequential decays through ${}^{10}\text{Li}$. According to Bocharov and Charity [31, 32], the energy difference between the initial and intermediate states needs to be greater than the width of that intermediate state for a sequential decay to be possible. Recent work from Egorova *et al.* set a more stringent limit with the observation of a “suppression of the sequential decay mechanism in favor of three-body democratic dynamics” at initial energies below twice the intermediate energy plus the intermediate width [47]. A decay through a low-lying $\ell = 1$ state in ${}^{10}\text{Li}$ at approximately 200 keV with a width of approximately 100 keV fits the description of a sequential decay and would produce sharp peaks in the Jacobi spectrum that are not seen in the data. This decay (represented by the blue line in Figure 5.5) is not considered. The lower-lying $\ell = 0$ ground state has a much larger width and remains in consideration.

The simulation should also include potential single neutron decays from direct population (via $2p1n$ -knockout) of ${}^{10}\text{Li}$. Those potential decays are shown in Figure 5.6. The gray dotted line indicates population of a higher-lying state in ${}^{10}\text{Li}$ and subsequent decay to the ground state of ${}^9\text{Li}$.

In addition to the two spectra seen in Figures 5.1 and 5.3, these two-neutron decay models were fit to two two-body decay energy spectra: one constructed with all events containing both a ${}^9\text{Li}$ fragment and an interaction in MoNA-LISA and another constructed with events containing a ${}^9\text{Li}$ fragment and *only one* interaction in MoNA-LISA. This second two-body decay energy spectrum enhances the signal due to one-neutron decay. All four decay energy spectra are shown together in Figure 5.7.

A fit was performed for each two-neutron decay path from ${}^{11}\text{Li}$. Each fit included a single decay path from ${}^{11}\text{Li}$ and all five one-neutron decay paths from ${}^{10}\text{Li}$. The energies and widths of the states were allowed to vary, as were the relative initial populations. In all the fits, the first three decay energy spectra were dominated by contributions from the one-neutron decays from ${}^{10}\text{Li}$, while the

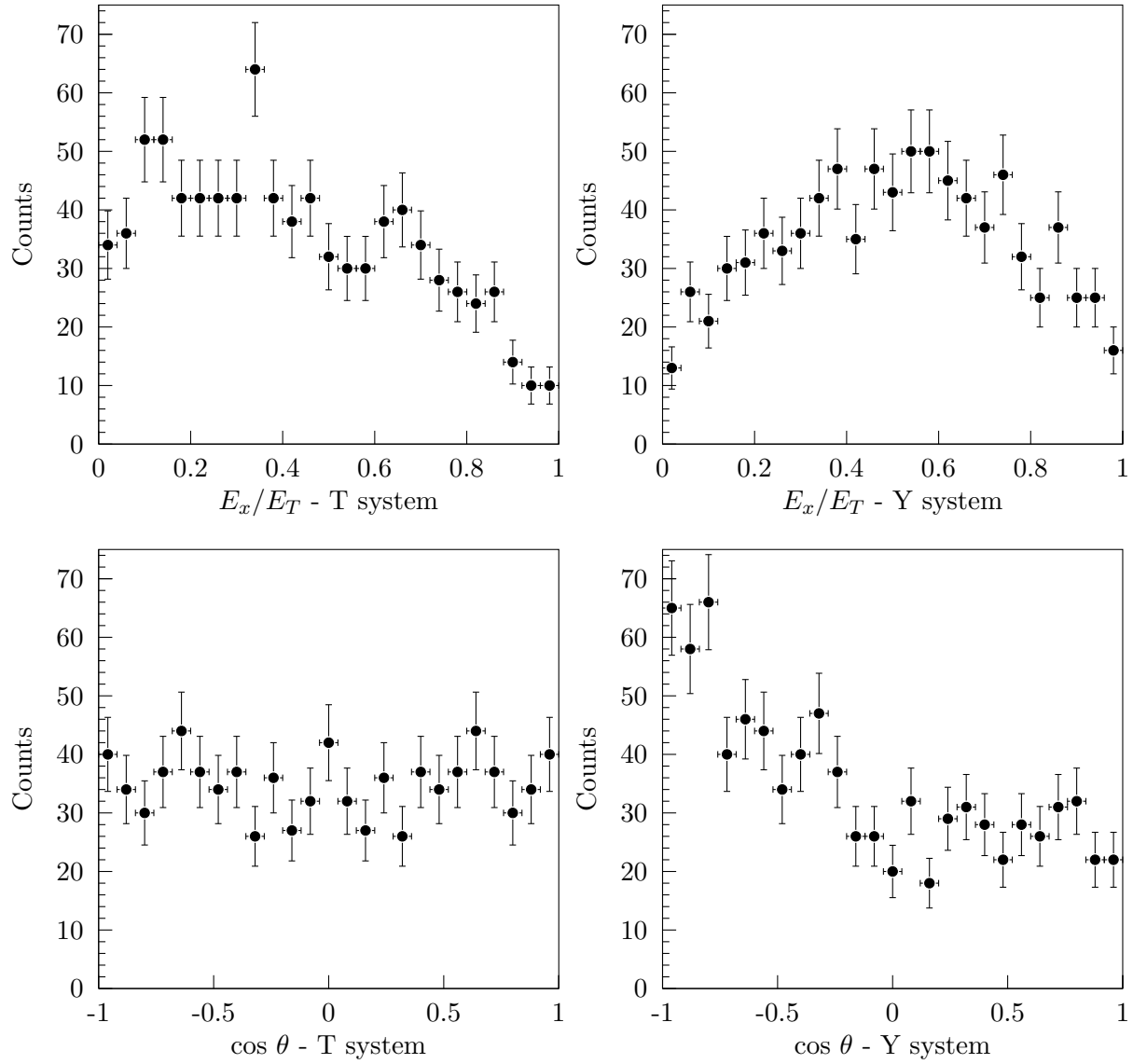


Figure 5.4: Jacobi plots for the ${}^9\text{Li}+n+n$ system. Causality cuts are applied, as well as a requirement that the total three-body decay energy be less than 1.6 MeV.

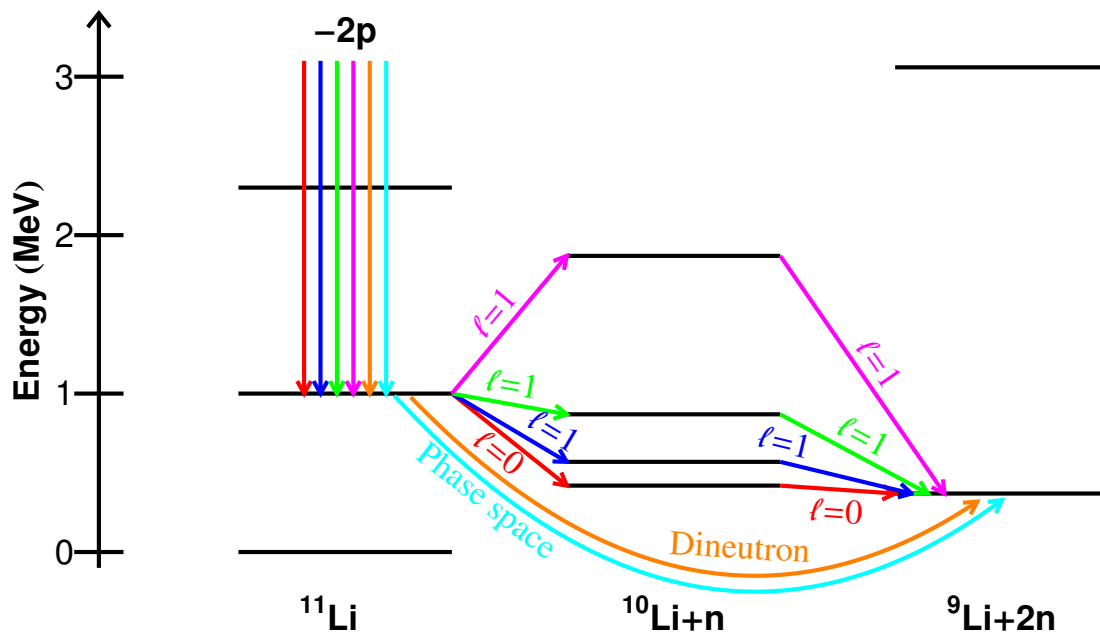


Figure 5.5: Possible decay paths from an ≈ 1 MeV state in ^{11}Li populated using a 2p knockout from the ^{13}B beam. The red, blue, green, and magenta decay paths go through intermediate states in ^{10}Li , while the orange and cyan decay paths explicitly bypass those states in favor of correlated (dineutron) or uncorrelated (phase space) two-neutron emission.

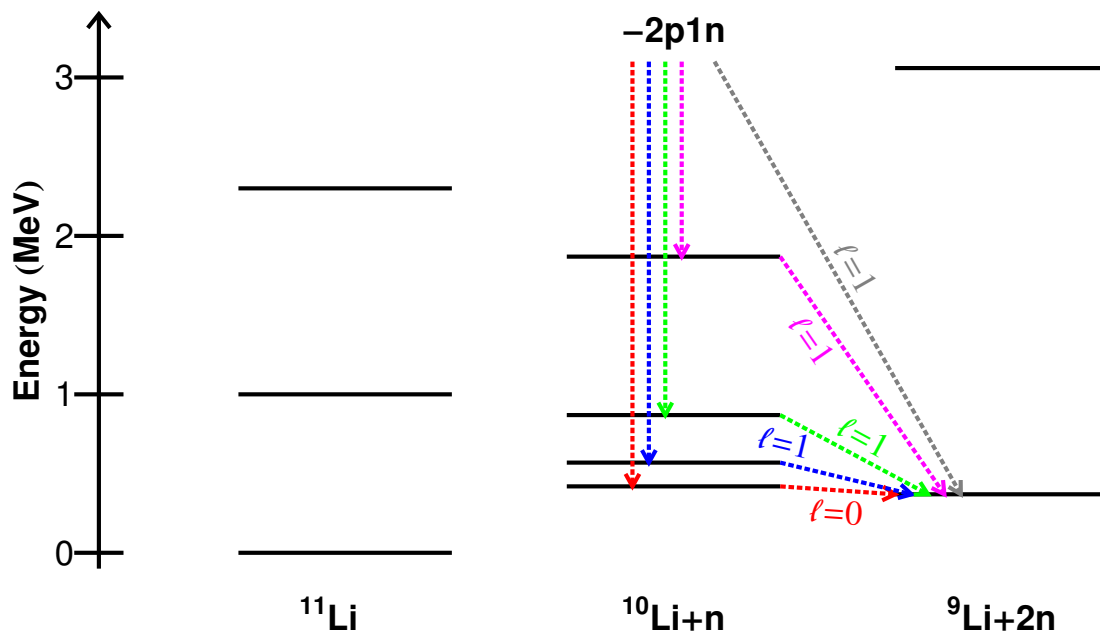


Figure 5.6: Possible decay paths from states in ^{10}Li populated using a 2p1n knockout from the ^{13}B beam. The gray path indicates population of and decay from a much higher-lying state.

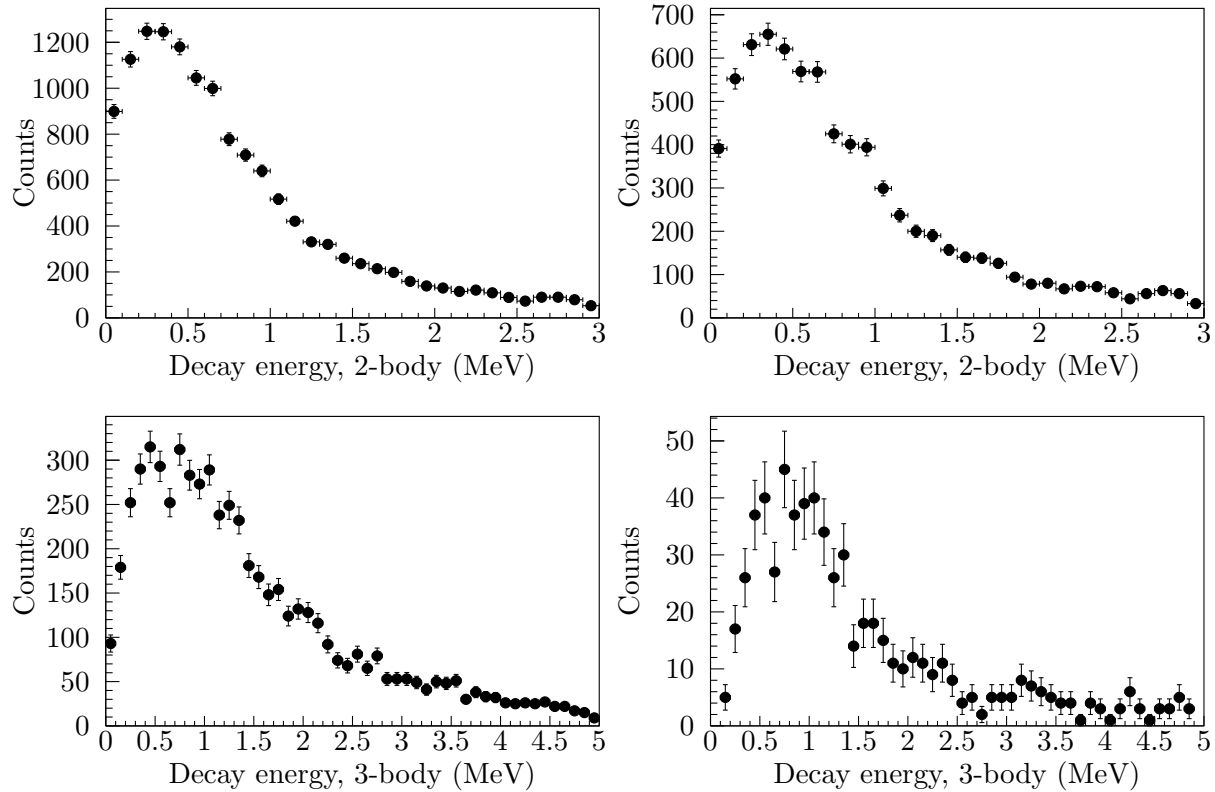


Figure 5.7: Decay energy plots used when fitting simulation to data. The upper left panel shows the two-body decay energy in coincidence with ${}^9\text{Li}$ and one neutron. The upper right panel shows the same two-body decay energy spectrum, but this time requiring only one interaction in MoNA-LISA. The lower left panel shows the three-body decay energy spectrum, as shown in Figure 5.1. The lower right panel shows the same three-body decay energy spectrum but with causality cuts, as shown in Figure 5.3.

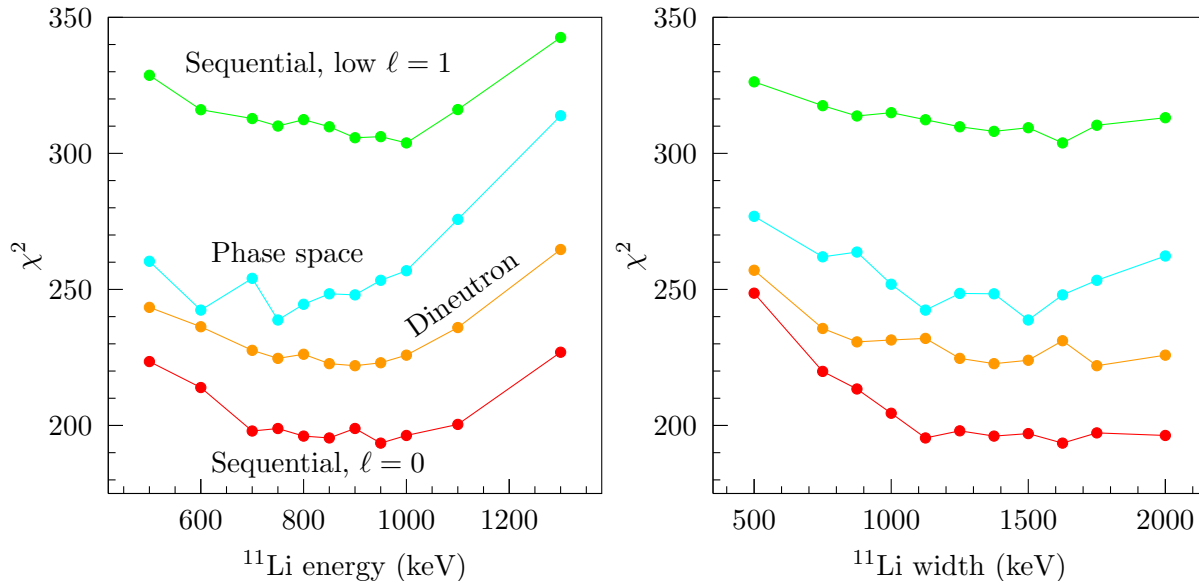


Figure 5.8: χ^2 minimization plots for the ^{11}Li energy (left) and width (right), for many different decay paths.

fourth, causality-gated spectrum was dominated by the two-neutron decay from ^{11}Li . The ratio of events between the different decay plots was best reproduced with a threshold of 1.0 MeVee for MoNA-LISA’s PMTs, rather than the initial setting of 0.6 MeVee. This generated an overall better fit as defined by χ^2 and did not influence the energy minimization.

Assuming a single decay path from a single unbound state in ^{11}Li allows another simplification. Decay through the highest-lying $\ell = 1$ state in ^{10}Li (shown as the magenta decay in Figure 5.6) is energetically unfavorable, but a decay through the tail of the state could occur if the state were wide enough. Regardless, given the other potential decay paths, it is unlikely to be the sole decay path and therefore has been removed from the analysis.

Two χ^2 minimization plots for the energy and width of the ^{11}Li state, broken down by decay path, are shown in Figure 5.8. In general, the minimization pushed the width to unphysical values, so the width was required to be less than or equal to twice the central energy value. The minimized energies and widths for each two-neutron decay model are shown in Table 5.1, along with statistical errors. Three of the models select consistent energies at 840 ± 70 , 860 ± 80 , and 890 ± 70 keV, while the phase space model minimizes at a lower energy of 750 ± 70 . The phase space decay path, while a good simple model for reference is considered an unphysical model. A phase space decay assumes no interactions between the decay products and there is a known neutron-neutron interaction. Eliminating the phase space result from consideration then shows that the measurements of the decay energy and width are insensitive to decay mode.

The model with the best fit to the decay energy spectra is a sequential decay through the $\ell = 0$ ground state of ^{10}Li , as suggested by Simon *et al.* [55]. The best fits from all four decay paths are shown in Figure 5.9. Although each fit is comprised of a single 2n decay and five 1n decays, only the summed spectra are shown for simplicity. The Jacobi spectra for each of these best fits is shown in Figure 5.10. As expected, the dineutron model fits the Jacobi spectra best. The dineutron lineshapes shown in Figures 5.9 and 5.10 were composed of one two neutron component from Figure

Table 5.1: Energies and widths for best fits of each two-neutron decay model. Error bars are only statistical.

Type of 2n decay	Decay energy (keV)	Width (keV)
Sequential, low $\ell = 1$	860 ± 80	>1300
Sequential, $\ell = 0$	890 ± 70	>1400
Phase space	750 ± 70	>1200
Dineutron	840 ± 70	>1400

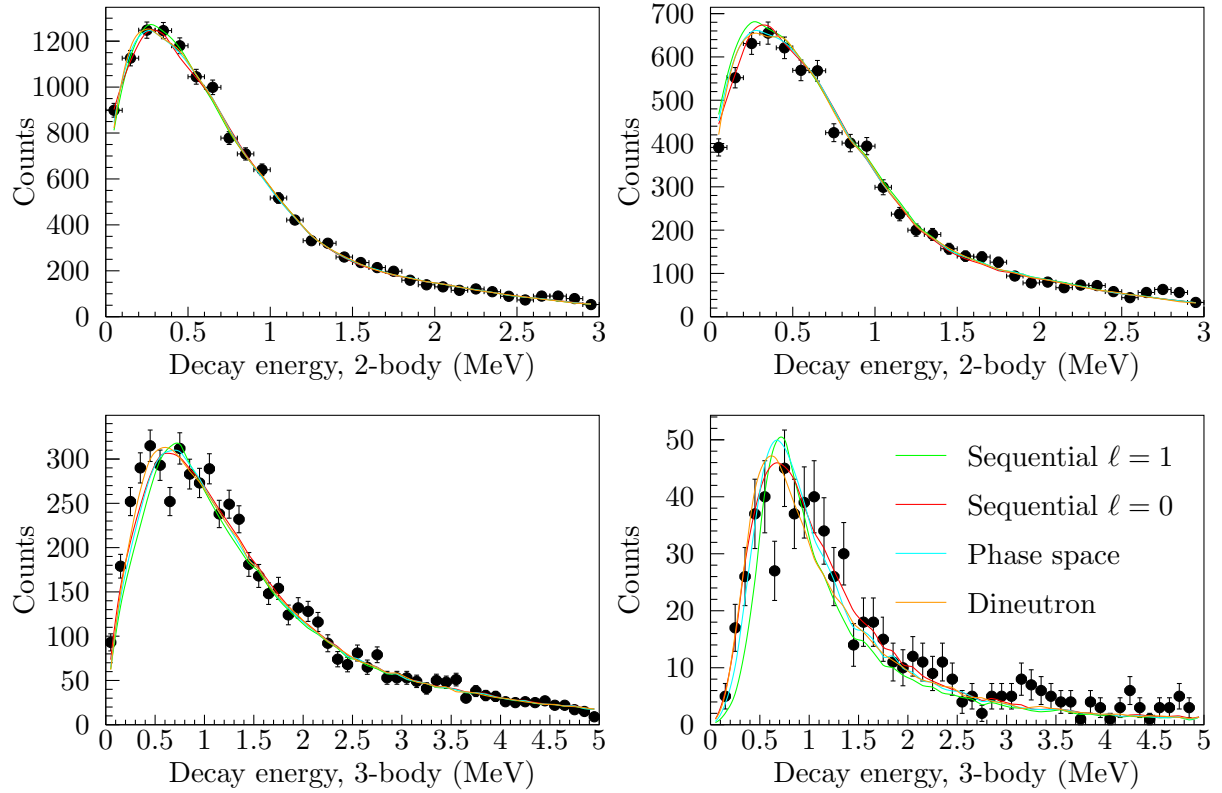


Figure 5.9: The best fits to the decay energy spectra from Figure 5.7 with all four decay models. The upper left panel shows the two-body decay energy in coincidence with ^9Li and one neutron. The upper right panel shows the same two-body decay energy spectrum, but this time requiring only one interaction in MoNA-LISA. The lower left panel shows the three-body decay energy spectrum. The lower right panel shows the same three-body decay energy spectrum but with causality cuts.

Table 5.2: Energies and widths used for the best dineutron fit shown in Figures 5.9 and 5.10. Decay through a ~ 200 keV $\ell = 1$ state, shown in Figure 5.5, was minimized at zero contribution to the total spectrum.

State	Decay energy (keV)	Width (keV)	Percent population	Color
$^{11}\text{Li}^*$	840	1600	9%	orange
^{10}Li $\ell = 0$ ground state	50	-	42%	red
^{10}Li $\ell = 1$ excited state	650	1000	18%	green
^{10}Li $\ell = 1$ excited state	1000	250	8%	magenta
^{10}Li $\ell = 1$ excited state	2250	1400	23%	gray

Table 5.3: Sources of systematic error in the ^{11}Li “dineutron” decay. Sources of error in the data are in the top section and sources of error in the simulation are in the second section. Here, MoNA-LISA is abbreviated with ML.

Source	Variance	Associated error	
		Energy (keV)	Width (keV)
ML global time offsets	± 0.2 ns	20	200
ML detector positions	± 2 cm	20	100
ML x-position resolution	3 ± 1 cm	10	-
ML time resolution	0.18 ± 0.05 ns	10	-
ML PMT threshold	$1.0^{+0.2}_{-0.4}$ MeVee	-	100
Error from fitting		-	200
Total systematic		30	300
Statistical		70	200
Total error		80	400

5.5 and all one neutron components from Figure 5.6. Those full lineshapes broken down into 2n and 1n decay path components and displayed against the decay energy spectra in Figure 5.11 and against the Jacobi spectra in Figure 5.13. Dalitz plots for both data and simulation are compared in Figure 5.14.

The addition of systematic error (detailed in Table 5.3) increases the error margins so the final values are a decay energy of 840 ± 80 keV (corresponding to an excitation energy of 1210 ± 80 keV) and a width greater than 1200 keV. This measurement is compared to previous results in Figure 5.12. It is consistent with 6 of the 8 measurements under 1.5 MeV. Two of those six measurements are from experiments dominated by Coulomb excitation [63,64]. Coulomb excitation was concluded to be a direct excitation to the continuum, not a resonant excitation [64,77], so the two Coulomb excitation measurements are measurements of peak values of an excitation function rather than measurements of a resonant state.

The double charge exchange reaction from Kobayashi *et al.* is expected to primarily populate positive parity states via the E1 mechanism, whereas a two-proton knockout from the $3/2^-$ ground state of a ^{13}B beam would favor the population of negative parity states. In a Faddeev calculation of unbound states in ^{11}Li , Garrido *et al.* predicted thirteen states of varying parity below 1.6 MeV excitation energy [82], suggesting it is reasonable to populate opposite parity states near the same energy. The width of the unbound state seems large compared to previous results and the calculations by Garrido *et al.*. Given the many potential states in that region and the general lack of understanding of the unbound structure, there is also the possibility that multiple states were

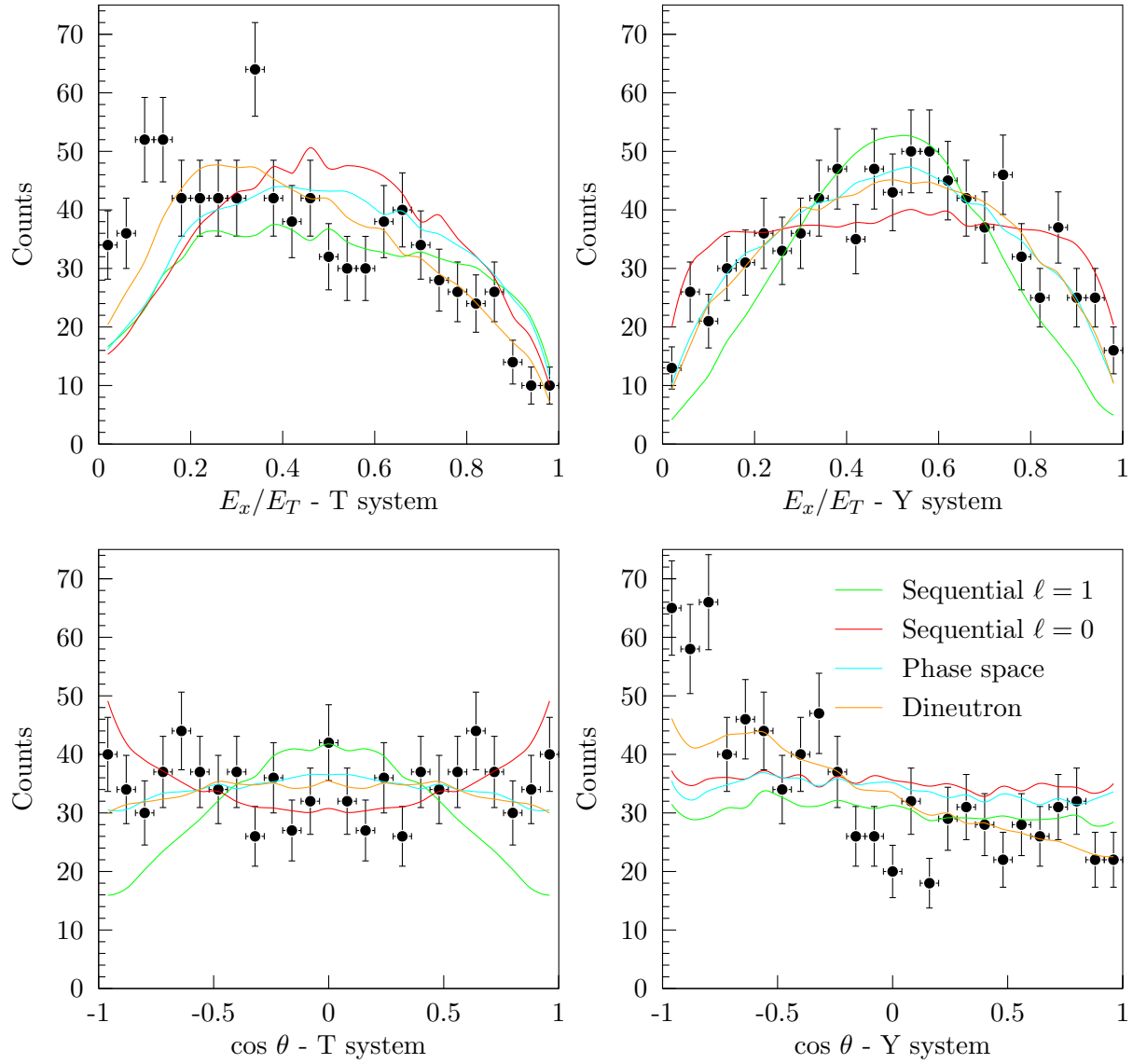


Figure 5.10: The Jacobi coordinate spectra (as shown in Figure 5.4) compared to the same spectra from the best fits of the four decay models.

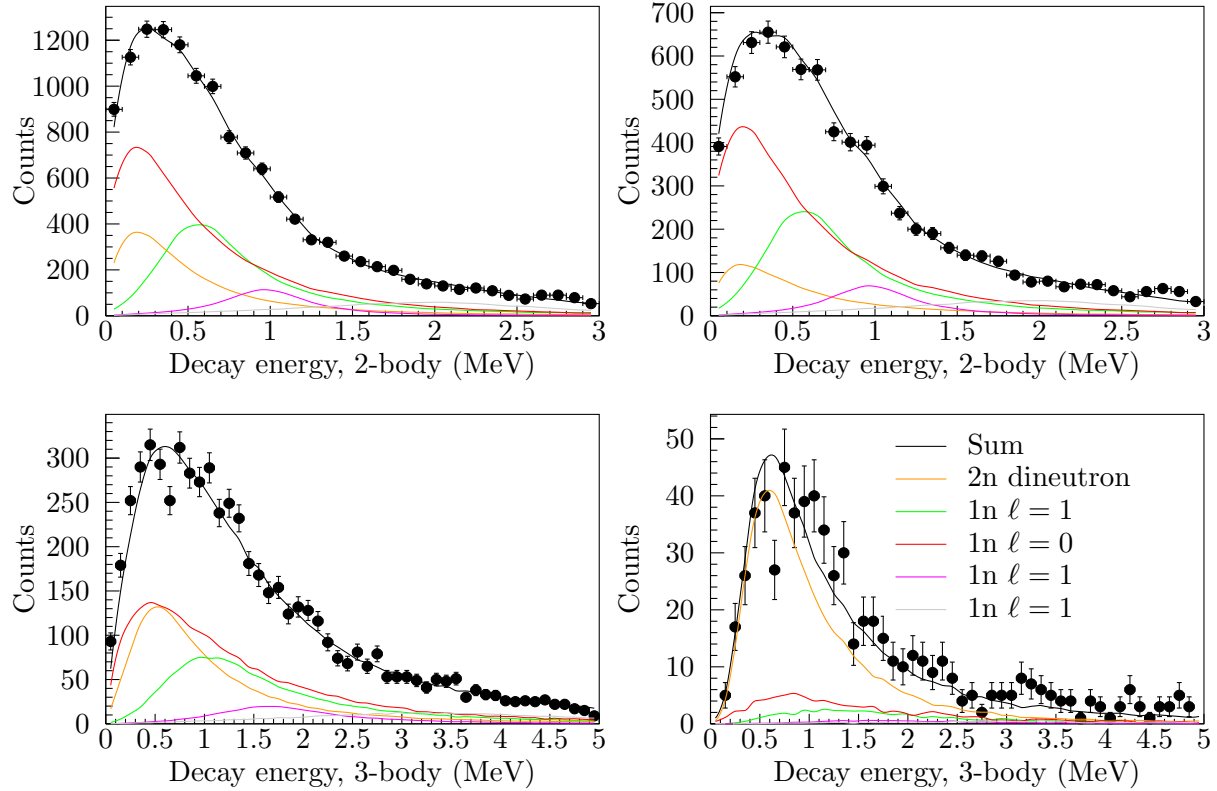


Figure 5.11: The best fit to the decay energy spectra of Figure 5.7 with the dineutron model. Different colored curves show the different components as labeled in Figures 5.5 and 5.6. The black line shows the summed total. The upper left panel shows the two-body decay energy in coincidence with ${}^9\text{Li}$ and one neutron. The upper right panel shows the same two-body decay energy spectrum, but this time requiring only one interaction in MoNA-LISA. The lower left panel shows the three-body decay energy spectrum. The lower right panel shows the same three-body decay energy spectrum but with causality cuts.

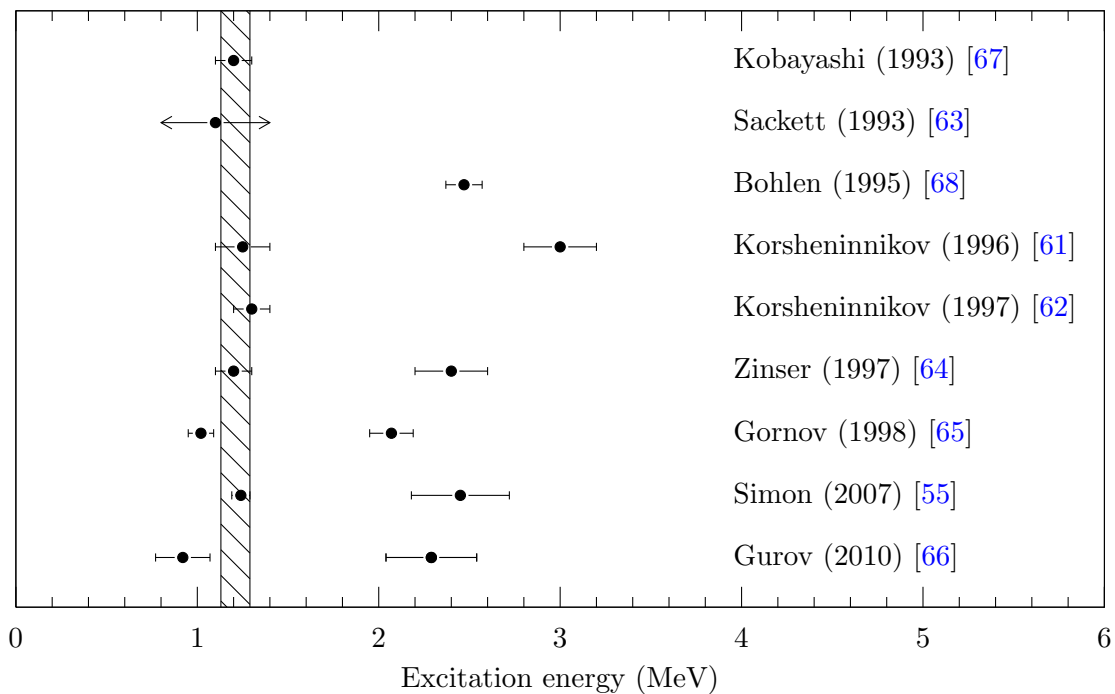


Figure 5.12: Previous measurements of ^{11}Li with excitation energies less than 3.5 MeV. The result from this work is shown by the box.

populated.

The population percentages in Table 5.2 show that approximately 10% of the events came from decay of an excited state of ^{11}Li while 90% came from unbound states in ^{10}Li directly populated via 2p1n knockout. A two proton knockout from ^{13}B in a $0s_{1/2}^2 0p_{3/2}^3$ configuration has ten different possible knockout pairs. Knocking out the paired $0p_{3/2}$ protons is most likely to populate the ground state and wouldn't show up in coincidence with ^9Li . Knocking out any of the deeply bound protons in the $0s_{1/2}$ orbital is likely to populate a high energy state in ^{11}Li . At least one of the neutrons emitted from the decay will have a high kinetic energy and be less likely to interact with MoNA-LISA. This would make the observed event appear much more like a ^{10}Li decay. Two of the remaining nine possible knockout combinations (subtracting the one likely to go to the ground state) only knock out protons from the $0p_{3/2}$ orbital and would be available for populating low-lying excited states in ^{11}Li . The inclusion of real ^{10}Li decays from a 2p1n knockout make the measured 10% a reasonable number.

The dineutron model used here parametrizes the interaction between the two neutrons as an $\ell = 0$ decay with a -18.7 fm scattering length, a value that is based on the neutron-neutron scattering length measured by Gonzalez Trotter *et al.* [153]. The use of the -18.7 fm scattering length is consistent with a democratic or phase-space decay modified by a final-state interaction between the two neutrons. It is also important to note that both the data and the model indicate a directional correlation, a correlation in momentum-space. Neither necessarily implies a spatial correlation of the neutrons within the nucleus.

The $\cos\theta$ Jacobi spectrum in the Y-system suggests a slight additional correlation between the two neutrons may be evident in the data (Figure 5.13). As a test, the scattering length was changed

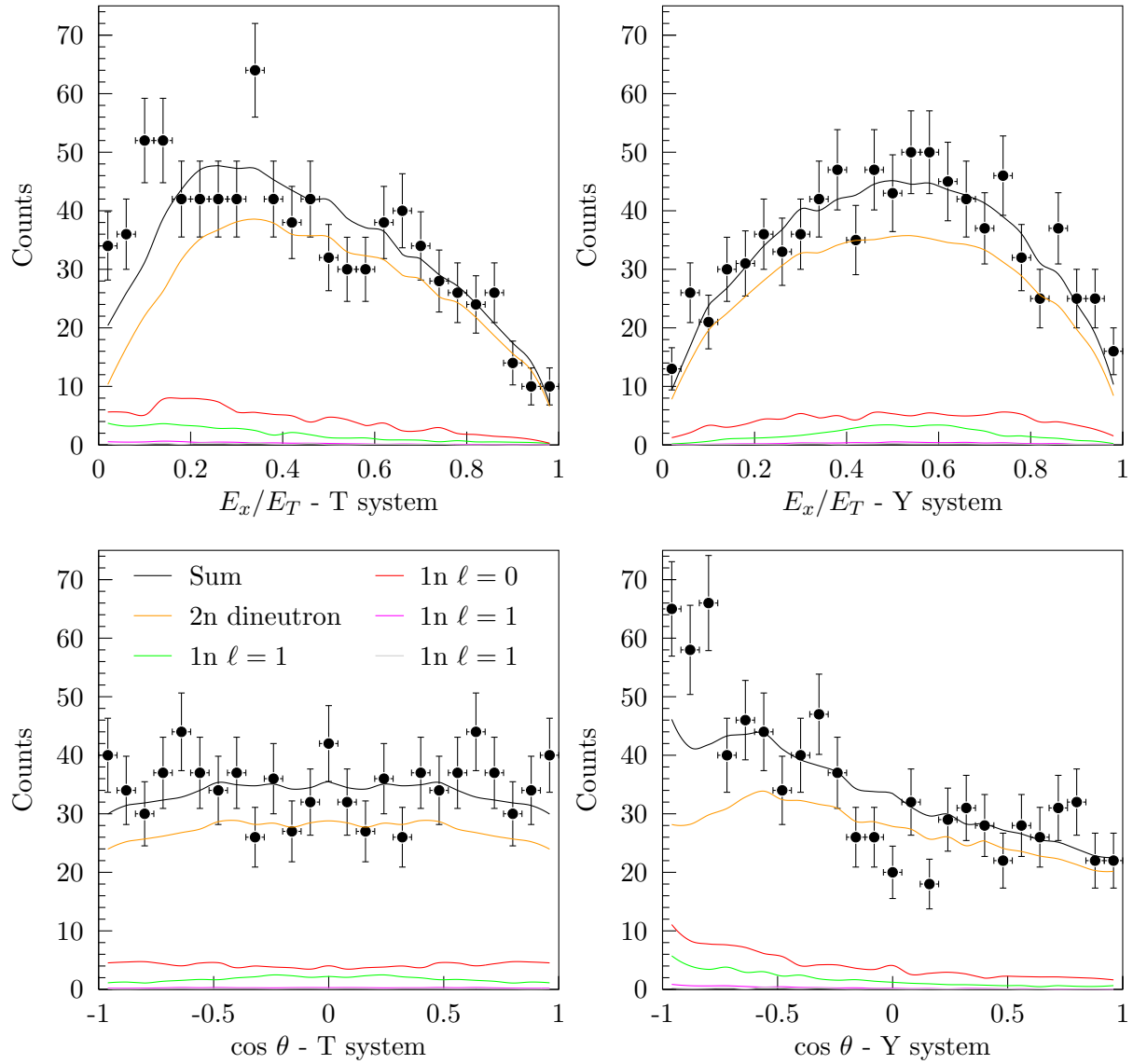


Figure 5.13: The Jacobi coordinate spectra (as shown in Figure 5.4) compared to the same spectra from the best fit from the dineutron model. Different colored curves show the different components as labeled in Figures 5.5 and 5.6. The black line shows the summed total.

Table 5.4: Best fit parameters as used in Figure 5.18. Quantities with error bars were measured. Other parameters, such as relative contribution and the width, are reported without error bars, simply for reference.

Color	Energy (MeV)	Width (MeV)	Percent population
Blue	0.11±0.04	0.2	13%
Green	0.5±0.1	0.8	55%
Magenta	1.1±0.1	1.0	32%

to -100 fm, increasing the directional correlation between the two neutrons. A comparison with the data and the -18.7 fm fit is shown in Figure 5.15. The simulation with increased correlation visually appears to be a better fit than the -18.7 fm simulation.

The two sequential decays ($^{11}\text{Li} \rightarrow ^9\text{Li} + 2n \rightarrow ^9\text{Li} + 2n$) used in the dineutron model of the simulation is a simplification of the physical process. A true calculation should track the neutrons behavior from inside the nucleus all the way through the decay. The better fit of the -100 fm scattering length in this model suggests that the data require an additional correlation beyond the final state interaction parametrized by the -18.7 fm scattering length. This correlation must come from some interaction inside the nucleus, but any discussion of the source or behavior of this correlation based on this data and model would be pure speculation.

There was no gamma-ray detection used in this experiment, so though we assume decay to the ground state of ^9Li , it is possible that the decay was to an excited state in ^9Li . A previous proton knockout from Chartier *et al.*, however, found that a single proton knockout from ^{11}Be to unbound ^{10}Li decayed to the first excited state of ^9Li only 7% of the time. This, combined with comparison to previous results, makes decay to the excited states of ^9Li unlikely.

5.2 ^{10}Li

Like ^{11}Li , ^{10}Li was populated from a two-proton knockout, this time from a ^{12}B beam. The two-body decay energy in coincidence with ^9Li is shown in Figure 5.16. A peak is visible around 500 keV and its full-width at half-maximum is approximately 800 keV. There is also some evidence of a shoulder around 1 MeV.

The two-proton knockout reaction is expected to selectively populate positive parity states in ^{10}Li . The 1^+ ground state of the ^{12}B beam has its three valence protons located primarily in the $p_{3/2}$ orbital. The odd proton couples with the odd neutron in the $p_{1/2}$ orbital. The two protons should principally be knocked out as a pair, which will selectively populate positive parity states. Any low-lying states will then decay by an $\ell = 1$ neutron to the $3/2^-$ ground state of ^9Li . This allows for the identification of any low-lying $\ell = 1$ states without significant background and without the broad $\ell = 0$ ground state component obscuring the identification.

The peak around 500 keV is consistent with the previous measurements shown in Figure 1.11. Most of those measurements, however, measured a width of <500 keV, in contrast with the wide peak seen in Figure 5.16. Using those measurements as a reference, the decay energy spectrum was fit with a single $\ell = 1$ decay lineshape whose central energy was constrained between 450 and 650 keV. When the width of this resonance was unconstrained, the minimization procedure pushed the width to unphysical values. To avoid this, the width was required to be less than or equal to twice the central energy. With this requirement applied, the best fit of a single $\ell = 1$ decay to the decay energy spectrum is shown in Figure 5.17.

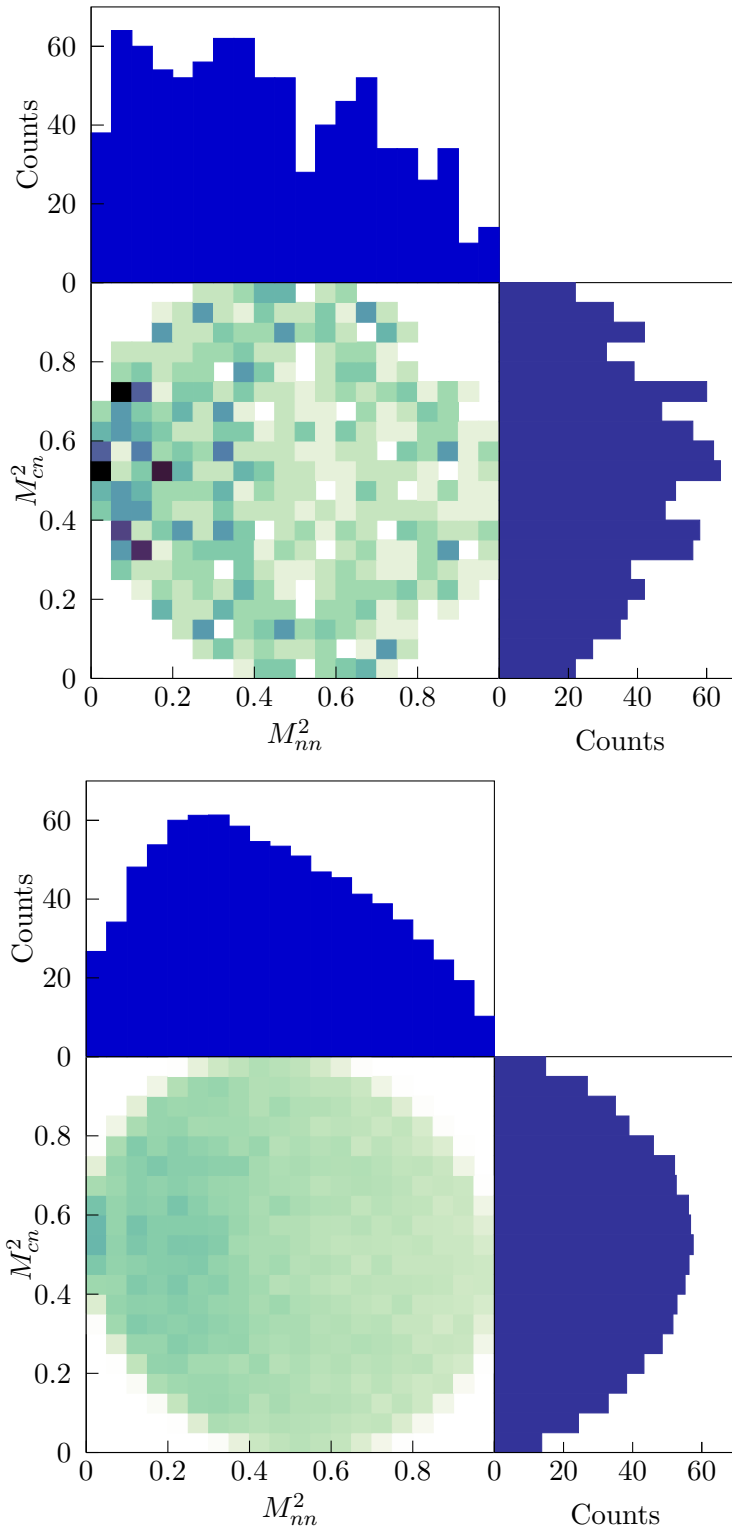


Figure 5.14: Dalitz plots for ^{11}Li . The top set is the data and the bottom set is the best fit simulation using the dineutron model. The data only uses events with a three-body decay energy less than 1.6 MeV that also passed the causality cuts.

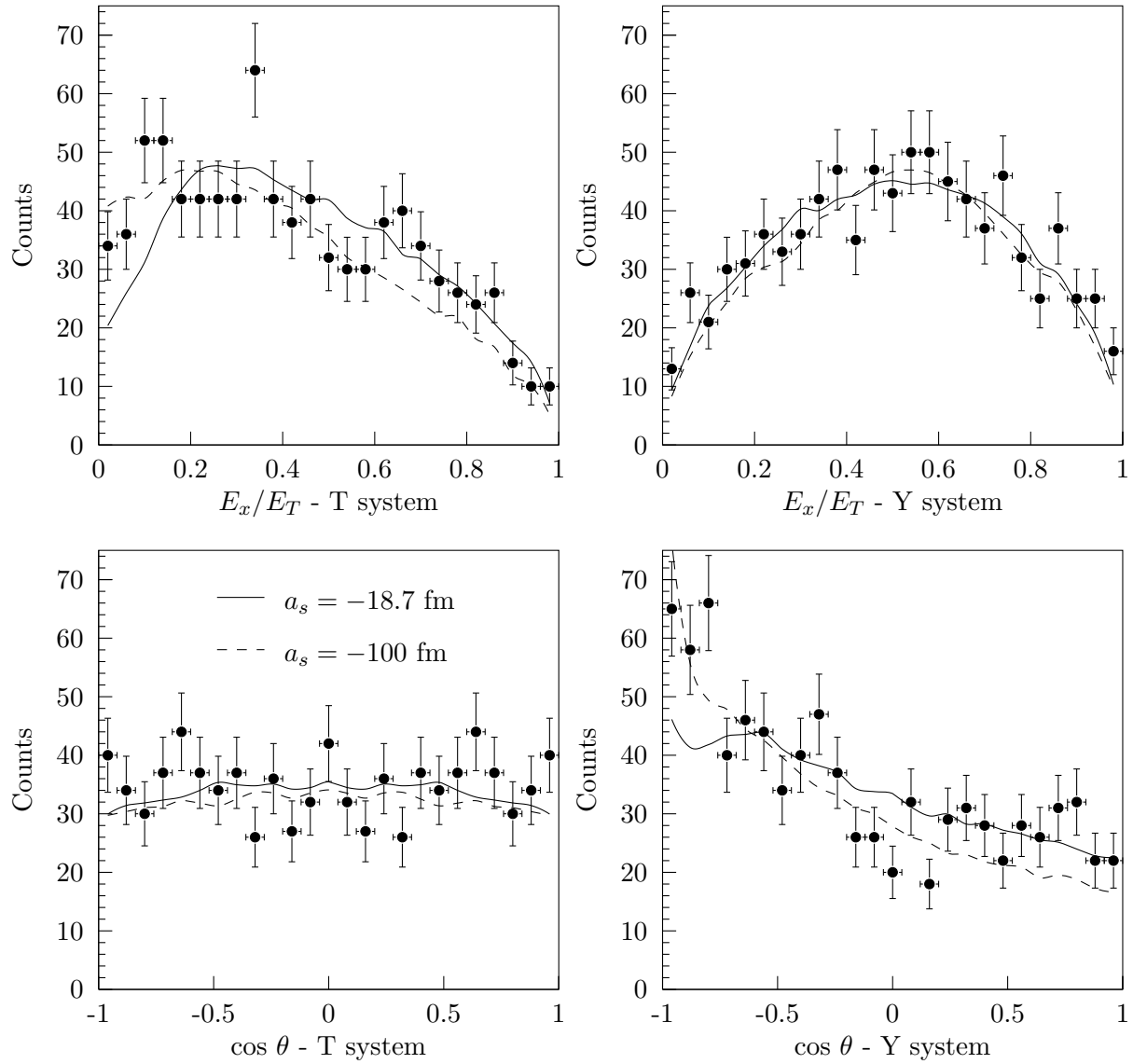


Figure 5.15: Two different dineutron models in comparison to the experimental data. The solid line simulation used a scattering length of -18.7 fm while the dashed line simulation used a scattering length of -100 fm, implying stronger correlation.

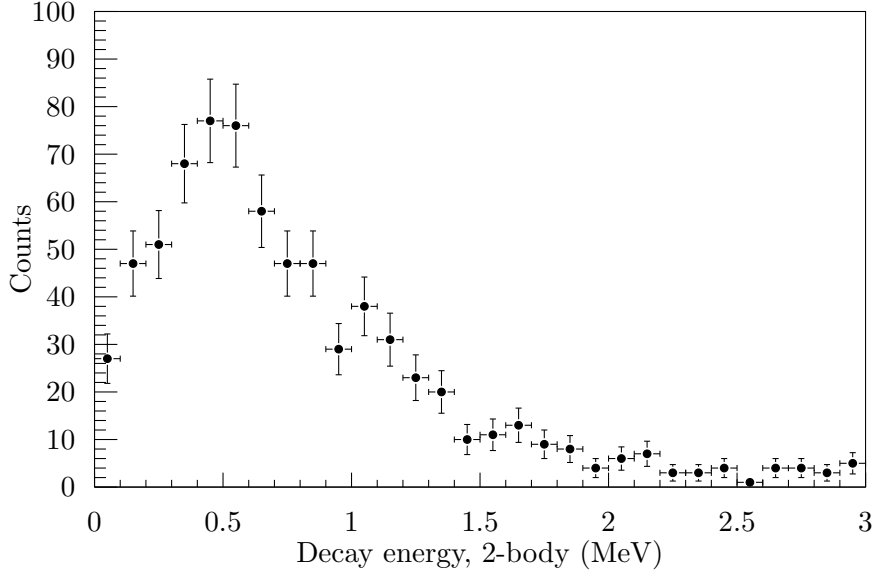


Figure 5.16: Decay energy in coincidence with ${}^9\text{Li}$ and one neutron, populated by two-proton knockout from a ${}^{12}\text{B}$ beam.

The residual shown in the lower panel of Figure 5.17 indicates that the fit underpredicts the lowest portion of the spectrum (<300 keV) and the shoulder area around 1 MeV. Including a single additional resonance could not fit both of those areas, so a fit with three $\ell = 1$ decays was performed and is shown in Figure 5.18. The best fit utilized resonances at 110 ± 50 keV (blue), 500 ± 100 keV (green), and 1100 ± 100 keV (magenta). The widths and relative populations of the fit shown in Figure 5.18 are shown in Table 5.4. The details of the systematic error are shown in Table 5.5.

The χ^2 plots for the lower two resonances are shown in Figure 5.19 and the values measured in this work have been superimposed on a summary of previous measurements in Figure 5.20. The resonance measured at 0.5 MeV is consistent with 10 previous measurements, whereas the resonance at 0.11 MeV is consistent only with the measurement from Santi *et al.*. Near that energy Young *et al.* fit a low-lying resonance with an $\ell = 0$ lineshape but “could be a p wave or an s wave” [94] and Zinser *et al.* fit another resonance with an $\ell = 1$ lineshape but stated that it was probably an

Table 5.5: Sources of systematic error in the ${}^{10}\text{Li}$ decay. Sources of error in the data are in the top section. The sources of error from the simulation tabulated in Table 5.3 (ML position resolution, ML time resolution, and ML PMT threshold) were all dominated by the error from the fitting. Here, MoNA-LISA is abbreviated as ML.

Source	Variance	Associated error in energy		
		Blue (keV)	Green (keV)	Magenta (keV)
ML global time offsets	± 0.2 ns	20	10	10
ML detector positions	± 2 cm	20	80	50
Error from fitting		10	20	-
Total systematic		30	80	50
Statistical		30	60	100
Total error		40	100	100

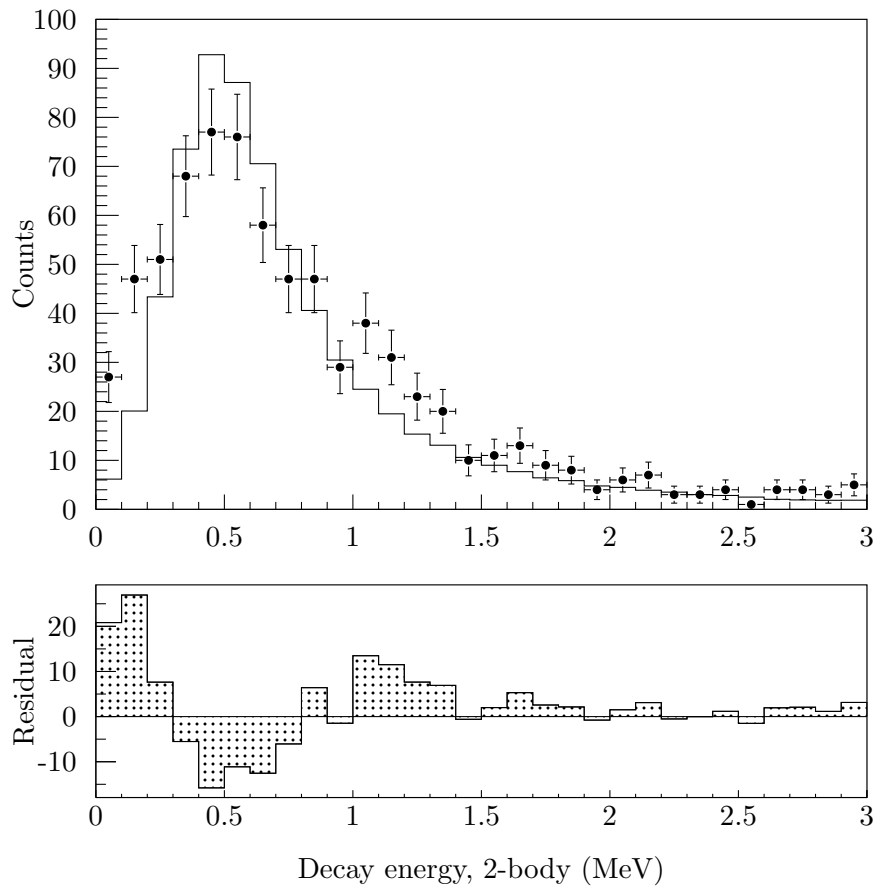


Figure 5.17: A fit of a single $\ell = 1$ decay energy lineshape to the data from Figure 5.16 (top) and the residual (bottom).

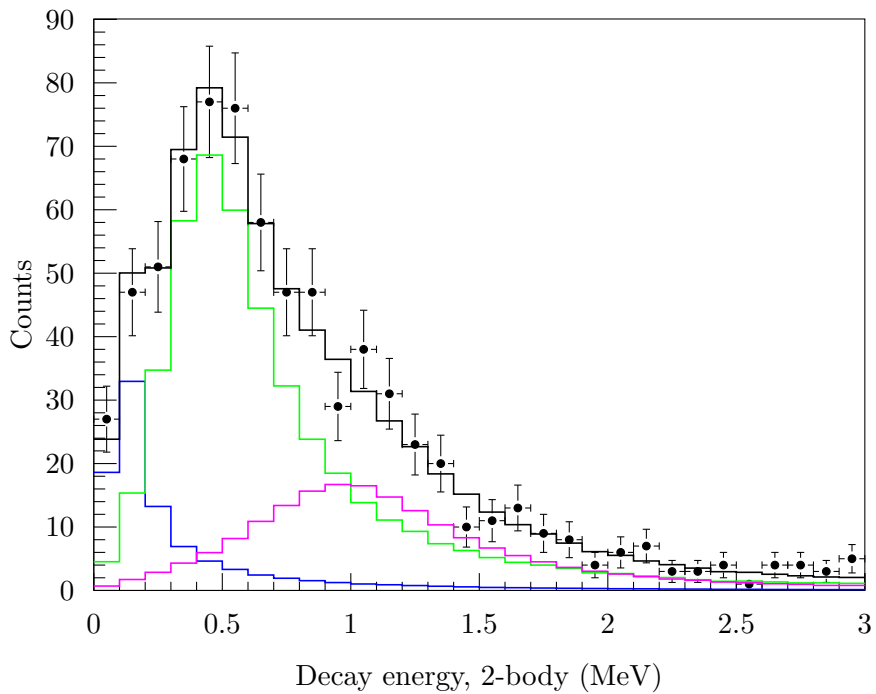


Figure 5.18: A fit of three $\ell = 1$ decay energy lineshapes to the data from Figure 5.16.

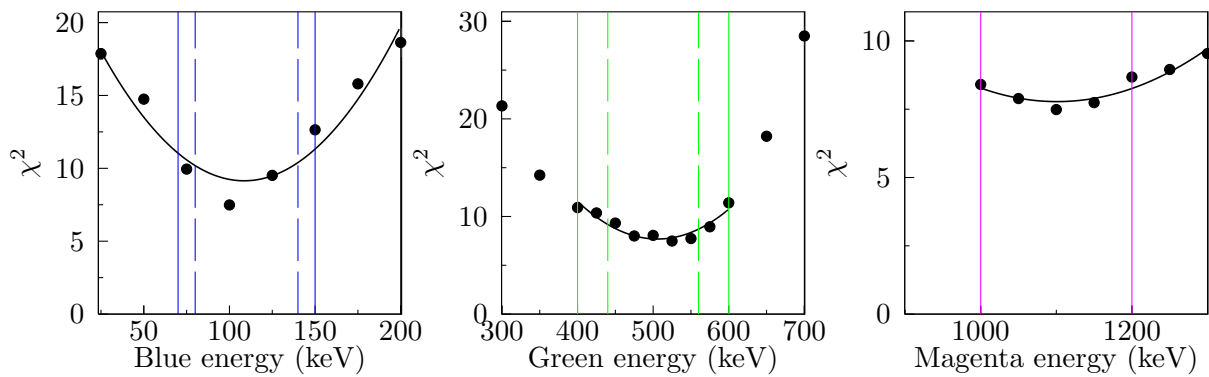


Figure 5.19: χ^2 plots that show the minimization of the central energies of the blue, green, and magenta lineshapes in Figure 5.18. Dashed lines indicate statistical error and solid lines indicate the total error margin.

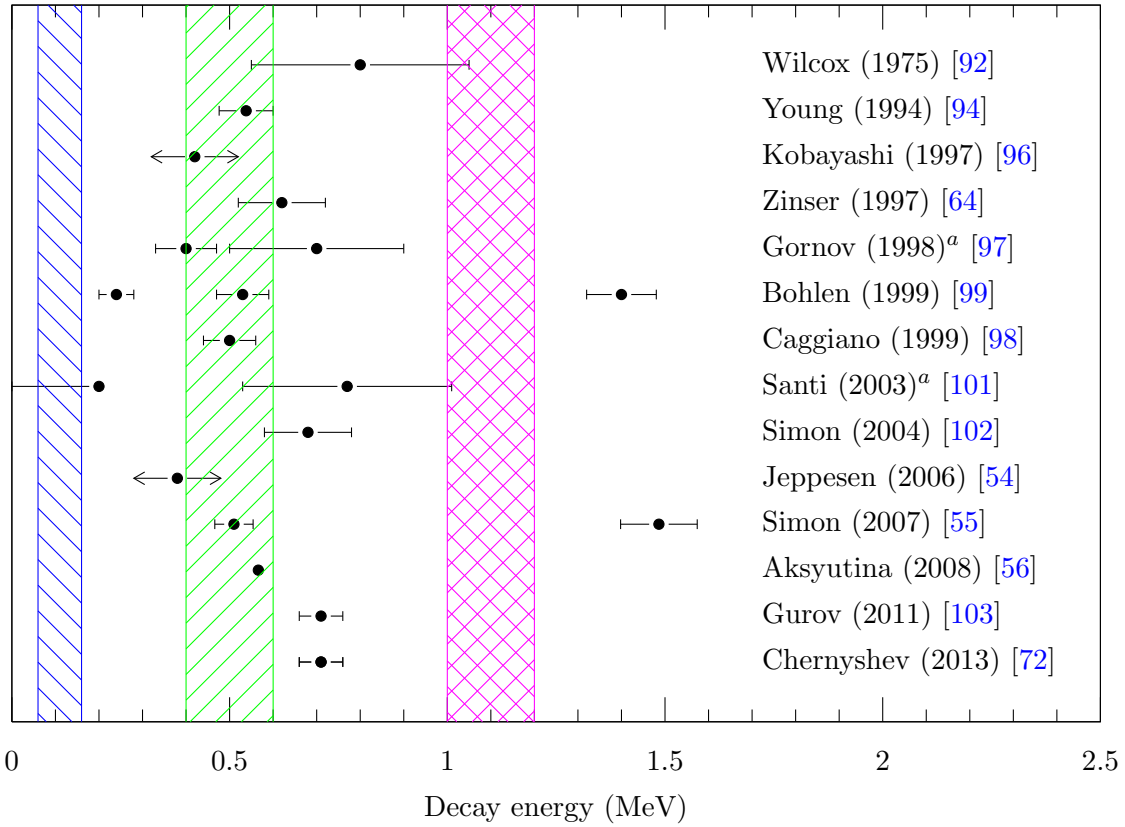


Figure 5.20: Previous measurements of unbound, $\ell = 1$ states in ^{10}Li (same as Figure 1.11) with the limits of the new measurements overlaid in blue, green, and magenta lines. Measurements reported without error have arrows for error bars. Two different measurements in Chernyshev’s 2013 paper produced two different measurements of 0.7 ± 0.05 and 0.78 ± 0.15 MeV, here the weighted average is used [72].

^aBoth Gornov’s 1998 paper [97] and Santi’s 2003 paper [101] found two possible fits for the data. Details are in Table 1.2 and footnotes within.

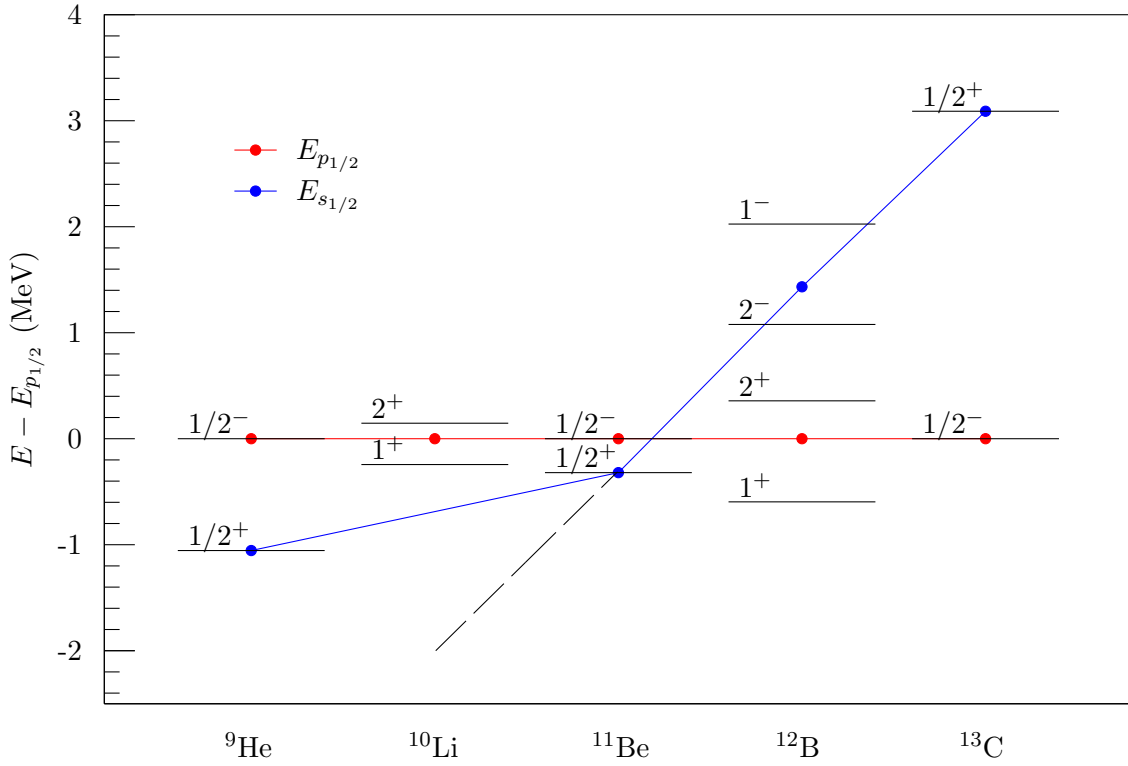


Figure 5.21: Calculations of $0p_{1/2}$ (red) and $1s_{1/2}$ single-particle levels of ^{10}Li , ^{11}Be , ^{12}B , and ^{13}C . Energies of single-particle levels and relevant energy eigenstates are given relative to the calculated $0p_{1/2}$ single particle energy level. Dashed line shows the extrapolation of the linear fit to the $1s_{1/2}$ single-particle levels. ^9He levels are from Ref. [155], ^{10}Li levels are from this work, ^{11}Be and ^{12}B levels are from Ref. [156], and ^{13}C levels are from Ref. [157].

$\ell = 0$ resonance, due to the slope of the lowest three data points [64].

The two lowest-lying positive parity states in ^{10}Li are likely the 1^+ , 2^+ doublet from the coupling of the single $0p_{3/2}$ proton with a neutron in the $0p_{1/2}$ state. Within the doublet, the strong Nordheim rule [154] predicts the 1^+ state to have a lower energy than the 2^+ state. This assignment is consistent with that of Bohlen *et al.* [99], but the energy measured here is approximately 0.1 MeV lower than in that work. Similarly, the two lowest-lying negative parity states in ^{10}Li are expected to be 2^- and 1^- from the coupling of the $0p_{3/2}$ proton with the $1s_{1/2}$ neutron. The relative populations of these two states, shown in Table 5.4, is inconsistent with this assignment. The ground state of ^{12}B is 1^+ and two-proton knockout from there is expected to populate the 1^+ state with a higher cross-section than the 2^+ state. This measurement was not the primary focus of the experiment and therefore received limited beam time. More experimental data might resolve these two peaks and clear up any uncertainty.

Given those spin assignments, the $0p_{1/2}$ single particle energy can be calculated using the weighted average described by Talmi and Unna [15]:

$$E_{p_{1/2}} = \frac{\sum_J (2J+1) E_J}{\sum_J (2J+1)} \quad (5.1)$$

where J is summed over the states that results from pairing a $0p_{1/2}$ neutron with a $0p_{3/2}$ proton.

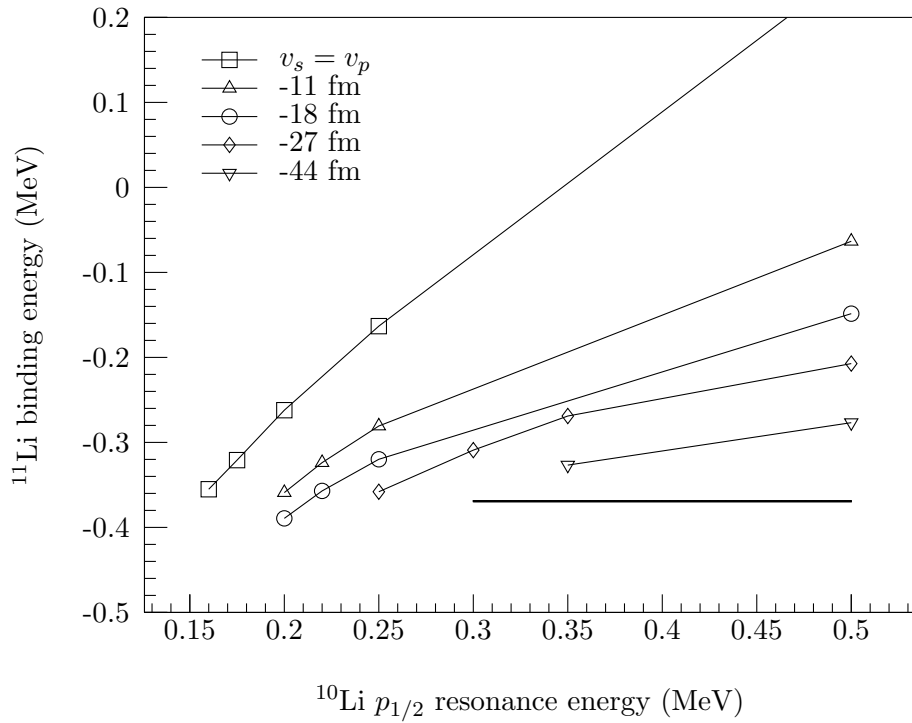


Figure 5.22: Calculations by Thompson and Zhukov show the relationship between the ^{11}Li binding energy and the $^{10}\text{Li } 0p_{1/2}$ single-particle energy as a function of the $1s_{1/2}$ scattering length [80]. The line at -0.369 MeV shows the limits imposed by the measurements of Smith *et al.* [51] and this thesis.

The same sum can be made for $E_{s_{1/2}}$. Talmi and Unna postulated that “the change in interaction energy of a $p_{1/2}$, or $s_{1/2}$, neutron when two $p_{3/2}$ protons are removed is twice the change due to the removal of one $p_{3/2}$ proton” [15]. Their paper extrapolated that linearity from measurements of ^{12}B and ^{13}C to ^{11}Be and predicted that the $1s_{1/2}$ level would be 0.21 MeV below the $0p_{1/2}$ level, only 0.11 MeV away from the measured 0.32 MeV level difference. When that same linearity is extrapolated out to ^{10}Li (Figure 5.21), it predicts a difference of 2 MeV between the $0p_{1/2}$ and $1s_{1/2}$ single-particle energies. Based on the measurements in this thesis, $E_{p_{1/2}} = 0.4 \pm 0.1$. Given the current understanding that at least one negative parity state lies below 0.05 MeV decay energy, this suggests that the second state would need to be at least 4 MeV lower than the currently known $\ell = 0$ ground state. This extrapolation would make ^{10}Li bound, which contradicts experimental evidence. Since the difference between the $0p_{1/2}$ and $1s_{1/2}$ orbitals would be greater in ^9He (where current measurements have it at approximately 1 MeV), the simple linear model presented by Talmi and Una is not appropriate for calculating the position of the $1s_{1/2}$ single-particle energy.

A Faddeev calculation by Thompson and Zhukov calculated the relationship between the ^{11}Li binding energy and the $0p_{1/2}$ single-particle energy in ^{10}Li [80] as a function of the $1s_{1/2}$ scattering length. Figure 1 from that paper has been redrawn here in Figure 5.22. The recent measurement of ^{11}Li at TITAN has placed stringent limits on the binding energy of ^{11}Li (369.15 ± 0.65 keV) [51]. That measurement and the weighted average of the two $\ell = 1$ states measured here constrain the box (that looks more like a line) shown in Figure 5.22. The location of the box indicates that the $1s_{1/2}$ virtual pole needs to be more negative than -44 fm, which means it needs to be lower than 10 keV. To keep the $1s_{1/2}$ weighted average below 10 keV requires that the highest-lying state of this negative parity doublet be below 27 keV. The currently known position of the $\ell = 0$ ground state is below 50 keV. If both the 2^- and the 1^- states are below 50 keV, it is unlikely they will be distinguished experimentally.

5.3 ^{12}Be

Unbound ^{12}Be was populated via a single-proton knockout from the ^{13}B beam. The two-body decay energy spectrum is shown in Figure 5.23. The spectrum is dominated by a Breit-Wigner-like peak around 1.2 MeV. Comparison with Figure 1.12 suggests that a state here is consistent with the energy of a previously measured state at 4580 ± 5 keV excitation energy [114].

Given the single-particle levels available to the valence neutrons in ^{12}Be , we expect the emitted neutron to have $\ell = 0, 1, 2$. The best fit with a single $\ell = 1$ resonance is shown in the left panel of Figure 5.24. A small background ($< 3\%$ population) was required to fit the small shoulder at low energies. The Maxwellian background used has a shape similar to the “decay energy” of a small amount of ^{12}Be contamination. The best-fit shown uses an energy of 1243 ± 20 keV and a width of 634 ± 50 keV. The χ^2 minimization curves for each of these parameters are shown in Figure 5.25 and a summary of the systematic error analysis is shown in Table 5.6. Neither an $\ell = 0$ or $\ell = 2$ lineshape (shown in Figure 5.26) fit the data equally well.

The two bound states in ^{11}Be allow for the possibility of decay to either the $1/2^+$ ground state or the $1/2^-$ excited state at 320 keV. Since no gamma detection was available for this experiment, there is no way to distinguish these two decays. The unbound state could be at 4412 ± 26 keV or at 4732 ± 26 keV excitation energy, depending on if it decayed to the ground or first excited state, respectively. If the previously measured 4580 ± 5 keV state were to decay to these states, it would decay with an energy of 1411 or 1091 keV, on either side of the measured 1243 ± 20 keV decay energy. To show the significance of this difference, two $\ell = 1$ lineshapes representing those two potential decay energies are shown in the right panel of Figure 5.24.

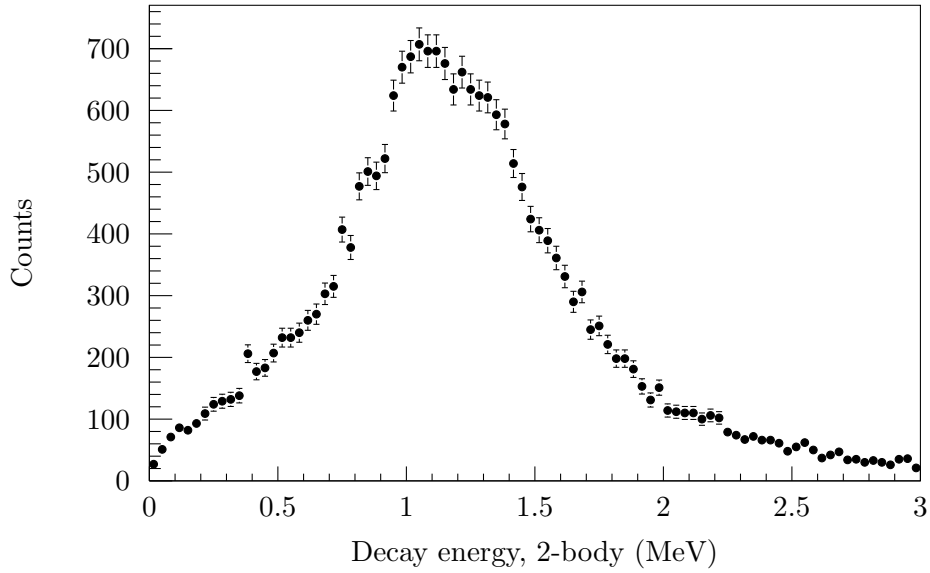


Figure 5.23: Decay energy of the $^{11}\text{Be}+n$ system after population of ^{12}Be via a two-proton knockout from a ^{13}B beam.

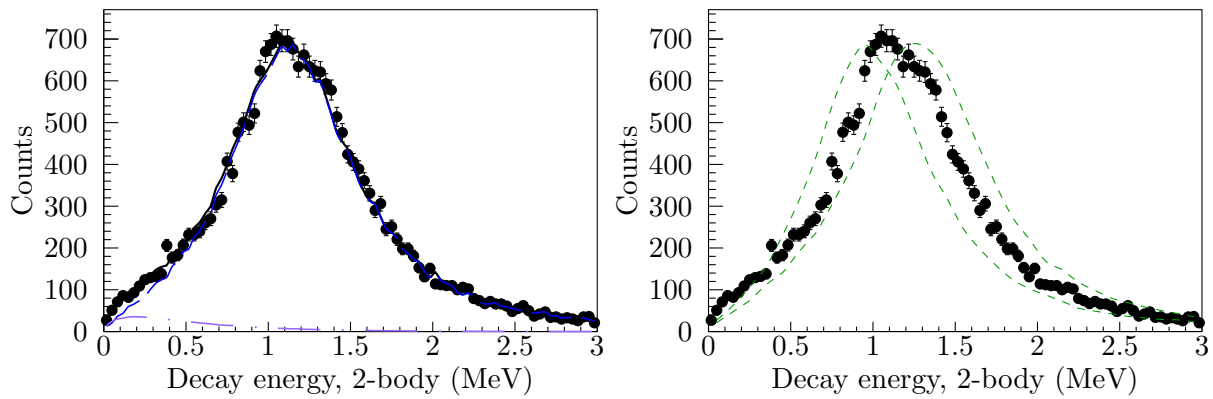


Figure 5.24: Different simulated lineshapes fitted or compared to the $^{11}\text{Be}+n$ decay energy lineshape shown in Figure 5.23. Left panel: data is fit with a single $\ell = 1$ resonant lineshape and a background. Right panel: data is compared to two lineshapes assuming total decay from a previously measured state at 4580 keV in ^{12}Be to the excited $1/2^-$ state in ^{11}Be (left lineshape) and to the $1/2^+$ ground state (right lineshape).

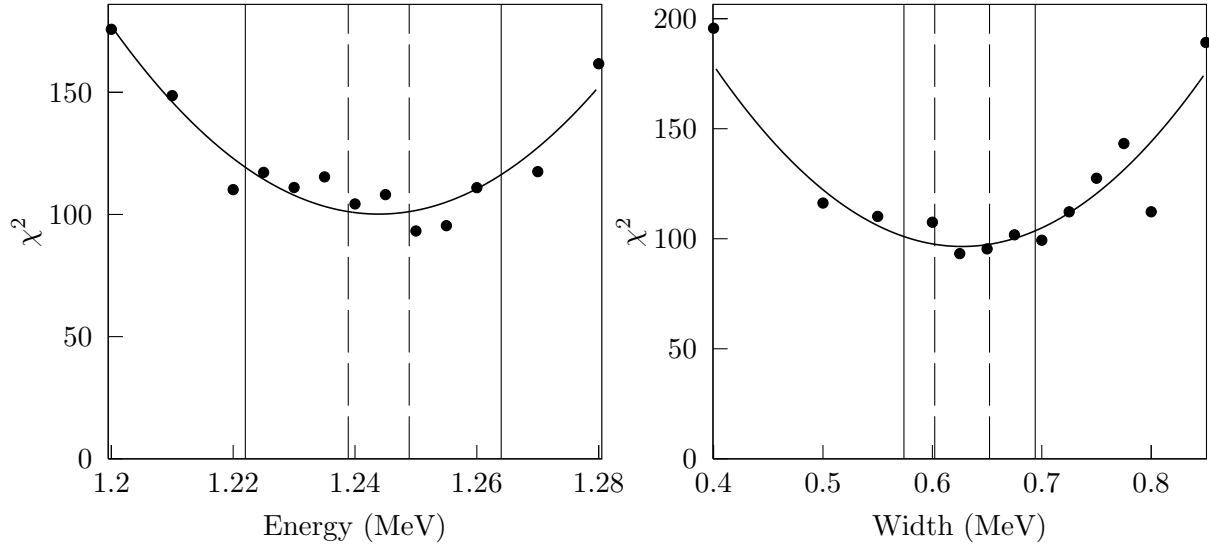


Figure 5.25: χ^2 plots for the energy (left) and width (right) of the single $\ell = 1$ decay fit to the data in the upper left panel of Figure 5.24. Dashed vertical lines show the statistical 1σ limits and the solid vertical lines indicate the additional systematic error.

Table 5.6: Sources of systematic error in the ^{12}Be decay. Sources of error in the data are in the top section and sources of error in the simulation are in the second section.

Source	Variance	Associated error	
		Energy (keV)	Width (keV)
MoNA-LISA global time offsets	± 0.2 ns	10	20
MoNA-LISA detector positions	± 2 cm	15	40
MoNA-LISA x-position resolution	3 ± 1 cm	5	13
MoNA-LISA time resolution	0.18 ± 0.05 ns	2	12
MoNA-LISA PMT threshold	$0.6^{+0.4}_{-0.15}$ MeVee	2	6
Error from fitting		2	4
Total systematic		20	50
Statistical		5	25
Total error		20	50

Table 5.7: Parameters for potential decays from positive and negative parity states in ^{12}Be , using $S_n = 3169 \pm 16$ keV [117].

	Positive	Negative
Decay energy (keV)	1243 ± 20	1243 ± 20
Multipolarity	$\ell = 1$	$\ell = 1$
Final state E^* (keV)	320	0
Final state J^π	$1/2^-$	$1/2^+$
$E^* - S_n$	1563 ± 20	1243 ± 20
E^*	4732 ± 26	4412 ± 26

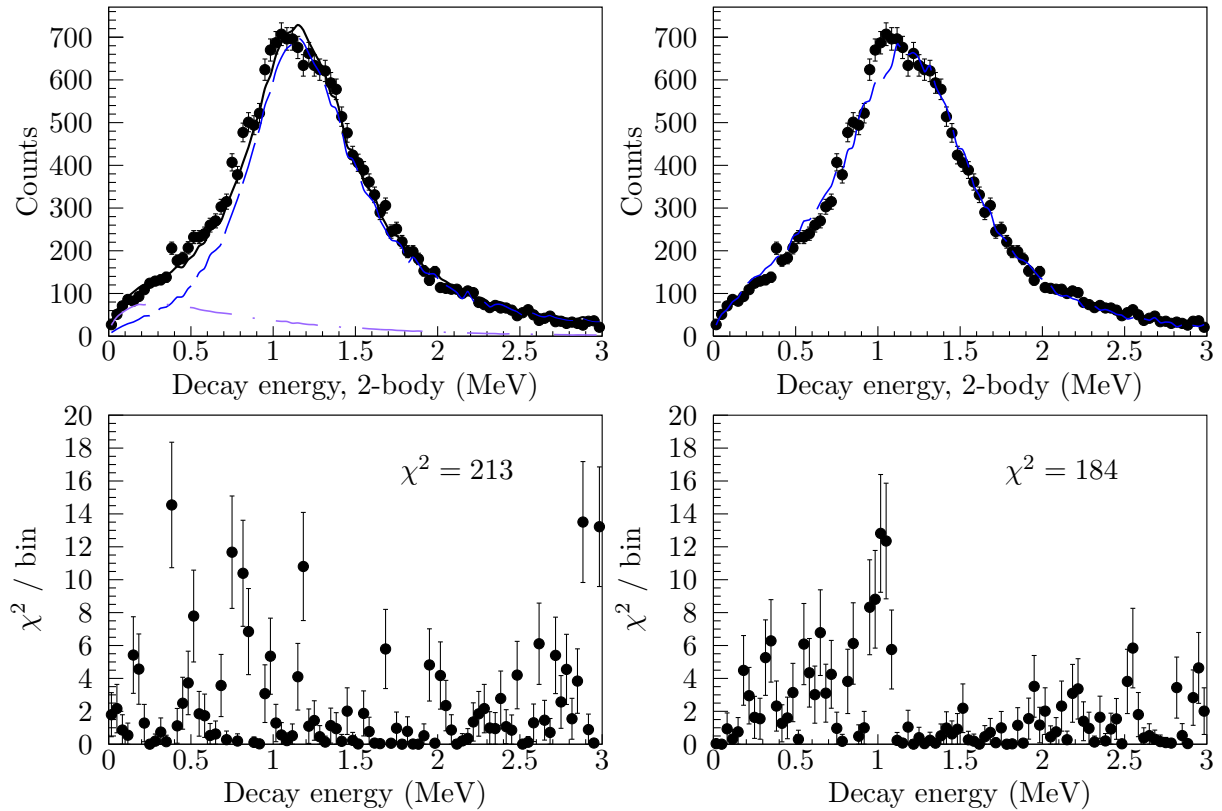


Figure 5.26: Fits of the ^{12}Be decay energy spectrum with an $\ell = 0$ (left) or $\ell = 2$ (right) lineshape. The fits are shown on the top row and the bin-by-bin contributions to the χ^2 value are shown in the bottom row.

These two potentially open decay channels also suggest that an unbound state in ^{12}Be could decay to both bound states of ^{11}Be . The parity of the unbound state can be determined by the multipolarity of the transition ($\ell = 1$) and the parity of the final state. Relevant information for the two possible decays are shown in Table 5.7.

Though a single $\ell = 0, 2$ decay does not fit the data, an admixture of decays is possible. An $\ell = 0, 2$ decay, which is of opposite multipolarity, would decay to the state left unpopulated by the $\ell = 1$ decay. Assuming a negative (positive) parity for the unbound state, the additional lineshape would have a central energy 320 keV lower (higher) than the $\ell = 1$ decay. The fit of these two lineshapes to the data would push the central energy of the $\ell = 1$ lineshape higher (lower) than 1243 keV, which would in turn push the excitation energy of 4412 (4732) keV higher (lower). The addition of a second open decay channel would keep the excitation energy within in the limits established by the $\ell = 1$ single channel decay. With this consideration in mind, the excitation energy measured here is between 4400 and 4800 keV.

Any state within this excitation energy range is also unbound to two-neutron decay and would be expected to release decay energies ranging from 738 to 1058 keV. The three-body decay energy spectrum in coincidence with ^{10}Be fragments is shown in the lower left panel of Figure 5.27. A peak is visible around 500 keV and perhaps another one around 1250 keV, but there appears to be a dip in the spectrum between 739 and 1058 keV. When the causality cut is applied (shown in the lower

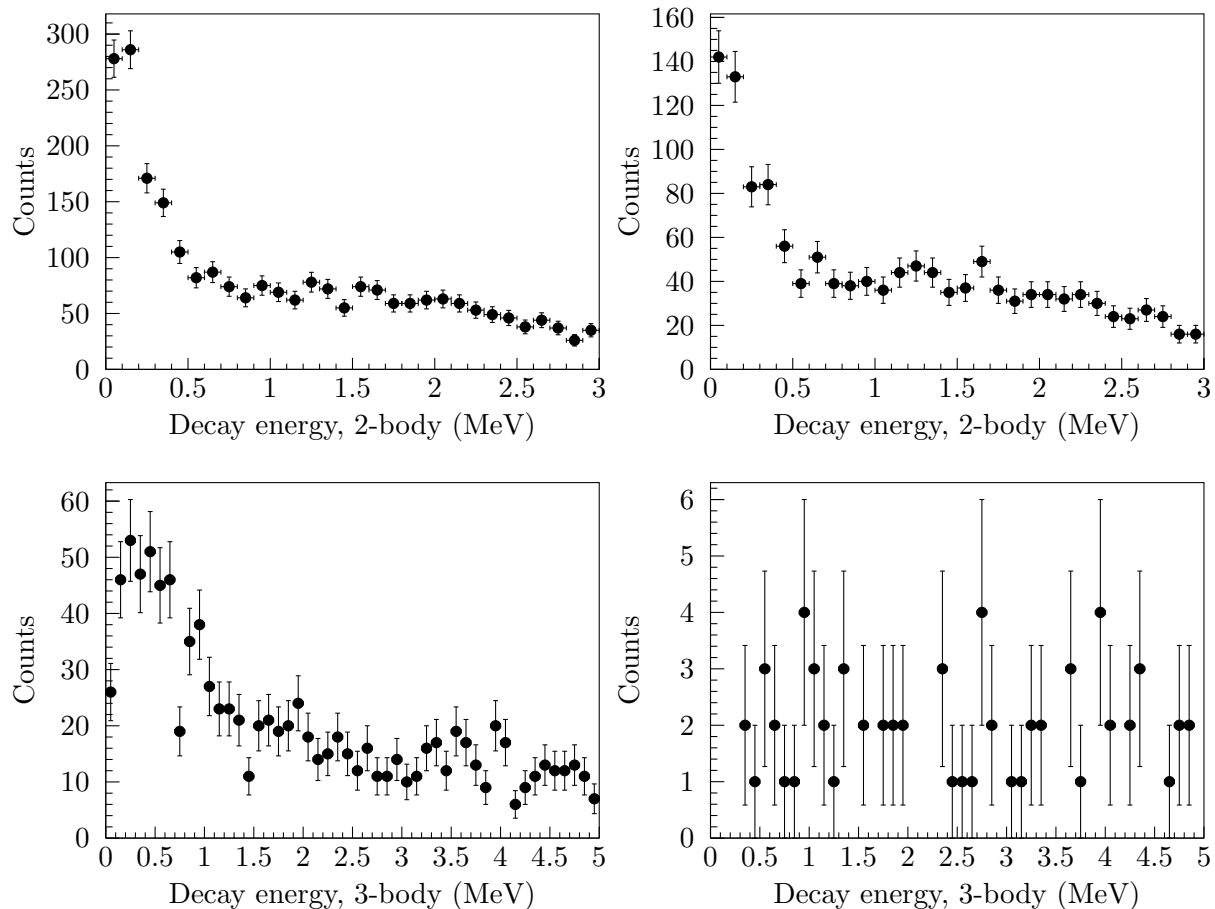


Figure 5.27: Various decay energy spectra in coincidence with ^{10}Be fragments. Upper left panel: two-body decay energy. Upper right panel: two-body decay energy spectrum, requiring only one interaction per event in MoNA-LISA. Lower left panel: three-body decay energy spectrum. Lower right panel: three-body decay energy spectrum with causality cuts applied.

right panel of Figure 5.27), very few events remain and no structure is visible. This decimation of counts suggests that very little of this unbound state in ^{12}Be decays by two neutron emission.

To put a more quantitative upper limit on the branching ratio to the two-neutron decay channel, simulations were fit to the two-body decay energy histogram, the two-body decay energy gated on only one interaction histogram, and the three-body decay energy histogram, all shown in Figure 5.27. The only histogram in Figure 5.27 not used in the fit was the causality-gated spectrum in the lower right. In addition to the two-neutron decay simulation, the fit included one-neutron decays from unbound states in ^{11}Be . These decays were taken from previous measurements of neutron decays after neutron removal reactions from ^{12}Be [109, 115] and included decays from the $5/2^+$ state and the first $3/2^-$ state in ^{11}Be to the ground state in ^{10}Be (decay energies of 1277 keV and 2690 keV, respectively) and the decay of the second $3/2^-$ state to the first excited state of ^{10}Be (with a decay energy of 80 keV). In all cases, the energies and widths were fixed and only the relative intensities of each component were varied.

The result of this fit is shown in Figure 5.28. The two-body decay energy spectra (top row)

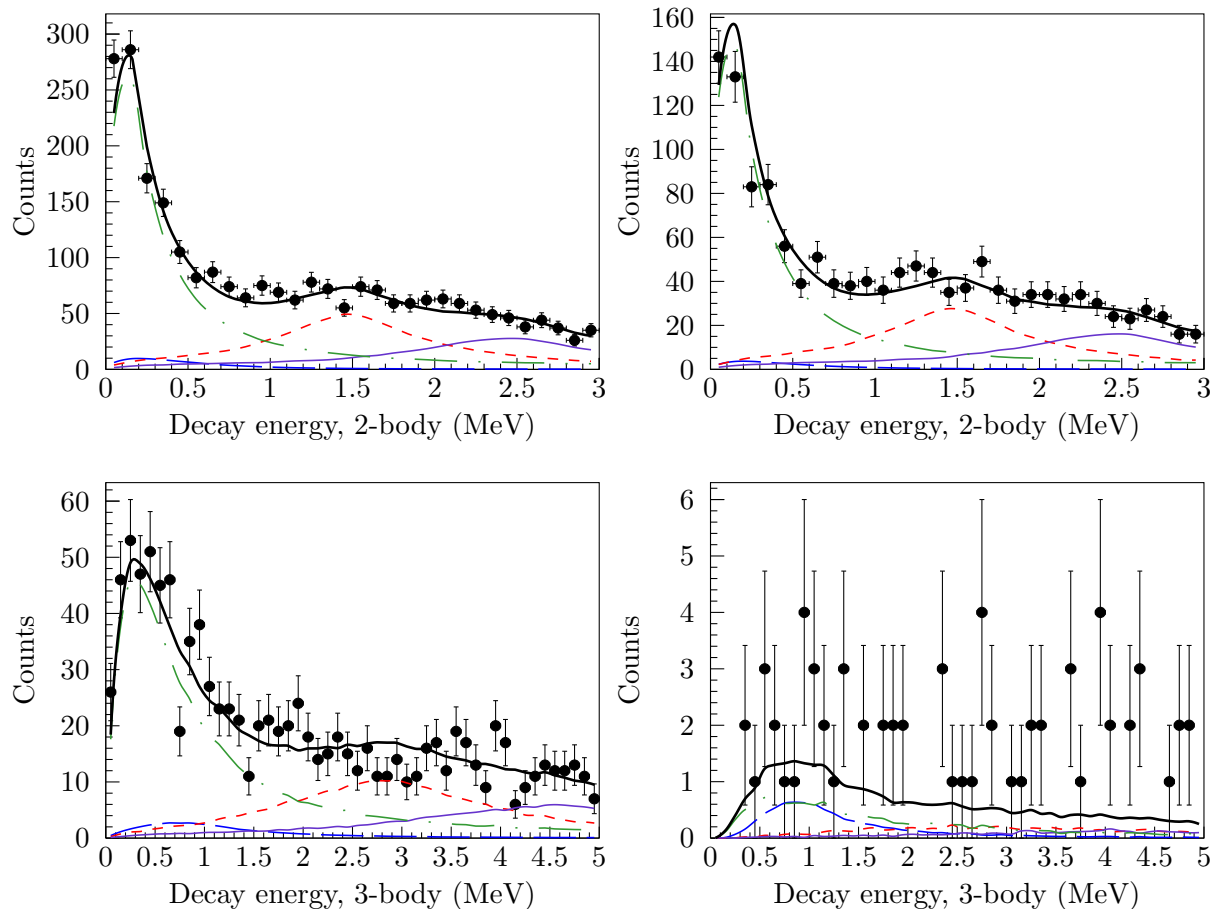


Figure 5.28: The data from Figure 5.27, fitted with simulated spectra. The green, red, and purple lineshape show single-neutron decays from ^{11}Be as used by Peters *et al.* [115]. The blue line shows a two-neutron decay. The energies and widths of each decay were fixed, leaving only the relative amplitudes to vary in the fitting. All spectra except the lower right were included in the fitting.

and the three-body ungated decay energy spectrum (bottom left panel) are dominated by signals from one-neutron decays, but a small proportion of the two-neutron decay (blue dashed line) still contributes. Combining this with the previous simulation results in Figure 5.24, the branching ratio to the two-neutron decay energy channel has a less than 5% branching ratio from the unbound state in ^{12}Be .

Although the range of possible excitation energies includes a 4580 keV decay, the total width of the state measured by Fortune *et al.* was 107 ± 17 keV [114], significantly smaller than the presently observed full-width at half-maximum (approximately 1 MeV) or the partial widths deduced from simulation. Even the inclusion of an empirical enhancement factor of 1.6 (suggested by Fortune in Ref. [158]) cannot reconcile this discrepancy. It is likely then, that this is a wider state with a similar energy that has not previously been measured.

Due to the ongoing discussion between Garrido and Fortune described in Section 1.6.2, the spins and parities of states in this regions are also of interest. The inability to fit a single $\ell = 0, 2$ decay to the data indicates that the decay must contain the emission of an $\ell = 1$ neutron. Since both of

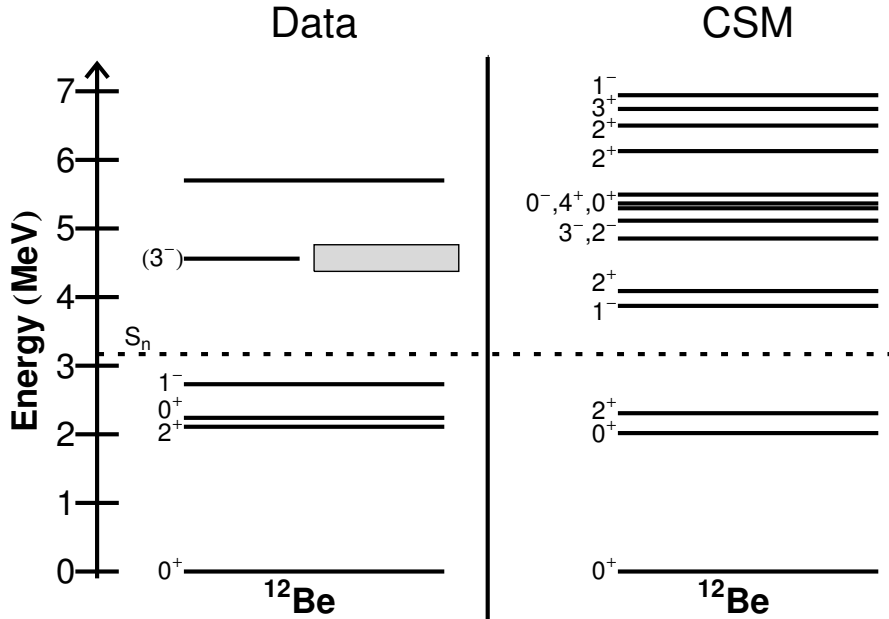


Figure 5.29: Level diagram of measured states in ^{12}Be from Figure 1.12 compared to a continuum shell model calculation of states in ^{12}Be [132]. The state presented here is represented by the grey box. The width of the box represents the error of the energy measurements.

the potential final states in ^{11}Be have a spin of $1/2$, this restricts the spin of this state to 0, 1, or 2. The restriction can be slightly strengthened by consideration of the reaction mechanism. The ground state of the ^{13}B beam is $3/2^-$. States of 0^+ and 2^+ can be populated by the knockout of a $p_{3/2}$ proton, 1^- and 2^- states can be populated by the knockout of a $s_{1/2}$ proton, and the knockout of a proton from the $p_{1/2}$ orbital can populate states with spin-parities of 1^+ and 2^+ . This leaves the 0^- state which can only be populated by coupling a $3/2^+$ hole to the $3/2^-$ ground state. This proton would have to come from the $0d_{3/2}$ orbital, which is very unlikely.

We can place a loose restriction on the parity by observing that the branching ratio to the two-neutron decay channel is very low. A recent paper by Garrido *et al.* reported calculations of branching ratios for different unbound states in ^{12}Be [122]. The positive parity states all showed significant branching to the two-neutron decay channel and the negative parity states showed significantly less. This calculation suggests then, that this new unbound state is likely of negative parity.

A continuum shell model calculation (CSM) [132] is compared to the experimental spectrum in Figure 5.29. The state measured here is shown by the grey box where the width indicates the uncertainty in the state's location. There are many predicted states in this energy range of the CSM calculation. Specifically, there is a 1^- state slightly lower in energy and a 2^- state slightly higher in energy. The calculated 1^- state likely corresponds to the bound 1^- state at just under 3 MeV excitation energy but the 2^- state is close.

The measurement of this new state doesn't contradict the previous (t, p) measurements. Fortune *et al.* stated that "Below 6 MeV excitation energy, our data allow us to set an upper limit of $30 \mu\text{b}/\text{sr}$ cross section for any possible missing narrow state of ^{12}Be " [114]. The state measured in this work, however, with a width of 634 keV, would not have been identifiable in that data set. This measurement is supported by a $^{11}\text{Be}(d, p)$ reaction reported in the PhD thesis of Johansen [159].

In that work, a neutron unbound state at an excitation energy of ≈ 4500 keV was observed. It was concluded to be the same state measured by Fortune *et al.*, but the width of the measurement (> 200 keV) was greater than that measured in the (t, p) experiment.

Finally, this state could resolve the ongoing discussion between Fortune [160] and Garrido *et al.* [123], by allowing the spin and parity of the narrow state to stand at 3^- while providing another state in that energy region that could be identified with the 1^- state calculated by Garrido *et al.*

Chapter 6

Summary and Conclusions

In this dissertation, measurements of three neutron-rich isotopes, ^{11}Li , ^{10}Li , and ^{12}Be have been reported. All three lie in the lightest known island of inversion on the chart of nuclides. In addition, ^{11}Li is a two-neutron halo nucleus whose excited states all decay by two-neutron emission to ^9Li . As one of the lighter Borromean nuclei, ^{11}Li is a testing ground for three-body models that will likely be used along the neutron drip-line at higher masses. Crucial to understanding ^{11}Li is accurately measuring the states of ^{10}Li , one of its subsystems. The unbound state measured in ^{12}Be is located near an unbound state whose spin and parity have been the subject of recent debate.

Previous measurements of unbound states in ^{11}Li suggested at least one state around 1000 keV excitation energy was present. The unbound state measured in this experiment had an excitation energy of 1210 ± 80 keV and a width greater than 1200 keV. Beyond the measurement of the energy and width of this state, Jacobi coordinate spectra and Dalitz plots were used to investigate correlations between the three decay products in order to gain insight into the decay mechanism. Jacobi coordinates constructed from the momentum vectors of the two neutrons and the daughter fragment showed a correlation between the neutrons that was stronger than that expected from a final state interaction alone.

The population of ^{10}Li from ^{12}B was expected to populate primarily positive parity states, which allowed for the measurement of low-lying positive parity states without interference from the negative parity ground state. The decay energy spectrum showed a broad peak around 500 keV decay energy. While the peak energy was consistent with previous measurements, the width was not. The decay energy spectrum was unable to be fit with a single peak and required two additional peaks to fit the spectrum and be consistent with previous measurements. A positive parity state below the 500 keV state was hinted at in previous papers but measurements have been plagued by background and interference from the ground state. The measurement of two low-lying $\ell = 1$ states at 110 ± 40 and 500 ± 100 keV decay energy are assumed to be the $1^+/2^+$ doublet from the coupling of the $0p_{3/2}$ proton to the $0p_{1/2}$ neutron. Comparison of these states with a Faddeev calculation suggests that both states of the $2^-/1^-$ doublet are below 50 keV and thus unlikely to be distinguished experimentally. A third $\ell = 1$ state was also measured at 1100 ± 100 keV.

The unbound state populated in ^{12}Be was best fit with an $\ell = 1$ decay at a decay energy of 1243 ± 20 keV. The two potential final states in ^{11}Be as well as the potential for an $\ell = 0, 2$ decay admixture complicated the assignment of the decay energy to an excitation energy in ^{12}Be . The range of potential excitation energies ranges from 4400 to 4800 keV. One state had previously been measured in this excitation energy range, at 4580 ± 5 keV, but a difference in widths (107 ± 17 keV for the 4580 keV state and 634 ± 50 for the state measured here) is evidence that the two states are not the same. Spin selectivity from the production mechanism and $\ell = 1$ best fit restricts the spin and parity of the unbound state. Although every excitation energy possible is above the two-neutron separation energy, no significant branching through the $2n$ decay channel to ^{10}Be is seen in the data. A limit of 5% branching ratio was placed on the $2n$ decay channel. Most two-neutron decays are expected to be emitted from the same orbital, so a negative-parity assignment for the unbound

state would likely produce a small branching ratio to the $2n$ channel. The most likely spin-parity assignments for the unbound state are 1^- or 2^- .

These results suggest a few other studies that could aid in understanding the complex relationships in three-body systems like those described here. A higher-statistics experiment studying the unbound structure of ^{10}Li that was able to distinguish the two low-lying $\ell = 1$ states would be helpful in confirming the single-particle energy of the $0p_{1/2}$ level. This would then be used to estimate the single-particle energy of the $1s_{1/2}$ orbital, a value which seems unlikely to be directly measurable. The more data that is gathered on ^{10}Li , the more accurate the calculations and predictions of ^{11}Li will be. Reconciling the assortment of measurements of unbound states in $^{10,11}\text{Li}$ would assist in understanding which components of a three-body system calculation are most important. With regards to the ^{12}Be system in particular, repeating this experiment with gamma-ray detection would allow the separation of multiple $1n$ decay channels and the assignment of a parity of the state as well as an excitation energy. It would also be useful to repeat Fortune's (t, p) reaction with neutron detection. Observation of the state's decay would assist in assignment of spin and parity and would also provide another way of distinguishing the two states.

REFERENCES

REFERENCES

- [1] National Nuclear Database Center. Information extracted from the Chart of Nuclides database, 2014.
- [2] W. M. Elsasser. Sur le principe de Pauli dans les noyaux. *J. Phys. le Radium*, **4**(10):549–556, October 1933.
- [3] Maria Mayer. On Closed Shells in Nuclei. *Phys. Rev.*, **74**(3):235–239, August 1948.
- [4] Otto Haxel, J. Jensen, and Hans Suess. On the “Magic Numbers” in Nuclear Structure. *Phys. Rev.*, **75**(11):1766–1766, June 1949.
- [5] Maria Goeppert Mayer. On Closed Shells in Nuclei. II. *Phys. Rev.*, **75**(12):1969–1970, June 1949.
- [6] C. R. Hoffman, B. P. Kay, and J. P. Schiffer. Neutron s states in loosely bound nuclei. *Phys. Rev. C*, **89**(6):061305, June 2014.
- [7] B. A. Brown. Islands of insight in the nuclear chart. *Physics (College Park, Md.)*, **3**:104, December 2010.
- [8] D. E. Alburger, C. Chasman, K. Jones, J. Olness, and R. Ristinen. Parity of ^{11}Be . *Phys. Rev.*, **136**(4B):B916–B919, November 1964.
- [9] C. Thibault, R. Klapisch, C. Rigaud, A. Poskanzer, R. Prieels, L. Lessard, and W. Reisdorf. Direct measurement of the masses of ^{11}Li and $^{26-32}\text{Na}$ with an on-line mass spectrometer. *Phys. Rev. C*, **12**(2):644–657, August 1975.
- [10] A. Navin, et al. Direct Evidence for the Breakdown of the $N = 8$ Shell Closure in ^{12}Be . *Phys. Rev. Lett.*, **85**(2):266–269, July 2000.
- [11] B. Bastin, et al. Collapse of the $N = 28$ Shell Closure in ^{42}Si . *Phys. Rev. Lett.*, **99**(2):022503, July 2007.
- [12] P. Adrich, et al. In-beam γ -ray spectroscopy and inclusive two-proton knockout cross section measurements at $N \approx 40$. *Phys. Rev. C*, **77**(5):054306, May 2008.

- [13] M. Stanoiu, et al. Disappearance of the $N = 14$ shell gap in the carbon isotopic chain. *Phys. Rev. C*, **78**(3):034315, September 2008.
- [14] S. Naimi, et al. Surveying the $N=40$ island of inversion with new manganese masses. *Phys. Rev. C*, **86**(1):014325, July 2012.
- [15] I. Talmi and I. Unna. Order of Levels in the Shell Model and Spin of Be^{11} . *Phys. Rev. Lett.*, **4**(9):469–470, May 1960.
- [16] D. Wilkinson and D. Alburger. Beta Decay of ^{11}Be . *Phys. Rev.*, **113**(2):563–571, January 1959.
- [17] R. Sherr and H. T. Fortune. Structure of ^{12}Be and ^{12}O ground states. *Phys. Rev. C*, **60**(6):064323, November 1999.
- [18] N. B. Shulgina, B. Jonson, and M. V. Zhukov. ^{11}Li structure from experimental data. *Nucl. Phys. A*, **825**(3-4):175–199, July 2009.
- [19] Isao Tanihata, Herve Savajols, and Rituparna Kanungo. Recent experimental progress in nuclear halo structure studies. *Prog. Part. Nucl. Phys.*, **68**:215–313, January 2013.
- [20] I. Tanihata, H. Hamagaki, O. Hashimoto, Y. Shida, N. Yoshikawa, K. Sugimoto, O. Yamakawa, T. Kobayashi, and N. Takahashi. Measurements of Interaction Cross Sections and Nuclear Radii in the Light p -Shell Region. *Phys. Rev. Lett.*, **55**(24):2676–2679, 1985.
- [21] I. Tanihata, T. Kobayashi, O. Yamakawa, S. Shimoura, K. Ekuni, K. Sugimoto, N. Takahashi, T. Shimoda, and H. Sato. Measurement of interaction cross sections using isotope beams of Be and B and isospin dependence of the nuclear radii. *Phys. Lett. B*, **206**(4):592–596, 1988.
- [22] T. Kobayashi, O. Yamakawa, K. Omata, K. Sugimoto, T. Shimoda, N. Takahashi, and I. Tanihata. Projectile Fragmentation of the Extremely Neutron-Rich Nucleus ^{11}Li at 0.79 GeV/nucleon. *Phys. Rev. Lett.*, **60**(25):2599–2602, June 1988.
- [23] P. G. Hansen and B. Jonson. The Neutron Halo of Extremely Neutron-Rich Nuclei. *Europhys. Lett.*, **4**(4), August 1987.
- [24] T. Kobayashi, et al. Electromagnetic dissociation and soft giant dipole resonance of the neutron-dripline nucleus ^{11}Li . *Phys. Lett. B*, **232**(1):51–55, November 1989.
- [25] B. V. Danilin, M. V. Zhukov, J. S. Vaagen, and J. M. Bang. Strength functions for ^6He excitations. *Phys. Lett. B*, **302**(2-3):129–133, March 1993.

- [26] M. V. Zhukov, B. V. Danilin, D. V. Fedorov, J. M. Bang, I. J. Thompson, and J. S. Vaagen. Bound state properties of Borromean halo nuclei: ${}^6\text{He}$ and ${}^{11}\text{Li}$. *Phys. Rep.*, **231**(4):151–199, August 1993.
- [27] F. M. Marqués, et al. Two-neutron interferometry as a probe of the nuclear halo. *Phys. Lett. B*, **476**(3-4):219–225, March 2000.
- [28] V. I. Goldansky. On neutron-deficient isotopes of light nuclei and the phenomena of proton and two-proton radioactivity. *Nucl. Phys.*, **19**(null):482–495, September 1960.
- [29] M. Pfützner, et al. First evidence for the two-proton decay of ${}^{45}\text{Fe}$. *Eur. Phys. J. A - Hadron. Nucl.*, **14**(3):279–285, July 2002.
- [30] J. Giovinazzo, et al. Two-Proton Radioactivity of ${}^{45}\text{Fe}$. *Phys. Rev. Lett.*, **89**(10):102501, August 2002.
- [31] R. J. Charity, et al. Investigations of three-, four-, and five-particle decay channels of levels in light nuclei created using a ${}^9\text{C}$ beam. *Phys. Rev. C*, **84**(1):014320, July 2011.
- [32] O. V. Bochkarev, L. V. Chulkov, A. A. Korshennikov, E. A. Kuz'min, I. G. Mukha, and G. B. Yankov. Democratic decay of ${}^6\text{Be}$ states. *Nucl. Phys. A*, **505**(2):215–240, December 1989.
- [33] Roderick V. Reid. Local phenomenological nucleon-nucleon potentials. *Ann. Phys. (N. Y.)*, **50**(3):411–448, December 1968.
- [34] K. Hagino, A. Vitturi, F. Pérez-Bernal, and H. Sagawa. Two-neutron halo nuclei in one dimension: dineutron correlation and breakup reaction. *J. Phys. G Nucl. Part. Phys.*, **38**(1):015105, January 2011.
- [35] R. H. Dalitz. CXII. On the analysis of τ -meson data and the nature of the τ -meson. *Philos. Mag. Ser. 7*, **44**(357):1068–1080, 1953.
- [36] R. H. Dalitz. Decay of τ Mesons of Known Charge. *Phys. Rev.*, **94**(4):1046–1051, May 1954.
- [37] F. Marqués, et al. Three-body correlations in Borromean halo nuclei. *Phys. Rev. C*, **64**(6):061301, November 2001.
- [38] K. Wimmer, et al. Correlations in Intermediate Energy Two-Proton Removal Reactions. *Phys. Rev. Lett.*, **109**(20):202505, November 2012.
- [39] B. V. Danilin, T. Rogde, J. Vaagen, I. Thompson, and M. V. Zhukov. Three-body continuum spatial correlations in Borromean halo nuclei. *Phys. Rev. C*, **69**(2):024609, February 2004.

- [40] B. V. Danilin, J. Vaagen, T. Rogde, S. Ershov, I. Thompson, and M. V. Zhukov. Three-body continuum energy correlations in Borromean halo nuclei. II. *Phys. Rev. C*, **73**(5):054002, May 2006.
- [41] B. V. Danilin, J. Vaagen, T. Rogde, S. Ershov, I. Thompson, and M. V. Zhukov. Three-body continuum energy correlations in Borromean halo nuclei. III. Short-range external fields. *Phys. Rev. C*, **76**(6):064612, December 2007.
- [42] C. Romero-Redondo, E. Garrido, D. V. Fedorov, and A. S. Jensen. Isomeric halo-states in ^{12}Be and ^{11}Li . *Phys. Lett. B*, **660**(1-2):32–36, February 2008.
- [43] R. Álvarez Rodríguez, H. Fynbo, A. Jensen, and E. Garrido. Distinction between Sequential and Direct Three-Body Decays. *Phys. Rev. Lett.*, **100**(19):192501, May 2008.
- [44] L. V. Grigorenko, et al. Complete correlation studies of two-proton decays: ^6Be and ^{45}Fe . 2009.
- [45] L. V. Grigorenko, et al. Three-body decay of ^6Be . *Phys. Rev. C*, **80**(3):034602, September 2009.
- [46] L. V. Grigorenko, I. A. Egorova, M. V. Zhukov, R. J. Charity, and K. Miernik. Two-proton radioactivity and three-body decay. V. Improved momentum distributions. *Phys. Rev. C*, **82**(1):014615, July 2010.
- [47] I. A. Egorova, et al. Democratic Decay of ^6Be Exposed by Correlations. *Phys. Rev. Lett.*, **109**(20):202502, November 2012.
- [48] Z. Kohley, et al. First observation of the ^{13}Li ground state. *Phys. Rev. C*, **87**(1):011304, January 2013.
- [49] L. V. Grigorenko, I. G. Mukha, and M. V. Zhukov. Lifetime and Fragment Correlations for the Two-Neutron Decay of ^{26}O Ground State. *Phys. Rev. Lett.*, **111**(4):042501, July 2013.
- [50] C. R. Hoffman, et al. Observation of a two-neutron cascade from a resonance in ^{24}O . *Phys. Rev. C*, **83**:031303(R), 2011.
- [51] M. Smith, et al. First Penning-Trap Mass Measurement of the Exotic Halo Nucleus ^{11}Li . *Phys. Rev. Lett.*, **101**(20), 2008.
- [52] S. Shimoura, et al. Isobaric analog state of ^{11}Li . *Nucl. Phys. A*, **630**(1-2):387–393, February 1998.

- [53] M. Thoennesen, et al. Population of ^{10}Li by fragmentation. *Phys. Rev. C*, **59**(1):111–117, 1999.
- [54] H. B. Jeppesen, et al. Study of ^{10}Li via the $^9\text{Li}(^2\text{H}, p)$ reaction at REX-ISOLDE. *Phys. Lett. B*, **642**(5-6):449–454, November 2006.
- [55] H. Simon, et al. Systematic investigation of the drip-line nuclei ^{11}Li and ^{14}Be and their unbound subsystems ^{10}Li and ^{13}Be . *Nucl. Phys. A*, **791**(3-4):267–302, July 2007.
- [56] Yu. Aksyutina, et al. Lithium isotopes beyond the drip line. *Phys. Lett. B*, **666**(5):430–434, September 2008.
- [57] E. Arnold, J. Bonn, R. Gegenwart, W. Neu, R. Neugart, E.-W. Otten, G. Ulm, and K. Wendt. Nuclear spin and magnetic moment of ^{11}Li . *Phys. Lett. B*, **197**(3):311–314, October 1987.
- [58] R. Middleton and D. J. Pullen. A study of some (t, p) reactions (I). Method and results for ^7Li , ^{10}B and ^{11}B . *Nucl. Phys.*, **51**:50–62, March 1964.
- [59] P. G. Young and Richard Stokes. New States in ^9Li from the Reaction $^7\text{Li}(t, p)^9\text{Li}$. *Phys. Rev. C*, **4**(5):1597–1601, November 1971.
- [60] F. Ajzenberg-Selove, E. Flynn, and Ole Hansen. (t, p) reactions on ^4He , ^6Li , ^7Li , ^9Be , ^{10}B , ^{11}B , and ^{12}C . *Phys. Rev. C*, **17**(4):1283–1293, April 1978.
- [61] A. A. Korshennikov, et al. Spectroscopy of the halo nucleus ^{11}Li by an experimental study of $^{11}\text{Li}+p$ collisions. *Phys. Rev. C*, **53**(2):R537–R540, 1996.
- [62] A. A. Korshennikov, et al. $L = 1$ Excitation in the Halo Nucleus ^{11}Li . *Phys. Rev. Lett.*, **78**(12):2317–2320, March 1997.
- [63] D. Sackett, et al. Electromagnetic excitation of ^{11}Li . *Phys. Rev. C*, **48**(1):118–135, 1993.
- [64] M. Zinser, et al. Invariant-mass spectroscopy of ^{10}Li and ^{11}Li . *Nucl. Phys. A*, **619**(1-2):151–176, June 1997.
- [65] M. G. Gornov, Yu. Gurov, S. Lapushkin, P. Morokhov, V. Pechkurov, T. K. Pedlar, Kamal K. Seth, J. Wise, and D. Zhao. Excited States of ^{11}Li . *Phys. Rev. Lett.*, **81**(20):4325–4328, 1998.
- [66] Yu. Gurov, E. Kalinin, V. Karpukhin, S. Lapushkin, I. Laukhin, V. Pechkurov, V. Sandukovsky, B. A. Chernyshev, and T. Shchurenkova. Heavy lithium isotope $^{11,12}\text{Li}$ production in pion absorption reactions on a ^{14}C radioactive target. *Bull. Russ. Acad. Sci. Phys.*, **74**(4):433–436, April 2010.

- [67] Toshio Kobayashi. Nuclear structure experiments on ^{11}Li . *Nucl. Phys. A*, **553**:465–472, March 1993.
- [68] H. G. Bohlen, et al. Spectroscopy of excited states of ^{11}Li . *Zeitschrift fur Phys. A Hadron. Nucl.*, **351**(1):7–8, March 1995.
- [69] M. J. G. Borge, et al. Elucidating halo structure by β decay: $\beta\gamma$ from the ^{11}Li decay. *Phys. Rev. C*, **55**(1):R8–R11, January 1997.
- [70] H. Simon, et al. Direct Experimental Evidence for Strong Admixture of Different Parity States in ^{11}Li . *Phys. Rev. Lett.*, **83**(3):496–499, July 1999.
- [71] I. Tanihata, et al. Measurement of the Two-Halo Neutron Transfer Reaction $^1\text{H}(^{11}\text{Li}, ^9\text{Li})^3\text{H}$ at 3A MeV. *Phys. Rev. Lett.*, **100**(19):192502, May 2008.
- [72] B. A. Chernyshev, Yu. B. Gurov, V. S. Karpukhin, L. Yu. Korotkova, S. V. Lapushkin, R. V. Pritula, and V. G. Sandukovsky. Spectroscopy of the heavy lithium isotopes $^{10-12}\text{Li}$. *Eur. Phys. J. A*, **49**(6):68, June 2013.
- [73] T Kobayashi. Projectile fragmentation of exotic nuclear beams. *Nucl. Phys. A*, **538**:343–352, March 1992.
- [74] K. Ieki, et al. Coulomb dissociation of ^{11}Li . *Phys. Rev. Lett.*, **70**(6):730–733, February 1993.
- [75] S. Shimoura, T. Nakamura, M. Ishihara, N. Inabe, T. Kobayashi, T. Kubo, R.H. Siemssen, I. Tanihata, and Y. Watanabe. Coulomb dissociation reaction and correlations of two halo neutrons in ^{11}Li . *Phys. Lett. B*, **348**(1-2):29–34, March 1995.
- [76] T. Nakamura, et al. Observation of Strong Low-Lying E1 Strength in the Two-Neutron Halo Nucleus ^{11}Li . *Phys. Rev. Lett.*, **96**(25):252502, June 2006.
- [77] K. Ieki, et al. Is there a bound dineutron in ^{11}Li ? *Phys. Rev. C*, **54**(4):1589–1591, October 1996.
- [78] Yu. Aksyutina, et al. Study of the ^{14}Be Continuum: Identification and Structure of its Second 2^+ State. *Phys. Rev. Lett.*, **111**(24):242501, December 2013.
- [79] S. Karataglidis, P. Hansen, B. A. Brown, K. Amos, and P. Dortmans. Is There an Excited State in ^{11}Li at Ex=1.3 MeV? *Phys. Rev. Lett.*, **79**(8):1447–1450, August 1997.
- [80] I. J. Thompson and M. V. Zhukov. Effects of ^{10}Li virtual states on the structure of ^{11}Li . *Phys. Rev. C*, **49**(4):1904–1907, 1994.

- [81] A. Cobis, D. Fedorov, and A. Jensen. Three-body halos.V. Computations of continuum spectra for Borromean nuclei. *Phys. Rev. C*, **58**(3):1403–1421, September 1998.
- [82] E. Garrido, A. Cobis, D. V. Fedorov, and A. S. Jensen. Structure and reactions of three-body Borromean halos. *Nucl. Phys. A*, **630**(1-2):409–416, February 1998.
- [83] I. Brida, F. M. Nunes, and B. A. Brown. Effects of deformation in the three-body structure of ^{11}Li . *Nucl. Phys. A*, **775**(1-2):23–34, August 2006.
- [84] C. R. Romero-Redondo, E. Garrido, D. V. Fedorov, and A. S. Jensen. Three-body structure of low-lying ^{12}Be states. *Phys. Rev. C*, **77**(5):054313, 2008.
- [85] G. F. Bertsch and H Esbensen. Pair correlations near the neutron drip line. *Ann. Phys. (N. Y.)*, **209**(2):327–363, August 1991.
- [86] H. Esbensen and G. F. Bertsch. Soft dipole excitations in ^{11}Li . *Nucl. Phys. A*, **542**(2):310–340, June 1992.
- [87] H. Esbensen, G. F. Bertsch, and K. Hencken. Application of contact interactions to Borromean halos. *Phys. Rev. C*, **56**(6):3054–3062, December 1997.
- [88] K. Hagino and H. Sagawa. Pairing correlations in nuclei on the neutron-drip line. *Phys. Rev. C*, **72**(4), 2005.
- [89] K. Hagino, H. Sagawa, T. Nakamura, and S. Shimoura. Two-particle correlations in continuum dipole transitions in Borromean nuclei. *Phys. Rev. C*, **80**(3):031301, September 2009.
- [90] Shigeyoshi Aoyama, Takayuki Myo, Kiyoshi Kat, and Kiyomi Ikeda. Coulomb breakup and pairing excitation of the two-neutron halo nucleus ^{11}Li . *Phys. Scr.*, **T125**(T125):100–102, July 2006.
- [91] E. Garrido, D. V. Fedorov, and A. S. Jensen. Momentum distributions of particles from three-body halo fragmentation: Final state interactions. *Phys. Rev. C*, **53**(6):3159–3162, June 1996.
- [92] K. H. Wilcox, R. B. Weisenmiller, G. J. Wozniak, N. A. Jelley, D. Ashery, and J. Cerny. The (^9Be , ^8B) reaction and the unbound nuclide ^{10}Li . *Phys. Lett. B*, **59**(2):142–144, 1975.
- [93] A. I. Amelin, et al. Production of ^{10}Li in absorption of stopped π^- mesons by ^{11}B nuclei. *Sov. J. Nucl. Phys.*, **52**(5):782–783, 1990.
- [94] B.M. Young, et al. Low-lying structure of ^{10}Li in the reaction $^{11}\text{B}(^7\text{Li}, ^8\text{B})^{10}\text{Li}$. *Phys. Rev. C*, **49**(1):279–283, January 1994.

- [95] M. Zinser, et al. Study of the Unstable Nucleus ^{10}Li in Stripping Reactions of the Radioactive Projectiles ^{11}Be and ^{11}Li . *Phys. Rev. Lett.*, **75**(9):1719–1722, 1995.
- [96] T. Kobayashi, K. Yoshida, A. Ozawa, I. Tanihata, A. A. Korshennikov, E. Nikolski, and T. Nakamura. Quasifree nucleon-knockout reactions from neutron-rich nuclei by a proton target: $p(^6\text{He},pn)^5\text{He}$, $p(^{11}\text{Li},pn)^{10}\text{Li}$, $p(^6\text{He},2p)^5\text{H}$, and $p(^{11}\text{Li},2p)^{10}\text{He}$. *Nucl. Phys. A*, **616**(1-2):223–230, April 1997.
- [97] M. G. Gornov, Yu. B. Gurov, S. V. Lapushkin, P. V. Morokhov, V. A. Pechkurov, K. Seth, T. Pedlar, J. Wise, and D. Zhao. Spectroscopy of $^7,8\text{He}$, ^{10}Li , and ^{13}Be nuclei in stopped π^- meson absorption reactions. *Bull. Russ. Acad. Sci. Phys.*, **62**(11):1781–1789, 1998.
- [98] J. A. Caggiano, D. Bazin, W. Benenson, B. Davids, B. M. Sherrill, M. Steiner, J. Yurkon, A. F. Zeller, and B. Blank. Spectroscopy of the ^{10}Li nucleus. *Phys. Rev. C*, **60**(6), 1999.
- [99] H. G. Bohlen, A. Blazevic, B. Gebauer, W. Von Oertzen, S. Thummerer, R. Kalpakchieva, S. M. Grimes, and T. N. Massey. Spectroscopy of exotic nuclei with multi-nucleon transfer reactions. *Prog. Part. Nucl. Phys.*, **42**:17–26, January 1999.
- [100] L. Chen, B. Blank, B. A. Brown, M. Chartier, A. Galonsky, P. G. Hansen, and M. Thoennessen. Evidence for an $l=0$ ground state in ^9He . *Phys. Lett. B*, **505**(1-4):21–26, April 2001.
- [101] P. Santi, et al. Structure of the ^{10}Li nucleus investigated via the $^9\text{Li}(d,p)^{10}\text{Li}$ reaction. *Phys. Rev. C*, **67**(2), 2003.
- [102] H. Simon, et al. Two- and three-body correlations: breakup of halo nuclei. *Nucl. Phys. A*, **734**:323–326, April 2004.
- [103] Yu. B. Gurov, E. M. Kalinin, V. S. Karpukhin, L. Yu. Korotkova, S. V. Lapushkin, I. V. Laukhin, P. V. Morokhov, V. G. Sandukovsky, and B. A. Chernyshev. Spectroscopy of the ^{10}Li isotope in stopped pion absorption reactions on a ^{14}C radioactive target. *Bull. Russ. Acad. Sci. Phys.*, **75**(4):459–462, May 2011.
- [104] A. Poskanzer, S. Cospser, Earl Hyde, and Joseph Cerny. New Isotopes: ^{11}Li , ^{14}B , and ^{15}B . *Phys. Rev. Lett.*, **17**(25):1271–1274, December 1966.
- [105] F. M. Nunes, J. A. Christley, I. J. Thompson, R. C. Johnson, and V. D. Efros. Core excitation in three-body systems: Application to ^{12}Be . *Nucl. Phys. A*, **609**(1):43–73, 1996.
- [106] H. Iwasaki, et al. Quadrupole deformation of ^{12}Be studied by proton inelastic scattering. *Phys. Lett. B*, **481**(1):7–13, 2000.
- [107] H. Iwasaki, et al. Low-lying intruder 1^- state in ^{12}Be and the melting of the $N = 8$ shell closure. *Phys. Lett. B*, **491**(1-2):8–14, October 2000.

- [108] S. Shimoura, et al. Isomeric 0^+ state in ^{12}Be . *Phys. Lett. B*, **560**(1-2):31–36, May 2003.
- [109] S. D. Pain, et al. Structure of ^{12}Be : Intruder d -Wave Strength at $N = 8$. *Phys. Rev. Lett.*, **96**(3):032502, 2006.
- [110] R. Meharchand, et al. Probing Configuration Mixing in ^{12}Be with Gamow-Teller Transition Strengths. *Phys. Rev. Lett.*, **108**(12):122501, March 2012.
- [111] D. E. Alburger, D. P. Balamuth, J. M. Lind, L. Mulligan, K. C. Young, R. W. Zurmühle, and R. Middleton. Core excited $T = 2$ levels in $A = 12$ from studies of ^{12}Be . *Phys. Rev. C*, **17**(5):1525–1530, May 1978.
- [112] J. G. Johansen, et al. Experimental study of bound states in ^{12}Be through low-energy $^{11}\text{Be}(d, p)$ -transfer reactions. *Phys. Rev. C*, **88**(4):044619, October 2013.
- [113] S. Shimoura, et al. Lifetime of the isomeric state in ^{12}Be . *Phys. Lett. B*, **654**(3-4):87–91, October 2007.
- [114] H. T. Fortune, G.-B. Liu, and D. E. Alburger. $(sd)^2$ states in ^{12}Be . *Phys. Rev. C*, **50**(3):1355–1359, September 1994.
- [115] W. A. Peters, et al. Neutron knockout of ^{12}Be populating neutron-unbound states in ^{11}Be . *Phys. Rev. C*, **83**(5):057304, May 2011.
- [116] J. H. Kelley, E. Kwan, J. E. Purcell, C. G. Sheu, and H. R. Weller. Energy levels of light nuclei $A = 11$. *Nucl. Phys. A*, **880**:88–195, 2012.
- [117] G. Audi, O. Bersillon, J. Blachot, and A. H. Wapstra. The NUBASE evaluation of nuclear and decay properties. *Nucl. Phys. A*, **624**(1):1–124, September 1997.
- [118] M. Wang, G. Audi, A.H. Wapstra, F.G. Kondev, M. MacCormick, X. Xu, and B. Pfeiffer. The Ame2012 atomic mass evaluation. *Chinese Phys. C*, **36**(12):1603–2014, December 2012.
- [119] D. E. Alburger, S. Mordechai, H. T. Fortune, and R. Middleton. Mass and excited states of ^{12}Be . *Phys. Rev. C*, **18**(6):2727–2730, December 1978.
- [120] H. G. Bohlen, W. Von Oertzen, T. Z. Kokalova, C. H. Schulz, R. Kalpakchieva, T.N. Massey, and M. Milin. Band Structures in ^{12}Be : Experimental Results. *Int. J. Mod. Phys. E*, **17**(10):2067–2070, November 2008.
- [121] H. T. Fortune and R. Sherr. Structure of $2^+, T = 2$ states in $A = 12$ nuclei. *Phys. Rev. C*, **83**(4):044313, April 2011.

- [122] E. Garrido, A. S. Jensen, D. V. Fedorov, and J. G. Johansen. Three-body properties of low-lying ^{12}Be resonances. *Phys. Rev. C*, **86**(2):024310, August 2012.
- [123] E. Garrido, A. S. Jensen, D. V. Fedorov, and J. G. Johansen. Reply to Comment on Three-body properties of low-lying ^{12}Be resonances. *Phys. Rev. C*, **88**(3):039802, September 2013.
- [124] D.L. Auton. Direct reactions on ^{10}Be . *Nucl. Phys. A*, **157**(1):305–322, 1970.
- [125] T. Aumann, et al. One-Neutron Knockout from Individual Single-Particle States of ^{11}Be . *Phys. Rev. Lett.*, **84**(1):35–38, January 2000.
- [126] R. Palit, et al. Exclusive measurement of breakup reactions with the one-neutron halo nucleus ^{11}Be . *Phys. Rev. C*, **68**(3):034318, September 2003.
- [127] G. Breit and E. Wigner. Capture of Slow Neutrons. *Phys. Rev.*, **49**(7):519–531, April 1936.
- [128] John Markus Blatt and Victor F. Weisskopf. *Theoretical Nuclear Physics*. Courier Dover Publications, 1952.
- [129] A. M. Lane and R. G. Thomas. R-Matrix Theory of Nuclear Reactions. *Rev. Mod. Phys.*, **30**(2):257–353, 1958.
- [130] E. I. Dolinsky, P. O. Dzhamalov, and A. M. Mukhamedzhanov. Peripheral-model approach to stripping into resonant states. *Nucl. Phys. A*, **202**(1):97–122, February 1973.
- [131] Ian J. Thompson and Filomena M. Nunes. *Nuclear Reactions for Astrophysics*. Cambridge University Press, New York, 1 edition, 2009.
- [132] Alexander Volya and Vladimir Zelevinsky. Continuum shell model. *Phys. Rev. C*, **74**(6):064314, December 2006.
- [133] Alexander Volya. Physics of unstable nuclei: from structure to sequential decays. *EPJ Web Conf.*, **38**:03003, December 2012.
- [134] A. Bohr and B. R. Mottelson. *Nuclear Structure*, volume 1. W.A. Benjamin, Inc., 1969.
- [135] F. Marti. Commissioning of the Coupled Cyclotron system at NSCL. In *AIP Conf. Proc.*, volume 600, pages 64–68. AIP, December 2001.
- [136] D. J. Morrissey, B. M. Sherrill, M. Steiner, A. Stolz, and I. Wiedenhoever. Commissioning the A1900 projectile fragment separator. *Nucl. Instruments Methods Phys. Res. Sect. B Beam Interact. with Mater. Atoms*, **204**:90–96, May 2003.

- [137] Isao Tanihata. Radioactive beam facilities and their physics program. *Nucl. Phys. A*, **553**:361–372, 1993.
- [138] M. D. Bird, S. J. Kenney, J. Toth, H. W. Weijers, J. C. DeKamp, M. Thoennessen, and A. F. Zeller. System Testing and Installation of the NHMFL/NSCL Sweeper Magnet. *IEEE Trans. Applied Supercond.*, **15**(2):1252–1254, June 2005.
- [139] Gregory Arthur Christian. *Spectroscopy of Neutron-Unbound Fluorine*. PhD thesis, Michigan State University, 2011.
- [140] Ichita Endo, Tatsuo Kawamoto, Yoshinari Mizuno, Takashi Ohsugi, Takashi Taniguchi, and Tohru Takeshita. Systematic shifts of evaluated charge centroid for the cathode read-out multiwire proportional chamber. *Nucl. Instruments Methods Phys. Res.*, **188**(1):51–58, September 1981.
- [141] Nathan Henry Frank. *Spectroscopy of Neutron Unbound States in Neutron Rich Oxygen Isotopes*. PhD thesis, Michigan State University, 2006.
- [142] William Alexander Peters. *Study of Neutron Unbound States Using the Modular Neutron Array (MoNA)*. PhD thesis, Michigan State University, 2007.
- [143] J. M. Paul. The density effect and rate of energy loss in common plastic scintillators. *Nucl. Instruments Methods*, **96**(1):51–59, September 1971.
- [144] S. Matsuno, et al. Cosmic-ray muon spectrum up to 20 TeV at 89 zenith angle. *Phys. Rev. D*, **29**(1):1–23, January 1984.
- [145] N. Frank, A. Schiller, D. Bazin, W. A. Peters, and M. Thoennessen. Reconstruction of nuclear charged fragment trajectories from a large-gap sweeper magnet. *Nucl. Instruments Methods Phys. Res. Sect. A Accel. Spectrometers, Detect. Assoc. Equip.*, **580**(3):1478–1484, October 2007.
- [146] S. Agostinelli, et al. Geant4—a simulation toolkit. *Nucl. Instruments Methods Phys. Res. Sect. A Accel. Spectrometers, Detect. Assoc. Equip.*, **506**(3):250–303, July 2003.
- [147] J. Allison, et al. Geant4 developments and applications. *IEEE Trans. Nucl. Sci.*, **53**(1):270–278, February 2006.
- [148] Z. Kohley, et al. Modeling interactions of intermediate-energy neutrons in a plastic scintillator array with Geant4. *Nucl. Instruments Methods Phys. Res. Sect. A Accel. Spectrometers, Detect. Assoc. Equip.*, **682**:59–65, 2012.
- [149] A. S. Goldhaber. Statistical models of fragmentation processes. *Phys. Lett. B*, **53**(4):306–308, December 1974.

- [150] K. Van Bibber, et al. Evidence for Orbital Dispersion in the Fragmentation of ^{16}O at 90 and 120 MeV/Nucleon. *Phys. Rev. Lett.*, **43**(12):840–844, September 1979.
- [151] O. Tarasov. Analysis of momentum distributions of projectile fragmentation products. *Nucl. Phys. A*, **734**:536–540, April 2004.
- [152] Frederick E. James. Monte Carlo phase space. In *Acad. Train. Lect.*, page 41, Geneva, Switzerland, 1968. CERN.
- [153] D. Gonzalez Trotter, et al. Neutron-deuteron breakup experiment at $E_n = 13$ MeV: Determination of the 1S_0 neutron-neutron scattering length a_{nn} . *Phys. Rev. C*, **73**(3):034001, March 2006.
- [154] C. A. Bertulani. *Nuclear Physics in a Nutshell*. Princeton University Press, Princeton, New Jersey, 2007.
- [155] T. Al Kalanee, et al. Structure of unbound neutron-rich ^9He studied using single-neutron transfer. *Phys. Rev. C*, **88**(3):034301, September 2013.
- [156] F. Ajzenberg-Selove. Energy levels of light nuclei $A = 1112$. *Nucl. Phys. A*, **506**(1):1–158, January 1990.
- [157] F. Ajzenberg-Selove. Energy levels of light nuclei $A = 1315$. *Nucl. Phys. A*, **523**(1):1–196, February 1991.
- [158] H. T. Fortune and R. Sherr. Consistent description of ^{11}Be and ^{12}Be and of the $^{11}\text{Be}(d, p)^{12}\text{Be}$ reaction. *Phys. Rev. C*, **85**(5):051303, May 2012.
- [159] Jacob Graversen Johansen. *Transfer reaction study of neutron rich beryllium isotopes*. PhD thesis, Aarhus University, 2012.
- [160] H. T. Fortune. Comment on Three-body properties of low-lying ^{12}Be resonances. *Phys. Rev. C*, **88**(3):039801, September 2013.